

BORON ACTIVATION AND DIFFUSION DURING MILLISECOND ANNEALING
OF ION-IMPLANTED SILICON

By

KEVIN ANDREW GABLE

A DISSERTATION PRESENTED TO THE GRADUATE SCHOOL
OF THE UNIVERSITY OF FLORIDA IN PARTIAL FULFILLMENT
OF THE REQUIREMENTS FOR THE DEGREE OF
DOCTOR OF PHILOSOPHY

UNIVERSITY OF FLORIDA

2004

Copyright 2004

by

Kevin Andrew Gable

ACKNOWLEDGMENTS

Not many people look forward to writing the acknowledgment section of their Ph.D. dissertation during their freshman year of college; however, I did. The list began right after my first class of Introduction to Materials Science and Engineering, taught by my future advisor Prof. Kevin S. Jones. Moments like that are few and far between, and I cannot thank Kevin enough for sharing with me his enthusiasm for the subject. I am also very grateful to Prof. Mark E. Law, who provided a great deal of insight regarding this research. I would also like to thank Profs. Cammy Abernathy, Paul Holloway, David Norton, and Dr. Lance Robertson for serving as members of my supervisory committee.

I would like to acknowledge the Semiconductor Research Corporation (SRC) for supporting me through the Graduate Fellowship Program (GFP). I am also indebted to Drs. Doug Mercer and Lance Robertson for providing me with two outstanding internship opportunities, with the Silicon Technology and Development (SiTD) group of Texas Instruments, Inc. (Dallas, TX); under the mentorship of Drs. Amitabh Jain and Majid Mansoori. The experience I gained from both of those opportunities was invaluable, and will not be forgotten. I would like to acknowledge Andrei Li-Fatou and Tommy Grey of Texas Instruments, Inc. for the great deal of SIMS data analysis they provided throughout this work. I am especially grateful for the material processing provided by Tom Rhodes and Larry Larson at SEMATECH in Austin, TX. I would also like to acknowledge Prof. Alexander Angerhofer from the Department of Chemistry for

his assistance in obtaining the electron paramagnetic resonance data contained throughout this work.

I am personally thankful for the members of the Software and Analysis of Advanced Materials Processing (SWAMP) center for providing an environment that encourages individual thought but relies on teamwork. In particular, I would like to thank Mark Clark for our discussions (and more importantly, his advice). I would also like to thank Carrie Ross for her assistance in processing material, and preparing samples on my behalf. Finally, I would like to thank both Ljubo Radic and Russ Robison for their assistance with the simulation work in this dissertation. I would like to acknowledge Sharon Carter for all her help; she made graduate school a much more enjoyable experience.

Although this work would be incomplete without the professional assistance provided by my colleagues, it would never have started had it not been for my friends and family. I would like to thank Gabriel Gawen for sharing with me his time (and more importantly his attitude; I have yet to find another like it). I am also grateful for Nicholas Nylund and his ability to affect people. Special thanks go to Patrick Cosgriff, with whom I've shared an apartment and an unforgettable college experience. I would also like to thank Joshua Calapa for making college so enjoyable, and also updating my music library when it needed it the most. I am personally thankful for Andrew King, who provided a source of entertainment throughout my graduate career. Special thanks go to my loving grandparents Helen and Thurmond Gable, and Evelyn and Richard Bordner. Most importantly, I would like to thank my parents Rev. Pamela Jo Gable and Rhett Eric Gable; I cannot tell them how proud I am to have them as parents, and how important

they are to me. Finally, I thank my brother, Brian Matthew Gable; once a source of bruises, now a source of inspiration. If there is one thing I know, it's that life is not the same without a big brother.

This is where it was supposed to end. This is where the list stopped, until last summer; when I was given the opportunity to go back to Dallas, TX, for another internship. While there, I met people who transcended the professional experience to make it more of a personal one. I would like to thank the rest of the Brewcrew (Justin Bennett, Dave Everett, Kyle Hoelscher, Rudy Karimi, Adam Keys, Dave Milliner, Rob Taylor, Steven Tom, and Steven Yager) for the great memories on the Guadalupe River; in Dallas, TX; Shreveport, LA; Austin, TX; and San Antonio, TX. Without their ingenuity, Splashball would be only a thought, and HOOF only a word; now, they're a sport and an attitude, respectively. Of course, those times would not have been as memorable without Christy Ballman and Bradley Werner. In addition, I would like to thank the *entire* "Big10" group for providing suitable arrangements throughout the football season; even without ESPN Gameplan. I would like to acknowledge Neal Brenner who not only joined me as a member of the Century Club, but also provided considerable insight into the perception of Purdue's basketball program. I would like to thank Dana Burnett, Jennifer Sturtz, Amy Schwab, and Katie Smothermon for making my time in Dallas, TX, so enjoyable. Especially important thanks go to Katherine Michelle Werner, who impresses me more than she will ever know.

TABLE OF CONTENTS

	<u>page</u>
ACKNOWLEDGMENTS	iii
LIST OF TABLES	viii
LIST OF FIGURES	ix
ABSTRACT	xx
CHAPTER	
1 INTRODUCTION	1
2 LITERATURE REVIEW	12
Ion-Implantation	12
Diffusion	23
Fickian Diffusion.....	24
Atomistic Diffusion.....	25
Transient Enhanced Diffusion.....	27
Electrical Activation	30
Rapid Thermal Processing	33
Alternatives to Conventional Thermal Annealing.....	35
Low Temperature Solid-Phase Epitaxial Regrowth.....	35
Non-melt Laser Annealing	37
Laser Thermal Processing	40
Ultra-high Temperature Annealing	44
3 ANALYTICAL TECHNIQUES	72
Secondary Ion Mass Spectrometry	72
Transmission Electron Microscopy	75
Variable Angle Spectroscopic Ellipsometry.....	79
Four-Point Probe.....	81
Electron Paramagnetic Resonance.....	84

4	EFFECT OF PRE-AMORPHIZATION ENERGY ON BORON ULTRA-SHALLOW JUNCTION FORMATION DURING ULTRA-HIGH TEMPERATURE ANNEALING OF ION-IMPLANTED SILICON	94
	Introduction.....	94
	Experimental Design	98
	Results.....	100
	Discussion.....	109
	Conclusions.....	152
5	EFFECT OF SOLID-PHASE EPITAXIAL REGROWTH BEFORE ULTRA-HIGH TEMPERATURE ANNEALING FOR BORON ULTRA-SHALLOW JUNCTION FORMATION OF ION-IMPLANTED SILICON	183
	Introduction.....	183
	Experimental Design	187
	Results.....	190
	Discussion.....	202
	Conclusion	231
6	EFFECT OF RECRYSTALLIZATION TEMPERATURE ON BORON ULTRA-SHALLOW JUNCTION FORMATION DURING ULTRA-HIGH TEMPERATURE ANNEALING OF ION-IMPLANTED SILICON	251
	Introduction.....	251
	Experimental Design	257
	Results.....	260
	Discussion.....	275
	Conclusions.....	338
7	SUMMARY AND FUTURE WORK	368
APPENDIX		
A	CODE TO MODEL BORON DIFFUSION IN AMORPHOUS SILICON	384
B	PARAMAGNETIC RESONANCE MEASUREMENT SETTINGS	385
	LIST OF REFERENCES	405
	BIOGRAPHICAL SKETCH	421

LIST OF TABLES

<u>Table</u>	<u>page</u>
2-1 Summary of defect classification scheme.	51

LIST OF FIGURES

<u>Figure</u>	<u>page</u>
1-1 Interpretation of Moore's law	7
1-2 Cross-section of a single planar p-type enhancement mode metal-oxide-semiconductor field-effect-transistor (p-MOSFET).....	8
1-3 International Technology Roadmap for Semiconductors, showing the R_s and x_j required for the SDE to produce devices with the performance characteristics outlined by the individual technology nodes (shown as rectangles).....	9
1-4 Solid solubility of a number of common impurities in Si	10
1-5 Secondary ion mass spectrometry profiles for a δ doped B marker layer before and after a 810 °C anneal for 15 min. a) Approximately 10 nm of diffusion was observed under equilibrium conditions. b) Approximately 170 nm of diffusion occurred (at a concentration of $1 \times 10^{17}/\text{cm}^3$) because of TED associated with the 40 keV Si^+ pre-amorphization implant to $1 \times 10^{15}/\text{cm}^2$	11
2-1 Processes associated with ion-implantation	52
2-2 Graph of the ion energy loss as a function of incident particle energy	53
2-3 Characteristic (a) R_p and (b) ΔR_p associated with common dopants used in CMOS technology as a function of implant energy	54
2-4 Equilibrium concentrations of interstitials, C_I^* , and vacancies, C_V^* , as a function of inverse temperature	55
2-5 Damage density as a function of depth for the three possible primary implant damage morphologies that may exist directly after ion-implantation	56
2-6 Plan-view TEM images of the damage produced by a 20 keV B^+ implant to $1 \times 10^{15}/\text{cm}^2$ after post-implant thermal processing at (a) 750 °C for 5 min and (b) 900 °C for 15 min	57
2-7 Concentration profile as a function of depth for a 4 keV B^+ implant to $1 \times 10^{14}/\text{cm}^2$ after post-implant thermal processing at 750 °C for various times.....	58
2-8 Saturation time for TED as a function of inverse temperature.....	59

2-9 Summary of the possible sources of TED	60
2-10 Carrier mobility as a function of active dopant concentration in Si at room temperature.....	61
2-11 Binary equilibrium phase diagram of B and Si	62
2-12 Energy density required to reach the melting point at the surface of a Si substrate irradiated with a square pulse of energy as a function of τ	63
2-13 Time required to regrow 50 nm of α -Si as a function of substrate temperature. Also plotted is the calculated absorbed laser power per spot radius as a function of the steady state temperature attained at the center of the spot	64
2-14 Segregation coefficient as a function of liquid phase regrowth velocity for a number of impurities in Si	65
2-15 Free energy of amorphous, crystalline, and liquid Si as a function of temperature or energy pulse.....	66
2-16 Radiant power as a function of wavelength showing the spectral distribution comparison of a water wall arc lamp and tungsten filament at 290 K	67
2-17 Integrated exitance as a function of wavelength showing the spectral distribution comparison of a water wall arc lamp and tungsten filament at 290 K	68
2-18 Temperature-time (T-t) and temperature-depth (T-d) profiles comparing spike RTP, impulse UHT annealing, and flash UHT annealing	69
2-19 Emissivity as a function of wavelength.....	70
2-20 Ramp-rate as a function of temperature for an iRTP anneal with a ramp-up rate of approximately 400 °C/s.....	71
3-1 (a) The ratio of negative ion yield (M^-) under Cs^+ bombardment to positive ion yield (M^+) under O^- bombardment as a function of atomic number showing enhanced yield for light elements such as H, C, and O and (b) the variation of positive ion yield as a function of atomic number for 1 nA 13.5 keV O^+ bombardment showing high yield for elements such as B.....	89
3-2 (a) The logarithm of positive ion yields plotted as a function of ionization potential. The ion yields are relative to Si in a Si lattice with O^+ sputtering and (b) a similar treatment for negative ions where the logarithms of relative ion yields are plotted against electron affinities. The ion yields are relative to Si for measurements in a Si lattice with Cs^+ ion sputtering.....	90

3-3 The various signals generated when a high-energy beam of electrons interacts with a sample. The directions shown indicate where the signal is strongest or where it is detected.....	91
3-4 Plot of the sample geometric correction factor as a function of sample thickness, t , to probe spacing, s , ratio.....	92
3-5 A traditional cw EPR set-up	93
4-1 Concentration profiles for a 1 keV B^+ implant to $1 \times 10^{15}/cm^2$ before and after a 1050 °C refined spike anneal for a substrate pre-amorphized with varying energies of Ge^+ each to $1 \times 10^{15}/cm^2$. The symbols are for identifications purposes only ...	155
4-2 Representative T-t profiles of the (a) iRTP and (b) fRTP anneal processes and the UHT annealing conditions used throughout this work.....	156
4-3 Bright field XTEM images showing the (a) continuous amorphous layer produced with the 48 keV and (b) 5 keV Ge^+ pre-amorphization implants to $5 \times 10^{14}/cm^2$, (c) 48 keV Ge^+ pre-amorphization implant to $5 \times 10^{14}/cm^2$ after a 585 °C furnace anneal for 45 min, and (d) PTEM image of the 48 keV Ge^+ pre-amorphization implant to $5 \times 10^{14}/cm^2$ after a 585 °C furnace anneal for 45 min under a WBDF g_{220} two-beam imaging condition.....	157
4-4 Concentration profiles showing the B^+ concentration as a function of depth for the 3 keV BF_2^+ implant to $6 \times 10^{14}/cm^2$ after each iRTP anneal temperature used in this study for the (a) 48 keV and (b) 5 keV Ge^+ pre-amorphization implants to $5 \times 10^{14}/cm^2$. The symbols are for identifications purposes only	158
4-5 Plan-view TEM images of the damage produced by the 48 keV Ge^+ pre-amorphization implant to $5 \times 10^{14}/cm^2$ under a WBDF g_{220} two-beam imaging condition after a (a) 760 (b) 800 (c) 900 (d) 1000 and (e) 1100 °C iRTP anneal. .	159
4-6 Concentration profiles showing the B^+ concentration as a function of depth for the 3 keV BF_2^+ implant to $6 \times 10^{14}/cm^2$ before and after the 1200 °C fRTP for the (a) 48 keV and (b) 5 keV Ge^+ pre-amorphization implants to $5 \times 10^{14}/cm^2$. The symbols are for identifications purposes only	160
4-7 Plan-view TEM images of the damage produced by the 48 keV Ge^+ pre-amorphization implant to $5 \times 10^{14}/cm^2$ under a WBDF g_{220} two-beam imaging condition for the 1200 °C fRTP using an (a) 760 (b) 800 and (c) 900 °C intermediate temperature.....	161
4-8 Concentration profiles showing the B^+ concentration as a function of depth for the 3 keV BF_2^+ implant to $6 \times 10^{14}/cm^2$ before and after the 1350 °C fRTP for the (a) 48 keV and (b) 5 keV Ge^+ pre-amorphization implants to $5 \times 10^{14}/cm^2$. The symbols are for identifications purposes only	162

4-9 Plan-view TEM images of the damage produced by the 48 keV Ge ⁺ pre-amorphization implant to $5 \times 10^{14}/\text{cm}^2$ under a WBDF g ₂₂₀ two-beam imaging condition for the 1350 °C fRTP using a (a) 760 (b) 800 and (c) 900 °C intermediate temperature	163
4-10 Concentration profiles showing the B ⁺ concentration as a function of depth for the 1 keV B ⁺ implant to $1 \times 10^{15}/\text{cm}^2$ before and after furnace annealing at 500 °C at various times for a substrate pre-amorphized with an 80 keV Ge ⁺ implant to $1 \times 10^{15}/\text{cm}^2$. The symbols are for identifications purposes only	164
4-11 Concentration profiles showing the B ⁺ concentration as a function of depth for the 1 keV B ⁺ implant to $1 \times 10^{15}/\text{cm}^2$ before and after furnace annealing at 550 °C at various times for a substrate pre-amorphized with an 80 keV Ge ⁺ implant to $1 \times 10^{15}/\text{cm}^2$. The symbols are for identifications purposes only	165
4-12 Concentration profiles showing the B ⁺ concentration as a function of depth for the 1 keV B ⁺ implant to $1 \times 10^{15}/\text{cm}^2$ before and after furnace annealing at either 500 or 550 °C at various times for a substrate pre-amorphized with an 80 keV Ge ⁺ implant to $1 \times 10^{15}/\text{cm}^2$. The symbols are for identifications purposes only	166
4-13 Concentration profiles showing the B ⁺ concentration as a function of depth for the 1 keV B ⁺ implant to $1 \times 10^{15}/\text{cm}^2$ before and after furnace annealing at 500 °C for (a) 41 and (b) 123 min for a substrate pre-amorphized with an 80 keV Ge ⁺ implant to $1 \times 10^{15}/\text{cm}^2$. The symbols are for identifications purposes only	167
4-14 Concentration profiles showing the B ⁺ concentration as a function of depth for the 1 keV B ⁺ implant to $1 \times 10^{15}/\text{cm}^2$ before and after furnace annealing at 550 °C for (a) 7 and (b) 13 min for a substrate pre-amorphized with an 80 keV Ge ⁺ implant to $1 \times 10^{15}/\text{cm}^2$. The symbols are for identifications purposes only	168
4-15 Concentration profiles showing the as-implanted dopant concentration as a function of depth for the 2 keV B ⁺ , 5 keV P ⁺ , and 8 keV Sb ⁺ implants each to $1 \times 10^{15}/\text{cm}^2$ into a Si substrate pre-amorphized with a 80 keV Ge ⁺ implant to $1 \times 10^{15}/\text{cm}^2$. The symbols are for identifications purposes only	169
4-16 Concentration profiles showing the B ⁺ concentration as a function of depth for the 2 keV B ⁺ implant to $1 \times 10^{15}/\text{cm}^2$ before and after iRTP annealing at 800 and 900 °C for a substrate pre-amorphized with an 80 keV Ge ⁺ implant to $1 \times 10^{15}/\text{cm}^2$. The symbols are for identifications purposes only	170
4-17 Concentration profiles showing the P ⁺ concentration as a function of depth for the 5 keV P ⁺ implant to $1 \times 10^{15}/\text{cm}^2$ before and after iRTP annealing at 800 and 900 °C for a substrate pre-amorphized with an 80 keV Ge ⁺ implant to $1 \times 10^{15}/\text{cm}^2$. The symbols are for identifications purposes only	171

4-18 Concentration profiles showing the Sb ⁺ concentration as a function of depth for the 8 keV Sb ⁺ implant to $1\times10^{15}/\text{cm}^2$ before and after iRTP annealing at 800 and 900 °C for a substrate pre-amorphized with a 80 keV Ge ⁺ implant to $1\times10^{15}/\text{cm}^2$. The symbols are for identifications purposes only.....	172
4-19 Concentration profiles showing the B ⁺ concentration as a function of depth for the 1 keV B ⁺ implant to $1\times10^{15}/\text{cm}^2$ before and after 800, 900, and 1000 °C iRTP annealing for the wafer (a) with and (b) without the 80 keV Ge ⁺ pre-amorphization implant to $1\times10^{15}/\text{cm}^2$. The symbols are for identifications purposes only	173
4-20 Concentration profiles showing the B ⁺ concentration as a function of depth for the 1, 2, and 4 keV B ⁺ implants each to $1\times10^{15}/\text{cm}^2$ before and after iRTP annealing at 800 °C for a substrate pre-amorphized with an 80 keV Ge ⁺ implant to $1\times10^{15}/\text{cm}^2$. The symbols are for identifications purposes only.....	174
4-21 Bright field XTEM image showing the 30 nm continuous amorphous layer produced with an 18 keV Ge ⁺ pre-amorphization implant to $1\times10^{15}/\text{cm}^2$	175
4-22 Concentration profiles showing the B ⁺ concentration as a function of depth for the 1 keV B ⁺ implant to $1\times10^{15}/\text{cm}^2$ before and after iRTP annealing over the temperature range of 600-800 °C for a substrate pre-amorphized with an 18 keV Ge ⁺ implant to $1\times10^{15}/\text{cm}^2$. The symbols are for identifications purposes only ...	176
4-23 Concentration profiles showing the B ⁺ concentration as a function of depth for the 1 keV B ⁺ implant to $1\times10^{15}/\text{cm}^2$ before and after iRTP annealing over the temperature range of 780-900 °C for a substrate pre-amorphized with an 18 keV Ge ⁺ implant to $1\times10^{15}/\text{cm}^2$. The symbols are for identifications purposes only ...	177
4-24 Concentration profiles showing the B ⁺ concentration as a function of depth for the shallowest B marker layer before and after iRTP annealing over the temperature range of 800-1000 °C. The deposition conditions were chosen to result in a B marker layer with a peak concentration of approximately $2\times10^{20}/\text{cm}^3$. The intrinsic Si layer thickness was targeted to be 100 nm. The 80 keV Ge ⁺ pre-amorphization implant to $1\times10^{15}/\text{cm}^2$ produced a continuous amorphous layer extending approximately 110 nm below the substrate surface	178
4-25 Concentration profiles showing the B ⁺ concentration as a function of depth for the second deepest B marker layer before and after iRTP annealing over the temperature range of 800-1000 °C. The deposition conditions were chosen to result in a B marker layer with a peak concentration of approximately $2\times10^{20}/\text{cm}^3$. The intrinsic Si layer thickness was targeted to be 200 nm. The 80 keV Ge ⁺ pre-amorphization implant to $1\times10^{15}/\text{cm}^2$ produced a continuous amorphous layer extending approximately 110 nm below the substrate surface.....	179
4-26 Concentration profiles showing the B ⁺ concentration as a function of depth for the deepest B marker layer before and after iRTP annealing over the temperature range	

of 800-1000 °C. The deposition conditions were chosen to result in a B marker layer with a peak concentration of approximately $2 \times 10^{20}/\text{cm}^3$. The intrinsic Si layer thickness was targeted to be 300 nm. The 80 keV Ge ⁺ pre-amorphization implant to $1 \times 10^{15}/\text{cm}^2$ produced a continuous amorphous layer extending approximately 110 nm below the substrate surface	180
4-27 Concentration profiles for a 1 keV B ⁺ implant to $1 \times 10^{15}/\text{cm}^2$ before and after a 1050 °C refined spike anneal for a substrate pre-amorphized with an 18 keV Ge ⁺ implant to $1 \times 10^{15}/\text{cm}^2$. The symbols are for identifications purposes only	181
4-28 Graph of the measured (●) and calculated (■) R _s values obtained for the 48 keV Ge ⁺ pre-amorphization implant to $5 \times 10^{14}/\text{cm}^2$ and the measured (▲) values obtained for the 5 keV Ge ⁺ pre-amorphization implant to $5 \times 10^{14}/\text{cm}^2$	182
5-1 Concentration profiles showing the B ⁺ concentration as a function of depth for the 3 keV BF ₂ ⁺ implant to $6 \times 10^{14}/\text{cm}^2$ after each iRTP anneal temperature used in this study for the 48 keV Ge ⁺ pre-amorphization implant to $5 \times 10^{14}/\text{cm}^2$ (a) without and (b) with the 585 °C furnace anneal for 45 min before UHT annealing. The symbols are for identifications purposes only	235
5-2 Plan-view TEM images of the damage produced by the 48 keV Ge ⁺ pre-amorphization implant to $5 \times 10^{14}/\text{cm}^2$ under a WBDF g ₂₂₀ two-beam imaging condition after the (a)(f) 760 (b)(g) 800 (c)(h) 900 (d)(i) 1000 and (e)(j) 1100 °C iRTP anneals for the wafer without and with the 585 °C furnace anneal for 45 min before UHT annealing, respectively	236
5-3 Concentration profiles showing the B ⁺ concentration as a function of depth for the 3 keV BF ₂ ⁺ implant to $6 \times 10^{14}/\text{cm}^2$ before and after the 1200 °C fRTP anneal for the 48 keV Ge ⁺ pre-amorphization implant to $5 \times 10^{14}/\text{cm}^2$ (a) without and (b) with the 585 °C furnace anneal for 45 min before UHT annealing. The symbols are for identifications purposes only	237
5-4 Plan-view TEM images of the damage produced by the 48 keV Ge ⁺ pre-amorphization implant to $5 \times 10^{14}/\text{cm}^2$ under a WBDF g ₂₂₀ two-beam imaging condition for the 1200 °C fRTP anneal using a (a)(d) 760 (b)(e) 800 and (c)(f) 900 °C intermediate temperature for the wafer without and with the 585 °C furnace anneal for 45 min before UHT annealing, respectively	238
5-5 Concentration profiles showing the B ⁺ concentration as a function of depth for the 3 keV BF ₂ ⁺ implant to $6 \times 10^{14}/\text{cm}^2$ before and after the 1350 °C fRTP anneal for the 48 keV Ge ⁺ pre-amorphization implant to $5 \times 10^{14}/\text{cm}^2$ (a) without and (b) with the 585 °C furnace anneal for 45 min before UHT annealing. The symbols are for identifications purposes only	239
5-6 Concentration profiles showing the B ⁺ concentration as a function of depth for the 3 keV BF ₂ ⁺ implant to $6 \times 10^{14}/\text{cm}^2$ before and after UHT annealing with an iRTP or	

intermediate temperature of (a) 800 °C and (b) 900 °C. The profile for the 585 °C furnace anneal is included to serve as a reference. The symbols are for identifications purposes only.....	240
5-7 Plan-view TEM images of the damage produced by the 48 keV Ge ⁺ pre-amorphization implant to $5 \times 10^{14}/\text{cm}^2$ under a WBDF g ₂₂₀ two-beam imaging condition for the 1350 °C fRTP anneal using a (a)(d) 760 (b)(e) 800 and (c)(f) 900 °C intermediate temperature for the wafer without and with the 585 °C furnace anneal for 45 min before UHT annealing, respectively	241
5-8 Concentration profiles showing the B ⁺ concentration as a function of depth for the 1 keV B ⁺ implant to $1 \times 10^{15}/\text{cm}^2$ before and after iRTP annealing at 800 °C for a substrate pre-amorphized with an 80 keV Ge ⁺ implant to various doses. The symbols are for identifications purposes only	242
5-9 Plan-view TEM images of the damage produced by the 80 keV Ge ⁺ pre-amorphization implant to (a) 5×10^{14} (b) 1×10^{15} and (c) $2 \times 10^{15}/\text{cm}^2$ under a WBDF g ₂₂₀ two-beam imaging condition for the 800 °C iRTP anneal	243
5-10 Concentration profiles showing the B ⁺ concentration as a function of depth for the 1 keV B ⁺ implant to $1 \times 10^{15}/\text{cm}^2$ before and after iRTP annealing at 800 and 900 °C for a substrate pre-amorphized with an 80 keV Ge ⁺ implant to various doses. The symbols are for identifications purposes only	244
5-11 Plan-view TEM images of the damage produced by the 80 keV Ge ⁺ pre-amorphization implant to (a) 5×10^{14} (b) 1×10^{15} and (c) $2 \times 10^{15}/\text{cm}^2$ under a WBDF g ₂₂₀ two-beam imaging condition for the 900 °C iRTP anneal	245
5-12 Concentration profiles showing the B ⁺ concentration as a function of depth for the 1 keV B ⁺ implant to $1 \times 10^{15}/\text{cm}^2$ before and after iRTP annealing at 800 and 1000 °C for a substrate pre-amorphized with an 80 keV Ge ⁺ implant to various doses. The symbols are for identifications purposes only	246
5-13 Plan-view TEM images of the damage produced by the 80 keV Ge ⁺ pre-amorphization implant to (a) 5×10^{14} (b) 1×10^{15} and (c) $2 \times 10^{15}/\text{cm}^2$ under a WBDF g ₂₂₀ two-beam imaging condition for the 1000 °C iRTP anneal	247
5-14 Graph of the measured (●)(▲) and calculated (■)(◆) R _s values obtained for the 48 keV Ge ⁺ pre-amorphization implant to $5 \times 10^{14}/\text{cm}^2$ without and with the 585 °C furnace anneal before UHT annealing, respectively	248
5-15 Concentration profiles showing the B ⁺ concentration as a function of depth for the 3 keV BF ₂ ⁺ implant to $6 \times 10^{14}/\text{cm}^2$ before and after the 800 °C iRTP anneal both without and with the 585 °C furnace anneal before UHT annealing for a substrate pre-amorphized with an 48 keV Ge ⁺ implant to $5 \times 10^{14}/\text{cm}^2$. The profile for the	

585 °C furnace anneal is included to serve as a reference. The symbols are for identifications purposes only.....	249
5-16 Plot of the estimated remaining amorphous layer thickness as a function of temperature for an anneal with a ramp-up rate of 400 °C/s	250
6-1 Bright field XTEM images showing that the (a) 760 °C iRTP anneal is sufficient to completely recrystallize the amorphous layer produced by the 48 keV Ge ⁺ pre-amorphization implant to $5 \times 10^{14}/\text{cm}^2$ and (b) the 12 keV F ⁺ implant to $1.5 \times 10^{15}/\text{cm}^2$ is sufficient to reduce the regrowth velocity of the α/c interface such that approximately 22 nm of amorphous material remains near the substrate surface after an 800 °C iRTP anneal.....	343
6-2 Concentration profiles showing the F ⁺ concentration as a function of depth for both the 12 keV F ⁺ implant to $1.5 \times 10^{15}/\text{cm}^2$ and 3 keV BF ₂ ⁺ implant to $6 \times 10^{14}/\text{cm}^2$ before and after iRTP annealing at 800 and 900 °C for the 48 keV Ge ⁺ pre-amorphization implant to $5 \times 10^{14}/\text{cm}^2$. The symbols are for identifications purposes only.....	344
6-3 Concentration profiles showing the as-implanted B ⁺ concentration as a function of depth for the 3 keV BF ₂ ⁺ implant to $6 \times 10^{14}/\text{cm}^2$ without and with the 12 keV F ⁺ implant to $1.5 \times 10^{15}/\text{cm}^2$ directly after the 48 keV Ge ⁺ pre-amorphization implant to $5 \times 10^{14}/\text{cm}^2$. The symbols are for identifications purposes only	345
6-4 Concentration profiles showing the B ⁺ concentration as a function of depth for the 3 keV BF ₂ ⁺ implant to $6 \times 10^{14}/\text{cm}^2$ after each iRTP anneal temperature used in this study for the 48 keV Ge ⁺ pre-amorphization implant to $5 \times 10^{14}/\text{cm}^2$ (a) without and (b) with the 12 keV F ⁺ implant to $1.5 \times 10^{15}/\text{cm}^2$. The symbols are for identifications purposes only.....	346
6-5 Plan-view TEM images of the damage produced by the 48 keV Ge ⁺ pre-amorphization implant to $5 \times 10^{14}/\text{cm}^2$ under a WBDF g ₂₂₀ two-beam imaging condition after the (a)(f) 760 (b)(g) 800 (c)(h) 900 (d)(i) 1000 and (e)(j) 1100 °C iRTP anneals for the wafer without and with the 12 keV F ⁺ implant to $1.5 \times 10^{15}/\text{cm}^2$, respectively	347
6-6 Concentration profiles showing the B ⁺ concentration as a function of depth for the 3 keV BF ₂ ⁺ implant to $6 \times 10^{14}/\text{cm}^2$ before and after a 1200 or 1350 °C fRTP anneal when using an intermediate temperature of 760 °C for the 48 keV Ge ⁺ pre-amorphization implant to $5 \times 10^{14}/\text{cm}^2$ (a)(c) without and (b)(d) with the 12 keV F ⁺ implant to $1.5 \times 10^{15}/\text{cm}^2$. The symbols are for identifications purposes only ..	348
6-7 Plan-view TEM images of the damage produced by the 48 keV Ge ⁺ pre-amorphization implant to $5 \times 10^{14}/\text{cm}^2$ under a WBDF g ₂₂₀ two-beam imaging condition for the (a)(c) 1200 and (b)(d) 1350 °C fRTP anneal using an intermediate	

temperature of 760 °C for the wafer without and with the 12 keV F ⁺ implant to 1.5×10 ¹⁵ /cm ² , respectively	349
6-8 Concentration profiles showing the B ⁺ concentration as a function of depth for the 3 keV BF ₂ ⁺ implant to 6×10 ¹⁴ /cm ² before and after a 1200 or 1350 °C fRTA anneal when using an intermediate temperature of 800 °C for the 48 keV Ge ⁺ pre-amorphization implant to 5×10 ¹⁴ /cm ² (a)(c) without and (b)(d) with the 12 keV F ⁺ implant to 1.5×10 ¹⁵ /cm ² . The symbols are for identifications purposes only ..	350
6-9 Plan-view TEM images of the damage produced by the 48 keV Ge ⁺ pre-amorphization implant to 5×10 ¹⁴ /cm ² under a WBDF g ₂₂₀ two-beam imaging condition for the (a)(c) 1200 and (b)(d) 1350 °C fRTA anneal using an intermediate temperature of 800 °C for the wafer without and with the 12 keV F ⁺ implant to 1.5×10 ¹⁵ /cm ² , respectively	351
6-10 Concentration profiles showing the B ⁺ concentration as a function of depth for the 3 keV BF ₂ ⁺ implant to 6×10 ¹⁴ /cm ² before and after a 1200 or 1350 °C fRTA anneal when using an intermediate temperature of 900 °C for the 48 keV Ge ⁺ pre-amorphization implant to 5×10 ¹⁴ /cm ² (a)(c) without and (b)(d) with the 12 keV F ⁺ implant to 1.5×10 ¹⁵ /cm ² . The symbols are for identifications purposes only ..	352
6-11 Plan-view TEM images of the damage produced by the 48 keV Ge ⁺ pre-amorphization implant to 5×10 ¹⁴ /cm ² under a WBDF g ₂₂₀ two-beam imaging condition for the (a)(c) 1200 and (b)(d) 1350 °C fRTA anneal using an intermediate temperature of 900 °C for the wafer without and with the 12 keV F ⁺ implant to 1.5×10 ¹⁵ /cm ² , respectively	353
6-12 Concentration profiles showing the as-implanted B ⁺ concentration as a function of depth for the 1 keV B ⁺ implant to 1×10 ¹⁵ /cm ² before and after pre-damaging or pre-amorphizing the substrate surface with a 48 keV Ge ⁺ implant to either 3×10 ¹³ /cm ² or 1×10 ¹⁵ /cm ² , respectively. The symbols are for identifications purposes only.....	354
6-13 Concentration profiles showing the as-implanted B ⁺ concentration as a function of depth for the 3 keV BF ₂ ⁺ implant to 6×10 ¹⁴ /cm ² without and with the 12 keV F ⁺ implant to 1.5×10 ¹⁵ /cm ² directly after the 48 keV Ge ⁺ pre-amorphization implant to 5×10 ¹⁴ /cm ² compared to the as-implanted B ⁺ for the 1 keV B ⁺ implant to 1×10 ¹⁵ /cm ² without any pre-amorphization implant. The symbols are for identifications purposes only.....	355
6-14 Concentration profiles showing the as-implanted B ⁺ concentration as a function of depth for either a 0.67 keV B ⁺ implant to 1×10 ¹⁵ /cm ² or 3 keV BF ₂ ⁺ implant to 1×10 ¹⁵ /cm ² without any additional processing and before and after a 12 keV F ⁺ implant to 1.5×10 ¹⁵ /cm ² for wafers with a 60 keV Ge ⁺ pre-amorphization implant to 1×10 ¹⁵ /cm ² . The symbols are for identifications purposes only	356

6-15 Concentration profiles showing the as-implanted B ⁺ concentration as a function of depth for either a 0.67 keV B ⁺ implant to $1\times10^{15}/\text{cm}^2$ or 3 keV BF ₂ ⁺ implant to $1\times10^{15}/\text{cm}^2$ without any additional processing and after implantation with either 12 keV F ⁺ , 46 keV Ge ⁺ , or 58 keV GeF ⁺ each to $1.5\times10^{15}/\text{cm}^2$ for wafers with a 60 keV Ge ⁺ pre-amorphization implant to $1\times10^{15}/\text{cm}^2$. The symbols are for identifications purposes only.....	357
6-16 Concentration profiles showing the as-implanted B ⁺ concentration as a function of depth for either a 0.67 keV B ⁺ implant to $1\times10^{15}/\text{cm}^2$ or 3 keV BF ₂ ⁺ implant to $1\times10^{15}/\text{cm}^2$ without any additional processing and before implantation with either 12 keV F ⁺ or 58 keV GeF ⁺ each to $1.5\times10^{15}/\text{cm}^2$ for wafers with a 60 keV Ge ⁺ pre-amorphization implant to $1\times10^{15}/\text{cm}^2$. The symbols are for identifications purposes only.....	358
6-17 Paramagnetic response from wafers pre-amorphized with a 60 keV Ge ⁺ implant to $1\times10^{15}/\text{cm}^2$. In two cases the wafers were subsequently implanted with 12 keV F ⁺ to either $1.5\times10^{15}/\text{cm}^2$ or $3.0\times10^{15}/\text{cm}^2$	359
6-18 Paramagnetic response from wafers pre-amorphized with a 60 keV Ge ⁺ implant to $1\times10^{15}/\text{cm}^2$. In two cases the wafers were subsequently implanted with 12 keV F ⁺ to either $1.5\times10^{15}/\text{cm}^2$ or $3.0\times10^{15}/\text{cm}^2$. Each wafer was then subject to a 500 °C structural relaxation anneal for 60 min	360
6-19 Comparison of the paramagnetic response from wafers pre-amorphized with a 60 keV Ge ⁺ implant to $1\times10^{15}/\text{cm}^2$. One wafer was then subject to a 500 °C structural relaxation anneal for 60 min	361
6-20 Concentration profiles showing the as-implanted B ⁺ concentration as a function of depth for the 2 keV B ⁺ implant to $1\times10^{15}/\text{cm}^2$ for the 80 keV Ge ⁺ pre-amorphization implant to $1\times10^{15}/\text{cm}^2$. Three of the wafers were previously implanted with 12 keV F ⁺ to various doses. The symbols are for identifications purposes only.....	362
6-21 Concentration profiles showing the as-implanted F ⁺ concentration as a function of depth for the 3 keV F ⁺ implant to doses of 1, 2, and $3\times10^{14}/\text{cm}^2$ for the 80 keV Ge ⁺ pre-amorphization implant to $1\times10^{15}/\text{cm}^2$. The symbols are for identifications purposes only.....	363
6-22 Concentration profiles showing the B ⁺ concentration as a function of depth for the 1 keV B ⁺ implant to $1\times10^{15}/\text{cm}^2$ before and after an 800 °C iRTP anneal for the 80 keV Ge ⁺ pre-amorphization implant to $1\times10^{15}/\text{cm}^2$. Three of the wafers were previously implanted with 12 keV F ⁺ to various doses. The symbols are for identifications purposes only.....	364
6-23 Concentration profiles showing the B ⁺ concentration as a function of depth for the 1 keV B ⁺ implant to $1\times10^{15}/\text{cm}^2$ before and after a 900 °C iRTP anneal for the	

80 keV Ge ⁺ pre-amorphization implant to $1 \times 10^{15}/\text{cm}^2$. Three of the wafers were previously implanted with 12 keV F ⁺ to various doses. The symbols are for identifications purposes only.....	365
6-24 Concentration versus inverse temperature. The data corresponding to this work refer to the plateau concentrations observed through the SIMS data. The data from the literature show that the C_{enh} is very well matched by the n_i at the anneal temperature and is approximately an order of magnitude lower than C_s	366
6-25 Graph of the measured (●)(▲) and calculated (■)(◆) R_s values obtained for the 48 keV Ge ⁺ pre-amorphization implant to $5 \times 10^{14}/\text{cm}^2$ without and with the 12 keV F ⁺ implant to $1.5 \times 10^{15}/\text{cm}^2$, respectively	367

Abstract of Dissertation Presented to the Graduate School
of the University of Florida in Partial Fulfillment of the
Requirements for the Degree of Doctor of Philosophy

**BORON ACTIVATION AND DIFFUSION DURING MILLISECOND ANNEALING
OF ION-IMPLANTED SILICON**

By

Kevin Andrew Gable

August 2004

Chair: Kevin S. Jones

Major Department: Materials Science and Engineering

The continued scaling of complementary metal-oxide-semiconductor (CMOS) technology requires the formation of highly-activated ultra-shallow p-type source/drain extension (SDE) region under the gate. One difficulty in improving the sheet resistance (R_s) is the thermodynamic solid solubility of impurities in Si, which limits the active dopant concentration. Decreasing the junction depth (x_j) of the SDE is made difficult by the significant amount of diffusion that occurs during post-implant thermal processing, such as the deep source/drain (S/D) activation anneal. Novel high-power arc lamp design has enabled ultra-high temperature (UHT) annealing as an alternative to conventional rapid thermal processing (RTP) for B ultra-shallow junction formation. This technique heats the wafer to an intermediate temperature (e.g., 800 °C) before discharging a capacitor bank into flash lamps, which anneals the device side of the wafer at a relatively high temperature (e.g., 1200 °C) for a few milliseconds. This time duration is significantly reduced from those obtained with conventional RTP, which are on the order

of 1-2 s within 50 °C of the peak temperature. Although this resolves one of the limiting issues associated with conventional RTP techniques, the activation and diffusion mechanisms that take place on these times scales are not well understood, and are the subject of this work.

It was found that dopant activation improves when solid-phase epitaxial recrystallization (SPER) of an implantation-induced amorphous layer occurs at higher temperature. This is thought to be because B solubility is higher in amorphous Si (α -Si) when compared to crystalline Si (c-Si), and because higher activation levels can be achieved when regrowth occurs at higher recrystallization temperatures. The phase transformation results in high activation levels presumably due to solute trapping at the moving amorphous/crystalline (α/c) interface. In addition to solubility, B diffusivity was also found to be much higher in α -Si.

The defect evolution was found to be significantly dependent on both the intermediate and peak UHT annealing temperature. These results show that, although the excess interstitials produced by pre-amorphization implant may evolve into large dislocation loops, the diffusion observed during the anneal is significantly less than what would be expected from a conventional RTP anneal. This difference is presumed to be due to the lack of thermal energy available to promote interstitial diffusion toward the surface.

CHAPTER 1 INTRODUCTION

Silicon technology development is supported by the significant advantages obtained by following the trend known as Moore's law, which suggests that the average geometrical dimensions and fabrication cost of a transistor will decrease by a factor of two every 18 to 24 months.¹ Figure 1-1 gives the general interpretation of this trend by plotting the minimum feature size as a function of year.² Figure 1-2 shows a cross-section of a single planar p-type enhancement mode metal-oxide-semiconductor field-effect-transistor (p-MOSFET), which is the most common device used in current electronics manufacturing.² The continued scaling of this transistor offers the ability to produce higher-speed/lower-power devices capable of increasing the functionality and applicability of the resulting product.

Front-end-of-the-line (FEOL) processing incorporates a number of chemical etching, ion-implantation, thin-film deposition, and thermal annealing steps to produce a substrate with the appropriate isolation, doping, and contact characteristics necessary for additional processing. In particular, ion-implantation is used to introduce dopants into a Si substrate, thereby changing the concentration profiles and electrical characteristics of the locally doped regions.³ This process inherently produces point-defects within the lattice, in the form of Si self-interstitials (which are created as a result of displacements from their equilibrium positions due to nuclear collisions with the primary ions and recoiled atoms).³⁻⁷ Post-implant thermal processing is required to repair the lattice damage accumulated during the implantation process and to activate the dopant atoms by

establishing them on substitutional sites where they are able to contribute holes (electrons) to the valence (conduction) band.^{3,8} During post-implant thermal processing, the Si self-interstitials coalesce into metastable crystallographic defects which have been shown to enhance dopant diffusion,⁹ assist in incomplete dopant activation,¹⁰ and contribute to junction leakage.^{11,12}

One challenge in successfully scaling the dimensions of the MOSFET transistor is in maintaining a highly activated ultra-shallow p-type source/drain extension (SDE) region under the gate. It should be noted that the p-type SDE is typically formed either by a relatively low energy (i.e., < 10 keV) B or BF₂ implant step. Figure 1-3 shows the International Technology Roadmap for Semiconductors (ITRS), which represents the sheet resistance (R_s) and junction depth (x_j) required for the SDE to produce devices with the performance characteristics outlined by the individual technology nodes (represented as rectangles).¹³ In addition, the graph includes a limited amount of experimental data showing the challenge in producing a junction with the proper R_s and x_j .

One difficulty in improving the R_s is the thermodynamic solid solubility of impurities in Si, which limits the active dopant concentration.¹⁴ Figure 1-4 shows the solid solubility of a number of common impurities in Si, which increases as a function of temperature until an upper limit is reached.^{14,15} Aside from solid solubility limiting the amount of active dopant in the substrate, lattice imperfections and ionized impurities may serve as scattering sites that reduce carrier mobility and further increase the R_s .¹⁶ Decreasing the x_j of the SDE is made difficult by the significant amount of diffusion that occurs during post-implant thermal processing, such as the deep source/drain (S/D) activation anneal. During post-implant thermal processing, the Si self-interstitials

generated during the implantation process redistribute throughout the lattice^{17,18} and remove the B atoms from their substitutional sites by a so-called kick-out reaction,¹⁹⁻²¹ allowing them to diffuse deep into the substrate through a well documented interstitial mechanism.²²⁻²⁵ Figure 1-5 shows secondary ion mass spectrometry (SIMS) profiles, which measures the B concentration as a function of depth, for a δ doped B marker layer before and after a 810 °C anneal for 15 min.⁷ As seen for the sample that received the 40 keV Si⁺ pre-amorphization implant to $1 \times 10^{15}/\text{cm}^2$, the amount of TED that occurred during this anneal was capable of increasing the x_j (at a concentration of $1 \times 10^{17}/\text{cm}^3$) by approximately 170 nm. This can be compared to the 1.6 nm of diffusion expected under equilibrium conditions.²⁶ It was shown that this phenomena decays with time and can be modeled by the following Arrhenius equation,

$$\Delta x_j^2 \propto N R_p \exp\left[\frac{-(-1.4 \text{ eV})}{kT}\right], \quad (1.1)$$

where Δx_j is the change in the x_j after complete annealing of the implant damage, N is the number of interstitials trapped within the implant related extended defects, and R_p is the projected range of the implant.³ It can be seen that this equation has an effective negative activation energy, which suggests that the amount of TED will decrease when the damage is annealed out at a higher temperature.^{3,27} This arises from the fact that the interstitial supersaturation due to the presence of extended defects is higher at a lower temperature.²⁷ This observation influenced the development of single-wafer thermal processes capable of producing a high temperature ambient with ramp rates on the order of 50-200 °C/s, and fast switching times in order to insulate the dopant from a high degree of TED.²⁸

Rapid thermal processing (RTP) has proven successful in producing junctions with the performance characteristics necessary for the continued scaling of complementary MOS (CMOS) technology to date.²⁹ Its ability to satisfy these requirements is associated with improved equipment capability in the form of spike annealing, which decreases the effective thermal budget allowing for higher annealing temperatures in order to improve activation and reduce the amount of diffusion that takes place during the thermal process.^{30,31} A spike anneal is characterized as a short thermal-anneal cycle that can be achieved by increasing the ramp-up and ramp-down rates and by minimizing the dwell time at the temperature of interest. The inability of this technique to produce junctions with the performance characteristics required by future technology nodes is in the cycle time of the thermal process, which results in an unacceptable amount of dopant diffusion. The minimum cycle times in conventional RTP techniques are limited by the maximum power delivered to the wafer, which determines the ramp-up rate, and the minimum response time of the relatively large thermal mass incandescent tungsten lamps, which determines both the soak time and the ramp-down rate. Without being able to minimize the soak time and the ramp-down rate, increasing the ramp-up rate above 100 °C/s results in no additional improvement in terms of forming a highly-activated ultra-shallow junction.³² This illustrates the need to investigate novel annealing technologies that may be able to produce highly activated junctions without being subject to a significant amount of TED.

Novel high-power arc lamp design has enabled ultra-high temperature (UHT) annealing as an alternative to conventional RTP for B ultra-shallow junction formation.³³ This technique heats the wafer to an intermediate temperature (e.g., 800 °C) before

discharging a capacitor bank into flash lamps, which anneals the device side of the wafer at a relatively high temperature (e.g., 1200 °C) for a few milliseconds.³⁴⁻³⁶ This time duration is significantly reduced from those obtained with conventional RTP, which are on the order of 1-2 s within 50 °C of the peak temperature. The UHT anneal heats the surface of interest while increasing the bulk wafer temperature not more than 50 °C of the intermediate temperature, allowing for conductive heat loss through the substrate. In contrast to tungsten lamp heating technology (i.e., RTP), this technique uses a water-wall arc lamp that provides the means for significantly reducing the heating-cycle time because of its ability to deliver higher power and because of its faster response time.³⁷ The arc lamp responds more rapidly than tungsten filament lamps because of the reduced thermal mass of the argon gas used in the arc lamp system. The lamps can be switched off in a few microseconds, allowing greater control and repeatability over the anneal process. Although these qualities resolve one of the limiting issues associated with conventional RTP techniques, the activation and diffusion mechanisms that take place on these time scales are not well understood, and are the subject of this work.

Contributions of this work to the field of materials science and engineering are as follows:

1. Observation of enhanced B diffusion in α -Si when compared to c-Si.
2. Conclusive evidence that interstitial backflow from the end-of-range damage is the initial source of TED.
3. Determination of an ultra-fast diffusion pulse that occurs during the early stages of annealing after regrowth of an implantation-induced amorphous layer.
4. Evidence that F is capable of occupying defect sites in α -Si, thereby de-trapping B atoms from these sites and causing a significant degradation in the as-implanted junction abruptness and x_j .

5. Evidence that B solubility is higher in α -Si when compared to c-Si, and that higher activation levels can be achieved if regrowth occurs at higher recrystallization temperatures.
6. Determination that F binds with Si self interstitials, thereby reducing B diffusion behavior during post-implant thermal processing.
7. Observation of B clustering in α -Si, as opposed to c-Si.
8. Evidence that B diffusion in α -Si is enhanced when in the presence of F because of a reduction in the regrowth velocity of the α/c interface.

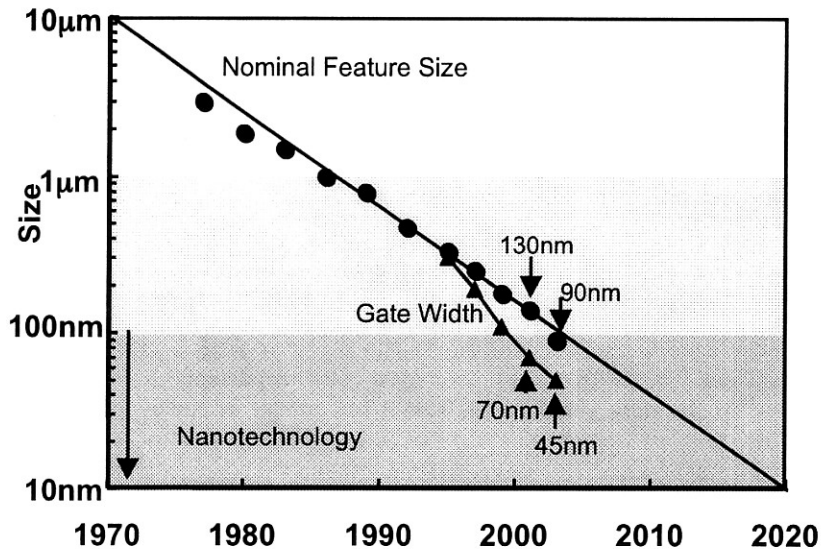


Figure 1-1 Interpretation of Moore's law. Reprinted with permission from J. D. Plummer, M. D. Deal, and P. Griffin, *Silicon VLSI Technology – Fundamentals, Practice and Modeling* (Prentice Hall, Upper Saddle River, New Jersey, 2000), Figure 1-2, p 3.

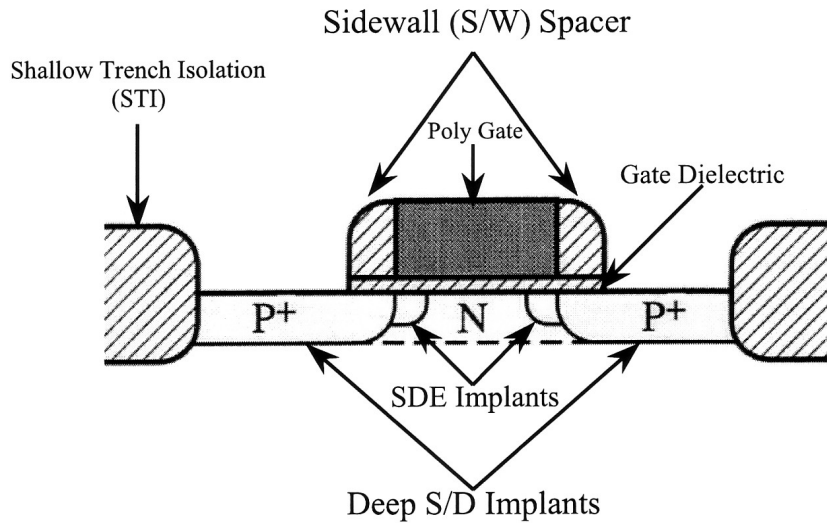


Figure 1-2 Cross-section of a single planar p-type enhancement mode metal-oxide-semiconductor field-effect-transistor (p-MOSFET). Reprinted with permission from J. D. Plummer, M. D. Deal, and P. Griffin, *Silicon VLSI Technology – Fundamentals, Practice and Modeling* (Prentice Hall, Upper Saddle River, New Jersey, 2000), Figure 2-34, p 83.

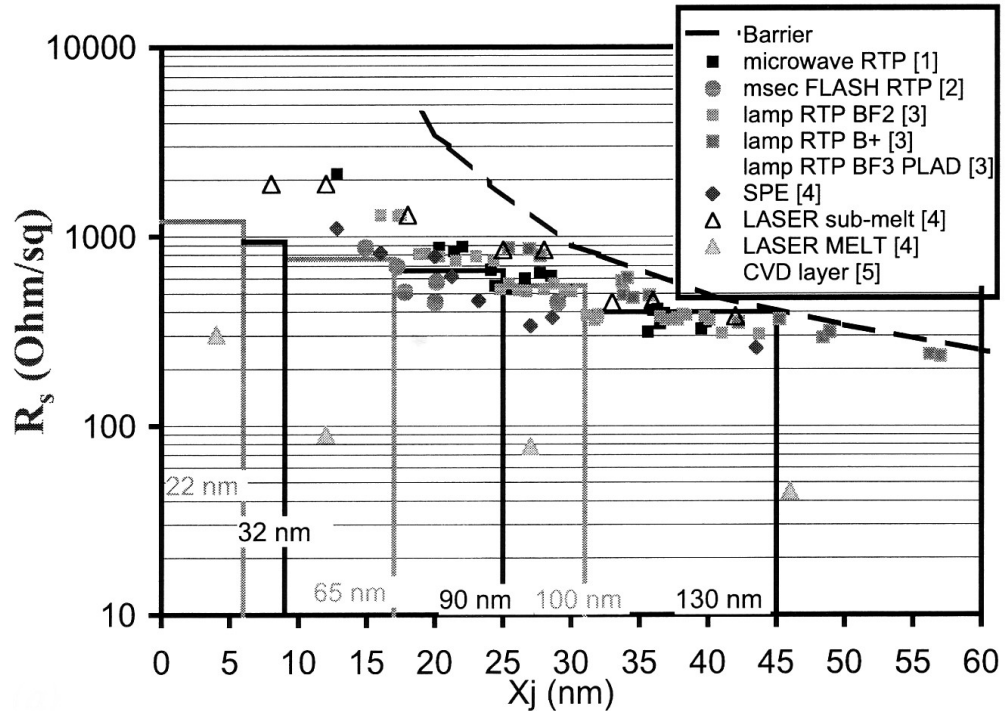


Figure 1-3 International Technology Roadmap for Semiconductors, showing the R_s and x_j required for the SDE to produce devices with the performance characteristics outlined by the individual technology nodes (shown as rectangles).

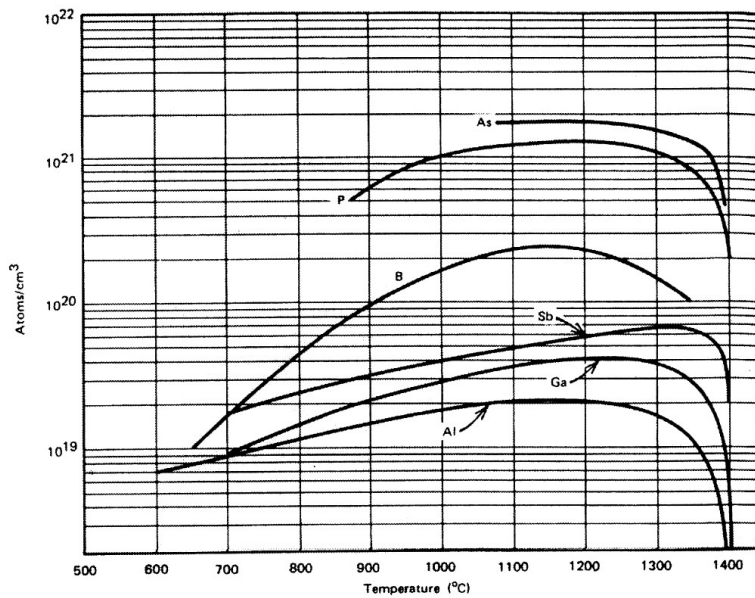


Figure 1-4 Solid solubility of a number of common impurities in Si.

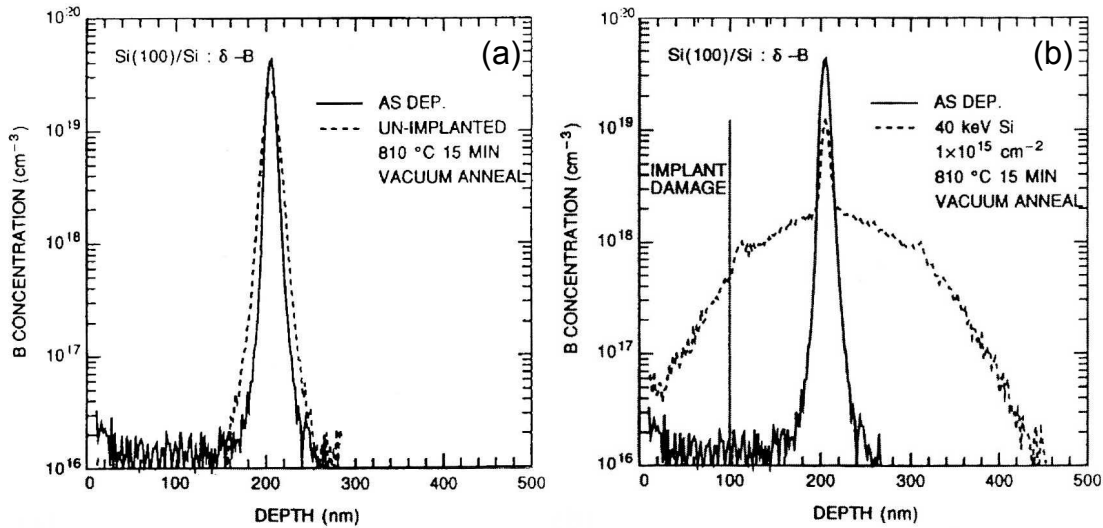


Figure 1-5 Secondary ion mass spectrometry profiles for a δ doped B marker layer before and after an 810°C anneal for 15 min. (a) Approximately 10 nm of diffusion was observed under equilibrium conditions. (b) Approximately 170 nm of diffusion occurred (at a concentration of $1\times 10^{17}/\text{cm}^3$) because of TED associated with the 40 keV Si^+ pre-amorphization implant to $1\times 10^{15}/\text{cm}^2$.

CHAPTER 2 LITERATURE REVIEW

Ion-Implantation

Ion-implantation is the current method by which dopant atoms are introduced into a Si substrate to form the source/drain extension (SDE) region in complementary metal-oxide-semiconductor (CMOS) technology.³ These dopants are accelerated by a predetermined potential supplied by the system and magnetically separated by the mass-to-charge ratio of the ionized particles, which are then directed toward the surface of interest, where they are incorporated into its interior at a depth consistent with a statistical distribution associated with the dominate stopping mechanisms of the implantation process.^{3,38} The two principle stopping mechanisms are elastic nuclear collisions of the primary ions and recoiled atoms with the lattice atoms of the substrate; and electronic dragging associated with the loss of inelastic energy arising from electrostatic interactions among electrons in the outer shell of the transmitted ions and lattice atoms of the substrate. Figure 2-1 shows the two mechanisms.² The nuclear collision process is a function of ion energy, $S_n(E)$, and can be modeled as

$$S_n(E) = 2.8 \times 10^{15} \cdot \frac{Z_1 Z_2}{(Z_1^{2/3} + Z_2^{2/3})^{1/2}} \cdot \frac{m_1}{m_1 + m_2}, \quad (2.1)$$

where Z_1 and m_1 are the ion and Z_2 and m_2 are the substrate atomic number and mass, respectively.² This form of stopping gives rise to the point-defect perturbations discussed next. The electronic stopping component, $S_e(E)$, depends directly on ion velocity and can be expressed by

$$S_e(E) = c v_{ion} = k E^{1/2}, \quad (2.2)$$

where c and k depend on the ion, the substrate, and the particular electronic stopping process being considered. Figure 2-2 graphs energy loss as a function of incident particle energy, and shows that the effectiveness of each stopping process is dependent on the species under consideration and the energy with which it is accelerated.² As can be seen, nuclear stopping increases with decreasing implant energy and increasing impurity mass; and electronic stopping increases with increasing implant energy. The mathematical expression for the rate at which an ion loses its energy is given by

$$\frac{dE}{dx} = -N[S_n(E) + S_e(E)], \quad (2.3)$$

where N is the atomic density of the target.² The total stopping power of an ion is typically on the order of a few 100 eV/nm.³⁸ The range, R , defined as the depth at which an ion comes to rest below the substrate surface, can be calculated if both $S_n(E)$ and $S_e(E)$ are known, by the use Equation 2.4.

$$R = \int_0^R dx = \frac{1}{N} \int_0^R \frac{dE}{S_n(E) + S_e(E)}. \quad (2.4)$$

The statistical nature of the implantation process typically produces an impurity profile similar to a Gaussian distribution with a characteristic projected range R_p (defined as the statistical mean of the depth normal to the substrate surface at which the ions comes to rest), and ion straggle ΔR_p (defined as the standard deviation about the R_p). This distribution can be modeled to first order by Equation 2.5,

$$C(x) = C_p \exp \left[-\frac{(x - R_p)^2}{2\Delta R_p^2} \right] \quad (2.5)$$

where C_p is the peak concentration where the Gaussian distribution is centered.² The total number of ions implanted is defined as the dose, Q , and is expressed as

$$Q = \sqrt{2\pi} \Delta R_p C_p. \quad (2.6)$$

It should be noted that implant profiles into crystalline Si (c-Si) can be significantly different than a Gaussian profile because of the phenomenon known as ion channeling. This occurs when the ion trajectory is aligned along atomic rows where it experiences a slower rate of energy loss, thereby producing a profile with an asymmetric distribution; one that is Gaussian toward the substrate surface, but supplemented by a characteristic broadening at lower concentrations into the bulk of the substrate. Ion channeling can be eliminated by implanting a heavy mass ion (Si^+ or Ge^+) before dopant incorporation, to bring the substrate surface to an amorphous state. Amorphization of the substrate surface effectively prevents the possibility of the ions aligning along atomic rows where they can travel for distances greater than expected. Figure 2-3 shows the R_p and ΔR_p associated with common dopants used in CMOS technology as a function of implant energy.² The distribution of implanted dopants can be described by a series of four moments.² The first moment is the R_p given by

$$R_p = \frac{1}{Q} \int_{-\infty}^{\infty} x C(x) dx \quad (2.7)$$

The second moment is the ΔR_p , which can be expressed as

$$\Delta R_p = \sqrt{\frac{1}{Q} \int_{-\infty}^{\infty} (x - R_p)^2 C(x) dx} \quad (2.8)$$

Equations 2.7 and 2.8 show that both the R_p and ΔR_p decrease with increasing ion and substrate mass. The third moment describes the skewness, γ , and is given by

$$\gamma = \frac{\int_{-\infty}^{\infty} (x - R_p)^3 C(x) dx}{Q \Delta R_p^3}, \quad (2.9)$$

whereas the fourth moment is the kurtosis, β , expressed by

$$\beta = \frac{\int_{-\infty}^{\infty} (x - R_p)^4 C(x) dx}{Q \Delta R_p^4}. \quad (2.10)$$

The γ of an implant describes the asymmetry of a profile about its R_p (i.e., its tendency to lean toward or away from the substrate surface); whereas the β characterizes the contribution of the tail on the flatness of the profile shape (e.g., a larger kurtosis results in a more horizontal profile near its peak).

One significant disadvantage throughout the course of the ion-implantation process is the lattice damage created as a result of the energy transfer associated with the nuclear collisions of the primary ions and recoiled atoms with the lattice atoms of the substrate. Lattice displacements occur when the energy transferred to a Si atom exceeds its displacement energy of 15 eV.³⁸ The creation of a large number of lattice displacements along an ion's traversal path is known as a collision cascade. The primary lattice damage introduced during the implantation process reduces the crystalline order of the substrate by producing point-defects in the form of interstitial and vacancy (i.e., Frenkel) pairs. A point-defect is defined as a crystalline defect associated with one or several atomic sites. An interstitial is defined as a normally unoccupied void space located between substitutional lattice sites, and a vacancy is defined as a normally occupied lattice site from which an atom or ion is no longer present.³⁹ A number of the Frenkel pairs undergo interstitial-vacancy (*I-V*) recombination during the relaxation of the collision cascade,

which occurs on the order of 10^{-13} s.⁴⁰ The probability of recombination of a Frenkel pair is dependent on the separation distance of the interstitial and vacancy, temperature, and the concentration of point-defect traps. The number of Frenkel pairs that remain after relaxation depends on a number of implant conditions including ion mass, ion dose, ion dose rate, and wafer temperature.

It should be noted that both interstitials and vacancies exist naturally in crystalline solids as defined by

$$N_p = N \exp\left(\frac{-Q_p}{kT}\right), \quad (2.11)$$

where N_p is the concentration of point-defects, N is the concentration of lattice sites, Q_p is the formation energy of the point-defect, k is Boltzmann's constant, and T is the temperature of the system.³⁹ The formation energies for interstitials and vacancies have been reported as 2 and 4.4 eV, respectively.⁴¹ The equilibrium values (Figure 2-4) are typically written as C_i^* and C_v^* , (the equilibrium concentration of interstitials and vacancies, respectively).⁴² The corresponding values extracted out to the melting temperature of Si are 3.5×10^{17} and $2.1 \times 10^{17}/\text{cm}^3$, respectively.⁴² Other observations, however, have shown discrepancies in the true values of these equilibrium concentrations.^{43,44}

Figure 2-5 shows the damage density as a function of depth for the three possible primary implant damage morphologies that may exist directly after ion-implantation.⁴⁵ The first profile shows a surface with a damage structure such that the entire profile remains below the amorphization threshold. It should be noted that, although the entire profile remains below the amorphization threshold, it may include isolated amorphous regions within the c-Si lattice. In this case, the damage density profile is similar to the

implant profile, and most of the point-defects are located near the R_p of the implant (where most of the nuclear collisions occur). For non-amorphizing implants, the stable damage is primarily small defect clusters, dopant-defect complexes, and some isolated Frenkel pairs.²

The second profile shows the formation of a buried amorphous layer centered around the peak of the damage profile with c-Si above and below the amorphous region. This morphology is typically avoided in CMOS processing because of the defect structure that forms during post-implant thermal processing.

The third profile shows an amorphous layer that is continuous from the substrate surface to a depth determined by the implant conditions. This shows that most of the point-defects are located just below the amorphous/crystalline (α/c) interface produced by the implant (since the amorphous phase is inherently composed of crystallographic imperfections and is assumed to be structurally uniform). The threshold damage density for the first-order phase transition and formation of an amorphous layer is often taken to be 10% of the Si lattice density.⁴⁶ After an amorphous state is reached, the damage accumulation saturates.² Although amorphous Si (α -Si) no longer exhibits long-range order, covalent bonding still exists between nearest neighbors because of bond stretching and the formation of 5- and 7-member rings. It was shown that α -Si has a melting temperature and atomic density approximately 225 ± 50 °C and $1.8 \pm 0.1\%$ below that of c-Si, respectively.⁴⁷⁻⁴⁹ In addition, it was shown that α -Si consists of an ideal covalently bonded continuous random network (CRN) that can exist as either an as-implanted or structurally relaxed state.⁵⁰⁻⁵⁵ The structurally relaxed α -Si differs from the as-implanted case in that the number of large-angle bond distortions and defect complexes produced

during the pre-amorphization implant are reduced and annihilated, respectively; typically by a low-temperature relaxation anneal (e.g., 500 °C for 60 min).⁵⁶⁻⁶² Regardless of the primary implant damage condition, post-implant thermal processing is required to repair the lattice damage accumulated during the implantation process. A number of defect structures, known as secondary implant damage, are produced as a result of post-implant thermal processing. These structures are dependent on the primary implant-damage condition (Figure 2-5) (Table 2-1).⁴⁵

The evolutionary pathways of point-defects generated during implantation are of significant interest because of their non-equilibrium nature and the effects they may introduce during subsequent thermal processing. It is assumed that the effective mobility of point-defects at room temperature is relatively low because of trapping of the point-defects at a number of sites with a higher capture-cross section than the complementary component of the Frenkel pair; and because any Frenkel defects that survive the initial *I-V* recombination process remain until post-implant thermal processing.⁶³ During post-implant thermal processing, the corresponding point-defect mobilities increase, and the interstitial and vacancy populations decrease as a result of recombination in the bulk or at the substrate surface. This recombination process reduces the free energy of the system by attempting to adjust the interstitial concentration, C_i , and vacancy concentration, C_v , to equilibrium values (C_i^* and C_v^*). The fraction of point-defects that do not participate in the recombination process form intermediate clusters with point-defects or dopant atoms, to obtain a more favorable energy state. The interstitial clusters are suggested to exist in a number of configurations including the di-interstitial, self-interstitial cluster, {311} rod-like defect, and dislocation loop.⁶⁴

The most unstable form of the Si self-interstitial is the free (i.e., single) interstitial. The free interstitial has a compressive strain associated with it because it is larger than any individual interstitial site. It also has a free energy of 1 eV from each unbonded orbital.⁶³ For this reason, in the as-implanted state, the interstitials and vacancies initially created by the implantation process diffuse (even at room temperature) and recombine until they can cluster into stable structures.⁶⁴ One stable structure at room temperature is the di-interstitial.⁶⁵ A di-interstitial represents a more stable configuration compared to the free interstitial, since it reduces the number of unbonded orbitals. Theoretically, by forming an interstitial chain in which interstitials are bonded both to the lattice and to each other in a linear fashion, the number of dangling bonds can be reduced further. This is supported by recent results obtained by modeling interstitial supersaturation measurements, which suggests that interstitial clusters have stable configurations below the size of a {311} defect (i.e., n = 8).⁶⁶

The interstitial-chain configuration was used in many models for the formation of extended defects in Si.⁶⁷⁻⁶⁹ In fact, formation of such an interstitial chain elongated in the ⟨110⟩ direction is the foundation for modeling {311} defects. This is done by adding several ⟨110⟩ chains in the ⟨233⟩ direction, forming an extrinsic stacking fault on the {311} habit plane with a Burgers vector $b = a/25\langle 116 \rangle$.⁷⁰⁻⁷² Figure 2-6a shows a plan-view transmission electron microscopy (PTEM) image of {311} defects produced by a 20 keV B⁺ implant to $1 \times 10^{15}/\text{cm}^3$ after annealing at 750 °C for 5 min.³ It was shown that this type of extended defect further reduces the free energy of the excess interstitials, since the {311} defect has no dangling bonds along the sides of the defect. It should be noted, however, that strained constructed bonds exist at the ends of the {311} defect.⁶⁷

The formation energy (i.e., the energy increase due to the addition of an extra Si atom into a defect) of a {311} defect was shown to be in the 1.0-1.3 eV range.^{73,74} It should be noted that the formation energy slowly decreases as the size of the defect increases.⁷² The asymptotical limit of this formation energy is given by the defect-fault energy (thought to be approximately 0.5-0.9 eV).^{68,75} Recent developments in quantitative TEM imaging have shown the ability to quantify the amount of interstitials contained within the {311} defect.^{17,18,76} The exponential dissolution decay rate of the {311} defect during annealing has an activation energy of approximately 3.7 eV.^{3,64,72} This value corresponds to the sum of the binding and migration energies of a free Si interstitial. It should be noted that the activation energy experimentally observed for the dissolution of the {311} defect corresponds to the difference between the activation energy for self-diffusion and the formation energy of the defect.⁷²

A number of experiments have been performed and show that the dissolution kinetics of {311} defects match the time scale of the effect known as transient enhanced diffusion (TED).^{77,78} Transient enhanced diffusion is a well known phenomenon that describes the enhanced diffusion of dopants during annealing of ion-implanted layers. One source of TED is the release of excess interstitials from the {311} defect.¹⁷ The threshold dose for {311} defect formation was shown to be as low as $5 \times 10^{12}/\text{cm}^2$.¹⁸ For doses above approximately $1 \times 10^{14}/\text{cm}^2$ both {311} defects and dislocation loops may exist. It was shown that, although the dislocation loop density increases while the {311} defect density decreases during subsequent thermal processing, the total number of atoms trapped within the defects remains relatively constant.²¹

Two different types of dislocation loops have been observed: so-called perfect prismatic loops with a Burgers vector $b = a/2\langle 110 \rangle$ and faulted Frank loops with a Burgers vector $b = a/3\langle 111 \rangle$. The Frank loop consists of an extra $\{111\}$ plane bound by a dislocation line.⁶⁴ It should be noted that for higher thermal budgets, dislocation loops of both types are observed, whereas for the highest temperatures only faulted dislocation loops are present.⁶⁴ Figure 2-6b shows a plan-view TEM image of dislocation loops produced by the same 20 keV B^+ implant to $1 \times 10^{15}/cm^3$ as in Figure 2-6a, however, after annealing at 900 °C for 15 min.³ These defects are more stable than $\{311\}$ defects. The threshold dose for $\{311\}$ defect formation was shown to be as low as $5 \times 10^{12}/cm^2$, whereas the threshold for dislocation loop formation is approximately $1 \times 10^{14}/cm^2$.¹⁸ For higher energy implants (380 keV to 1 MeV) the threshold dose for loops can drop as low as $4 \times 10^{13}/cm^2$.⁷⁹ The decrease in threshold dose with increasing implant energy is thought to be due to either the increase in damage deposition in the crystal⁷⁸ or to increased separation of the Frenkel pairs^{80,81} which reduces $I-V$ recombination efficiency. It was proposed that dislocation loops evolve from the unfaluting of $\{311\}$ defects.⁷⁸ It was reported that, for non-amorphizing implants, all the dislocation loops that were observed after post-implant thermal processing formed from the interstitials initially bound in $\{311\}$ defects.⁸² Similar to the interstitial exchange observed between the $\{311\}$ defects and dislocation loops during subsequent thermal processing, the interstitial population within faulted dislocation loops remains relatively constant as they coarsen (i.e., increase in size and decrease in density) during post-implant thermal processing.⁸³⁻⁸⁷ Such a coarsening process which involves atomic diffusion between interstitial sources such that larger dislocation loops grow at the expense of smaller ones can be described by

a conservative Ostwald ripening process. The Gibbs-Thompson equation predicts that a precipitate of diameter $2r$ is in equilibrium with a supersaturation of free interstitials by

$$S(r) = \exp\left(\frac{E_f}{kT}\right), \quad (2.12)$$

where E_f is the formation energy of the defect, k is Boltzmann's constant, and T is temperature. Since the formation energy for a given defect type decreases as its size increases, the supersaturation of Si interstitials around a large defect is smaller than around a small defect.⁶⁴ For this reason, a net flux of interstitials is created from the smaller defects to the larger ones. When the dislocation loop growth consists of an exchange of atoms between the loops, the loop density varies with $1/t$ and the mean radius increases with \sqrt{t} independent of the limiting phenomenon (i.e., diffusion or interface reaction).²¹ The activation energy for the loop growth was determined to be approximately 4.5 eV for long annealing times, which is similar to the value of self diffusion in Si.⁶⁴ This means that the faulted loops are very stable defects and the steady-state equilibrium between the faulted dislocation loops and the supersaturation of Si interstitials around them has been reached. Although dislocation loop dissolution can produce an additional diffusion enhancement during subsequent thermal processing,⁸⁸ the annealing temperature is usually high enough so that the relative enhancement, C_l/C_l^* , is not as large as the effect from {311} dissolution at lower temperatures. It should be noted that if dislocation loops exist in the space charge region of a junction, they can cause high leakage currents.⁸⁹ It was shown during subsequent thermal processing of both types of dislocation loops (i.e., perfect and faulted dislocation loops) that the mean size and density of perfect dislocation loops decreases as a function of time, whereas the total number of interstitials bound in both types of dislocation loops remained relatively

constant. This shows that the Si atoms emitted from the perfect dislocation loops are trapped by the faulted dislocation loops.^{90,91} However, when the proximity of the substrate surface is brought closer to the dislocation loops, it was shown that the perfect dislocation loops dissolve faster and that the emitted interstitials are not captured by the faulted dislocation loops, as in the previous case. Regardless of the proximity of the substrate surface, it can be said that the perfect dislocation loops are less stable than the faulted dislocation loops. The difference between the stability of the two types of dislocation loops is due to the formation energy of the perfect loop being higher than the formation energy of the faulted loop containing the same number of atoms.⁶⁴ Since the reverse transformation of a dislocation loop into a {311} defect has never been observed, the formation energy of a {311} defect has to be higher than the formation energy of either dislocation type; therefore, the probability of forming one or the other type of dislocations loop must depend on the reaction barrier a {311} defect has to overcome to transform into a dislocation loop of either type. From this discussion it can be said that the driving force for the growth of a given type of defects is due to the decrease of the formation energy as its size increases. The change from one type of defect to the next is driven by the reduction of the formation energy after the crystallographic reordering of the same number of Si atoms into the new defect.

Diffusion

In addition to repairing lattice damage accumulated during the implantation process, post-implant thermal annealing assists in the redistribution of dopant atoms throughout the Si lattice through random atomic oscillations which reduce the chemical potential gradient within the system; a process known as diffusion.³⁹ The chemical

potential can also be described as following a concentration gradient as long as the free energy curve displays a positive curvature at the temperature of interest.⁹²

Fickian Diffusion

Macroscopic understanding of the diffusion process can be described by the use of Fick's first law of diffusion which states that the concentration flux per unit area of the diffusing species under steady state conditions is proportional to the concentration gradient, which is expressed as

$$J = -D \left(\frac{\partial c}{\partial x} \right)_t, \quad (2.13)$$

where J is the flux per unit area, D is the diffusion coefficient, C is the concentration of the diffusing species, x is the gradient direction, and t is time. In order to describe a system with a time dependent diffusion characteristic, Fick's second law is used and given by

$$\frac{\partial C(x,t)}{\partial t} = \frac{\partial}{\partial x} D \frac{\partial C(x,t)}{\partial x} = D \frac{\partial^2 C(x,t)}{\partial x^2}, \quad (2.14)$$

which assumes that D is independent of time and space. An Arrhenius relation is used to calculate the diffusion coefficient by

$$D(T) = D_0 \exp \left(\frac{-E}{kT} \right), \quad (2.15)$$

where D_0 is the pre-exponential factor, E is the activation energy for the diffusing species, k is Boltzmann's constant, and T is temperature. (Table 2.2 gives a list of D_0 and E_a values for common dopants and other impurities in Si.)² The characteristic diffusion length of a dopant can be calculated by

$$x = 2\sqrt{Dt}, \quad (2.16)$$

where x is the diffusion distance.³⁸

Atomistic Diffusion

Since Fickian diffusion only considers the temperature dependence of the diffusivity and not the dependence of diffusivity on point-defect populations, additional factors need to be taken into consideration to accurately describe diffusion under non-equilibrium point-defect populations. The two point-defect mediated diffusion processes that dominate in covalently bonded Si are the interstitial and vacancy mechanisms.⁹³ Interstitially mediated diffusion is known to occur by two mechanisms; the kick-out mechanism and interstitialcy exchange. The kick-out mechanism occurs when a substitutional dopant atom is replaced by a Si self-interstitial where it is then able to diffuse as a pure interstitial before returning to a substitutional site as a result of a kick-in mechanism or $I-V$ recombination. Interstitialcy exchange occurs when a dopant atom and a Si self-interstitial occupy a single lattice site. When this occurs, the dopant diffuses by translating positions with nearest neighbors through bond exchange without displacing the Si atoms from their lattice sites. No distinction is made between the interstitial kick-out mechanism and interstitialcy exchange as they are indistinguishable by empirical methods. Vacancy mediated diffusion occurs when a substitutional dopant atom exchanges position with a vacant near-neighbor lattice site. It should be noted that it is possible for both interstitial and vacancy diffusion mechanisms to occur simultaneously within a system.

If both interstitial and vacancy diffusion mechanisms are allowed to operate independently, then the diffusion coefficient can be defined as

$$D_A = D_{AI} \left(\frac{C_{AI}}{C_A} \right) + D_{AV} \left(\frac{C_{AV}}{C_A} \right), \quad (2.17)$$

where D_A is the diffusion coefficient of species A, D_{AI} is the interstitial diffusion coefficient of species A, C_{AI} is the concentration of species A occupying interstitial positions in the host lattice, C_A is the concentration of species A, D_{AV} is the vacancy diffusion coefficient of species A, and C_{AV} is the concentration of species A occupying host lattice sites with adjacent vacancies.⁶ The fractional diffusion of a species through each mechanism may then be defined for the interstitial mechanism as

$$f_{AI} = \left(\frac{D_{AI}}{D_A} \right) \left(\frac{C_{AI}}{C_A} \right), \quad (2.18)$$

and for the vacancy mechanism

$$f_{AV} = \left(\frac{D_{AV}}{D_A} \right) \left(\frac{C_{AV}}{C_A} \right), \quad (2.19)$$

where f_{AI} and f_{AV} are the fractional interstitial and vacancy diffusion components for species A, respectively. By definition

$$f_{AI} + f_{AV} = 1, \quad (2.20)$$

and if it is assumed that the fractional interstitial and vacancy diffusion components are defined under intrinsic conditions, it follows that

$$\frac{D_A}{D_A^*} = f_{AI} \left(\frac{C_{AI}}{C_{AI}^*} \right) + (1 - f_{AI}) \left(\frac{C_{AV}}{C_{AV}^*} \right), \quad (2.21)$$

where D_A^* , C_{AI}^* , and C_{AV}^* are the equilibrium diffusivity component, equilibrium interstitial concentration, and equilibrium vacancy concentration of species A, respectively. In this case, the diffusivity is affected by non-equilibrium concentrations of point-defects and is weighted by the preferred diffusion mechanism of the dopant under consideration. It was shown that the $f_{AI} \approx 1$ for B under intrinsic diffusion conditions.^{94,95}

Now Equation 2.17 can be written as

$$\frac{D_A}{D_A^*} = \frac{C_{AI}}{C_{AI}^*} \quad (2.22)$$

It is apparent from Equation 2.18 that the amount of B diffusion (divided by its equilibrium diffusion value) is directly proportional to the supersaturation of interstitial point-defects.

Transient Enhanced Diffusion

Although post-implant thermal processing results in the recombination of Frenkel pairs, an excess of interstitials similar to the implanted dose is expected to remain after relaxation of the collision cascade. Indeed, it was shown that during the early stages of annealing, the total number of Si self-interstitials stored in the extended defects is approximately the same as the ion dose.⁶⁴ This became known as the “+1” model.²¹ Additional work showed that there are ion mass and implant energy effects that can increase the interstitial supersaturation, resulting in an effective plus factor that is different than that predicted by the “+1” model.⁹⁶ Transient enhanced diffusion (TED) is the phenomena associated with an increase in dopant diffusion behavior during post-implant thermal processing. In the case of B, the Si self-interstitials generated during the implantation process redistribute throughout the lattice^{17,18} during post-implant thermal processing and remove the B atoms from their substitutional sites by a so-called kick-out reaction,¹⁹⁻²¹ allowing them to diffuse deep into the substrate through a well documented interstitial mechanism.²²⁻²⁵ The interstitial B atom will continue to diffuse until it removes a substitutional Si atom from a lattice site by a corresponding kick-in reaction, which produces an additional Si self-interstitial capable of removing another substitutional B atom. This process continues until C_I equals C_I^* . The interest of

understanding TED is being able to successfully predict and/or prevent its ability to increase the junction depth of the SDE to unacceptable levels.

One example of TED is shown in Figure 2-7, which shows secondary ion mass spectrometry (SIMS) profiles of a 4 keV B^+ implant to $1 \times 10^{14}/cm^2$ after annealing at 750 °C.⁹⁷ As can be seen, the low concentration region of the profile experiences a large diffusion enhancement after only 3 min of annealing at 750 °C. The diffusion enhancement is similar for the 13 and 30 min profiles suggesting that the diffusion enhancement is complete by 13 min. The peak of the B profile remains stationary because the high local concentration of excess Si interstitials and B atoms, which form immobile electrically inactive sub-microscopic B-interstitial clusters (BIC's).⁹⁸ The most notable feature of this experiment was that both cross-sectional and plan-view TEM (XTEM and PTEM, respectively) imaging revealed that no extended defects formed during post-implant thermal processing throughout the 700-800 °C temperature range investigated. Since there were no {311} defects or dislocation loops available to provide the interstitials necessary to produce the observed diffusion enhancement, this shows that another source of interstitials was responsible for the increase in B diffusion behavior after annealing at 750 °C. This source was presumably BIC dissolution during the first 13 min of annealing at 750 °C, which is faster than corresponding several hour-long saturation times associated with {311} dissolution.⁹⁹ Figure 2-8 shows a graph of TED saturation time as a function of inverse temperature with experimental data from a number of sources, and shows that the activation energy for TED saturation without the presence of {311} defects is approximately 1.3 eV, which is considerably lower than the

activation energy for TED saturation with {311} defects which is approximately 3.7 eV.^{3,64} Figure 2-9 provides a summary of all the possible sources of TED.³

It was shown that Si⁺ implants into a substrate with a δ doped B marker layer resulted in TED characteristics similar to the exponential dissolution rate of the {311} defects.³ There, the interstitial concentration within the {311} defects was similar to the implanted dose consistent with the “+1” model. The diffusion characteristics are, however, different for B⁺ implants which result in diffusion behavior that suggest an initial diffusion enhancement occurs due to BIC dissolution which is followed by diffusion characteristics similar to the dissolution rate of the {311} defects.³ The thought that BIC dissolution causes the initial diffusion enhancement is consistent with Ref. 97, which showed a weakly activated increase in diffusion behavior during the first 13 min of annealing at 750 °C (outside the presence of {311} defects and dislocation loops). In addition, it was shown that a 60 keV Si⁺ implant to $1 \times 10^{14}/\text{cm}^2$ resulted in a decreasing interstitial density within the {311} defects with increasing B background doping level, supporting the formation of BIC’s.¹⁸ Although {311} defects are relatively unstable, the dissolution rate of these defects decreases for B⁺ implants when compared to Si⁺ implants. This is presumed to be due to BIC dissolution, which provides a high background concentration of interstitials (thereby decreasing the dissolution rate of the {311} defects).³

It is well known that the increase in junction depth (x_j) as a result of TED can be estimated by

$$\Delta x_j^2 = NR_p \exp\left[\frac{-(-1.4 \text{ eV})}{kT}\right], \quad (2.23)$$

where Δx_j is the change in x_j after complete annealing of the defects, N is the number of interstitials trapped within the implant related extended defects, and R_p is the projected range of the implant.³ It can be seen that this equation has an effective negative activation energy, which suggests that the amount of TED will decrease when the damage is annealed out at a higher temperature.^{3,9,27} This arises from the fact that the interstitial supersaturation because the presence of extended defects is larger at a lower temperature.²⁷ This observation influenced the development of single-wafer thermal processes capable of producing a high temperature ambient with ramp rates on the order of 50-200 °C/s, and fast switching times to insulate the dopant from a high degree of TED.²⁸

Electrical Activation

Although a significant amount of diffusion may occur during post implant thermal processing, it is required to repair lattice damage accumulated during the implantation process as well as activate dopants by establishing them on substitutional sites where they are able to contribute their holes (electrons) to the valence (conduction) band. When a dopant resides on a substitutional site, it participates in local covalent bonding within the Si lattice. Since dopants have either fewer (group III, e.g., B) or greater (group V, e.g., As) valence electrons than Si (group IV), covalent bonding between these dopants and Si atoms results in a weakly bound hole or electron, respectively. Although B may reside on a substitutional site, it is still possible that the hole created by bond orbital deficiency of the B atom will not contribute to the electrical conductivity of the system. First, the hole must have sufficient thermal energy to overcome the ionization potential of the B atom. At room temperature, substitutional B atoms have enough thermal energy

that all holes are assumed to be ionized.⁶³ Although there is enough thermal energy available to ionize B atoms at room temperature, ionized holes still may not contribute to the conductivity if there are compensating species in the Si lattice which recombine with or trap the holes. The possibility of hole compensation is an important consideration when impurities are present in concentrations comparable to the B concentration.

Since the concentration of charge carriers controls the conductivity of the SDE, it is desirable to be able to increase this concentration as high as possible. The basic formula for determining the conductivity, σ , of a material is given by

$$\sigma = e(n\mu_n + p\mu_p) \quad (2.24)$$

where e is the charge of an electron, n and p are the electron and hole concentrations, respectively, and μ_e and μ_p are the effective mobility of electrons and holes, respectively. It should be noted that the mobility itself is dependent on scattering from ionized impurities and shows lower mobility as the active doping concentration increases.

Figure 2-10 shows the effect of active dopant concentration on electron and hole mobility.³⁸ Figure 2-11 shows the binary equilibrium phase diagram of B and Si.¹⁰⁰ A phase diagram is most easily defined as a graphical representation of the relationships between environmental constraints (i.e., temperature and pressure), composition, and regions of phase stability, ordinarily under conditions of equilibrium.³⁹ While the binary phase diagram of B and Si describes the maximum concentration of substitutional B under equilibrium conditions, there are phenomena, such as point-defect mediated clustering, which can prevent these concentrations from being achieved.

It is well known that the pairing between both B atoms and Si interstitials results in the formation of an immobile B complex which is presumed to be inactive.¹⁸ It was

shown that this clustering only occurs when the concentration of B atoms and Si interstitials is sufficiently high.⁹ The exact structure (i.e., stoichiometry) of this complex has been the subject of ongoing investigation. Direct observation of these clusters by such techniques as high resolution TEM or x-ray diffraction (XRD) is complicated by their small size (being approximately 3 to 8 atoms clusters). Thus, evidence of these clusters can only be obtained by electrical measurements and theoretical calculations.⁹ After exceeding the temperature dependent B solid solubility limit, an inactive phase forms which is presumably SiB₃ as predicted by the equilibrium phase diagram.¹⁰⁰ Some discussion exists that perhaps SiB₄ or SiB₆ is the true equilibrium phase.^{101,102} A phase is defined as a homogeneous part of a system which, having definite bounding surfaces, has uniform physical and chemical characteristics.^{39,103} This phase formation process results in self-interstitial injection into the Si lattice. The interstitial injection process leads to enhanced diffusion of the B and is known as B enhanced diffusion (BED).¹⁰⁴ A number of different cluster models have been proposed, however, all observations show that increasing the number of either B atoms or Si interstitials will lead to an increase in the amount of BIC's that form during post-implant thermal processing.^{18,105-110} Although BIC's cannot be directly observed by TEM, the formation of BIC's reduces the formation of {311} defects. This was observed by noting the reduction in trapped interstitial density in {311} defects when in the presence of B.¹¹¹ In addition, it was shown that low energy B implants exhibit BIC's outside the presence of {311} defects and dislocation loops.⁹⁷ Others have observed B clustering by comparing differences in the number of {311} defects that form in doping wells with different B concentrations.¹¹² This experiment showed that samples with increasing B concentration (and therefore

increasing number of BIC's) exhibit a decrease in {311} defect density. It is apparent from the above discussion that BIC's have a significant impact on both the electrical activation characteristics and extended defect evolution kinetics of ion-implanted Si. Regardless of the mechanisms that dominate dopant activation and defect evolution, post implant thermal processing is required to repair lattice damage accumulated during the implantation process as well as activate the B atoms by establishing them on substitutional sites where they are able to contribute their holes to the valence band.

Rapid Thermal Processing

The observation that TED decreases when the extended defects are annealed at a higher temperature³ influenced the development of single-wafer thermal processes capable of producing a high temperature ambient with ramp rates on the order of 50-200 °C/s.²⁸ This technique, known as rapid thermal processing (RTP), has proven successful in producing junctions with performance characteristics necessary for the continued scaling of CMOS technology to date.²⁹ Its ability to satisfy these requirements is associated with improved equipment capability in the form of spike annealing, which decreases the effective thermal budget, allowing for higher annealing temperatures to improve activation and reduce the amount of diffusion of the dopant during the thermal process.^{30,31} A spike anneal is characterized as a short thermal-anneal cycle that can be achieved by increasing the ramp-up and ramp-down rates and by minimizing the time at the temperature of interest. The inability of this technique to produce junctions with the performance characteristics required by future technology nodes is in the cycle time of the thermal process, which results in an unacceptable amount of dopant diffusion. The minimum cycle times in conventional RTP techniques are limited by the maximum

power delivered to the wafer, which determines the ramp-up rate, and the minimum response time of the relatively large thermal mass incandescent tungsten lamps, which determines both the soak time and the ramp-down rate. Without being able to minimize the soak time and the ramp-down rate, increasing the ramp-up rate above 100 °C/s results in no additional improvement in terms of forming a highly-activated ultra-shallow junction.^{30,32}

Another process limitation associated with RTP is that a significant amount of TED occurs during the early stages of annealing, which promotes diffusion, resulting in a profile with lack of abruptness and an unacceptable increase in x_j .^{9,66} This initial interstitial injection mechanism occurs because either the dissolution of unstable sub-microscopic interstitial clusters, or the inability of the extended defects in capturing the entire interstitial population during their formation.^{98,113,114} In addition, although increased spike sharpness enhances the ability to increase the annealing temperature to achieve higher activation levels and improve junction abruptness,¹¹⁵ the amount of diffusion that occurs during the thermal process is still unacceptable. As the spike anneal approaches time durations on the order of 1-2 s within 50 °C of the peak temperature the advantages offered by annealing at higher temperatures are cancelled by the lack of concentration enhanced diffusion (CED) that takes place during the thermal process, which results in a profile with an unacceptable x_j due to the diffusion produced by TED during the early stages of annealing.¹¹⁶ It should be noted that the ramp-down rate for conventional RTP is limited to 50-80 °C/s because radiative cooling of the substrate to the ambient.^{3,117} This radiative cooling may be sufficient to keep the wafer at high enough temperatures to produce more diffusion than would be expected if only the

surface of the wafer was heated, which would allow for rapid conductive heat loss through the substrate. This annealing technique is also limited by equilibrium activation levels (i.e., $1\text{-}2 \times 10^{20}/\text{cm}^3$) due to the solid solubility of B in c-Si. These limitations illustrate the need to investigate novel annealing technologies that may be able to produce junctions with above solid solubility activation levels without being subject to a significant amount of TED.

Alternatives to Conventional Thermal Annealing

Conventional RTP is unable to further improve the R_s and continue to decrease the x_j of the SDE because the solid solubility limited activation levels in c-Si and the amount of diffusion that occurs during the thermal process, respectively. Both these limits need to be overcome to produce devices with the performance characteristics required by the future technology nodes as outlined by the International Technology Roadmap for Semiconductors (ITRS).¹³ A number of techniques are being considered as alternatives to conventional RTP for B ultra-shallow junction formation, and are discussed in the following sections.

Low Temperature Solid-Phase Epitaxial Regrowth

Recent attention has been given to low temperature solid-phase epitaxial regrowth of α -Si layers because its ability to activate dopants well above their solid solubility levels as well as limit the amount of diffusion observed during the thermal process.¹¹⁸ This process involves using either a deposited or implantation-induced amorphous layer in contact with c-Si substrate, which upon heating to sufficient temperatures (i.e., 550-600 °C) allows the amorphous layer to crystallize using the c-Si substrate as a heterogeneous nucleation source. It was shown that thermal heating,¹¹⁹⁻¹²³ electron-beam

heating,^{124,125} ion-beam assisted regrowth,¹²⁶⁻¹²⁹ and laser heating¹³⁰⁻¹³³ techniques are all capable of regrowing an amorphous layer by providing enough energy for recrystallization. During recrystallization, a well-defined α/c interface moves toward the substrate surface at a rate dependent on several factors such as substrate orientation¹³⁴⁻¹³⁶ and impurity concentration.¹³⁷⁻¹⁴¹ In general, the regrowth velocity follows an Arrhenius temperature dependence given by

$$v = v_0 \exp\left(\frac{-E_a}{kT}\right), \quad (2.25)$$

where v is the regrowth velocity, v_0 is the pre-exponential factor, E_a is the activation energy, k is Boltzmann's constant, and T is temperature. It was shown that the E_a is approximately 2.7 eV over a large range of temperatures.¹⁴² As was mentioned above, the amorphous layer may be deposited onto a crystalline layer or substrate using a growth technique such as chemical vapor deposition (CVD) or created by implanting a heavy ion (e.g., Si^+ or Ge^+) to a dose sufficient to create a continuous amorphous layer that extends from the substrate surface down to a depth consistent with the implant conditions. The most noticeable disadvantage to using a deposition technique is the need to control impurity concentration on the surface of the substrate, which may prevent growth of a high quality epitaxial layer. The more common approach involves solid-phase epitaxial regrowth (SPER) of an implantation-induced amorphous layer, which has the advantage of producing a cleaner amorphous layer and α/c interface.

The main disadvantage with SPER of an implantation-induced amorphous layer is that a significant amount of damage remains below the original α/c interface. If no further high temperature thermal processing is to be used to form the SDE, in a disposable spacer process for example, this damage can give rise to a large amount of

leakage current. It is well known that defects in the space-charge region of a device contribute to leakage current in bipolar transistors.^{11,12} According to the ITRS, junction leakage should only contribute a small amount to the total leakage during the off-state of metal-oxide-semiconductor field-effect-transistors (MOSFETs).¹³ If, however, a subsequent high temperature RTP anneal is used, during a deep source/drain (S/D) activation anneal for example, this damage will result in an unacceptable amount of diffusion due to TED. Therefore, although this technique satisfies the criteria for producing above solid solubility activation levels and results in a limited amount of diffusion during the thermal process, the damage that exists below the α/c interface will result in an excessive amount of junction leakage or enhanced diffusion (depending on the approach used to activate the dopants in the deep S/D region of the device), thereby making this technique inappropriate for activation of the SDE.

Non-melt Laser Annealing

Non-melt laser annealing is also being investigated as an alternative to conventional RTP for B ultra-shallow junction formation because its ability to activate dopants above their solid solubility levels as well as limit the amount of diffusion observed during the thermal process. Non-melt laser annealing (NLA) [also known as laser spike annealing (LSA) or dynamic surface annealing (DSA)] can be used two different ways; either by using a continuous wave (cw) laser which continuously scans across the substrate surface or by stepping a pulsed laser tuned below the melting temperature threshold of either α -Si (if the surface was pre-amorphized) or c-Si. The radiation power densities achievable at the sample surface for the cw process are much lower than the pulsed laser situation and the local dwell time of the cw beam is on the

order of a few milliseconds which is a much longer time scale than the pulsed laser process which occurs on the order of nanoseconds. It should be noted the relatively extended heat pulse duration during cw laser annealing ensures that the dominant annealing (and presumably activation) mechanism is SPER of the irradiated layer (provided a pre-amorphization implant is performed before dopant incorporation).^{143,144} Although some preliminary work has been reported on the nanosecond process, the millisecond process will be the focus of the present discussion.

For cw laser annealing, when the characteristic penetration depth, W , is much less than the square root of the product of the heat diffusion coefficient, D , and the pulse duration, τ , (i.e., $W \ll \sqrt{D\tau}$) the surface temperature increases with the square root of the time during the laser scan by

$$T(0,t) = 2 \frac{I_0}{\kappa} \sqrt{\frac{Dt}{\pi}} (1 - R), \quad (2.26)$$

where T is temperature, t is time, I is the power density, κ is the thermal conductivity of the system, D is the heat diffusion coefficient, and R is the reflectivity of the system.¹⁴⁵ For cw irradiation, a steady state temperature is reached as a result of the balance between heat absorption and diffusion by

$$\Delta T = \frac{P}{\sqrt{2\pi a \kappa}}, \quad (2.27)$$

where T is the temperature, P is the power, a is the laser beam radius, and κ is the thermal conductivity. The typical size of cw laser beam is approximately 50-100 μm in diameter. In this geometry, the relevant parameter governing the temperature rise is the ratio P/a (i.e., absorbed power/beam radius). A steady state temperature is reached after a transient time on the order of $C_p a / \kappa$, where C_p is the specific heat at constant pressure.¹⁴³

Figure 2-12 shows the energy density required to reach the melting temperature (T_m) of the substrate surface for a pulse duration in the range of 10^{-6} - 10^{-2} s.¹⁴⁵ For irradiation at this threshold value, a temperature in the range of $0.9T_m - T_m$ is maintained for a time interval on the order of 0.2τ .¹⁴⁵ This temperature-time combination can be enough to activate dopants during SPER of an implantation-induced amorphous layer. It was shown that a time of approximately 10^{-5} s is enough to regrow 50 nm of α -Si at a substrate temperature close to the melting point.¹⁴⁴ This extrapolation to high temperature of the low temperature data is shown in Figure 2-13, where the time required to grow 50 nm of α -Si is plotted as a function of the substrate temperature.¹⁴⁵ From this data and it can be said that, for $\tau > 10^{-5}$ s, solid-phase effects are important for irradiations near the melt threshold value.

It was shown that this NLA annealing technique results in very little diffusion during the thermal process. In addition, it was reported that this technique is capable of activating dopants above solid solubility, although deactivation to equilibrium solubility levels takes place during subsequent thermal processing.¹⁴⁶ Additional TEM results show that the defect density after cw laser annealing is significantly reduced when compared to conventional furnace annealing.^{147,148} This shows that the NLA technique is sufficient to produce a highly activated junction with a significant amount of EOR damage evolution without appreciable diffusion.

The two main disadvantages of the NLA technique are the Gaussian profile of the scanned laser and the defects that can be incorporated into the annealed layers. Under most annealing conditions the irradiation source can no longer be considered planar and transverse heat flow must be taken into account. The Gaussian profile of the scanned

laser results in non-uniform energy input across the each scan line. This will produce, for example, a number of regrowth velocities across the profile of the scanned laser, requiring overlapping scans to ensure complete regrowth of the amorphous layer of pre-amorphized substrates. Also, annealing of crystalline substrates may result in melting of the surface layer near the center of the scan line because the intensity of the power near the center of the Gaussian distribution of the laser profile.¹⁴⁵ Regardless of the surface layer being annealed, overlapping scans will be needed for reliable dopant activation in both pre-amorphized and crystalline materials. In addition to the issues regarding the Gaussian profile of the scanned laser, it was shown that this annealing technique results in defect formation under certain annealing conditions. It was shown that slip dislocations can be produced if the local temperature produced by the scanned laser is too high.¹⁴⁹⁻¹⁵² In addition to slip dislocation formation, excess point-defects have been shown to exist in the annealed layers. For example, deep level transient spectroscopy (DLTS) studies revealed hole emission centers at $E_v + 0.28$ eV in material implanted with As⁺.¹⁵³ Additional work showed that, although these centers can be removed by furnace annealing at 450 °C, electron emission centers at $E_c - 0.28$ eV then remain.¹⁴⁵ These types of defects, in addition to the issues regarding the Gaussian profile of the scanned laser, complicate the use of NLA for activation of the SDE.

Laser Thermal Processing

Another technique being considered as an alternative to conventional RTP for B ultra-shallow junction formation is melt laser annealing. Laser thermal processing (LTP) incorporates an excimer pulsed laser capable of melting the near surface region of the c-Si substrate.¹⁵⁴ When the energy supplied to the system per unit time is less than that

needed to sustain the Si melt the severely undercooled liquid regrows by liquid phase epitaxy with regrowth velocities on the order of 3 m/s,¹⁵⁵ which is sufficient for incorporating dopants on substitutional sites. This annealing technique is beneficial in that the dopant diffusivities are on the order of 2×10^{-4} cm²/s in the liquid phase,¹⁵⁶ and the segregation coefficient for the most common dopants approaches unity as shown in Figure 2-14.¹⁴⁵ Both of these characteristics contribute to the formation of the desired hyper-abrupt box-like profile. This method is capable of producing junctions with improved characteristics over those obtained through conventional RTP due to the rapid quenching associated with the liquid phase transition which results in supersaturated solid solutions, and the time duration of the laser anneal, which allows for conductive heat loss through the substrate.

When considering pulsed laser annealing, the energy required to melt a given thickness of material depends on the coupling of the laser energy with the target and the thermodynamic properties of the irradiated substrate. As can be seen in Figure 2-15 the free energy of α -Si is higher than that of c-Si and, because of this, the melting temperature and enthalpy of α -Si is lower than c-Si.^{145,157} Indeed, experiments performed with both electron and laser pulses have confirmed that the melting temperature and enthalpy of α -Si are lower than the corresponding c-Si values.¹⁴⁵ The coupling of the laser energy with α -Si is different from that with c-Si because of its greater absorbance (i.e., shallower W), leading to a different threshold for surface melting. The threshold for surface melting of α -Si scales approximately as $\tau^{1/2}$, which is shorter than that for c-Si because its higher absorbance. For ion-implanted materials, the thickness of the amorphous layer can be made either thinner or thicker than the W in the

amorphous material. In the first case, only a fraction of the entire energy is used to heat and melt the surface, the remaining fraction being distributed over a greater depth because of the larger value of W in the c-Si. The energy density threshold for surface melting will then be intermediate between those for the case where the amorphous layer is sufficiently thick to completely absorb the laser energy and the case where a crystalline substrate is being used. For the intermediate cases, the threshold for surface melting will depend on the amorphous layer thickness.

One characteristic of this annealing technique is that the melt depth displays a linear dependence with the energy density produced by the irradiation source. Since the maximum melt depth determines the x_i directly after irradiation, the pulse to pulse energy density variation of the irradiation source makes it difficult to produce a constant x_i across the wafer. This is circumvented by pre-amorphization of the substrate surface prior to dopant incorporation, which introduces a 225 ± 50 °C melting temperature depression associated with the α -Si phase transition.^{47,48} When the liquid front reaches the α/c interface, the difference between the melt thresholds serves as an energy barrier which disallows further melting. This results in a process window corresponding to the difference between the energy required to melt to the α/c interface and the energy required to propagate the melt front into the underlying c-Si, and accounts for the pulse to pulse energy density variation of the irradiation source.

The main disadvantages of this annealing technique are the laser absorption dependence on both the dopant specie and concentration, the epitaxial defects produced as a result of laser annealing within the process window, and the anomalous diffusion behavior associated with the liquid phase epitaxial regrowth of the irradiated material. It

was shown that laser annealing can result in different process window bounds depending on the dopant specie and concentration near the substrate surface.^{158,159} Variable angle spectroscopic ellipsometry (VASE) measurements revealed that the dopants reduced the reflectivity of the near surface region, thereby allowing more irradiation energy to be transmitted to the substrate. This increase in transmitted energy to the substrate was presumed to be sufficient to change the process window bounds accordingly. This dopant dependence may be overcome by using an absorber layer to couple the laser energy uniformly over the irradiated region and transfer a controlled amount of heat to the underlying substrate. This will increase the number of processing steps required to anneal the material and may complicate processing. It is well known that regrowth related defects exist after laser annealing with an irradiation energy density within the process window and that these defects have a significant effect on the dopant diffusion behavior and extended defect evolution during subsequent thermal processing.⁴¹ The density of these regrowth related defects decreases with increasing energy density within the process window [or by performing a relatively low temperature (i.e., 450 °C) anneal in order to smooth the α/γ interface before laser annealing].^{41,160} Since both the diffusion behavior and defect evolution are dependent on the regrowth related defect density, these differences reintroduce an irradiation energy density dependence even when an energy density within the process window is used. In addition to the regrowth related defects that form when laser annealing within the process window, it has also been shown that rapid liquid phase regrowth results in an anomalous diffusion enhancement which can have a significant effect on dopant diffusion behavior during subsequent thermal processing. It was shown that a significant diffusion enhancement can occur during

post-LTP thermal processing even when no regrowth related defects are present and the entire EOR interstitial profile is completely consumed during the melt.¹⁶¹ Additional SIMS results showed that this diffusion enhancement increased with increasing pre-amorphization dose and irradiation energy density (when melting past the entire EOR interstitial profile).^{161,162} Since the EOR damage was completely consumed before post-LTP thermal processing, a secondary source of submicroscopic defects must be responsible for supplying the interstitials necessary for the observed diffusion enhancement during subsequent thermal processing, and that the number of these defects increase with pre-amorphization dose and irradiation energy density. One possible source of interstitials is quenched in point-defects associated with the rapid liquid phase epitaxial regrowth of the Si surface after irradiation. It can be seen that each of these considerations make activation of the SDE with a single pulse of energy density difficult.

Ultra-high Temperature Annealing

Novel high-power arc lamp design has enabled ultra-high temperature (UHT) annealing as an alternative to conventional RTP for B ultra-shallow junction formation.³³ This technique heats the wafer to an intermediate temperature (e.g., 800 °C) before discharging a capacitor bank into flash lamps, which anneals the device side of the wafer at a relatively high temperature (e.g., 1200 °C) for a few milliseconds.³⁴⁻³⁶ The UHT anneal heats the surface of interest while increasing the bulk wafer temperature not more than 50 °C of the intermediate temperature, allowing for conductive heat loss through the substrate. These qualities resolve one of the limiting issues associated with conventional RTP techniques.

The minimum cycle times in conventional RTP techniques are limited by the maximum power delivered to the wafer, which determines the ramp-up rate, and the minimum response time of the relatively large thermal mass incandescent tungsten lamps, which determines both the soak time and the ramp-down rate. Without being able to minimize the soak time and the ramp-down rate, increasing the ramp-up rate above 100 °C/s results in no additional improvement in terms of forming a highly-activated ultra-shallow junction.^{30,32} In contrast to tungsten lamp heating technology, a water-wall arc lamp provides the means for significantly reducing the heating-cycle time because of its ability to deliver higher power and because of its faster response time.¹⁶³ The arc lamp responds more rapidly than tungsten filament lamps due to the reduced thermal mass of the argon gas used in the arc lamp system. The lamps can be switched off in a few microseconds, allowing greater control and repeatability over the anneal process. The response realized in practice is determined by the power supply and control system. An approximate value for the response time of the arc lamp system is 50 ms when excited with a 3-phase rectifying bridge supply.³⁴ It should be noted that a switch mode supply is capable of even faster response times. The switching time constant for tungsten incandescent lamps is on the order of 0.5 s.¹⁶³ A second advantage of the arc lamp design is its spectral distribution, which is shown in Figure 2-16 in terms of radiant power as a function of wavelength.³³ Figure 2-17 shows the integrated spectra as a function of wavelength and shows that over 95% of the arc radiation is below the 1.2 μm band gap absorption of Si at room temperature (compared to 40% for tungsten).³³ It should be noted that as the electrical power is reduced the spectra from tungsten sources shift to longer wavelengths and absorption drops below 40%. In contrast, the arc lamp spectral

output is constant with electrical power and the absorption characteristics do not change.³³ Arc lamp radiation is strongly absorbed in Si due to band-to-band transitions with very low transmission through the wafer.¹⁶⁴

The temperature-time and temperature-depth profiles for a conventional tungsten-based system and the arc lamp-based system are shown in Figure 2-18.¹⁶⁵ The impulse anneal (iRTPTM) is produced by continuous wave mode arc lamp irradiation of the front surface of the wafer and is responsible for producing the bulk wafer temperature, known as the intermediate temperature, at which the flash anneal (fRTPTM) is to be introduced. The fRTP anneal is produced by discharging a capacitor bank into flash lamps which increases the temperature of the surface of interest while increasing the bulk wafer temperature not more than 50 °C of the intermediate temperature.¹⁶⁶ The iRTP anneal provides a means to better understand the advantages gained by the fRTP anneal. The conventional tungsten-based system temperature-time profile is characterized by a rounded thermal profile, which is produced as a result of the wafer response being similar to the heating source. The iRTP temperature-time profile is characterized by a peaked thermal profile, which is produced as a result of the heating source being faster than the wafer while keeping the bulk temperature relatively uniform. The temperature-depth profiles for both the tungsten-based system and arc lamp-based system under iRTP annealing conditions are similar in that the entire wafer is brought to the peak annealing temperature of interest. The temperature-time profile for the arc lamp-based system under fRTP annealing conditions illustrates the relatively short time of the fRTP anneal when compared to the iRTP anneal. The corresponding temperature-depth profile shows that fRTP annealing only significantly heats the surface

of interest while raising the ambient temperature not more than 50 °C of that produced by the intermediate anneal, allowing for conductive heat loss through the substrate. These qualities resolve the limiting issues associated with conventional RTP annealing.

It was recently shown that this UHT annealing technique results in very little diffusion during the thermal process and produces junctions capable of satisfying the activation requirements for future technologies nodes, presumably because the high activation levels obtained during SPER of an implantation-induced amorphous layer.¹⁶⁶ Although the corresponding PTEM images of the damage produced by the pre-amorphization implant were not included, one could argue that a significant amount of defect evolution occurred because the relatively high annealing temperatures used (similar to the cw laser annealing case); therefore, it is put forward that the UHT annealing technique is sufficient to produce a highly activated junction with a significant amount of EOR damage evolution without appreciable diffusion.

The two most foreseeable challenges facing the successful integration of this annealing technique into a conventional CMOS process flow are the highly non-equilibrium nature of the fRTP annealing technique which may be difficult to control over an appreciably large area (e.g., the surface of a 300 mm wafer), and the complex structures that exist on the surface of a patterned wafer which may introduce emissivity effects. An example of the second challenge can be seen in Figure 2-19 which shows the change in spectral emissivity of Si as a function of wavelength with different thin film composites.^{167,168} Although both of these issues could affect the activation characteristics in the SDE region of the device, this annealing technique represents the most natural extension of conventional RTP and is presumed to be as likely as cw non-melt laser

annealing in being implemented as the SDE annealing technique for future technology nodes. Even though this annealing technique may be considered as one of the most likely candidates to form the SDE for future technology nodes, the activation and diffusion mechanisms that take place on these times scales are not well understood and are the subject of this work.

For high-volume manufacturing, it is essential that the absolute temperature of the system be reliably measured on a real time basis to be able to close the control loop for consistent process results. In particular, it is desirable to be able to monitor the relative temperature distribution over the entire wafer area for process development and to maintain quality control during production. These temperature measurements must be made on production wafers and must be independent of the wafer properties (i.e., emissivity effects).³³

Both the water-wall arc lamp design and black body absorbing chamber technology used for this UHT annealing technique introduce novel measurement opportunities. The arc lamp system can be turned off and on in less than 1 ms because the low thermal mass of the argon gas in the arc lamp. This is much shorter than wafers thermal time constant. With this fast response time it is possible to turn the lamp off, measure the wafer thermal radiation, and then turn the lamp back on before the wafer temperature changes. A measurement of radiation reflected from the wafer is obtained by comparing measurements with the lamp both on and off. Using the known spatial and angular distribution of primary radiation on the wafer, combined with the measured reflected radiation from the wafer surface, provides an estimate of reflectivity as a function of angle and hemispherical reflectivity. Using these real time measurements of

reflectivity to estimate emissivity (and using the thermal radiation measurements) permits calculation of the wafer temperature. The absorbing chamber eliminates the cavity effect, ensuring that the actual wafer emissivity is measured.³³

The wafer temperature, T , is calculated using the emission from a gray body, which is expressed by

$$I = \varepsilon \frac{2\pi c^2 h \Delta\lambda}{\lambda^5} \left[\exp\left(\frac{hc}{\lambda k T}\right) - 1 \right], \quad (2.28)$$

where I is the emitted intensity at the wavelength, λ , of interest in a band $\Delta\lambda$ wide, ε is the emissivity, c is the speed of light, h is Plank's constant, k is Boltzmann's constant, and T is temperature. The pass band and sensor response are factored out by using a reference object at a fixed temperature, T_{Ref} , with a known emissivity, ε_{Ref} . This reference is placed in the field of view so that simultaneous measurements of reference, I_{Ref} , and wafer radiation, I , are obtained in one image. Both reference and wafer obey Equation 2.28. Solving simultaneous equations for temperature yields

$$T = \left(\frac{hc}{\lambda k} \right) \left\langle \ln \left\langle \left[\frac{I_{\text{ref}} \varepsilon}{I \varepsilon_{\text{ref}}} \right] \cdot \left[\exp\left(\frac{hc}{\lambda k T_{\text{ref}}}\right) - 1 \right] \right\rangle^{-1} \right\rangle. \quad (2.29)$$

The λ can be accurately selected by placing an interference filter in front of the camera used to make the measurement. The emissivity of Si is not a strong function of temperature at a wavelength of 900 nm,¹⁶⁴ and since the Si wafer is opaque at 900 nm, the emissivity of the opaque body can be inferred from the reflectivity by

$$R = 1 - \varepsilon = \frac{I_{\text{reflected}}}{I_{\text{incident}}}, \quad (2.30)$$

where R is the reflectivity. The reflected light is measured directly by a charge-coupled device (CCD) camera and the incident light can be calibrated before the measurement is taken or determined by reflection from a reference. The CCD camera is capable of measuring the thermal radiation from the wafer to give relative temperature measurements within ± 0.25 °C. Emissivity measurements within 1% produce absolute temperature to within ± 3 °C at 1050 °C.¹⁶⁹

The relative emissivity from each side of the wafer is determined by two radiometers that operate independently of one another. One radiometer measures the backside ambient temperature during the iRTP anneal and the other measures the surface temperature when the fRTP anneal is used. The ramp-up rate of the iRTP anneal is determined by the power supply of the system and can vary from 250-400 °C/s. The ramp-down rate is approximately 150 °C/s at 900 °C, which is determined by an instantaneous derivative of the radiation-cooling curve for a gray body with an emissivity and thickness comparable to the Si substrate. The ramp-down rate is greater than those obtained through conventional techniques because the use of absorbing chamber technology, which reduces radiation return to the substrate, providing an improved cooling rate.¹¹⁷ Figure 2-20 shows a graph of the ramp-rate as a function of temperature for the iRTP anneal technique using a ramp-up rate of 400 °C.³⁴ The fRTP anneal produces ramp-up and ramp-down rates on the order of 10^6 °C/s, which introduces advantages in promoting electrical activation with less dopant diffusion due to the differing activation energies for the equilibrium diffusivities of B and Si self-interstitials, 3.5 and 4.9 eV, respectively.^{31,165,170}

Summary of defect classification scheme.

	As-implanted condition	Extended defects after annealing	Possible reasons for defects
Type I (subthreshold)	Damaged above a critical dose but not amorphized	Dislocation loops Voids Stacking fault tetrahedra located near the projected range or the surface	Inability of all vacancies and interstitials to recombine injection of extra atoms into the lattice
Type II (end of range)	Amorphous layer formed either buried or continuous to the surface	Band of dislocation loops located below the amorphous-crystalline interface (end of range)	Recoil of extra atoms from the amorphous layer and/or injection of extra implanted atoms beyond the amorphous layer
Type III (regrowth related)	Amorphous layer formed, either buried or continuous to the surface	Stacking faults Microtwins Hairpin dislocations located in the recrystallized layer	Poor recrystallization of the amorphous layer (i.e. (111) silicon, strained SiGe alloys or compound semiconductors)
Type IV (clamshell or zipper)	Buried amorphous layer formed	Dislocation loops located at the interface where the two recrystallizing interfaces meet	Lack of perfect coherency when the two regrowing amorphous-crystalline interfaces meet
Type V (solubility related)	Crystalline or amorphous	Precipitates Dislocation loops Half loop dislocations located around the ion projected range	Exceeding the solid solubility of the impurity also defects from point defects generated by the precipitation process

Table 2-1 Summary of defect classification scheme.

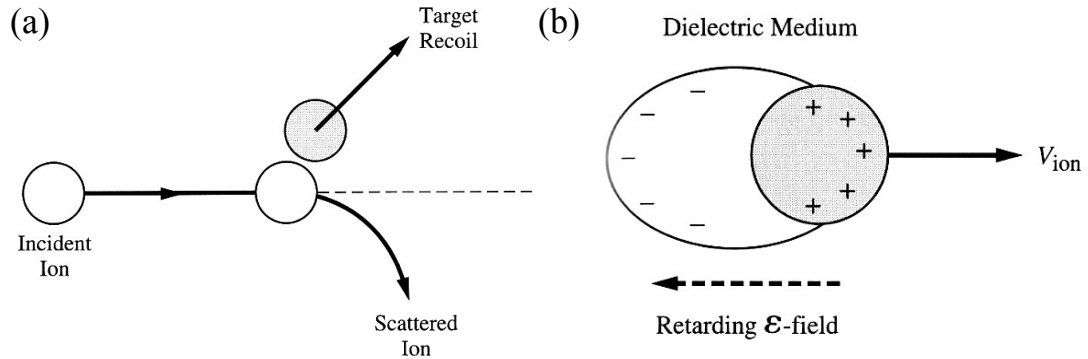


Figure 2-1 Schematic representation of the (a) nuclear and (b) electronic stopping processes associated with ion-implantation. Reprinted with permission from J. D. Plummer, M. D. Deal, and P. Griffin, *Silicon VLSI Technology – Fundamentals, Practice and Modeling* (Prentice Hall, Upper Saddle River, New Jersey, 2000), Figures 8-16 and 8-17, p 472-473.

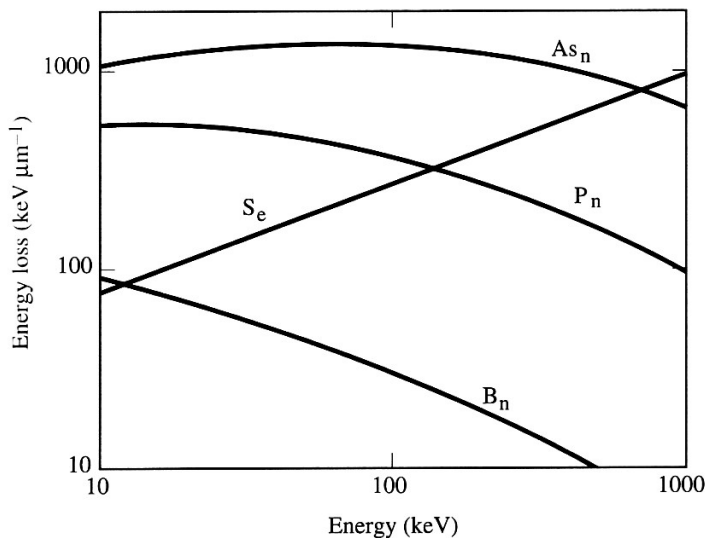


Figure 2-2 Graph of the ion energy loss as a function of incident particle energy.

Reprinted with permission from J. D. Plummer, M. D. Deal, and P. Griffin, *Silicon VLSI Technology – Fundamentals, Practice and Modeling* (Prentice Hall, Upper Saddle River, New Jersey, 2000), Figure 8-19, p 475.

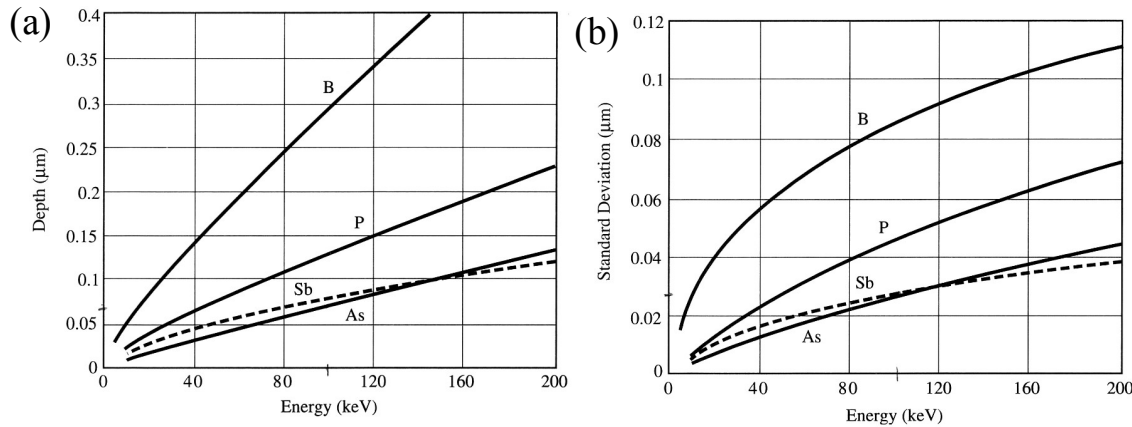


Figure 2-3 Characteristic (a) R_p and (b) ΔR_p associated with common dopants used in CMOS technology as a function of implant energy. Reprinted with permission from J. D. Plummer, M. D. Deal, and P. Griffin, *Silicon VLSI Technology – Fundamentals, Practice and Modeling* (Prentice Hall, Upper Saddle River, New Jersey, 2000), Figure 8-3, p 454.

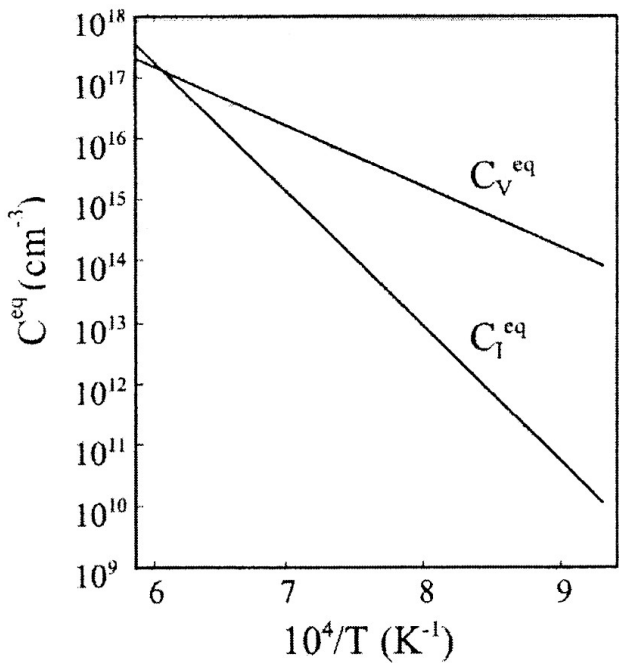


Figure 2-4 Equilibrium concentrations of interstitials, C_I^* , and vacancies, C_V^* , as a function of inverse temperature.

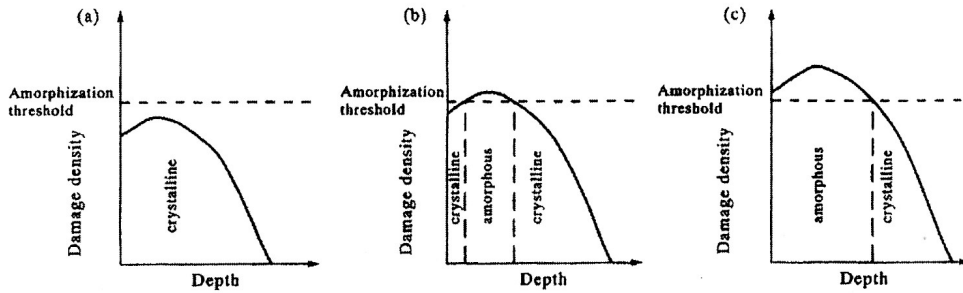


Figure 2-5 Damage density as a function of depth for the three possible primary implant damage morphologies that may exist directly after ion-implantation.

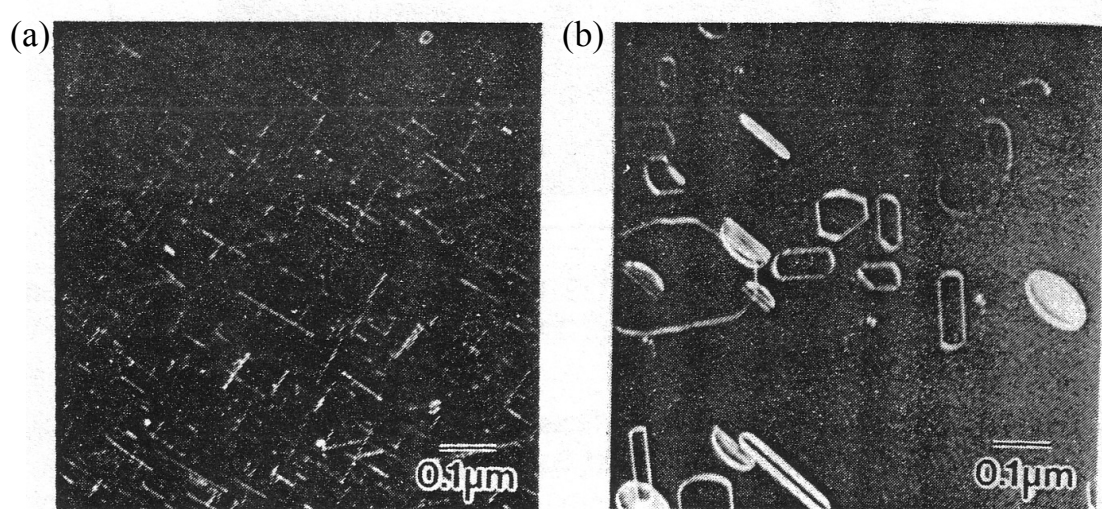


Figure 2-6 Plan-view TEM images of the damage produced by a 20 keV B^+ implant to $1 \times 10^{15}/\text{cm}^2$ after post-implant thermal processing at (a) 750°C for 5 min and (b) 900°C for 15 min. Note that only $\{311\}$ defects are present in (a) whereas only dislocation loops are present in (b).

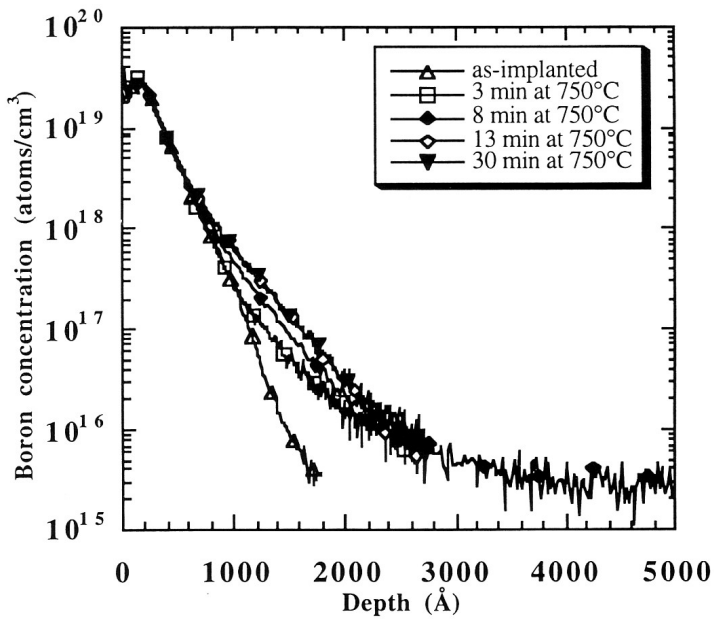


Figure 2-7 Concentration profile as a function of depth for a 4 keV B^+ implant to $1 \times 10^{14}/cm^2$ after post-implant thermal processing at $750\text{ }^\circ\text{C}$ for various times.

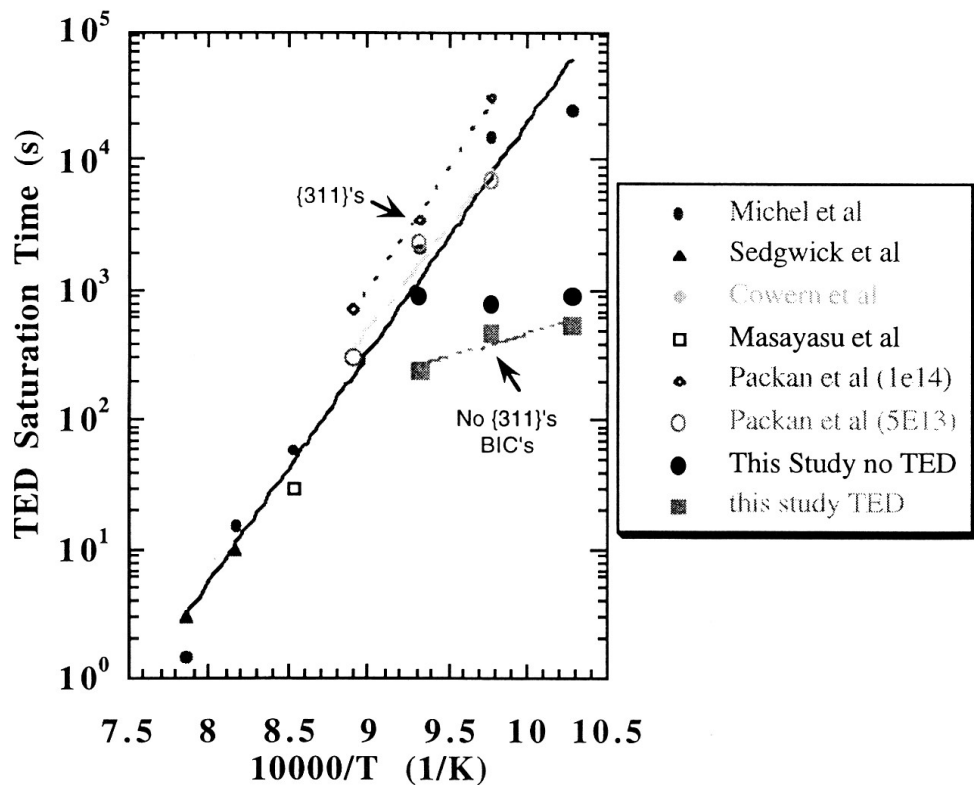


Figure 2-8 Saturation time for TED as a function of inverse temperature. Note that the activation energy associated BIC dissolution is less than that of {311} defect dissolution.

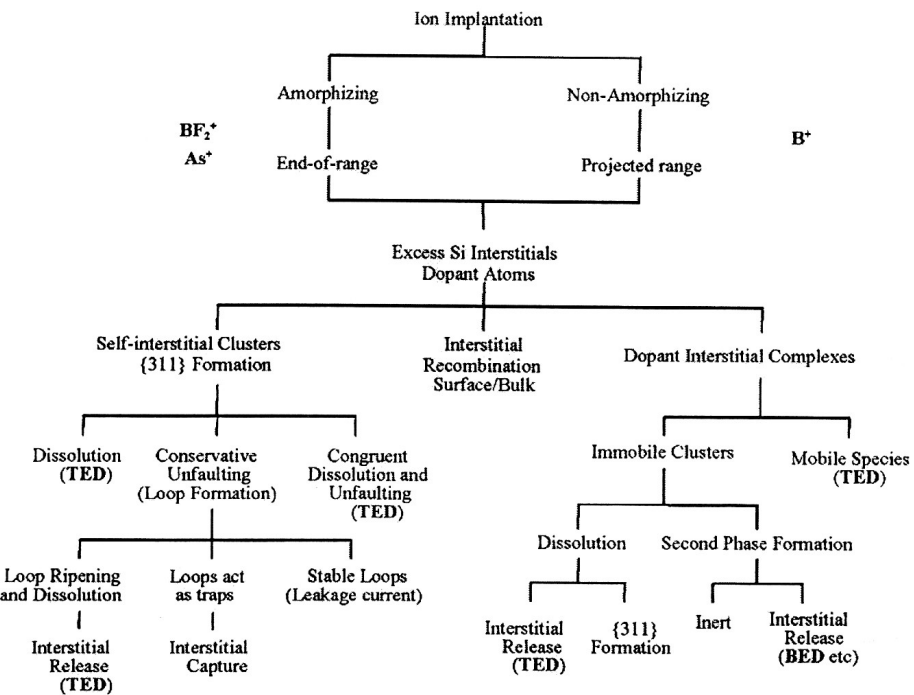


Figure 2-9 Summary of the possible sources of TED.

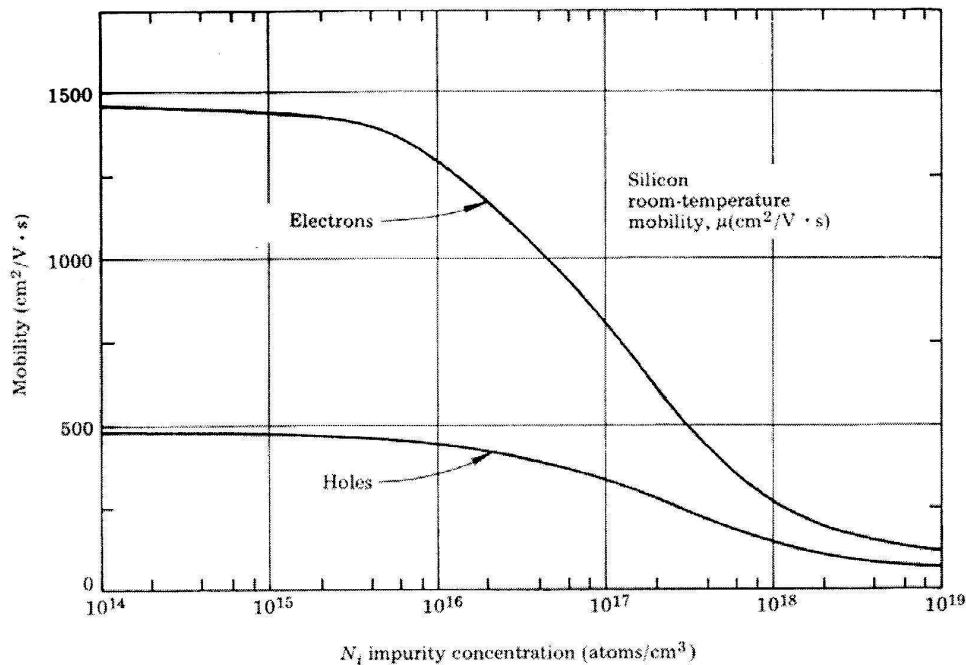


Figure 2-10 Carrier mobility as a function of active dopant concentration in Si at room temperature.

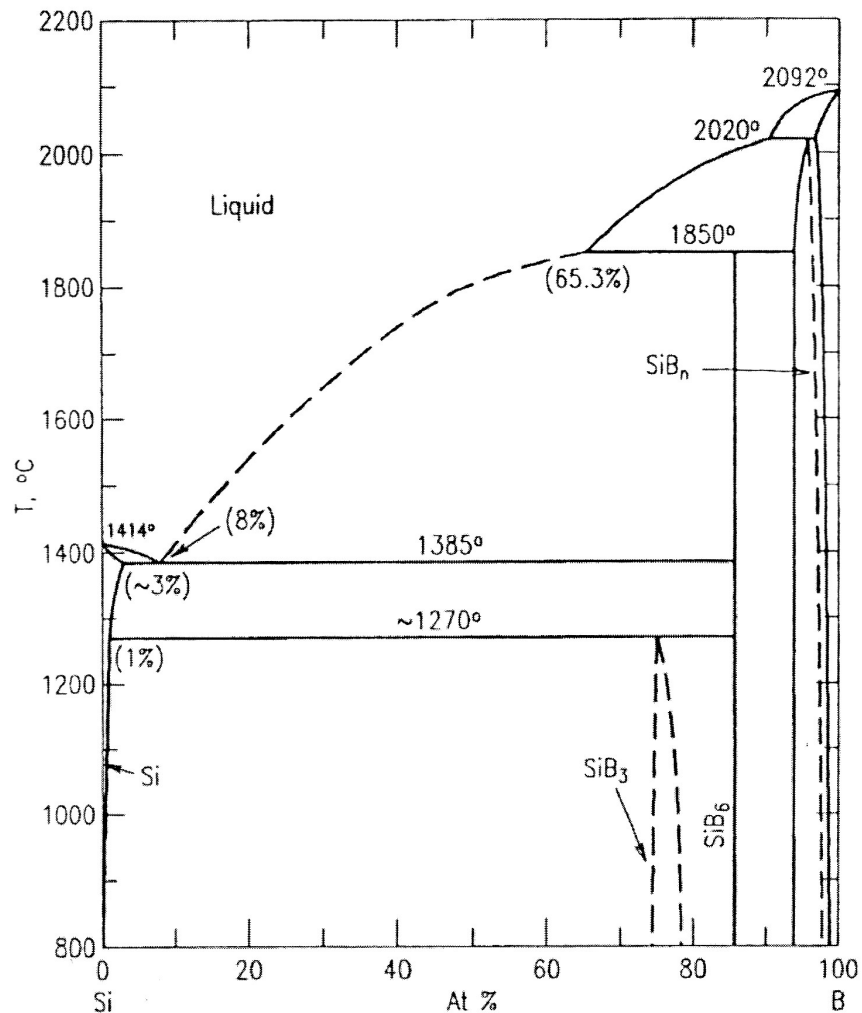


Figure 2-11 Binary equilibrium phase diagram of B and Si.

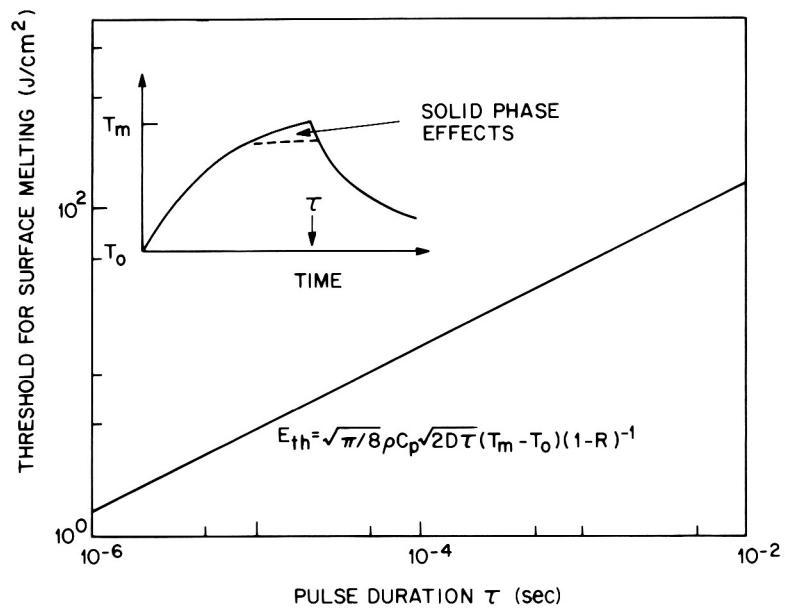


Figure 2-12 Energy density required to reach the melting point at the surface of a Si substrate irradiated with a square pulse of energy as a function of τ .

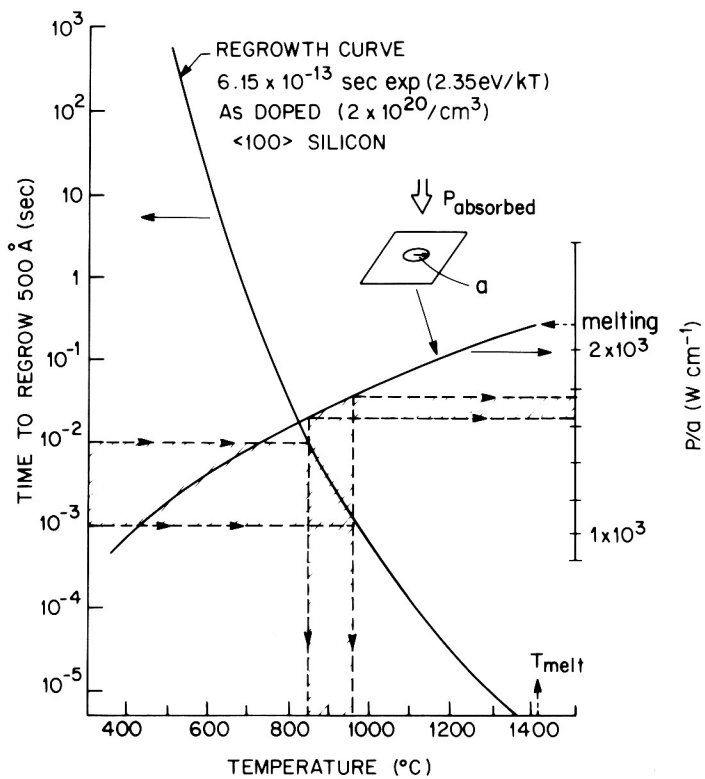


Figure 2-13 Time required to regrow 50 nm of α -Si as a function of substrate temperature. Also plotted is the calculated absorbed laser power per spot radius as a function of the steady state temperature attained at the center of the spot.

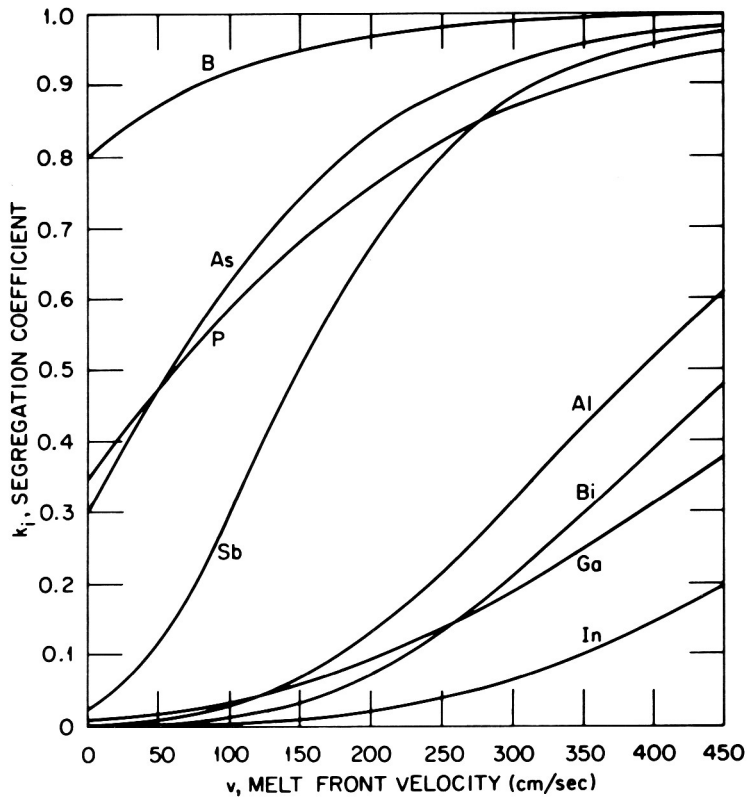


Figure 2-14 Segregation coefficient as a function of liquid phase regrowth velocity for a number of impurities in Si. Note that the segregation coefficient approaches unity for the most common dopants.

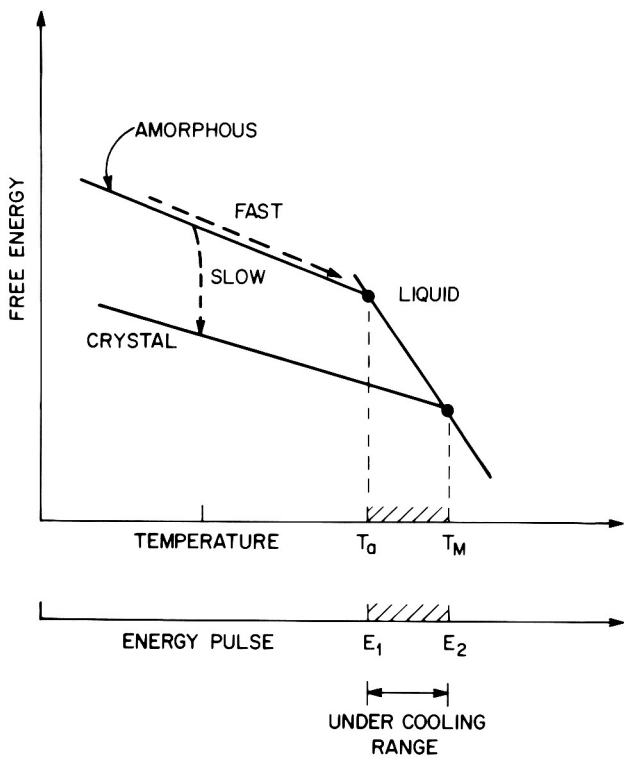


Figure 2-15 Free energy of amorphous, crystalline, and liquid Si as a function of temperature or energy pulse.

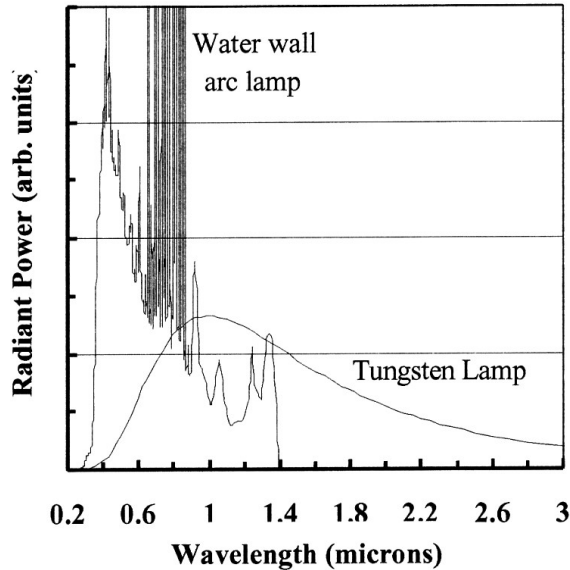


Figure 2-16 Radiant power as a function of wavelength showing the spectral distribution comparison of a water wall arc lamp and tungsten filament at 290 K.

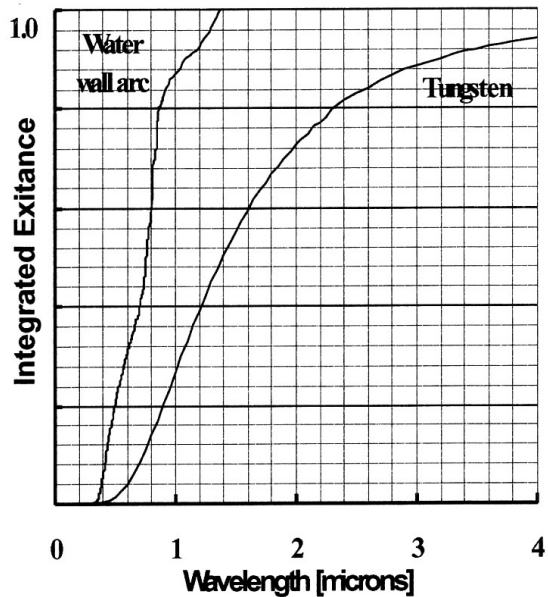


Figure 2-17 Integrated exitance as a function of wavelength showing the spectral distribution comparison of a water wall arc lamp and tungsten filament at 290 K. Note that over 95% of the arc radiation is below the $1.2 \mu\text{m}$ band gap absorption of Si at room temperature (compared to 40% for tungsten).

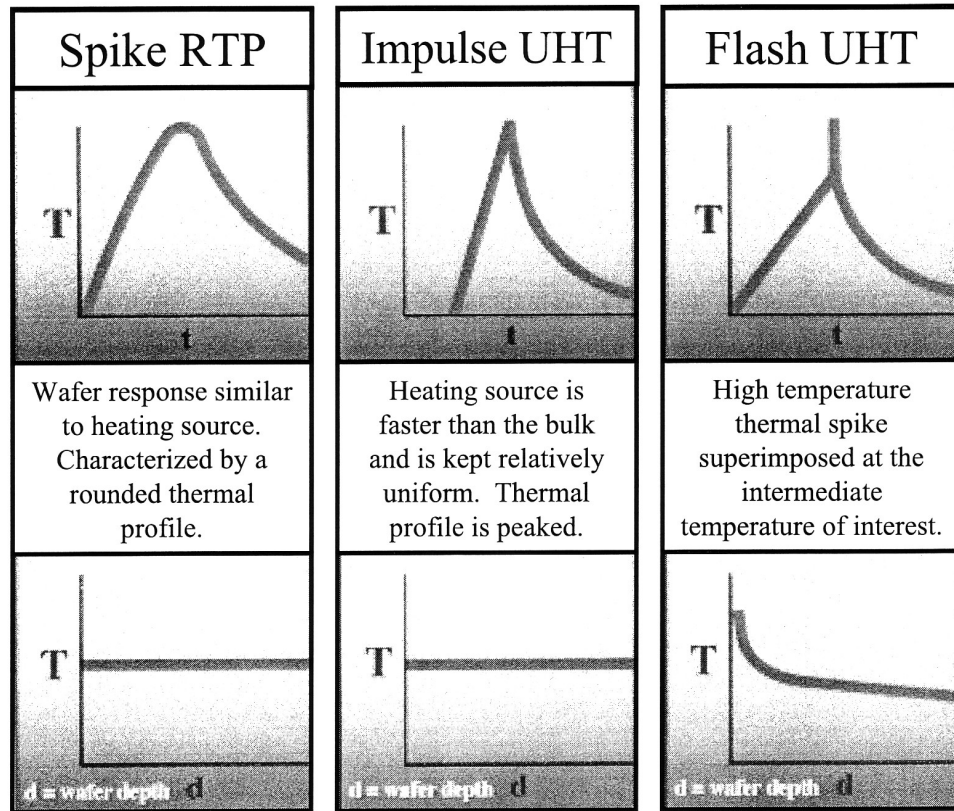


Figure 2-18 Temperature-time ($T-t$) and temperature-depth ($T-d$) profiles comparing spike RTP, impulse UHT annealing, and flash UHT annealing.

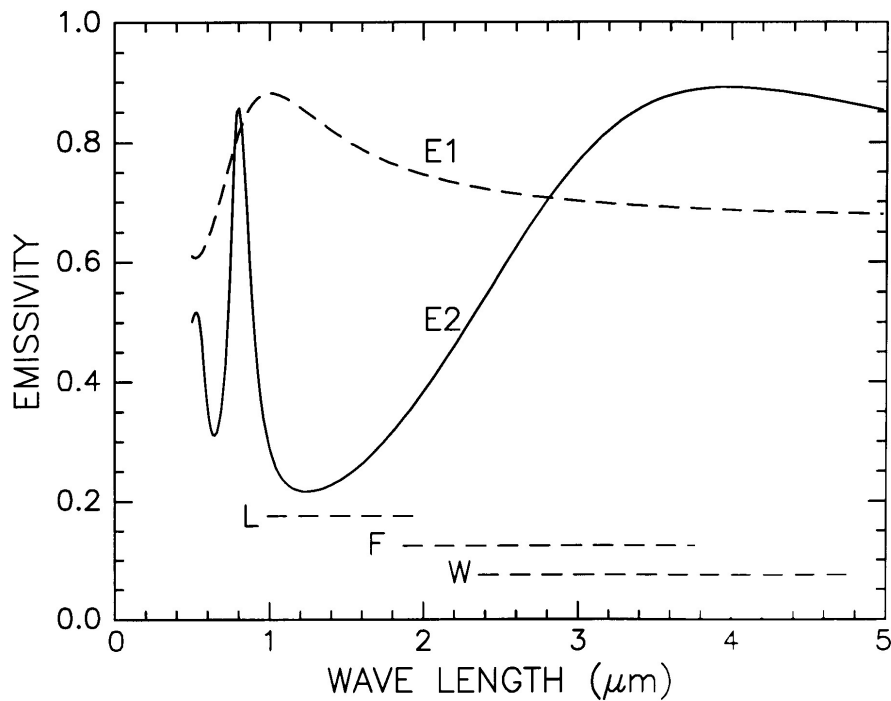


Figure 2-19 Emissivity as a function of wavelength. Note the change in spectral emissivity of Si as a function of wavelength with different thin film composites.

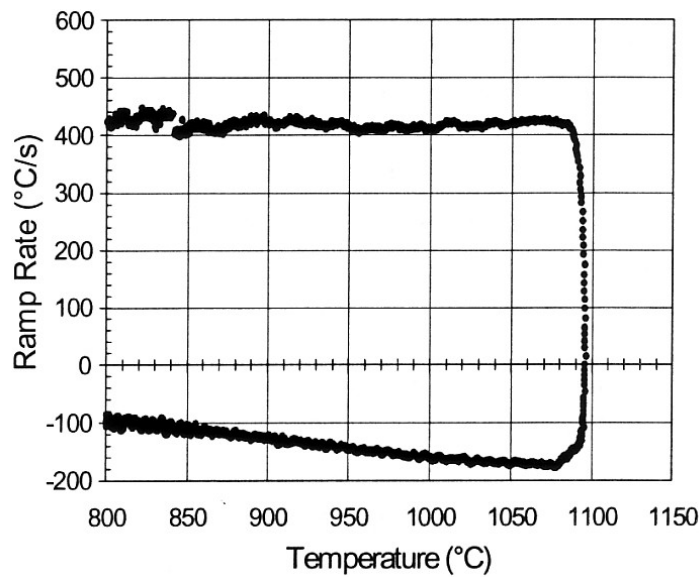


Figure 2-20 Ramp-rate as a function of temperature for an iRTP anneal with a ramp-up rate of approximately 400 °C/s.

CHAPTER 3 ANALYTICAL TECHNIQUES

This chapter will be used to describe the analytical techniques used throughout this work to characterize the materials properties as a result of different processing conditions. A brief overview of each technique will be presented to make known the capabilities and limitations of each technique. The techniques are discussed in the order of the frequency with which they are used throughout this work.

Secondary Ion Mass Spectrometry

With dynamic secondary ion mass spectrometry (SIMS), the surface of a sample is bombarded with a continuous focused beam of primary ions. The impact of the ions sputters atoms from the surface of the material, producing secondary ions in the process. The secondary ions are extracted into a mass spectrometer, which uses electrostatic and magnetic fields to separate the ions according to their mass-to-charge ratio. Ions of different mass-to-charge ratios are measured by changing the strength of the magnetic field. A plot of the intensity of a given mass signal as a function of time, is a direct reflection of the variation of its concentration with depth below the substrate surface. A profilometer is used to measure the sputter crater depth to convert the time axis into depth. A profilometer is a separate instrument that determines depth by dragging a stylus across the crater and noting vertical deflections. Total crater depth is then divided by total sputter time, providing the average sputter rate. Relative sensitivity factors (RSF's) convert the vertical axis from ion counts into concentration. This technique is capable of resolving dopant and impurity levels whose concentration is as much as nine orders of

magnitude less than the atomic composition of the substrate material, which is particularly important for profiling implanted dopants which are often present at very low concentrations. The SIMS detection limits for most trace elements are between 1×10^{12} and $1\times10^{16}/\text{cm}^3$. This technique identifies all elements or isotopes present in a material, from hydrogen to uranium. It should be noted that this is the only surface analysis technique capable of directly detecting hydrogen and deuterium in materials.

Traditionally, only the positive ions are mass analyzed in SIMS. This is primarily for practical ease, however, it does lead to problems with quantifying the compositional data since the positive ions are but a small, non-representative fraction of the total sputtered species. It should be noted that the displaced ions have to be energy filtered before they are mass analyzed (i.e., only ions with kinetic energies within a limited range are mass analyzed). The bombarding primary ion beam produces both monatomic and polyatomic particles of sample material and re-sputtered primary ions, along with electrons and photons. The secondary particles carry negative, positive, and neutral charges. The two most commonly employed incident ions used for bombarding the sample are O^+ and Cs^+ (at energies between 1 and 30 keV) but other ions (e.g., Ar^+ and alkali metal ions, such as Ga^+) are preferred for some applications. As can be seen in Figure 3-1, the Cs^+ beam is especially useful for the analysis of lighter elements such as H, C, and O, whereas the O^+ beam is used to enhance sensitivity for B and transition metals.¹⁷¹ It should be noted that primary ions are implanted and mix with sample atoms to depths of 1 to 10 nm. Sputter rates in typical SIMS experiments vary between 0.5 and 5 nm/s. Sputter rates depend on primary beam intensity, sample material, and crystal orientation. The sputter yield is the ratio of the number of atoms sputtered to the number of impinging primary ions. Typical

SIMS sputter yields fall in a range from 5 and 15. The mass analyzer is typically either a quadrupole or magnetic sector, but high specification time-of-flight (TOF) analyzers are also used and provide substantially higher sensitivity and a much greater mass range. The depth resolution of the SIMS technique is dependent on such factors as the sputter uniformity of the incident ion beam, the absolute depth below the original surface to which material removal has already occurred, and the nature of the ion beam being used (i.e., the mass and energy of the ions). A thorough review of this analytical technique has been given elsewhere.¹⁷²

The SIMS ionization efficiency is called ion yield and defined as the fraction of sputtered atoms that become ionized. Ion yields vary over many orders of magnitude for various elements. The most obvious influences on ion yield are ionization potential for positive ions and electron affinity for negative ions. For example, Figure 3-2a shows the logarithm of positive ion yields plotted as a function of ionization potential. The ion yields are relative to Si in a Si lattice with O⁺ sputtering. Variations in the ionization potential with secondary ion yield depend both on the sample and the element being measured. For example, the presence of O in the sample enhances positive ion yields for most elements, but F exhibits anomalously high positive ion yields in nearly all samples. Figure 3-2b shows a similar treatment for negative ions where the logarithms of relative ion yields are plotted against electron affinities. The ion yields are relative to Si for measurements in a Si lattice with Cs⁺ ion sputtering. The O enhancement occurs as a result of metal-oxygen bonds in an oxygen rich zone. When these bonds break in the ion emission process, the O becomes negatively charged because its high electron affinity favors electron capture and its high ionization potential inhibits positive charging;

therefore, the metal is left with the positive charge. It should be noted that sputtering with an O beam increases the concentration of O in the surface layer. The enhanced negative ion yields produced with Cs⁺ bombardment can be explained by work functions that are reduced by implantation of Cs⁺ into the sample surface. More secondary electrons are excited over the surface potential barrier and increased availability of electrons leads to increased negative ion formation. The variability in ionization efficiencies leads to different analysis conditions for different elements.

This depth profiling technique will be used to monitor B diffusion behavior as a function of ultra-high temperature (UHT) annealing conditions. This technique will also be used to profile for other impurities such as F.

Transmission Electron Microscopy

Transmission electron microscopy (TEM) uses a high-energy electron beam to image the microstructure of a material.¹⁷³ This technique allows for high-resolution imaging, with point-to-point resolution of better than 2 nm. Most electron microscopes use a thermionic gun as its electron source. A thermionic electron gun functions by applying a positive electrical potential to the anode while the cathode (i.e., filament) is heated to the point where an electron beam is produced. The electrons are subsequently accelerated by the potential of the electron column. As the electrons move toward the anode, any electrons emitted from the filament side are repelled by the negative electrical potential applied to the Whent Cap and directed toward the optic axis. A collection of electrons, called the space charge, occurs in the space between the filament tip and Whent Cap. Those electrons at the bottom of the space charge (i.e., nearest to the anode) exit the electron gun through a small (< 1 mm) hole in the Whent Cap. These

electrons move down the column and are those electrons used for imaging. This process of electron production insures a number of things. For example, the electrons used for imaging will be emitted from a nearly perfect point source (i.e., the space charge), be of a similar energy (i.e., monochromatic), and the only electrons allowed out of the gun area are those nearly parallel to the optic axis. The electrons that leave the gun area are focused to a small coherent beam by the use of two condenser lenses. The first of the two lenses determines the so-called spot size of the beam whereas the second lens actually changes the size of the spot on the sample, changing it from a widely dispersed spot to a focused beam. The electron beam is controlled by circular electro-magnets capable of projecting a precise circular magnetic field in a specified region. The field acts like an optical lens, having the same attributes (e.g., focal length and angle of divergence) and errors (e.g., spherical aberration and chromatic aberration). The transmitted portion of the electron beam is focused by the objective lens into an image. Optional objective and selected-area apertures can restrict the beam; the objective aperture enhancing contrast by blocking out high-angle diffracted electrons, the selected-area aperture enabling the user to examine the periodic diffraction of electrons by ordered arrangements of atoms in the sample. The image is then passed down the electron column through the intermediate and projector lenses, which enlarge the image. The image strikes the phosphor image screen and light is generated, allowing the user to see the image. The darker areas of the image represent those areas of the sample that fewer electrons were transmitted through (i.e., they are thicker or denser). The lighter areas of the image represent those areas of the sample that more electrons were transmitted through (i.e., they are thinner or less

dense). It should be noted that sample preparation for TEM analysis is critical due to the fact that a thin electron transparent edge is required for high quality imaging.

A number of various reactions occur when the electron beam interacts with the sample. A diagram showing the various electron-sample interactions is shown in Figure 3-3.¹⁷³ The volume inside the sample in which interactions occur depends on a number of factors, such as the atomic number of the material being imaged, the accelerating voltage being used, and the angle of incidence for the electron beam. Higher atomic number materials absorb more electrons and therefore have smaller interaction volume, higher accelerating voltages penetrate farther into the sample and generate larger interaction volumes, and the greater the angle (i.e., further from the sample normal) the smaller the interaction volume. Regardless of the interaction volume, these electron-sample interactions can be used to study various aspects of the material being imaged. It is well known that a portion of the electrons within the beam are transmitted through the sample without any interaction occurring inside the sample. These are commonly referred to as unscattered electrons. The transmission of unscattered electrons is inversely proportional to the specimen thickness. Areas of the specimen that are thicker will have fewer transmitted unscattered electrons and so will appear darker, conversely the thinner areas will have more transmitted and thus will appear lighter. Elastically scattered electrons are incident electrons that are scattered (i.e., deflected from their original path) by atoms in the sample in an elastic fashion (i.e., no loss of energy). These scattered electrons are then transmitted through the remaining portion of the sample. Since all the electrons that follow Bragg's Law scatter according to

$$\lambda = 2d \sin \theta, \quad (3.1)$$

where d is the interplanar spacing for a particular set of planes and θ is the angle conditioned between the incident beam and the lattice plane of interest, all incidents scattered by the same atomic spacing will be scattered by the same angle. These scattered electrons can be collected using magnetic lenses to form a diffraction pattern; an array of spots each of which corresponds to a specific interplanar spacing (i.e., an atomic plane). The exact interplanar spacing can be calculated by use of

$$Rd = \lambda L, \quad (3.2)$$

where R is the measured distance between the transmitted beam and the spot of interest, λ is the wavelength of the electron beam, and L is the camera length being used. Since both λ and L are set by the instrument, the interplanar spacing can be calculated by measuring R and comparing the resulting value to

$$d = \frac{a}{\sqrt{h^2 + k^2 + l^2}}, \quad (3.3)$$

where a is the lattice parameter of the material being examined, and h , k , and l correspond to the Miller indices of the atomic plane.³⁹ If the a is known, then the correct combination of Miller indices can be calculated. It should be noted that since the λL product is constant for a particular micrograph, the $R_1/d_2 = R_2/d_1$ comparison can be used to conveniently calculate neighboring lattice planes. The diffraction pattern can be used to yield information about the orientation, atomic arrangements, and phases present in the area being examined. Inelastically scattered electrons are incident electrons that interact with the atoms in the sample in a inelastic fashion, loosing energy during the interaction. These electrons are then transmitted trough the rest of the specimen. Inelastically scattered electrons can be used two ways. The inelastic loss of energy by the incident

electrons is characteristic of the elements that the beam interacted with. These energies are unique to each bonding state of each element and thus can be used to extract both compositional and bonding (i.e., oxidation state) information on the specimen region being examined. This type of interaction is used in electron energy loss spectroscopy (EELS). In addition, the Kikuchi bands (i.e., bands of alternating light and dark lines formed by inelastic scattering interactions that are related to atomic spacings in the sample) can be either measured (their width is inversely proportional to atomic spacing) or used to locate the elastically scattered electron pattern.

This imaging technique will be used to monitor the implantation-induced damage as a function of both implant and annealing conditions. Cross-sectional TEM (XTEM) will be used to image the amorphous layer thickness produced by various pre-amorphization implants before and after post-implant thermal processing. Plan-view TEM (PTEM) will be used to image the evolution of the damage produced by the various pre-amorphization implants as a function of post-implant thermal processing.

Variable Angle Spectroscopic Ellipsometry

Ellipsometry is a technique that is used to characterize materials that are comprised of multiple layers by measuring the change in the polarization state of a light beam as it is transmitted or reflected by the material of interest. This technique measures a complex quantity using a beam obliquely incident on a sample. The measured complex quantity is a function of the dielectric constants and geometrical structure of a sample and is an amplitude reflection ratio between p- and s-polarization. The p- and s-polarization corresponds to electric field parallel and perpendicular to the plane of incidence, respectively. It should be noted that the plane of incidence includes incident and reflected light. Spectroscopic ellipsometry measures the complex quantity as a function

of wavelength. Both complex amplitude reflection coefficient and dielectric constants are response functions; however, the real and imaginary parts of a response function are not independent of each other. They are related to one another by the Kramers-Kronig relations, which are based on the causality principle. A typical optical ellipsometer consists of a source, polarizer for defining the input polarization state, compensator or modulator for varying the polarization in a known manner, and an analyzer for determining the polarization state after interaction with the sample. This non-destructive optical technique is typically used for determining optical parameters, thickness of thin films and multilayer structures, and for making thin film measurements. It should be noted that the index of refraction cannot be determined from a fixed wavelength measurement at a single angle of incidence. To address this problem, the spectroscopic ellipsometer has to take data over a wide range of wavelengths and at several angles. This is known as variable angle spectroscopic ellipsometry (VASE) and is particularly suited to thickness and refractive index measurements. Furthermore, ellipsometry can provide information regarding microstructural material properties that include optical anisotropy and surface or interfacial roughness. Optical anisotropy is important, as it will control the degree to which the refractive index changes when the orientation of the sample is changed. Measuring the index of refraction (n) and the extinction coefficient (k) for a single layer permits one to determine the material composition, electronic structure, and modeling of optical performance. If the optical constants are approximately known, then ellipsometry can determine the thickness, interface roughness, and inhomogeneity in multilayer structures with thickness from sub-monolayer to millimeters. In addition, ellipsometry can be used to study the formation and properties of thin films on thick

substrates (e.g., SiO₂ on a Si substrate). One of the special features of this technique is the large spectral range available for measurements. By using either a photomultiplier tube or a germanium detector, samples can be studied over the spectral range from the ultraviolet to the near-infrared (e.g., 0.3-1.7 μm). A polarization analyzer and photodetector are used to measure Ψ and Δ angles as a function of incident angle and wavelength. These measured parameters are defined as

$$\tan \Psi_{\text{exp}}^{(i\Delta)} = \frac{R_p}{R_s}, \quad (3.4)$$

where R_p and R_s are the pseudo-Fresnel reflection coefficients of the sample, with p denoting the direction of the plane of incidence and s the direction perpendicular to the incident plane. These measurements allow for the characterization of the various polarization properties and thin layer effects in most solid-state material. In addition, ellipsometry operates in any transparent ambient, including vacuum, gases, liquids, and air. This allows ellipsometry to be applied *in-situ* to study the deposition and processing of materials. One limitation of the technique, however, is that the material being measured must, in general, have parallel interfaces and smooth, speculum surfaces. A thorough review of this analytical technique has been given elsewhere.¹⁷²

This optical technique will be used to measure the amorphous layer thickness produced by various pre-amorphization implants before and after post-implant thermal processing. These results will then be compared to the micrographs produced by XTEM imaging.

Four-Point Probe

The resistivity, ρ , of a semiconductor is a particularly important parameter because it can be directly related to the active impurity content in a sample. The four-point probe

technique is used to measure the average resistance of a thin layer (e.g., annealed junction).^{2,174} The four-point probe consists of four thin collinear tungsten probes which are made to contact the sample by lowering a probe arm. Current, I , is made to flow between the two outer probes while the voltage, V , is measured between the two inner probes (ideally without drawing any current). If there is equal spacing, s , between the tungsten probes and it is assumed that the sample is of semi-infinite volume, then the ρ can be given by

$$\rho_0 = 2\pi s \frac{V}{I}. \quad (3.5)$$

The subscription in Equation 3.2 indicates the measured value of the resistivity, and is equal to the actual value, ρ , only if the sample is of semi-infinite volume; however practical samples are of finite size. Therefore, in general, $\rho_0 \neq \rho$. Geometrical correction factors for six different boundary configurations have been derived by Valdes.¹⁷⁵ Figure 3-4 shows that, in general, if the thickness to probe spacing ratio, t/s , is at least $5s$, no correction factor is required. For all other cases, the actual ρ can be calculated from

$$\rho = a 2\pi s \frac{V}{I} = a \rho_0, \quad (3.6)$$

where a is the geometrical correction factor. Figure 3-4 shows that the correction factor for values of $t/s \leq 0.5$ can be estimated by

$$a = K \left(\frac{t}{s} \right)^m, \quad (3.7)$$

where K is the value of a at $t/s = 1$, and m is the slope of the line. The plot shows that $m = 1$ in this case. By extrapolating the linear region of the graph to $t/s = -1$, it can be

said that $K \cong 0.72$ [the exact value is $1/(2\ln 2)$]. Therefore, for junctions equal to or less than one half the probe spacing

$$a = 0.72 \left(\frac{t}{s} \right). \quad (3.8)$$

Now, for $t/s \leq 0.5$,

$$\rho = a 2\pi s \left(\frac{V}{I} \right) = 4.53 t \left(\frac{V}{I} \right). \quad (3.9)$$

If both sides of Equation 3.6 are divided by t then

$$\frac{\rho}{t} = R_s = 4.53 \left(\frac{V}{I} \right), \quad (3.10)$$

for $t/s \leq 0.5$, where R_s is the sheet resistance. When t is negligible, as would be the case for an implanted or diffused layer, this is the preferred measurement quantity. It should be noted that the R_s is independent of any geometrical dimension and is therefore only a function of the material being measured. The significance of the R_s can be more clearly seen after referring to the end-to-end resistance of a rectangular sample. From the resistance, R , formula

$$R = \frac{\rho l}{wt}, \quad (3.11)$$

where l is the length of the material being measured, and w is the width of a side. If $l = w$ (i.e., for a square sample) then

$$R = \frac{\rho}{t} = R_s. \quad (3.12)$$

Therefore, the R_s can be interpreted as the R of a square sample. For this reason, the units of R_s are taken to be ohm/sq. Dimensionally, this is the same as ohms but this notation serves as a reminder of the geometrical significance of R_s .

It should be noted that the layer to be measured must be of the opposite conductivity type to that of the substrate (i.e., electrically insulated from the substrate). A layer of the same conductivity type cannot be measured by the four-point probe method because the substrate offers an easier path for the current, and the measured resistivity is effectively that of the substrate. Also, the sample may need to be etched to remove any oxide that may impede Ohmic contact with the material being measured; however, if the layer is thin (i.e., $< \mu\text{m}$) caution must be taken not to puncture the layer by excessive loading of the probe arm, by the use of sharp or rough needle tips, or by lowering the probe arm too quickly. All these effects cause some leakage into the substrate, so that the measuring current in the layer is reduced, and the resistivity measured is too low.

This electrical technique will be used to measure the R_s for a number of B^+ implant conditions as a function of post-implant thermal processing. It should be noted that the geometric correction factor is negligible for the wafer sections used throughout this work (because they have surface areas greater than those below which edge effects reduce measurement accuracy).

Electron Paramagnetic Resonance

Electron paramagnetic resonance (EPR), also known as electron spin resonance (ESR) and electron magnetic resonance (EMR), is the name given to the process of resonant absorption of microwave radiation by paramagnetic ions or molecules, with at least one unpaired electron spin, and in the presence of a static magnetic field. By application of a strong magnetic field, B_0 , to a material containing paramagnetic species, the individual magnetic moment arising via the electron spin (i.e., spin quantization

number, $S = 1/2$) of the unpaired electron can be oriented either parallel or anti-parallel to the applied field, resulting in two energy states of the electron. Irradiation with microwaves (usually X-band microwaves of circa 9 GHz with an external magnetic field of 0.35 T) can induce transitions between these different energy states resulting in an EPR signal. The local field also depends on the nuclear magnetic moments of various nuclei that may be present within the bulk material. Examples of such nuclei are interstitial atoms (or ions) within a crystal. This creates additional splittings for the unpaired electrons through hyperfine coupling between electron and nuclear spins. The situation referred to as the resonance condition takes place when the magnetic field and the microwave frequency are properly tuned (i.e., the energy of the microwaves corresponds to the energy difference of the pair of involved spin states). One of the fundamental roles of any spectroscopic technique is identification of the chemical species being studied. In cases where two or more paramagnetic species co-exist, the spectral EPR lines arising from each can be simultaneously observed. Often definitive identification of the individual species is realized solely from the analysis of the EPR spectrum. Furthermore, EPR spectroscopy is capable of providing molecular structural details inaccessible by any other analytical tool. It can be seen that EPR provides the opportunity for studying the internal structure of a material in great detail. A thorough review of this analytical technique has been given elsewhere.¹⁷⁶

This technique provides a rather sensitive method of detecting unpaired electrons within a given system. The transition that is induced is a magnetic-dipole process and, consequently, the selection rule for the transition is that the spin component along the

direction of the applied magnetic field, M_s , must change by $\Delta M_s \pm 1$. The energy equation for resonance to occur is

$$\Delta E = h\nu_0 = g\mu_B B_0, \quad (3.13)$$

where $h\nu_0$ is the microwave energy, g is the Zeeman splitting tensor (where elements are determined by the anisotropic spin-orbit interaction of the unpaired electron), μ_B is the Bohr magneton, and B_0 is the applied magnetic field. For a single unpaired electron, $S = 1/2$. The splitting factor (i.e., g -tensor) can have as many as three values, g_x , g_y and g_z , each corresponding to the value when the external magnetic field is parallel to one of three perpendicular directions (often lying along structural axes within the molecule). The symmetry of the g -tensor is dependent on the symmetry of the system under study and results in very different shapes of the EPR signal. For systems with more than one unpaired electron (i.e., $S > 1/2$) the ground state can be split in the absence of an external magnetic field due to the local site symmetry (i.e., zero-field splitting). For odd-electron systems this results in pairs of energy levels known as Kramer's doublets. The observed EPR spectrum can contain transitions within each of the ground state Kramer's doublets. It should be noted that there are two important conditions under which it may not be possible to observe an EPR signal, even when unpaired electrons are present: if the system has an even number of unpaired electrons then zero-field splitting within the ground state may result in the EPR transitions being undetectable at X-band (although detectable at different microwave frequencies), or if the paramagnetic centers occur in pairs then antiferromagnetic coupling of the individual spins may result in the EPR signal being undetectable or even absent, although the individual centers may have an odd number of unpaired electrons.

The intensity of the EPR signal is dependent on a number of factors. Some of these factors include the number of relevant paramagnetic centers in the sample, the S and g-tensor of each species within the sample, the transition probability for each spin per second, the number of lines in the spectrum, the sublevel populations which are affected by sample temperature, microwave frequency, the effective amplitude, B_1 , of the microwave magnetic field at the sample, the field modulation amplitude, B_m , and phase at the sample, and the overall spectrometer gain, including multi-scanning spectral superposition capability. It should be noted that knowledge of the microwave power, P_0 , cavity quality factor, Q_u , and the distribution of \mathbf{B}_1 within the cavity as well as the filling factor, η , is required to determine the B_1 of the microwave magnetic field at the sample.

A traditional continuous wave (cw) EPR set-up is shown in Figure 3-5. The region labeled source contains those components that produce the excitation electromagnetic waves and control their frequency. The modulation and detection system monitor, amplify, and record the signal. The magnet system provides a stable, homogeneous and linearly variable magnetic field within the desired range. The reference arm in Figure 3-5 takes microwave power from the waveguide ahead of the circulator and restores it, with adjusted power levels and phase, behind the circulator (and resonator). With suitable settings, this arm not only allows for appropriate biasing of the power level in the detector, but also allows phase control and thus the choice of whether the absorption or dispersion signal from the system is detected.

This resonance technique will be used to measure the relative concentration of paramagnetic centers in amorphous Si (α -Si) as a function of implant and post-implant thermal processing. In theory, there is a linear dependence between the EPR signal

intensity and the number of paramagnetic centers in a sample. Thus EPR can be used to determine paramagnetic spin concentrations. Although the absolute concentrations of spins are possible to determine using EPR, the errors associated with this determination are typically on the order of 10-20% because of the great number of experimental parameters that must be taken into account. As a result of this large error, only the relative concentration of spins between samples will be presented and discussed.

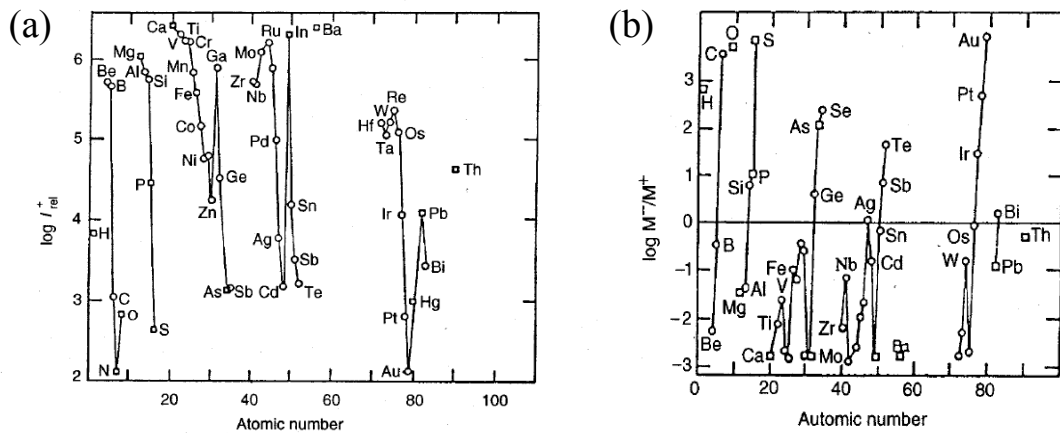


Figure 3-1 (a) The ratio of negative ion yield (M^-) under Cs^+ bombardment to positive ion yield (M^+) under O^- bombardment as a function of atomic number showing enhanced yield for light elements such as H, C, and O and (b) the variation of positive ion yield as a function of atomic number for 1 nA 13.5 keV O^+ bombardment showing high yield for elements such as B.

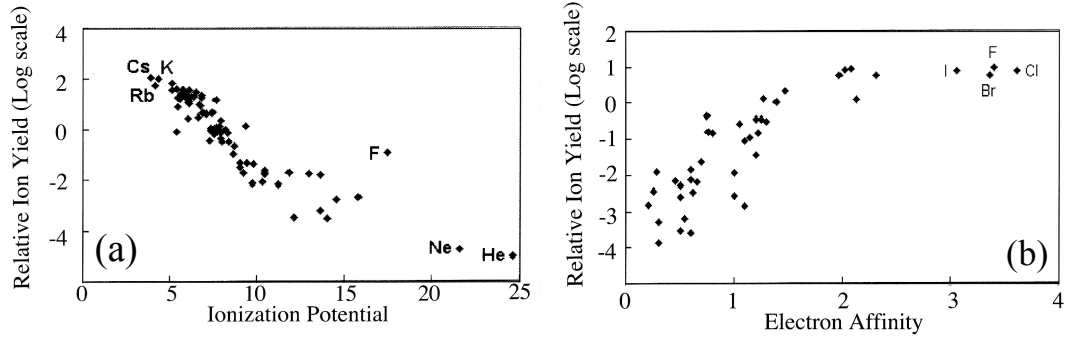


Figure 3-2 (a) The logarithm of positive ion yields plotted as a function of ionization potential. The ion yields are relative to Si in a Si lattice with O⁺ sputtering and (b) a similar treatment for negative ions where the logarithms of relative ion yields are plotted against electron affinities. The ion yields are relative to Si for measurements in a Si lattice with Cs⁺ ion sputtering.

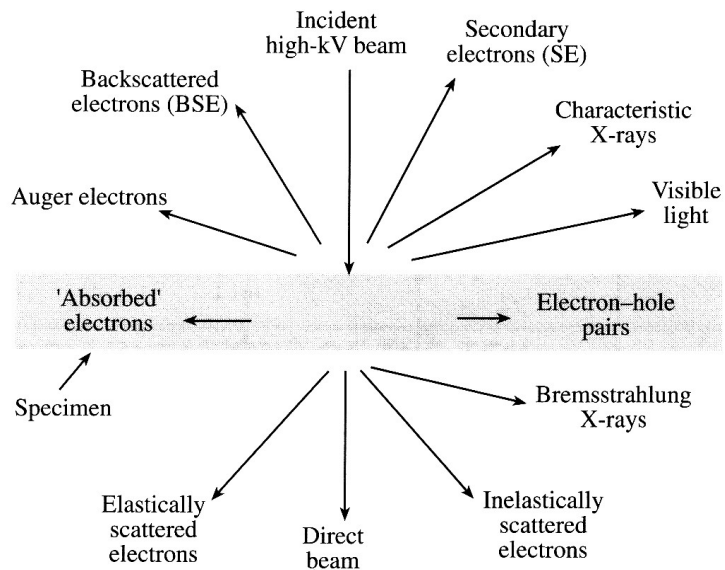


Figure 3-3 The various signals generated when a high-energy beam of electrons interacts with a sample. The directions shown indicate where the signal is strongest or where it is detected.

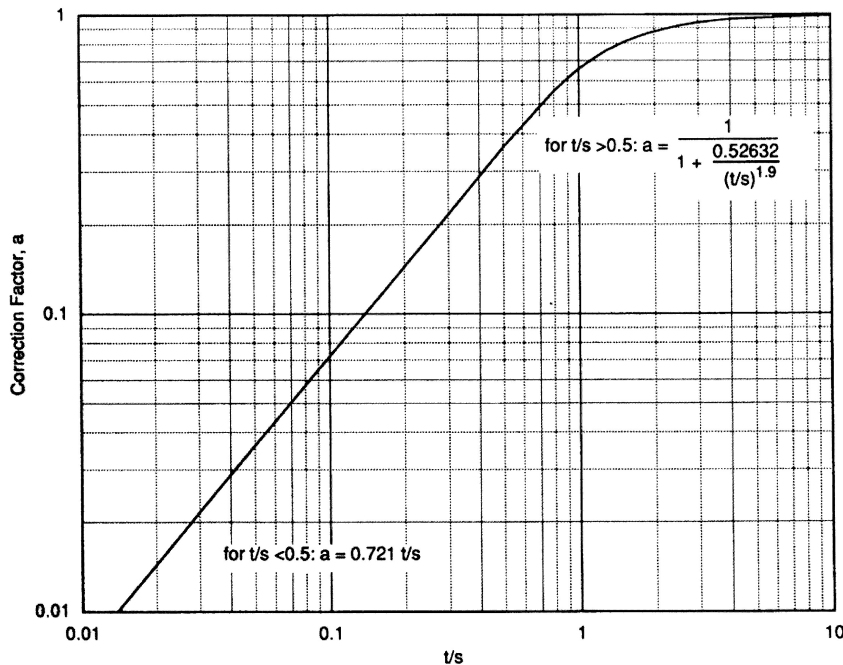


Figure 3-4 Plot of the sample geometric correction factor as a function of sample thickness, t , to probe spacing, s , ratio. Note that no sample geometric correction factor is required when t/s is approximately $5s$.

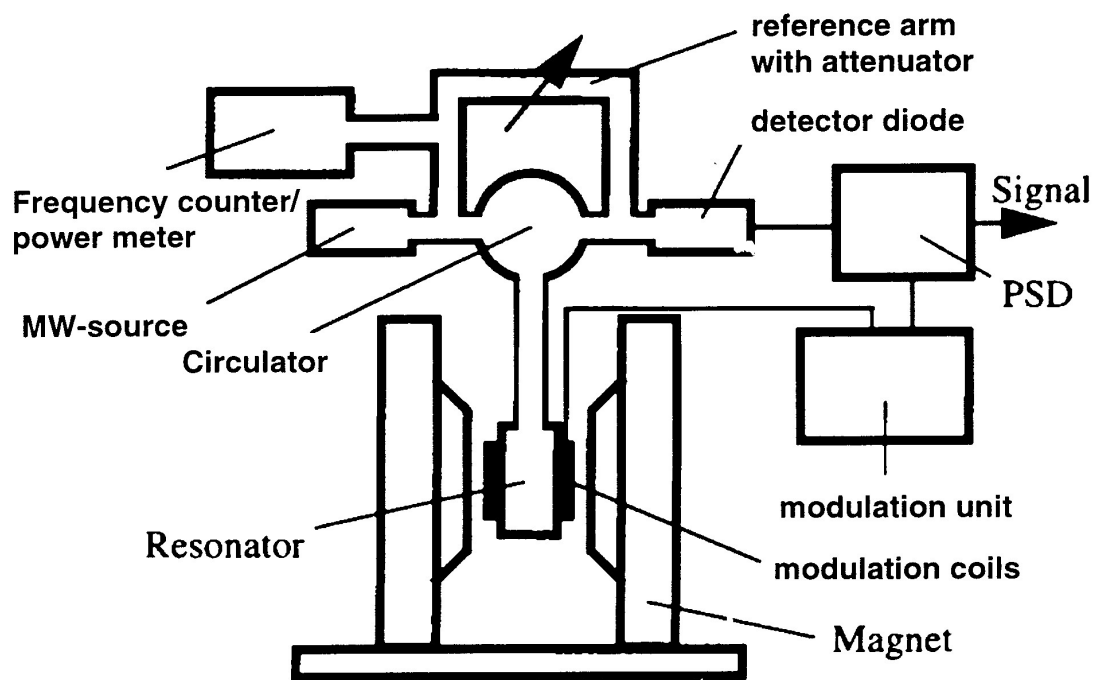


Figure 3-5 A traditional cw EPR set-up.

CHAPTER 4

EFFECT OF PRE-AMORPHIZATION ENERGY ON BORON ULTRA-SHALLOW JUNCTION FORMATION DURING ULTRA-HIGH TEMPERATURE ANNEALING OF ION-IMPLANTED SILICON

Introduction

Silicon technology is approaching a transition period for which novel front-end processing techniques must be developed and explicitly understood in order to maintain the aggressive scaling trend outlined by the International Technology Roadmap for Semiconductors (ITRS).¹³ Ion-implantation is currently used to introduce dopants into a Si substrate to control the concentration profiles and electrical characteristics of the locally doped regions.³ This process inherently produces point-defects within the lattice in the form of Si self-interstitials that are created as a result of displacements from their equilibrium positions due to nuclear collisions with the primary ions and recoiled atoms.^{4,5} Implants of sufficient energy and areal density are capable of producing continuous amorphous layers, which assist in the reduction of ion channeling associated with B implantation.^{3,177} Post-implant thermal processing is required to induce solid-phase epitaxial regrowth (SPER) of the implantation-induced amorphous layer, which repairs the lattice damage accumulated during the implantation process as well as activates the B atoms by establishing them on substitutional sites where they are able to contribute holes to the valence band.^{178,179}

During post-implant thermal annealing of continuous surface amorphous layers, the Si self-interstitials coalesce into type II end-of-range (EOR) defects and participate in an anomalous B diffusion enhancement.^{9,18,180,181} Transient enhanced diffusion (TED) is the

phenomena associated with increased diffusion behavior as a result of the Si self-interstitials redistributing throughout the lattice^{17,18} and interacting with B in such a way to remove it from its substitutional site,¹⁹⁻²¹ allowing for diffusion through a well documented interstitial mechanism.²²⁻²⁵ This phenomena decays with time and can be modeled by the following Arrhenius equation

$$\Delta x_j^2 \propto N R_p \exp\left[\frac{-(-1.4 \text{ eV})}{kT}\right], \quad (4.1)$$

where Δx_j is the change in the junction depth (x_j) after complete annealing of the damage, N is the number of interstitials trapped within the extended defects, and R_p is the projected range of the implant.³ It can be seen that this equation has an effective negative activation energy, which suggests that the amount of TED will decrease when the damage is annealed out at a higher temperature.^{3,27} This arises from the fact that the interstitial supersaturation because the presence of extended defects is larger at a lower temperature.²⁷ This observation influenced the development of single-wafer thermal processes that are capable of producing a high temperature ambient with ramp rates on the order of 50-200 °C/s, and fast switching times to insulate the dopant from a high degree of TED.²⁸

Rapid thermal processing (RTP) has proven successful in producing junctions with the performance characteristics necessary for the continued scaling of complementary metal-oxide-semiconductor (CMOS) technology to date.²⁹ Its ability to satisfy these requirements is associated with improved equipment capability in the form of spike annealing, which decreases the effective thermal budget, allowing for higher annealing temperatures to improve activation and reduce the amount of diffusion that takes place during the thermal process.^{30,31} A spike anneal is characterized as a short thermal-anneal

cycle that can be achieved by increasing the ramp-up and ramp-down rates and by minimizing the dwell time at the temperature of interest. One process limitation associated with RTP is that a significant amount of TED occurs during the early stages of annealing, which promotes diffusion, resulting in a profile with lack of abruptness and an unacceptable increase in x_j .^{9,66} This initial interstitial injection mechanism occurs due to either the dissolution and evolution of unstable sub-microscopic interstitial clusters, or the inability of the extended defects in capturing the entire interstitial population during their formation.^{99,113,114} Although increased spike sharpness enhances the ability to increase the annealing temperature to achieve higher activation levels and improve junction abruptness,¹¹⁵ the amount of diffusion that occurs during the thermal process is still unacceptable. As the spike anneal approaches time durations on the order of 1-2 s within 50 °C of the peak temperature, the advantages offered by annealing at higher temperatures are cancelled by the lack of concentration enhanced diffusion (CED) that takes place during the thermal process, which results in a profile with an unacceptable x_j due to the TED that occurs during the early stages of annealing.¹¹⁶ This illustrates the need to investigate novel annealing technologies that may be able to produce junctions without being subject to a significant amount of TED.

Novel high-power arc lamp design has enabled ultra-high temperature (UHT) annealing as an alternative to conventional RTP for B ultra-shallow junction formation.³³ This technique heats the wafer to an intermediate temperature (e.g., 800 °C) before discharging a capacitor bank into flash lamps, which anneals the device side of the wafer at a relatively high temperature (e.g., 1200 °C) for a few milliseconds.³⁴⁻³⁶ The UHT anneal heats the surface of interest while increasing the bulk wafer temperature not more

than 50 °C of the intermediate temperature, allowing for conductive heat loss through the substrate. These qualities resolve one of the limiting issues associated with conventional RTP techniques. In addition to developing novel activation processes, advanced implant conditions are required to satisfy the performance characteristics required by future technology nodes. Recent attention has been given to low energy Ge⁺ implantation because the 1.0 eV activation energy associated with the defect dissolution kinetics, which may serve to improve device leakage characteristics after thermal processing.¹⁸² In addition to the low activation energy associated with the defect dissolution kinetics, it is well known that decreasing the Ge⁺ pre-amorphization implant energy results in a more abrupt and shallower junction after the same post-implant thermal process. As can be seen in Figure 4-1, decreasing the Ge⁺ pre-amorphization energy from 18 to 6 keV improves the junction abruptness and decreases the x_j from 10.3 nm/dec and 57.2 nm to 8.9 nm/dec and 51.2 nm after a 1050 °C refined spike anneal, respectively. Junction abruptness is defined as the inverse slope of the SIMS profile between the concentration range of 1×10^{18} and $1\times10^{19}/\text{cm}^3$, and the x_j is defined as the depth of the profile at a dopant concentration of $1\times10^{18}/\text{cm}^3$. The refined spike refers to an optimized thermal profile that decreases the amount of time the wafer spends within 50 °C of the peak temperature in order to reduce the amount of diffusion that occurs during the thermal process. This type of anneal is typical of those used for the deep source/drain (S/D) activation anneal in current microelectronics manufacturing. In this chapter, the effect of Ge⁺ pre-amorphization energy on B ultra-shallow junction formation after UHT annealing of ion-implanted Si is investigated.

Experimental Design

Two 200 mm 3-5 $\Omega\cdot\text{cm}$ (100) n-type Czochralski (CZ) grown Si wafers were pre-amorphized with either 48 keV or 5 keV Ge⁺ implantation to $5\times 10^{14}/\text{cm}^2$, and subsequently implanted with 3 keV BF₂⁺ molecular ions to $6\times 10^{14}/\text{cm}^2$. The implants were carried out in the drift mode and performed at room temperature with the ion beam normal to the surface plane using an Applied Materials Leap-II system. The implant parameters were monitored to ensure they remained within predetermined limits. The wafers were then sectioned and annealed at Vortek Industries to investigate the effects of the UHT annealing technique on the resulting junction characteristics. Representative temperature-time (T-t) profiles of the two UHT annealing techniques as well as the processing conditions that were used are shown in Figure 4-2. The impulse anneal (iRTPTM) is produced by continuous wave mode arc lamp irradiation of the front surface of the wafer and is responsible for producing the bulk wafer temperature, known as the intermediate temperature, at which the flash anneal (fRTPTM) is to be introduced. The fRTP anneal is produced by discharging a capacitor bank into flash lamps which increases the temperature of the surface of interest while increasing the bulk wafer temperature not more than 50 °C of the intermediate temperature, allowing for conductive heat loss through the substrate. The iRTP anneal provides a means to better understand the advantages gained by the fRTP anneal. All of the anneals were carried out in a N₂ ambient with less than 10 ppm O₂. The iRTP and fRTP anneal temperatures were determined by a radiometer, which determined the wafer emissivity through a reflectance calculation that expresses the temperature of the system. In this experiment, iRTP anneals were performed over the range of 760 to 1100 °C using a ramp-up rate of

400 °C/s, and a ramp-down rate which was estimated to be approximately 150 °C/s at 900 °C. The ramp-down rate was determined by an instantaneous derivative of the radiation-cooling curve for a gray body with an emissivity and thickness comparable to the Si substrate. It should be noted that the ramp-down rate for conventional RTP is limited to 50-80 °C/s because radiative cooling of the substrate to the ambient.^{3,117} The ramp-down rate is greater than that obtained through conventional techniques because the use of absorbing chamber technology, which reduces radiation return to the substrate, providing the improved cooling rate.¹¹⁷ The fRTP anneals were performed over the range of 1200 to 1350 °C using ramp-up and ramp-down rates on the order of 10⁶ °C/s.

Dynamic secondary ion mass spectrometry (SIMS) was used to quantify dopant concentration as a function of depth. The ¹⁰B⁺ and ¹¹B⁺ counts were obtained on a CAMECA IMS-6f analytical tool using an O₂⁺ primary beam with a nominal beam current of 50-70 nA and a net impact energy of 800 eV directed 50° from the sample normal. The depth profile was established by continuously rastering a 200 by 200 μm area, and collected from a centered circular area 30-60 μm in diameter under an isobaric O₂ ambient, which provided an adequate condition for complete oxidation of the Si surface during analysis. The system was configured so as to maintain a sputtering rate of 0.08-0.1 nm/s. Variable angle spectroscopic ellipsometry (VASE) was used to determine the thickness of the implantation-induced amorphous layers. The VASE measurements were performed on a J. A. Woollam Co., Inc. multi-wavelength ellipsometer with the 75 W Xe light source tilted 20° from the surface plane. The system was calibrated by fitting a known oxide thickness from a control Si substrate, and each subsequent measurement assumed a 2 nm native oxide above the continuous amorphous layer in

order to more accurately measure the amorphous layer thickness. Cross-sectional transmission electron microscopy (XTEM) was used to verify the thickness of the amorphous layers measured by VASE, and image the depth of the EOR defect layer produced by the 48 keV pre-amorphization implant. The XTEM samples were thinned by 5 kV Ar⁺ ion milling, with the plasma sources tilted 12° from the surface plane. All XTEM images were captured on a JEOL 200 CX TEM operating at 200 kV under a bright field imaging condition with the objective aperture centered over the transmitted beam. Plan-view TEM (PTEM) was used to investigate the EOR defect evolution and morphology as a function of the two UHT annealing techniques. The PTEM sample surfaces and backside periphery were insulated from the 3:1 HNO₃:49% HF solution used to introduce an electron transparent edge surrounding an interstice. The PTEM images were captured on a JEOL 200 CX TEM operating at 200 kV in **g.3g** centered weak-beam dark-field (WBDF) using a **g**₂₂₀ two-beam imaging condition.¹⁷³ A Prometrics RS-20 four-point probe was used to measure the sheet resistance (R_s) for each anneal condition. The sample geometric correction factor is negligible for the wafer sections, which have surface areas greater than those below which edge effects reduce measurement accuracy.

Results

The 48 keV and 5 keV Ge⁺ pre-amorphization implants to $5 \times 10^{14}/\text{cm}^2$ produced continuous amorphous layers extending 76 nm and 12 nm below the substrate surface, as determined by VASE and verified through XTEM, images of which are shown in Figure 4-3a and b, respectively. Figure 4-3c shows an XTEM image of a control sample that received the 48 keV pre-amorphization implant followed by a 585 °C furnace anneal

for 45 min. This relatively low temperature anneal was done to allow sufficient time for proper microstructural reconstruction during SPER of the implantation-induced amorphous layer to monitor any regrowth related defects associated with the iRTP anneals that may be introduced as a result of the roughness of the amorphous/crystalline (α/c) interface produced by the higher energy Ge^+ implant.¹⁸³ It was shown that a combination of 400 keV and 30 keV Ge^+ pre-amorphization implants to $5 \times 10^{14}/\text{cm}^2$ with a subsequent 5 keV BF_2^+ implant to $5 \times 10^{14}/\text{cm}^2$ resulted in hairpin dislocation formation after both a 800 °C anneal for 30 min and a 900 °C anneal for 10 s.¹⁸³ These defects may in turn provide easy diffusion paths, via pipe diffusion, for the B to segregate toward the substrate surface.¹²⁰ As can be seen in Figure 4-3c, the furnace anneal is sufficient to completely regrow the amorphous layer and produce a visible EOR defect band without forming any regrowth related defects. Although it is difficult to determine the morphology of the defects from the XTEM image, they are located below the original α/c interface, which is consistent with EOR defect formation.³ The corresponding PTEM image of the sample that received the furnace anneal is shown in Figure 4-3d. The diffraction pattern in the image inset confirms that the anneal is sufficient to completely regrow the amorphous layer and results in high quality single crystalline Si. This image shows that the defect structure that forms as a result of the furnace anneal consists of defect clusters approximately 4 to 12 nm in diameter, a morphology which is typical of low temperature-short time thermal processing.^{9,184} Additional XTEM results (not shown) were similar to Figure 4-3c and showed that the 760 °C iRTP anneal was sufficient to completely regrow the amorphous layer generated by the 48 keV pre-amorphization implant and was free of hairpin dislocations. It is presumed that

hairpin dislocation formation did not occur for any of the iRTP or intermediate temperatures used in this study due to the fact that they should form during regrowth of the amorphous layer. Figure 4-3 did not include any additional images from the wafer that received the 5 keV pre-amorphization implant because neither PTEM nor XTEM characterization showed any observable defect formation after iRTP annealing.

Figures 4-4a and b show the SIMS results for each of the iRTP anneals used in this study for the 48 keV and 5 keV pre-amorphization implants, respectively. As can be seen, the diffusion characteristics are dependent on the pre-amorphization implant energy. Each profile shows an increase in x_j when compared to the as-implanted profile, which has a junction abruptness of 3.3 nm/dec and a x_j of 16.3 nm. It should be noted that the as-implanted profile in Figure 4-4b is slightly deeper below a concentration of $1 \times 10^{18}/\text{cm}^3$, which is presumably due to channeling of the B atoms implanted past the original a/c interface produced by the 5 keV pre-amorphization implant.³ Figure 4-4a shows that the 760 and 800 °C iRTP anneals display similar profiles with 3.2 nm/dec junction abruptness and a 19.3 nm x_j , which is a 3.0 nm increase in x_j when compared to the as-implanted profile for the 48 keV pre-amorphization implant. The SIMS profile for the 585 °C furnace anneal for 45 min is included with the data in Figure 4-4a and shows that the 3.7 nm increase in x_j is associated with B diffusion during SPER of the amorphous layer produced by the 48 keV pre-amorphization implant.¹⁸⁵⁻¹⁸⁸ Figure 4-4b shows that the 760 and 800 °C iRTP anneals produce similar profiles with 5.3 and 5.5 nm/dec junction abruptness and 17.9 and 18.4 nm x_j , respectively, which is approximately a 2.0 nm increase in x_j when compared to the as-implanted profile for the 5 keV pre-amorphization implant. The profiles are comparable to the as-implanted

profile above a concentration of $1 \times 10^{19}/\text{cm}^3$. Since the motion occurs below the original α/c interface produced by the 5 keV pre-amorphization implant, it can be said that the diffusion observed for the 760 and 800 °C iRTP anneals in Figure 4-4b occurs in crystalline Si (c-Si).

Figure 4-4 shows that the 900 °C iRTP anneal produces profiles with 5.5 and 8.4 nm/dec junction abruptness and a 22.5 and 24.2 nm x_j for the 48 keV and 5 keV pre-amorphization implants, respectively. A significant amount of additional B diffusion occurs for the 5 keV pre-amorphization implant during the 900 °C iRTP anneal when compared to the 48 keV pre-amorphization implant. This is inconsistent with data that suggests that the lower energy pre-amorphization implant should result in a shallower x_j after the same anneal. Figure 4-4b shows that the 900 °C iRTP anneal is sufficient to produce a peak approximately 14 nm below the substrate surface. It is presumed that this peak forms because the high local concentration of interstitials in that region and that these interstitials induce B interstitial cluster (BIC) formation. An alternative explanation for this peak could be that it is a gettering peak associated with the EOR damage, as it was shown that defects can getter metal impurities (and that these impurities can introduce scattering sites which reduce carrier mobility if located entirely within the same electrical region).¹⁶ However, since TEM characterization showed no observable defect formation for the 5 keV pre-amorphization implant, it is less likely that this peak is associated with the gettering of B atoms at the EOR damage and more likely that BIC formation occurred [since BIC's cannot be directly observed by TEM because their small size (e.g., 3 to 8 atom clusters)].⁹ Further increasing the iRTP anneal temperature results in a degradation of the junction abruptness and increase in x_j .

The 1000 and 1100 °C iRTP anneals produce profiles with 15.0 and 11.0 nm/dec junction abruptness and a 29.5 and 30.4 nm x_j for the 5 keV pre-amorphization implant, respectively. This shows that a negligible amount of additional diffusion occurs for the 1000 and 1100 °C iRTP anneals, even though the peak observed for the 900 °C iRTP anneal is no longer present after the 1000 °C iRTP anneal. It is interesting to note that approximately 15 nm below the substrate surface the 1000 °C iRTP anneal produces a profile which is concave upwards, whereas the 1100 °C iRTP anneal produces a profile which is concave downwards. The 1000 and 1100 °C iRTP anneals produce profiles with 10.1 and 8.7 nm/dec junction abruptness and a 31.7 and 36.1 nm x_j for the 48 keV pre-amorphization implant, respectively. The 48 keV pre-amorphization implant results in increased diffusion behavior for the 1000 and 1100 °C iRTP anneals when compared to the 5 keV pre-amorphization implant. This shows that the pre-amorphization implant that results in the shallowest x_j depends on the iRTP anneal temperature of interest (considering the 5 keV pre-amorphization implant resulted in a deeper x_j after the 900 °C iRTP anneal). It should be noted that the 1100 °C iRTP anneal has improved junction abruptness compared to the 1000 °C iRTP anneal. Although this characteristic applies to both graphs in Figure 4-4, the junction abruptness is more degraded for the 5 keV pre-amorphization implant.

Figure 4-4a shows that the iRTP anneals produce profiles with plateau concentrations on the order of $1.4\text{-}1.8 \times 10^{20}/\text{cm}^3$ for the 48 keV pre-amorphization implant. The plateau concentration is defined as the concentration at which the anneal produces an inflection point. These profiles show inflection points between 7-8 nm below the substrate surface. These inflection points correspond to the concentration

levels below which B is diffusing and presumed to be active and above which inactive B cluster formation or precipitation occurs and the B remains immobile.^{5,9,98} It should be noted that the 1100 °C iRTP anneal dissociated of some of the initially inactive dopant near the Si surface independent of the pre-amorphization implant energy.

Figure 4-5 shows the PTEM images of the EOR damage produced by the 48 keV pre-amorphization implant after each of the iRTP anneals used in this study. No observable defects formed for the 5 keV pre-amorphization implant. As can be seen by the images, the 760, 800, and 900 °C iRTP anneals produce a high density defect structure consisting of defect clusters.^{9,184} These defect clusters are approximately 4 to 12 nm and 6 to 18 nm in diameter for the 760 and 900 °C iRTP anneals, respectively. Although the morphology of the defects appears independent of the iRTP anneal over this temperature range, the average size of these defects increases and the defect density decreases with increasing iRTP anneal temperature which suggests that defect coarsening is occurring.⁹ The PTEM image for the 1000 °C iRTP anneal shows that it is sufficient to produce a defect structure mainly consisting of {311} defects and dislocation loops.⁹ The {311} defects range from 29 to 88 and average 60 nm in length and the dislocation loops range from 21 to 29 and average 26 nm in diameter. Increasing the iRTP anneal temperature to 1100 °C results in a defect structure consisting only of dislocation loops, which shows that {311} defect dissolution is complete between 1000 and 1100 °C. The dislocation loops range from 24 to 32 and average 29 nm in diameter.

Figures 4-6a and b show the SIMS profiles for a collective subset of intermediate temperatures with the 1200 °C fRTP anneal for the 48 keV and 5 keV pre-amorphization implants, respectively. As can be seen, the 760 and 800 °C intermediate temperatures

produce similar profiles with 3.4 nm/dec junction abruptness and 19.9 nm x_j after the 1200 °C fRTP anneal for the 48 keV pre-amorphization implant. The 0.6 nm of diffusion during the fRTP anneal shows that most the overall diffusion occurs during SPER of the implantation-induced amorphous layer. As was shown in Figure 4-4a, the 900 °C iRTP anneal produces a profile with degraded junction abruptness and an increased x_j compared to the 760 and 800 °C iRTP anneals for the 48 keV pre-amorphization implant. These characteristics remain with the introduction of the 1200 °C fRTP anneal, which produces a profile with 5.9 nm/dec junction abruptness and 23.7 nm x_j . The diffusion behavior for each of the profiles is much less than would be expected from a conventional RTP anneal. Figure 4-6b shows that the 760 and 800 °C intermediate temperatures produce an increase in diffusion behavior with the 1200 °C fRTP anneal for the 5 keV pre-amorphization implant when compared to the 48 keV pre-amorphization implant. The 760 and 800 °C intermediate temperatures produced profiles with 5.4 and 6.7 nm/dec junction abruptness and 20.6 and 22.3 nm x_j , respectively. This shows that the 800 °C intermediate temperature produces an increase in diffusion behavior compared to the 760 °C intermediate temperature, which was not observed for the 48 keV pre-amorphization implant in Figure 4-6a. The 900 °C intermediate temperature results in a profile with an exponentially decreasing tail with 11.1 nm/dec junction abruptness and a 26.3 nm x_j after the 1200 °C fRTP anneal for the 5 keV pre-amorphization implant. It should be noted that the 1200 °C fRTP anneal produces only a slight increase in x_j for the 900 °C intermediate temperature and that the peak observed after the 900 °C iRTP anneal is no longer present after the 1200 °C fRTP anneal.

Figure 4-7 shows the PTEM images of the EOR damage produced by the 48 keV pre-amorphization implant after the 1200 °C fRTP anneal. No observable defects formed for the 5 keV pre-amorphization implant. The 760 and 800 °C intermediate temperatures result in a defect structure consisting of defect clusters and possibly small dislocation loops; it is unclear whether the areas of large contrast are dislocation loops or large defect clusters. For the 760 °C intermediate temperature, these defects are approximately 4 to 12 nm in diameter, which are similar to those produced by the corresponding iRTP anneal in Figure 4-5. The 800 °C intermediate temperature produces defects 9 to 22 nm in diameter, which are on average larger than those produced by the corresponding iRTP anneal in Figure 4-5. When comparing these images, it can be seen that the 800 °C intermediate temperature produced a defect structure with the defects increasing in size and decreasing in density when compared to the 760 °C intermediate temperature. The 900 °C intermediate temperature is sufficient to produce a defect structure consisting of defect clusters, {311} defects, and dislocation loops. The {311} defects range from 21 to 29 and average 25 nm in length and the dislocation loops range from 13 to 19 and average 17 nm in diameter. Although these images show subtle differences in the defect morphologies as a function of intermediate anneal temperature, thus far it is unclear whether the intermediate anneal temperature significantly effects the final defect structure after a fRTP anneal.

Figures 4-8a and b show the SIMS results for the 1350 °C fRTP anneals for the 48 keV and 5 keV pre-amorphization implants, respectively. As can be seen, the 760 and 800 °C intermediate temperatures produce profiles with 4.4 and 4.9 nm/dec junction abruptness and a 21.3 and 22.4 nm x_j after the 1350 °C fRTP anneal for the 48 keV

pre-amorphization implant. This shows that the 760 °C intermediate temperature results in a slightly shallower profile with the introduction of the 1350 °C fRTP anneal when compared to the 800 °C intermediate temperature, which was not observed after the 1200 °C fRTP anneal shown in Figure 4-6a. The 900 °C intermediate temperature produces a profile with a 5.8 nm/dec junction abruptness and 25.0 nm x_j . It should be noted that the diffusion enhancement produced by the 900 °C intermediate temperature causes the degraded junction characteristics compared to the 760 and 800 °C intermediate temperatures. Also, these profiles are deeper than those produced by the 1200 °C fRTP anneal, showing that the diffusion characteristics are dependent on the fRTP anneal temperature. As can be seen in Figure 4-8b, the 1350 °C fRTP anneal results in similar profiles independent of the intermediate temperature for the 5 keV pre-amorphization implant, all of which display an average junction abruptness of 7.9 nm/dec and a x_j of approximately 23.3 nm. It should be noted that the peak observed for the 900 °C iRTP anneal is no longer present after the 1350 °C fRTP anneal, independent of the intermediate temperature. Additional SIMS results (not shown) reveal that similar profiles are also obtained when using a 1300 °C fRTP anneal.

Figure 4-9 shows the PTEM images of the EOR damage produced by the 48 keV pre-amorphization implant after the 1350 °C fRTP anneal. No observable defects formed for the 5 keV pre-amorphization implant. The 760 °C intermediate temperature produced a defect structure consisting of defect clusters, {311} defects, and dislocation loops. The {311} defects range from 19 to 29 and average 25 nm in length and the dislocation loops range from 18 to 24 and average 19 nm in diameter. The 800 °C intermediate

temperature produced a defect structure mainly consisting of {311} defects and dislocation loops. The {311} defects range from 19 to 43 and average 32 nm in length and the dislocation loops range from 19 to 59 and average 32 nm in diameter. The 900 °C intermediate temperature produced a defect structure consisting of dislocation loops. The dislocation loops range from 24 to 115 and averaged 62 nm in diameter. The most marked difference between these images is the size and overall evolution of the dislocation loops, which increases with the intermediate annealing temperature. The largest dislocation loops in each of the images are approximately 24, 59, and 115 nm in diameter for the 760, 800, and 900 °C intermediate temperatures, respectively. When comparing these images it can be seen that the resulting defect structure after a fRTP anneal is significantly dependent on the intermediate anneal temperature, suggesting that both the intermediate and fRTP anneal temperatures need to be considered when using this UHT annealing technique.

Discussion

The results of these experiments suggest that no extended defects form for the 5 keV pre-amorphization implant after a 760 °C iRTP anneal. This is inconsistent with recently reported results which show that observable defects are present for approximately 1 hr during furnace annealing at 750 °C for the same pre-amorphization implant condition.¹⁸⁹ It should be noted that the current experiment had the additional 3 keV BF₂⁺ implant to $6 \times 10^{14}/\text{cm}^2$, and that it has been reported that the addition of B can delay extended defect formation.¹¹² While a delay in defect formation may have occurred, this is not expected to be the reason for observing no defects. Instead, it is expected that BIC formation occurred which consumed a significant fraction of the

excess interstitial population. It is presumed that any interstitials that did not participate in BIC formation were insufficient to coalesce into extended defects during post-implant thermal processing. This thought is consistent with the TEM results in Figure 4-5 in that BIC's cannot be directly observed by TEM because their small size (e.g., 3 to 8 atom clusters).⁹ An alternative explanation for not observing defects could be that the annealing conditions used in this study were unable to capture the evolutionary process, and that defect dissolution occurs at some intermediate stage between two of the iRTP annealing conditions. In other words, the annealing conditions used in this work may represent conditions that are either insufficient for producing observable defects or enough to dissolve the defects completely. The former explanation based on BIC formation is more plausible and presumed to be correct.

The SIMS results for the 760 and 800 °C intermediate temperatures in Figure 4-6a show that, even though the sample was annealed at a peak temperature of 1200 °C, most of the diffusion occurs during SPER of the amorphous layer produced by the 48 keV pre-amorphization implant. It was shown that B in a shallow δ-doped structure segregates to the surface during SPER of an implantation-induced amorphous layer.¹⁸⁵ Huang *et al.* showed that this surface segregation increased when increasing the SPER anneal temperature from 500 to 600 °C, and was attributed to enhanced diffusion due to the proximity of the δ-doped structure to the surface. In Figure 4-4a, the surface does not appear to have a strong effect on the diffusion characteristics of the profiles, which diffuse deeper into the substrate as opposed to toward the surface.

In addition to surface segregation, it was shown that B atoms from both B⁺ and BF₂⁺ implants into pre-amorphized Si substrates display a similar diffusion enhancement

during SPER of an implantation-induced amorphous layer at 550 °C.¹⁸⁸ Since B thermal diffusion in c-Si is negligible at 550 °C this diffusion enhancement was attributed to TED, possibly due to the large amount of damage from the 20 keV Si⁺ pre-amorphization implant to $5 \times 10^{14}/\text{cm}^2$; however, the fact that the diffusion behavior observed in Figure 4-4a are similar for the SPER furnace anneal at 585 °C and both the 760 and 800 °C iRTP anneals suggests that the diffusion is not controlled by TED. Instead, it is proposed here that the diffusion behavior observed in Figure 4-4a for the SPER furnace anneal at 585 °C and both the 760 and 800 °C iRTP anneals is associated with B diffusion in α -Si before complete recrystallization of the implantation-induced amorphous layer (i.e., not TED). It should be noted that the diffusion enhancement observed during SPER of the implantation-induced amorphous layer in Ref. 188 is also expected to be due to B diffusion in α -Si, and not TED.

It was shown that B diffusivity in α -Si at 600 °C is more than five orders of magnitude greater than that estimated for the diffusivity of B in c-Si.¹⁹⁰ This was done by growing three narrow B profiles with a peak concentration of $1.3 \times 10^{20}/\text{cm}^3$ at depths of 170, 338, and 508 nm with respect to the substrate surface. These three B profiles were then implanted at -196 °C with 600 keV Si⁺ to $5 \times 10^{15}/\text{cm}^2$ and subsequently implanted with 70 keV Si⁺ to $5 \times 10^{14}/\text{cm}^2$ to produce a continuous amorphous layer extending 900 nm below the substrate surface. The amorphous layer was then recrystallized at 600 °C and continuously monitored by time resolved reflectivity (TRR). The data show that the three B profiles are slightly broadened by the two Si⁺ pre-amorphization implants, and that the three B profiles are further broadened during the SPER of the implantation-induced amorphous layer. The broadening of the three profiles

increases with decreasing depth from the substrate surface (i.e., the profiles that spend the most time within the α -Si show the most broadening during SPER of the amorphous layer). This result is inconsistent with TED of the B caused by interstitial injection from the EOR defects, as these interstitials would cause the deepest B profile to broaden the most. In addition, this result is inconsistent with the suggestion that dopant segregation across the advancing α /c interface caused the observed increase in diffusion behavior. It was shown that Sb segregation occurs during SPER of a deposited amorphous layer and that this segregation, which presumably occurred at the α /c interface, was controlled by a local interfacial diffusion coefficient and not a bulk α -Si diffusion coefficient.¹⁹¹ If the observed B diffusion occurred due to mass transfer across the α /c interface then it should be independent of the amount of time the B spends in α -Si, which was not the case in Ref. 190.¹⁹¹ Their results estimate the B diffusivity in α -Si to be approximately $(2.6 \pm 0.5) \times 10^{-16} \text{ cm}^2/\text{s}$ at 600°C .¹⁹⁰ The results from our experiment support the suggestion that the diffusion behavior observed for the SPER furnace anneal at 585°C and both the 760 and 800°C iRTP anneals in Figure 4-4a is due to B diffusion in α -Si, as the 3 keV BF_2^+ implant is near the surface and spends a reasonable amount of time in α -Si before complete recrystallization. It should be noted that the diffusion coefficient of Ge in α -Si was reported to be very low and is not expected to have a significant impact on the results contained within this work.¹⁹² Figure 4-4b shows no B diffusion during SPER of the amorphous layer produced by the 5 keV pre-amorphization implant. One could argue that the amorphous layer produced by the 5 keV pre-amorphization implant completely recrystallized before any observable B diffusion in α -Si was able to occur; however, no appreciable regrowth of the amorphous layer is expected to occur during

ramp-up to the anneal temperature until approximately 600 °C (which was estimated from an Arrhenius equation used to describe the regrowth velocity of an implantation-induced amorphous layer as a function of ramp rate and temperature). This estimated temperature is comparable to the 585 °C used for the furnace anneal, which was sufficient to produce a measurable amount of B diffusion in α -Si before complete recrystallization of the amorphous layer produced by the 48 keV pre-amorphization implant. Instead of complete recrystallization before B diffusion in α -Si is able to occur, it is more likely that the high local concentration of excess interstitials produced by the 5 keV pre-amorphization implant couple with the B atoms and form immobile clusters which prevent any observable motion in α -Si. It is put forward that B clustering may also be occurring in the amorphous phase.

By using the value given for B diffusivity in α -Si at 600 °C the estimated amount of diffusion at 585 °C results in a calculated (i.e., $2\sqrt{Dt}$) value of approximately 4.0 nm, assuming that the B remains in the α -Si for 2.5 min of the 45 min furnace anneal, which was estimated from the regrowth velocity of the α/c interface at 585 °C being approximately equal to 30 nm/min.^{190,193} It was shown that impurity diffusion in α -Si decreases with decreasing temperature.^{37,194} With this in mind, it should be noted that the above calculation may slightly overestimate the amount of diffusion that is expected to occur during the 585 °C furnace anneal. The calculated 4.0 nm of diffusion is similar to the increase in x_j observed in Figure 4-4a for the SPER furnace anneal, which was approximately 3.7 nm, and supports the suggestion that B diffusion in α -Si is responsible for the initial increase in x_j for the 48 keV pre-amorphization implant. The assumption that the regrowth velocity remains constant during regrowth of the amorphous layer is not

fully correct, as is it was shown that B concentrations of approximately $2.5 \times 10^{20}/\text{cm}^3$ increase the regrowth velocity approximately 25 times that of intrinsic Si.⁵⁹ This increase in regrowth velocity reduces to an order of magnitude for B concentrations on the order of $1 \times 10^{21}/\text{cm}^3$.¹³⁷ This increase in the regrowth velocity will decrease the amount of time available for B diffusion in α -Si. Although the increase in regrowth velocity may have reduced the amount of time the B profile spends in α -Si, it is not expected to significantly affect the estimated diffusion enhancement calculated above. This arises from the 30 nm/min regrowth velocity expected at 585 °C and the fact that the 48 keV pre-amorphization implant produced a 76 nm continuous amorphous layer, requiring the B to remain within the α -Si for approximately 2 min before the α/c interface reaches the profile at a B concentration of approximately $1 \times 10^{18}/\text{cm}^3$ which is 16 nm below the substrate surface. It was shown that the regrowth velocity begins to increase for B concentrations of approximately $1 \times 10^{18}/\text{cm}^3$.¹⁹⁵ A similar calculation to the one above results in approximately 3.5 nm of B diffusion at 585 °C assuming that the B remains in the α -Si approximately 2 min before complete recrystallization of the implantation-induced amorphous layer. This value is similar to the 3.7 nm of diffusion observed for the 585 °C furnace anneal in Figure 4-4a and supports the idea that B diffusion in α -Si causes the initial increase in x_j for the 48 keV pre-amorphization implant. It should be noted that the regrowth rate is expected to vary throughout the B profile due to the Gaussian nature of the implantation process. It is tempting to consider B diffusion in α -Si to be similar to a interstitial diffusion process in c-Si. In fact, diffusion of other impurities in α -Si was modeled by an interstitial mechanism mediated by defect trapping.^{37,195}

It has recently been shown that B diffusion in α -Si is enhanced in the presence of F.¹⁹⁶ This enhanced diffusion was suggested to occur due to the F interactions with Si dangling bonds. It was proposed that the F atoms decrease the dangling bond concentration, thereby reducing the formation energy required for B diffusion. The XTEM results from Ref. 196 showed that the regrowth velocity increases when the α/c interface reaches a B concentration of $1\times 10^{18}/\text{cm}^3$ and decreases when it reaches a F concentration of $1\times 10^{18}/\text{cm}^3$. The 180 nm implantation-induced amorphous layer generated by the 70 keV Si^+ implant to $1\times 10^{15}/\text{cm}^2$ completely recrystallized after 30 min of annealing at 550 °C for the sample implanted with B^+ alone, and was complete after 130 min of annealing for the sample that was co-implanted with B^+ and F^+ . These results estimate the B diffusivity within α -Si at 550 °C in the presence of F as being approximately $3\times 10^{-17}\text{cm}^2/\text{s}$, which is more than five orders of magnitude larger than the equilibrium diffusivity of B in c-Si.¹⁹⁶ Elliman *et al.* showed that B diffusivity within α -Si at 600 °C is enhanced more than five orders of magnitude without the presence of F.¹⁹⁰ In addition, it was shown that B from both B^+ and BF_2^+ implants into Si display similar diffusion behavior during SPER of an implantation-induced amorphous layer at 550 °C.¹⁸⁸ These observations, coupled with the fact that it was shown that the presence of the F decreases the regrowth velocity, suggests that the effect of F on increasing the amount of B diffusion within α -Si may also be due to the additional time available for B diffusion in α -Si for the co-implanted sample.

Two additional experiments were performed to better understand the mechanisms controlling B diffusion in α -Si. The first experiment was designed to obtain the so-called pre-exponential factor and activation energy of B diffusion in α -Si, assuming that

diffusion in α -Si is a thermally activated process which follows an Arrhenius relationship similar to the c-Si case. For this experiment, a 200 mm 3-5 $\Omega\cdot\text{cm}$ (100) n-type CZ grown Si wafer was pre-amorphized with an 80 keV Ge^+ implant to $1\times 10^{15}/\text{cm}^2$ and subsequently implanted with 1 keV B^+ to $1\times 10^{15}/\text{cm}^2$. The implants were carried out in the drift mode and performed at room temperature with the ion beam normal to the surface plane using an Applied Materials Leap-II system. The implant parameters were monitored to ensure they remained within predetermined limits. The pre-amorphization energy of the Ge^+ implant was increased to 80 keV to produce the thickest possible continuous amorphous layer under the available implant capabilities, which was determined to be approximately 110 nm by XTEM imaging (not shown). This relatively thick amorphous layer offered the ability to perform low temperature (e.g., 500 °C) furnace anneals for exact periods of time without complete recrystallization of the implantation-induced amorphous layer. The wafer was then subject to post-implant thermal processing in a conventional tube furnace under a N_2 ambient over the temperature range of 475-550 °C for various times. The longest time at each annealing temperature was to result in not more than 80 nm of regrowth in order to maintain the B profile in the amorphous layer throughout the entire anneal. It should be noted that the times reported for each anneal correspond to the time the material spends in the center of the furnace (even though it was shown that the quartz boat used to hold the wafer pieces takes as long as 2-3 min to reach the peak temperature of the furnace).¹¹⁸ Figure 4-10 shows the SIMS profiles for the 1 keV B^+ implant to $1\times 10^{15}/\text{cm}^2$ before and after annealing at 500 °C for up to 123 min. As can be seen, the junction abruptness and x_j change from 3.4 nm/dec and 21.5 nm for the as-implanted profile to 2.9 nm/dec and

22.2 nm after a 500 °C furnace anneal for 41 min. This shows that the low temperature furnace anneal is capable of significantly improving the junction abruptness over that produced during the implantation process. The improvement in junction abruptness is due to the increased diffusion behavior at higher B concentrations when compared to the lower concentration region. For example, the B profile diffuses approximately 1.4 nm at a concentration of $3 \times 10^{19}/\text{cm}^3$ whereas it only diffuses 0.7 nm at a concentration of $1 \times 10^{18}/\text{cm}^3$. It can be seen that, after the initial increase in diffusion behavior at higher B concentrations, the profile appears to diffuse the same distance independent of concentration after an additional 41 and 82 min annealing at 500 °C. It is interesting to note that, although the x_j increased with annealing time, the junction abruptness remained approximately 2.9 nm/dec throughout the entire 123 min of annealing. Figure 4-11 shows the SIMS profiles for the 1 keV B⁺ implant to $1 \times 10^{15}/\text{cm}^2$ before and after annealing at 550 °C for up to 13 min. As can be seen, the junction abruptness and x_j change from 3.4 nm/dec and 21.5 nm for the as-implanted profile to 2.9 nm/dec and 22.0 nm after a 550 °C furnace anneal for 7 min, which is similar to the profile produced by furnace annealing at 500 °C for 41 min. This shows that the same profile can be obtained by decreasing the time spent at higher annealing temperatures, consistent with the thought that B diffusion in α-Si is a thermally activated process. Although B diffusion in α-Si appears to be a thermally activated process, the increase in B diffusion behavior at higher B concentrations results in a non-Gaussian diffusion profile; one that is difficult to extract a meaningful pre-exponential factor. Even though the pre-exponential factor cannot be accurately obtained from the current data, the activation energy associated with the diffusion process can be calculated if two different annealing

temperatures produce the same diffusion profile after an anneal (i.e., result in the same diffusivity). The SIMS profiles for a select number of annealing times at 500 and 550 °C are shown in Figure 4-12. As can be seen, the anneals result in two different diffused profiles. The profile produced by annealing at 500 °C for 41 min or 550 °C for 7 min has junction abruptness and average x_j of 2.9 nm/dec and 22.1 nm, respectively, whereas the profile produced by annealing at 500 °C for 123 min or 550 °C for 13 min has average junction abruptness and x_j of 2.8 nm/dec and 22.9 nm. This data can be used to estimate the activation energy of B diffusion in α -Si by the use of

$$D_1 t_1 = D_2 t_2, \quad (4.2)$$

where D is the diffusivity at a certain annealing temperature, and t is the time spent at that annealing temperature. The D is a function of temperature expressed by

$$D = D_0 \exp\left(\frac{-E_a}{kT}\right), \quad (4.3)$$

where D_0 is the pre-exponential factor, E_a is the activation energy of the thermal process, k is Boltzmann's constant, and T is the annealing temperature. Equation 4.2 can be used to determine the activation energy of B diffusion in α -Si because the 500 and 550 °C anneals in Figure 4-12 resulted in the same diffusion profile after annealing. Rearranging terms in Equations 4.2 and 4.3 to solve for the activation energy for two different annealing temperatures gives

$$E_a = \frac{k T_2 [\ln(t_2) - \ln(t_1)]}{\left(\frac{T_1 - T_2}{T_1}\right)}, \quad (4.4)$$

where the subscripts refer to the temperature and time used for each anneal to produce the same diffusion profile after post-implant thermal processing (e.g., 500 °C for 123 min).

The data in Figure 4-12 result in an activation energy for B diffusion in α -Si of 2.2 ± 0.26 eV. It should be noted that the time the material spends in the furnace waiting for the quartz boat to reach the set temperature is expected to result in a certain amount of error for the anneals that spend a relatively short time in the furnace throughout the duration of the anneal (e.g., 7 min at 550 °C). In other words, caution should be taken when using data where the total annealing time is not significantly greater than the amount of time it takes for the quartz boat to equilibrate with the peak temperature in the furnace. Even with a possibly large error in the calculated activation energy, this value is remarkably similar to the diffusion enthalpy observed for the diffusion of Pt in α -Si which is approximately 2.2 eV.³⁷ This is an interesting result considering Pt diffuses via the kick-out mechanism in c-Si, which was also reported for B.¹⁹⁷

FLorida Object Oriented Process Simulator (FLOOPS) simulations were performed to better understand the physical mechanisms controlling the observed diffusion behavior in Figure 4-12. It should be noted that these simulations were performed using a database of values associated with B diffusion in c-Si, which may be significantly different for the amorphous case. Each simulation used the database activation energy value for B solubility; however, the activation energy for B diffusivity was reduced to the calculated value from the data in Figure 4-12 (i.e., 2.2 eV). The pre-exponential factors for both the B solubility and diffusivity were adjusted to give the best fit for all profiles (i.e., without changing the pre-exponential values between profiles). The exact values and FLOOPS code used for each simulation can be found in Appendix A. Figure 4-13 shows the SIMS data for the profiles corresponding to the 500 °C furnace anneals in Figure 4-12. As can be seen in Figure 4-13a, the junction

abruptness and x_j change from 3.4 nm/dec and 21.5 nm for the as-implanted profile to 2.9 nm/dec and 22.2 nm after a 500 °C furnace anneal for 41 min. The FLOOPS simulation for a 500 °C furnace anneal for 41 min under intrinsic conditions shows no observable difference between the as-implanted profile and the profile after the anneal; however, the addition of charged species diffusion results in a profile remarkably close to the SIMS data for the 500 °C furnace anneal for 41 min. A similar comment can be made regarding the data corresponding to the 500 °C furnace anneal for 123 min in Figure 4-13b. The simulations for the 550 °C furnace anneal are shown in Figure 4-14. Similar to the results for the 500 °C furnace anneal, the FLOOPS simulations show no measurable diffusion under intrinsic conditions; however, the addition of charged species diffusion closely matches the SIMS data. As was mentioned earlier, these SIMS profiles show an increase in diffusion at higher B concentrations when compared to the low concentration region; this is well matched by the simulation results. This concentration dependence cannot be easily associated with extrinsic diffusion effects such as concentration enhance diffusion or an electric field effect due to the limited knowledge regarding point-defect charge states in α -Si. It is put forward that the concentration dependence may be due to B trapping at defect sites inherent to the amorphous phase. It is well known that defect sites in α -Si trap impurities, reducing their diffusivity; therefore, it is reasonable to say that when the defect states are occupied by B atoms they are no longer able to affect the diffusion of near by B atoms. This would result in B diffusing more at higher concentrations than in low concentration regions where sites are still available to trap B atoms, which is observed empirically. It should be noted that a D_0 of 5.8×10^{-6} cm²/s was used to fit the SIMS data in Figures 4-13 and 4-14. These results

show that the diffusion behavior in α -Si observed during the early stages of low temperature furnace annealing can be well matched by simulations that take into account charged species diffusion.

Since point-defect mediated diffusion processes in c-Si are defined as having interstitial and vacancy components, the second experiment was designed to determine if the diffusion behavior observed in α -Si could also be separated into interstitial and vacancy based diffusion mechanisms.⁶ It was shown that both B and P diffuse in c-Si primarily through an interstitial(cy) based mechanism whereas Sb diffuses mostly through a vacancy based mechanism.^{2,22} It is well known that ion-implanted α -Si contains a number of structural imperfections such as large-angle bond distortions and defect complexes.^{194,198,199} The defect complexes associated with α -Si are expected to be similar to point-defects and small point-defect clusters in heavily damaged c-Si due to the fact that both are fourfold coordinated covalently bonded materials.¹⁹⁸ Previous work showed that although impurity diffusion in α -Si is much slower than that in c-Si, the diffusion mechanisms in c-Si are similar in α -Si (i.e., interstitial diffusers in c-Si also diffuse by an interstitial mechanism in α -Si).^{37,199,200} The slower diffusion in α -Si was explained by frequent trapping of the diffusing impurity at structural defects intrinsic to the amorphous structure.^{37,199,200} In addition to evidence of interstitial point-defects in α -Si, positron annihilation spectroscopy (PAS) studies have shown that a large variety of stable vacancies and small vacancy clusters are present in α -Si.²⁰¹⁻²⁰⁴ This data suggests that dopants may possibly diffuse by interstitial(cy) and vacancy type mechanisms in α -Si, which is the subject of following experiment. For this experiment, three 200 mm 3-5 $\Omega\cdot\text{cm}$ (100) n-type CZ grown Si wafers were pre-amorphized with an 80 keV Ge⁺

implantation to $1\times10^{15}/\text{cm}^2$ and subsequently implanted with either 2 keV B⁺, 5 keV P⁺, or 8 keV Sb⁺ each to $1\times10^{15}/\text{cm}^2$. The implants were carried out in the drift mode and performed at room temperature with the ion beam normal to the surface plane using an Applied Materials Leap-II system. The implant parameters were monitored to ensure they remained within predetermined limits. The pre-amorphization energy of the Ge⁺ implant was increased to 80 keV to produce the thickest possible continuous amorphous layer under the available implant capabilities, which was determined to be approximately 110 nm by XTEM imaging (not shown). This relatively thick amorphous layer provided the most time for the dopants to diffuse in α -Si before complete recrystallization of the implantation-induced amorphous layer. The implant energies of the dopants were adjusted to result in the same R_p so each would spend the same amount of time in α -Si before the α/c interface reached the respective dopant profiles. In general, it can be said that the addition of B, P, or Sb increases the regrowth velocity of the α/c interface until concentrations on the order of approximately $1\times10^{21}/\text{cm}^3$ are reached, above which the regrowth velocity of the α/c interface reduces below intrinsic values.^{118,137,139} It is well known that a high concentration of dopant is sufficient to prevent complete recrystallization of the amorphous layer without poly-crystalline Si (p-Si) formation.^{118,137,139} Figure 4-15 shows the SIMS results for the as-implanted profiles of each species used in this study. As can be seen, adjusting the implant energies results in all three profiles having the same R_p , which is approximately 7 nm below the substrate surface. This R_p is somewhat lower than that predicted by TRansport of Ions in Matter (TRIM) simulations for each dopant, which is approximately 10 nm. The B, P, and Sb implants result in as-implanted profiles with junction abruptness of 5.2, 6.5, and

8.7 nm/dec and x_j of 33.3, 33.4, and 35.8 nm, respectively. The differences between the as-implanted profiles are due to the so-called skewness (γ) and kurtosis (β) (i.e., the third and fourth moments) of the implantation process, which are different for the various dopants. The γ of an implant describes the asymmetry of a profile about its R_p (i.e., its tendency to lean toward or away from the substrate surface), whereas the β characterizes the contribution of the tail on the flatness of the profile shape (e.g., a larger kurtosis results in a more horizontal profile near its peak). Each of the wafers were then sectioned and subject to 800 and 900 °C iRTP anneals to investigate the effect of the defects in α -Si on the diffusion behavior during UHT annealing. All of the anneals were carried out in a N₂ ambient with less than 10 ppm O₂ using a ramp-up rate of 400 °C/s, and a ramp-down rate which was estimated to be approximately 150 °C/s at 900 °C. It should be noted that XTEM results (not shown) revealed that recrystallization of the implantation-induced amorphous layer was complete during the 800 °C iRTP anneal, independent of the implanted dopant. Figure 4-16 shows the SIMS results for the 2 keV B⁺ implant to $1 \times 10^{15}/\text{cm}^2$ for both of the iRTP anneals used in this study. As can be seen, the 800 and 900 °C iRTP anneals produce profiles with junction abruptness of 5.1 and 7.1 nm/dec and x_j of 34.8 and 39.2 nm, respectively. This shows that the 800 °C iRTP anneal is capable of improving the junction abruptness compared to the as-implanted case, presumably due to the increased diffusion behavior at higher B concentrations (similar to what was observed for the low temperature furnace anneals in Figures 4-10 and 4-11). It can be seen that the B profile diffuses up to a concentration of approximately $2 \times 10^{20}/\text{cm}^3$, above which inactive B cluster formation or precipitation occurs and the B remains immobile. It is presumed that the diffusion that occurred during the 800 °C iRTP anneal is due to B

diffusion in α -Si, and not TED. It should be noted that, even though the 80 keV pre-amorphization implant produced a thicker amorphous layer than that generated by the 48 keV pre-amorphization implant, the increase in x_j during the 800 °C iRTP anneal is not as great as that observed in Figure 4-4a. This difference is presumed to be due to the B implant energy, and will be discussed later. Although B diffusion in α -Si is expected to control the motion observed for the 800 °C iRTP anneal, the 900 °C iRTP anneal appears to be subject to interstitial injection from the EOR damage and, therefore, TED. This will be discussed in further detail later in the chapter. Figure 4-17 shows the SIMS results for the 5 keV P⁺ implant to $1 \times 10^{15}/\text{cm}^2$ for both of the iRTP anneals used in this study. As can be seen, the 800 and 900 °C iRTP anneals produce profiles with junction abruptness of 10.6 and 12.7 nm/dec and x_j of 37.9 and 41.6 nm, respectively. Although motion is observed for both iRTP annealing conditions, the P diffusion behavior only results in a significant amount of motion in the low concentration (i.e., below $2 \times 10^{19}/\text{cm}^3$) region of the profile. This is inconsistent with the data in Figure 4-16, which showed B diffusion at concentrations as high as $1 \times 10^{20}/\text{cm}^3$. This suggests that, although interstitial point-defects may exist in the amorphous phase, these point-defects are insufficient to produce an appreciable amount of P diffusion in α -Si during recrystallization of an implantation-induced amorphous layer. This is not to say that P does not diffuse in α -Si, only that the iRTP anneals used here did not provide enough evidence for such a statement. The SIMS results for the 8 keV Sb⁺ implant to $1 \times 10^{15}/\text{cm}^2$ for both of the iRTP anneals used in this study are shown in Figure 4-18. As can be seen, the 800 and 900 °C iRTP anneals produce profiles with junction abruptness of 8.7 and 8.8 nm/dec and x_j of 35.7 and 35.8 nm, respectively. It can be seen that the 800 and

900 °C iRTP anneals result in profiles very similar to the as-implanted profile, suggesting that the Sb does not diffuse during recrystallization of an implantation-induced amorphous layer or during the initial stages after complete recrystallization. This suggests that, although a large variety of stable vacancies and small vacancy clusters may exist in the amorphous material, these defects are insufficient to produce an appreciable amount of Sb diffusion in α -Si before complete recrystallization of the implantation-induced amorphous layer. This is not to say that Sb dose not diffuse in α -Si, rather that the iRTP anneals used here did not provide enough evidence for Sb diffusion in α -Si. The data of this experiment suggest that, although both interstitial and vacancy point-defects exist in α -Si, these point-defects do not have a significant effect on the diffusion behavior of P or Sb; however, it can be said that B diffuses appreciably in α -Si, consistent with the observation that fast interstitial diffusers in c-Si also diffuse quickly in α -Si.¹⁹⁸ These differences in diffusion behavior during recrystallization of an implantation-induced amorphous layer makes difficult defining interstitial and vacancy point-defect mediated diffusion mechanisms in α -Si.

An additional experiment was performed to determine the effect of solute trapping at the α/c interface on B activation during SPER of an implantation-induced amorphous layer. For this experiment, one 200 mm 3-5 Ω·cm (100) n-type CZ grown Si wafer was pre-amorphized with an 80 keV Ge⁺ implant to $1 \times 10^{15}/\text{cm}^2$. This wafer and an additional c-Si wafer were subsequently implanted with 1 keV B⁺ to $1 \times 10^{15}/\text{cm}^2$. The implants were carried out in the drift mode and performed at room temperature with the ion beam normal to the surface plane using an Applied Materials Leap-II system. The implant parameters were monitored to ensure they remained within predetermined limits.

The pre-amorphization energy of the Ge⁺ implant was increased to 80 keV to produce the thickest possible continuous amorphous layer under the available implant capabilities, which was determined to be approximately 110 nm by XTEM imaging (not shown). This relatively thick amorphous layer provided the most time for the dopant to diffuse in α -Si before complete recrystallization of the implantation-induced amorphous layer. Each of the wafers were then sectioned and subject to 800, 900, and 1000 °C iRTP anneals to investigate the effect of solute trapping at the α /c interface on B activation during SPER of an implantation-induced amorphous layer. All of the anneals were carried out in a N₂ ambient with less than 10 ppm O₂ using a ramp-up rate of 400 °C/s, and a ramp-down rate which was estimated to be approximately 150 °C/s at 900 °C. It should be noted that XTEM results (not shown) revealed that recrystallization of the implantation-induced amorphous layer was complete during the 800 °C iRTP anneal. Figure 4-19 shows the SIMS results for the 1 keV B⁺ implant to $1 \times 10^{15}/\text{cm}^2$ for each of the iRTP anneals used in this study. As can be seen, the as-implanted profiles for each wafer have junction abruptness of 3.4 and 10.5 nm/dec and x_j of 21.5 and 40.8 nm, respectively. This shows that the as-implanted profile for the wafer with the 80 keV Ge⁺ implant to $1 \times 10^{15}/\text{cm}^2$ is significantly improved compared to the wafer without the additional Ge⁺ implant. The as-implanted profile displays a non-Gaussian distribution that is broadened into the substrate, presumably due to ion channeling. It is well known that implant profiles into c-Si can be significantly different than a Gaussian profile because of ion channeling. This occurs when the ion trajectory is aligned along atomic rows where it experiences a slower rate of energy loss, thereby producing a profile with an asymmetric distribution; one that is Gaussian towards the substrate surface but supplemented by a characteristic

broadening at lower concentrations into the bulk of the substrate. As can be seen in Figure 4-19a, ion channeling can be eliminated by implanting Ge^+ before dopant incorporation to bring the substrate surface to an amorphous state. Amorphization of the substrate surface effectively prevents the possibility of the ions aligning along atomic rows where they can travel for distances greater than expected. The iRTP anneals result in profiles with junction abruptness of 3.6, 5.6, and 9.2 nm/dec and x_j of 25.3, 28.5, and 39.8 nm for the 800, 900, and 1000 °C iRTP anneals for the wafer pre-amorphized with the 80 keV Ge^+ implant to $1 \times 10^{15}/\text{cm}^2$, respectively. The iRTP anneals for the wafer without the additional Ge^+ implant produce profiles with junction abruptness of 13.5, 21.4, and 24.6 nm/dec and x_j of 43.3, 52.1, and 57.9 nm for the 800, 900, and 1000 °C iRTP anneals, respectively. These results show that the junction abruptness and x_j are consistently degraded for the wafer without the 80 keV Ge^+ implant to $1 \times 10^{15}/\text{cm}^2$. It should be noted that the diffusion behavior observed for the wafer without the additional Ge^+ implant is similar to that observed for the SIMS results in Figure 4-17; supporting the suggestion that no appreciable P diffusion occurs in α -Si during an iRTP anneal.

Sheet resistance measurements were performed to determine the effect of solute trapping at the α/c interface on B activation during SPER of an implantation-induced amorphous layer. The R_s measurements result in values of approximately 354, 367, and 431 Ohm/sq for the 800, 900, and 1000 °C iRTP anneals for the wafer pre-amorphized with the 80 keV Ge^+ implant to $1 \times 10^{15}/\text{cm}^2$, respectively. The iRTP anneals for the wafer without the additional Ge^+ implant produce profiles with R_s values of approximately 939, 974, and 722 Ohm/sq for the 800, 900, and 1000 °C iRTP anneals, respectively. These results show that, not only does the pre-amorphization implant affect the resulting junction

abruptness and x_j , but it also has a significant effect on the R_s after the same iRTP anneal. The improved activation for the wafer subject to the 80 keV Ge^+ pre-amorphization implant is presumably due to solute trapping at the advancing α/c interface. It is well known that impurity incorporation onto substitutional sites occurs during both liquid- and solid-phase regrowth of an implantation-induced amorphous layer.¹⁷⁹ It is this solute trapping which is presumably responsible for such high activation levels for the wafer with the Ge^+ pre-amorphization implant. The data in Figure 4-19a show that B diffusion (in $\alpha\text{-Si}$) occurs at concentrations well above $1 \times 10^{20}/\text{cm}^3$ for the 800 °C iRTP anneal. This can be compared to the diffusion behavior observed in Figure 4-19b, which shows that B remains immobile above a concentration of $2 \times 10^{19}/\text{cm}^3$ independent of peak iRTP annealing temperature. It is well known that immobile B is inactive. Assuming that the diffusing portion of the B profile is active, it can be said that significantly more dopant is active for the wafer with the 80 keV Ge^+ pre-amorphization implant to $1 \times 10^{15}/\text{cm}^2$, presumably because of effective solute trapping at the advancing α/c interface. It can be seen that, even though both wafers were brought to the same annealing temperature, the wafer with the 80 keV Ge^+ pre-amorphization implant to $1 \times 10^{15}/\text{cm}^2$ results in a lower R_s for each anneal used in this experiment. This data is consistent with the thought that SPER is able to produce junctions with above solid solubility levels. It should be noted that the R_s values for the wafer with the additional Ge^+ implant increases with increasing iRTP anneal temperature. This is presumably because the above solid solubility activation levels obtained during SPER of the implantation-induced amorphous layer deactivating to equilibrium values in c-Si due to prolonged annealing. In addition, it can be seen that the R_s values for the wafer without the Ge^+ pre-amorphization implant are

relatively constant for the 800 and 900 °C iRTP anneals, whereas it decreases for the 1000 °C iRTP anneal. This is presumably due to the fact that dopant solubility in c-Si increases with increasing temperature, and the thought that dopant activation only becomes noticeable at sufficiently high annealing temperatures. In other words, the R_s data for both wafers are converging toward the same value: the equilibrium solid solubility in c-Si at the peak annealing temperature. These results illustrate the importance of SPER on dopant activation.

Although the 760 and 800 °C iRTP anneals increase the x_j of the B profile, the diffusion that takes place during SPER of the amorphous layer generated by the 48 keV pre-amorphization implant produces profiles with slightly improved junction abruptness over that of the as-implanted profile. The as-implanted profile has a junction abruptness of 3.3 nm/dec, whereas both the 760 and 800 °C iRTP anneals have junction abruptness of 3.2 nm/dec. The B profiles after the 760 and 800 °C iRTP anneals in Figure 4-4a show approximately 3 nm of diffusion up to a concentration of $1.8 \times 10^{20}/\text{cm}^3$, above which inactive B cluster formation or precipitation occurs and the B remains immobile during SPER of the amorphous layer produced by the 48 keV pre-amorphization implant. Similar profiles were observed by Jin *et al.*, who showed that this characteristic is independent of B^+ or BF_2^+ implantation after a 550 °C furnace anneal for 40 min.¹⁸⁸ It should be noted the junction abruptness and x_j might be improved by ultra-low energy ion-implantation, assuming that the diffusion during SPER of the amorphous layer is independent of the initial dopant profile.

An additional experiment was performed to better understand the effect of the as-implanted profile on the resulting junction abruptness after an iRTP anneal. For this

experiment, three 200 mm 3-5 $\Omega\cdot\text{cm}$ (100) n-type CZ grown Si wafers were pre-amorphized with an 80 keV Ge^+ implantation to $1\times 10^{15}/\text{cm}^2$, and subsequently implanted with either 1, 2, or 4 keV B^+ to $1\times 10^{15}/\text{cm}^2$. The implants were carried out in the drift mode and performed at room temperature with the ion beam normal to the surface plane using an Applied Materials Leap-II system. The implant parameters were monitored to ensure they remained within predetermined limits. The pre-amorphization energy of the Ge^+ implant was increased to 80 keV to produce the thickest possible continuous amorphous layer under the available implant capabilities, which was determined to be approximately 110 nm by XTEM imaging (not shown). This relatively thick amorphous layer provided the most time for the dopants to diffuse in $\alpha\text{-Si}$ before complete recrystallization of the implantation-induced amorphous layer. The energy of the B implant was varied to change the junction abruptness of the as-implanted profile. The as-implanted junction abruptness degrades with increasing implant energy because of the increase in the vertical straggle (ΔR_p) of the implanted ions. Each of the wafers were then sectioned and subject to an 800 °C iRTP anneal to investigate the effect of the as-implanted profile on the resulting junction abruptness during UHT annealing. All of the anneals were carried out in a N_2 ambient with less than 10 ppm O_2 using a ramp-up rate of 400 °C/s. Figure 4-20 shows the SIMS results for the 1, 2, and 4 keV B^+ implants to $1\times 10^{15}/\text{cm}^2$ both before and after the 800 °C iRTP anneal used in this study. As can be seen, the junction abruptness and x_j for each of the as-implanted profiles are 3.4, 5.2, and 8.3 nm/dec and 21.5, 33.3, and 53.2 nm for the 1, 2, and 4 keV B^+ implants, respectively. The junction abruptness and x_j for each of the B implant conditions after the 800 °C iRTP anneal are 3.6, 5.1, and 8.4 nm/dec and 25.3, 34.8, and 54.5 nm for the 1, 2, and 4 keV B^+

implants, respectively. It can be seen that, although the junction abruptness is not improved over the as-implanted case, it is very similar to the as-implanted junction abruptness (varying only 0.2 nm/dec for the 1 keV B⁺ implant). These results show that B diffusion in α-Si cannot be easily described as a random jump process governed by Fick's first law of diffusion, which would result in a profile that not only broadens but also reduces the concentration gradient of the profile. Although the random jumping of individual atoms produces a net flow of atoms down the concentration gradient (i.e., deeper into the substrate), it can be seen that the diffusion behavior during the 800 °C iRTP anneal results in a profile that broadens but does not reduce the concentration gradient.⁹² It should be noted that, although the probability of jumps is equal in each direction for any cubic lattice, the probability of jumps in non-cubic lattices (e.g., tetragonal) is not equal for different crystallographic directions. This shows that the junction abruptness after a relatively low temperature iRTP anneal can be improved by decreasing the B implant energy, which is a significant result considering the importance on maintaining highly abrupt junctions in ultra-shallow junction formation. It should be noted that the diffusion that occurs during the 800 °C iRTP anneal decreases with increasing B implant energy, presumably due to the fact that the mobile portion of the B profile (i.e., below a concentration of approximately $2 \times 10^{20}/\text{cm}^3$) spends less time in α-Si during recrystallization of the implantation-induced amorphous layer as a result of the B being implanted deeper below the substrate surface. This data is consistent with the idea that B will undergo more diffusion when it spends more time in α-Si at approximately the same annealing temperature. The decrease of B diffusion in α-Si with increasing implant

energy is presumably the reason why less diffusion was observed for the SIMS results corresponding to the 800 °C iRTP anneal in Figure 4-16.

Even though the 760 and 800 °C iRTP anneals produce profiles with slightly improved junction abruptness compared to the as-implanted profile for the 48 keV pre-amorphization implant, it can be seen that the 585 °C furnace anneal for 45 min results in a profile with a junction abruptness of 3.6 nm/dec and a x_j of 20.0 nm, which is degraded compared to the 3.2 nm/dec junction abruptness and 19.3 nm x_j produced by the 760 and 800 °C iRTP anneals. The differences between the profiles for the sample that received the 585 °C furnace anneal and those that received the 760 and 800 °C iRTP anneals are presumed to be due to the time duration of the respective anneals. The PTEM image in Figure 4-3d shows that the 585 °C furnace anneal is sufficient to evolve the EOR damage produced by the 48 keV pre-amorphization implant into defect clusters, which are similar in size to those observed for the 760 and 800 °C iRTP anneals in Figure 4-5a and 4-5b, respectively. It is not expected that the time duration of the furnace anneal was sufficient to allow some of the excess interstitials to be released from the EOR damage region, causing the additional diffusion enhancement for the 585 °C furnace anneal compared to the 760 and 800 °C iRTP anneals. Instead, it is expected that the relatively slow regrowth velocity of the 585 °C furnace anneal increases the amount of time available for B diffusion in α -Si, allowing for more diffusion compared to the 760 and 800 °C iRTP anneals. This is supported by the calculations that estimated approximately 3.5-4.0 nm of B diffusion in α -Si during the 585 °C furnace anneal. Since additional XTEM results (not shown) show that the 76 nm continuous amorphous layer

completely recrystallized during the 760 °C iRTP anneal, it can be said that the 760 and 800 °C iRTP anneals result in similar dopant profiles due to the fact that the B remains in α -Si the same amount of time before recrystallization of the implantation-induced amorphous layer is complete. It is believed that the 760 and 800 °C iRTP anneals are insufficient to evolve the excess interstitials to the point where TED begins to influence the overall diffusion profile.

The observation of similar dopant profiles for the 760 and 800 °C iRTP anneals in Figure 4-4a suggests that there is a temperature range in which the iRTP anneal will result in equivalent dopant profiles, and that using an iRTP anneal within this temperature range will result in junctions with improved characteristics, as this temperature range defines the lower limit associated with the junction abruptness and x_j for the 48 keV pre-amorphization implant.

Figure 4-4a shows that each of the profiles for iRTP anneals above 800 °C display increased diffusion behavior in addition to that observed during SPER of the amorphous layer produced by the 48 keV pre-amorphization implant. The 900 °C iRTP anneal increased the x_j from 19.3 to 22.5 nm when compared to the 760 and 800 °C iRTP anneals. Both FLOOPS simulations and calculations based on an Arrhenius equation that describes intrinsic diffusivity of B in Si estimate that approximately 3 min at 900 °C are required to produce the observed 3.2 nm increase in x_j for the 900 °C iRTP anneal.²⁶ Since the entire 900 °C iRTP anneal cycle was complete on the order of 8-10 s, the increase in diffusion behavior is attributed to TED. The PTEM results in Figure 4-5 show that the 760, 800, and 900 °C iRTP anneals produce defect structures consisting of a high density of defect clusters. These images suggest that either interstitial cluster

dissolution and evolution or a non-conservative defect coarsening process of the EOR damage is responsible for the diffusion enhancement observed in the corresponding SIMS profiles for the 900 °C iRTP anneal in Figure 4-4a.

When comparing the profiles in Figure 4-4 it can be seen that the 900 °C iRTP anneal in Figure 4-4a shows less of a diffusion enhancement than that in Figure 4-4b. This difference can be explained by considering the excess interstitial profiles produced by the pre-amorphization implants and the effect of interstitial release from the EOR damage region. Since the 5 keV pre-amorphization implant produced a 12 nm amorphous layer, it can be said that the excess interstitial population is near the tail region of the B profile. These interstitials require less thermal energy to interact with the B in such a way to produce the observed diffusion enhancement. In addition, it was shown that the interstitial flux from the EOR damage is approximately an order of magnitude greater into the substrate than toward the surface for overlapping 112 keV and 30 keV Si⁺ implants to $1 \times 10^{15}/\text{cm}^2$ performed at (20±1) °C.²⁰⁵ The decrease in the interstitial flux toward the surface was attributed to the EOR damage acting as interstitial traps, which prevent a significant fraction of the interstitials from diffusing toward the substrate surface. Jones *et al.* correlated the EOR dislocation loop density with the amount of interstitial backflow toward the surface, which increased with decreasing implant temperature, presumably due to the fact that less EOR damage is available to prevent the interstitials from diffusing toward the substrate surface.²⁰⁶ It should be noted that the interstitial backflow toward the surface was shown to be equal to that into the bulk for Si implants performed at -196 °C.²⁰⁷ The difference in the interstitial flux for near room temperature pre-amorphization implants offers an explanation for observing

increased diffusion enhancement below and the lack of diffusion behavior above the original a/c interface for the 5 keV pre-amorphization implant. Although the TEM results show that no defects were observed for the damage produced by the 5 keV pre-amorphization implant, Figure 4-4b shows that the 900 °C iRTP anneal is capable of producing a peak associated with BIC formation. It is presumed that these clusters behave in a similar way to EOR damage in that they are capable of obstructing interstitial backflow toward the surface. The excess interstitial profile produced by the 48 keV pre-amorphization implant is further separated from the initial B profile, and thus more thermal energy is required for the interstitials to reach the B profile and introduce the observed diffusion enhancement during the 900 °C iRTP anneal.²⁰⁵ It should be noted that these results provide some evidence that the interstitial profile can be produced at a depth such that the 900 °C iRTP anneal may result in a profile similar to those produced by the 760 and 800 °C iRTP anneals for the 48 keV pre-amorphization implant.

It is believed that the increase in x_j for the 1000 and 1100 °C iRTP anneals is also associated with TED, as additional FLOOPS simulations and calculations based on the Arrhenius equation that describes intrinsic diffusivity of B in Si for each of these anneal temperatures estimates that approximately 2 min at 1000 °C and 20 s at 1100 °C are required to produce the observed increase in x_j for the 48 keV pre-amorphization implant.²⁶ Since both iRTP anneal cycles are complete within approximately 8-10 s, the increased diffusion behavior is associated with TED. The observation that the 1100 °C iRTP anneal only requires 20 s at 1100 °C to be described in terms of intrinsic diffusivity suggests that the diffusion enhancement is decaying. The suggestion that TED is causing the increased diffusion behavior for 1000 and 1100 °C iRTP anneals is supported by the

data in Figure 4-4b, which shows that the increase in x_j between the 900 and 1000 °C iRTP anneals is much less than that observed in Figure 4-4a. In addition, a negligible increase in x_j is observed between the 1000 and 1100 °C iRTP anneals in Figure 4-4b for the 5 keV pre-amorphization implant, whereas Figure 4-4a shows that the 1100 °C iRTP anneal is capable of increasing the x_j approximately 4.4 nm when compared to the 1000 °C iRTP anneal for the 48 keV pre-amorphization implant.

The results in Figure 4-4 are supported by the observation that the interstitial flux from EOR damage is approximately an order of magnitude greater into the substrate than it is toward the surface (for near room temperature implants). Figure 4-4a shows that the 900, 1000, and 1100 °C iRTP anneals increase the x_j 3.2, 12.4, and 16.8 nm, respectively, compared to the 760 and 800 °C iRTP anneals for the 48 keV pre-amorphization implant. These results show that the largest difference in the diffusion behavior is observed for the 1000 °C iRTP anneal. The increase in diffusion behavior for the 1000 °C iRTP anneal is most likely because a significant fraction of the interstitial flux toward the surface, which is capable of reaching the B profile during the 1000 °C iRTP anneal but is less pronounced for the 900 °C iRTP anneal. Such a significant pulse of TED was shown to occur for 40 keV Si⁺ implants to both $2 \times 10^{13}/\text{cm}^2$ and $5 \times 10^{13}/\text{cm}^2$ during the first 15 s of annealing at 700 °C.¹¹³ This pulse of TED was shown to be in excess of the enhancement caused by {311} defect dissolution, suggesting a different source of interstitials.¹¹³ Although a similar mechanism may be causing such a large diffusion enhancement for the 1000 °C iRTP anneal in Figure 5-1, it is also expected that interstitial injection from the extended defects in the EOR damage region is also contributing to the diffusion behavior during the 1000 °C iRTP anneal for the 48 keV pre-amorphization implant.

Figure 4-4b shows that the 900, 1000, and 1100 °C iRTP anneals increase the x_j 8.4, 11.6, and 12.5 nm, respectively, compared to the x_j of the 760 °C iRTP anneal for the 5 keV pre-amorphization implant. These results show that the 900 °C iRTP anneal produces the largest difference in the diffusion behavior, and that the 1000 and 1100 °C iRTP anneals produce little additional diffusion compared to the 900 °C iRTP anneal. The significant increase in the diffusion behavior for the 900 °C iRTP anneal could be associated with the large interstitial flux into the substrate, the effect of which decreases with increasing annealing temperature, presumably due to the fact that once the interstitials pass the B profile they are no longer able to enhance its diffusion behavior.

The PTEM image for the 1000 °C iRTP anneal in Figure 4-5d shows that it is sufficient for producing a defect structure consisting of {311} defects and dislocation loops. The corresponding SIMS profile in Figure 4-4a shows a diffusion enhancement with respect to the 900 °C iRTP anneal suggesting that, in addition to any interstitial pulse that may have occurred during early stages of annealing, the extended defects may have released some of the interstitials required to produce the observed diffusion enhancement. The diffusion enhancement could have been caused by a combination of {311} defect dissolution, non-conservative dislocation loop formation, and/or dislocation loop ripening and dissolution.³ In addition, the PTEM image for the 1100 °C iRTP anneal in Figure 4-5e shows that {311} defect dissolution is complete, and that the diffusion enhancement observed in the corresponding SIMS profile in Figure 4-4a can be associated with interstitial injection from {311} defect dissolution and possibly dislocation loop ripening and dissolution.³ The stability of the dislocation loops after the

1100 °C iRTP anneal is unknown, and an additional diffusion enhancement may occur during subsequent thermal processing due to dislocation loop dissolution.

Two additional experiments were performed to determine whether interstitial injection from the EOR damage or dissolution of unstable sub-microscopic clusters causes the additional diffusion observed for the 900 °C iRTP anneal in Figure 4-4a (when compared to the 760 and 800 °C iRTP anneals). The first experiment was designed to investigate the B diffusion behavior during recrystallization of an implantation-induced amorphous layer as well as during the initial stages after complete recrystallization. For this experiment, a 200 mm 3-5 Ω·cm (100) n-type CZ grown Si wafer was pre-amorphized with an 18 keV Ge⁺ implantation to $1\times10^{15}/\text{cm}^2$, and subsequently implanted with 1 keV B⁺ to $1\times10^{15}/\text{cm}^2$. The implants were carried out in the drift mode and performed at room temperature with the ion beam normal to the surface plane using an Applied Materials Leap-II system. The implant parameters were monitored to ensure they remained within predetermined limits. The pre-amorphization energy of the Ge⁺ implant was decreased to 18 keV to produce a 30 nm thick amorphous layer and place the EOR damage approximately 35 nm below the substrate surface, which is near the proximity of the B profile. This offers the ability to study the B diffusion behavior at relatively low iRTP anneal temperatures to determine the highest temperature that can be used without being subject to TED. In other words, by placing the EOR damage close to the B profile, one can determine the lowest annealing temperature at which point either interstitial injection from the EOR damage or dissolution of unstable sub-microscopic clusters begins to affect the B profile. This information can then be used to design an experiment to determine the cause of the additional diffusion behavior for the 900 °C

iRTP anneal in Figure 4-4a (when compared to the 760 and 800 °C iRTP anneals).

Figure 4-21 shows that the 18 keV pre-amorphization implant produced a continuous amorphous layer extending approximately 30 nm below the substrate surface. The wafer was then sectioned and annealed under various iRTP annealing conditions to investigate the effect of the peak annealing temperature on the B diffusion behavior during recrystallization of an implantation-induced amorphous layer as well as during the initial stages after complete recrystallization. All of the anneals were carried out in a N₂ ambient with less than 10 ppm O₂ using a ramp-up rate of 400 °C/s. Figure 4-22 shows the SIMS results for the 1 keV B⁺ implant to $1 \times 10^{15}/\text{cm}^2$ after iRTP annealing over the temperature range of 600-800 °C. The as-implanted profile has a junction abruptness and x_j of 3.7 nm/dec and 21.0 nm, respectively. As can be seen, there is no measurable difference between the as-implanted profile and the profile for the sample that was subject to a 600 °C iRTP anneal. The 650 °C iRTP anneal does, however, produce a slight amount of diffusion up to a concentration of approximately $2 \times 10^{20}/\text{cm}^3$, above which inactive B cluster formation or precipitation occurs and the B remains immobile. Increasing the iRTP anneal temperature to 700 °C increases the B diffusion behavior, however, only at higher B concentrations. This anneal produces a profile with junction abruptness and x_j of 3.4 nm/dec and 21.6 nm, respectively. This improvement in junction abruptness compared to the as-implanted profile is similar to that observed in Figure 4-10, which showed increased motion at higher B concentrations during the early stages of furnace annealing at 500 °C. The nature of this diffusion behavior is unclear. Although the SIMS results show an increase in B diffusion behavior at higher B concentration for the 700 °C iRTP anneal, it can be seen that the 750 °C iRTP anneal

produces a profile with junction abruptness and x_j of 3.8 nm/dec and 22.7 nm, which is similar in junction abruptness to that of the as-implanted profile. It can be seen that increasing the iRTP annealing temperature to 800 °C produces the same profile as that produced by the 750 °C iRTP anneal. This suggests that recrystallization of the implantation-induced amorphous layer is complete, since no additional B diffusion in α -Si is observed between the 750 and 800 °C iRTP anneals. This data is consistent with what was observed for the 760 and 800 °C iRTP anneals in Figure 4-4a, in that the profiles show the same shape and form after recrystallization of the implantation-induced amorphous layer is complete. This data supports the suggestion that there exists a temperature range over which the only diffusion that occurs is B diffusion in α -Si (i.e., no TED). This is a significant result considering TED is traditionally the mechanism that dominates B diffusion behavior during post-implant thermal processing. Additional iRTP annealing was performed to investigate the B diffusion behavior during the initial stages after complete recrystallization. Figure 4-23 shows the SIMS results for the 1 keV B^+ implant to $1 \times 10^{15}/cm^2$ after iRTP annealing over the temperature range of 780-900 °C. The as-implanted profile has a junction abruptness and x_j of 3.7 nm/dec and 21.0 nm, respectively. As can be seen, both the 780 and 800 °C iRTP anneals produce the same profile with junction abruptness and x_j of 3.8 nm/dec 22.7 nm, respectively. These profiles are similar to that in Figure 4-22 for the 750 °C iRTP anneal. However, increasing the iRTP annealing temperature to 820 °C produces a profile with junction abruptness and x_j of 4.6 nm/dec and 23.7 nm, which is approximately a 1.0 nm increase in x_j when compared to the 800 °C iRTP anneal. It can be seen that increasing the iRTP anneal temperature above 820 °C further degrades the junction abruptness and increases

the x_j . This shows that, in this case, the highest iRTP anneal temperature that can be used without being subject to TED is approximately 800 °C. This can now be used to investigate the cause of the additional diffusion observed for the 900 °C iRTP anneal in Figure 4-4a (when compared to the 760 and 800 °C iRTP anneals), which is the purpose of the following experiment.

The second additional experiment was designed to determine whether interstitial injection from the EOR damage or dissolution of unstable sub-microscopic clusters causes the additional diffusion observed for the 900 °C iRTP anneal in Figure 4-4a (when compared to the 760 and 800 °C iRTP anneals). The easiest way of separating the two effects is by studying the B diffusion behavior during post-implant thermal processing when the interstitial profile is at varying depths compared to the B profile. There are two convenient ways for separating the interstitial profile from the B profile while maintaining the same interstitial population. One way to do this is to produce a relatively thick amorphous layer by use of a high energy pre-amorphization implant. The substrate can then be sectioned and the amorphous layer can be thinned to various thicknesses by using chemical-mechanical polishing (CMP) to remove a portion of the amorphous layer from the substrate surface. After a number of samples are made, the wafer sections can be implanted with the same B^+ implant. This process will result in samples with the same interstitial profile beyond the α/c interface with varying distances between the Si interstitials and B atoms. It should be noted that, although varying the pre-amorphization energy will also result in different amorphous layer thicknesses, the different implant energies will result in different interstitial profiles beyond the α/c interface which may complicate interpretation of the results. The other way of separating the interstitial

profile from the B profile is to epitaxially deposit a δ doped B marker layer at varying depths below the substrate surface. These wafers can then be implanted with the same pre-amorphization implant, which produces the same interstitial profile beyond the α/c interface but at different distances between the δ doped B marker layers. This second method was used in this work. For this experiment, a δ doped B marker layer was deposited on three different 200 mm 3-5 $\Omega\cdot\text{cm}$ (100) n-type CZ grown Si wafers. Varying thicknesses of intrinsic Si were then deposited on each wafer to isolate the B marker layers from the interstitial profile, which was subsequently produced by an 80 keV Ge^+ implant to $1\times 10^{15}/\text{cm}^2$. The δ doped B marker layer was deposited using an ASM Epsilon 2000 single-wafer rapid thermal chemical vapor deposition (RTCVD) reactor. Before the B marker layer was deposited, each wafer was subject to an *ex-situ* HF acid etch specified to remove 2 nm of thermal oxide and an *in-situ* 1000 °C thermal bake for 5 min in a reducing H_2 ambient. The HF etch was used to remove any native oxide that may exist on the wafer and leave a mostly H terminated surface before being placed in the epitaxial reactor. The 1000 °C thermal bake was used to remove any residual contaminants that may exist after the HF etch and prevent proper epitaxial growth (e.g., hydrocarbons). The B marker layer deposition was carried out at 700 °C and a base pressure of 20 Torr and produced by mixing 50 sccm of SiH_4 and 190 sccm of B_2H_6 with 20 slm of flowing H_2 . The deposition conditions were chosen to result in a B marker layer with a peak concentration of approximately $2\times 10^{20}/\text{cm}^3$, which is similar to the concentration below which B diffusion in α -Si is observed. The intrinsic Si layers were deposited at 700 °C and a base pressure of 20 Torr and produced by mixing 50 sccm of SiH_4 with 20 slm of flowing H_2 . The intrinsic Si layer thicknesses were targeted to be

100, 200, and 300 nm for each of the three respective wafers. The 80 keV Ge⁺ pre-amorphization implant to $1 \times 10^{15}/\text{cm}^2$ produced a continuous amorphous layer extending approximately 110 nm below the substrate surface. The implant energy was chosen to place the interstitial profile approximately halfway between the substrate surface and the shallowest B marker layer, which resulted in having the same distance between the Si interstitials and B atoms as was in the original experiment based on the 48 keV pre-amorphization implant. The implant was carried out in the drift mode and performed at room temperature with the ion beam normal to the surface plane using an Applied Materials Leap-II system. The implant parameters were monitored to ensure they remained within predetermined limits. Each of the wafers were then sectioned and subject to various iRTP annealing conditions to determine whether interstitial injection from the EOR damage or dissolution of unstable sub-microscopic clusters causes the additional diffusion observed for the 900 °C iRTP anneal in Figure 4-4a (when compared to the 760 and 800 °C iRTP anneals). All of the anneals were carried out in a N₂ ambient with less than 10 ppm O₂ using a ramp-up rate of 400 °C/s. Figure 4-24 shows the SIMS results for the shallowest B marker layer (approximately 175 nm below the substrate surface) both before and after iRTP annealing at 800, 900, and 1000 °C. It should be noted that this marker layer is approximately the same distance away from the interstitial profile produced by the 80 keV Ge⁺ pre-amorphization implant to $1 \times 10^{15}/\text{cm}^2$ as the 3 keV BF₂⁺ implant to $6 \times 10^{14}/\text{cm}^2$ was away from the interstitial profile produced by the 48 keV Ge⁺ pre-amorphization implant to $5 \times 10^{14}/\text{cm}^2$. As can be seen, the 800 °C iRTP anneal results in a measurable amount of diffusion at lower B concentrations (i.e., $1 \times 10^{17}/\text{cm}^3$), while the higher concentration region remains immobile. Increasing

the iRTP annealing temperature increases the B diffusion behavior at lower B concentrations whereas the B remains immobile at higher concentrations. Both FLOOPS simulations and calculations based on an Arrhenius equation that describes intrinsic diffusivity of B in Si estimate that approximately 18 hr at 800 °C are required to produce the observed 11 nm increase in x_j (at a concentration of $1\times10^{17}/\text{cm}^3$) for the 800 °C iRTP anneal.²⁶ Since the amount of motion that occurs during the iRTP anneals is much greater than that expected under equilibrium conditions, it can be said that the portion of the marker layer that undergoes diffusion is due to TED. The immobile peak of the marker layer is presumably due to BIC formation which occurs because the high local concentration of Si interstitials and B atoms and is consistent with data from other experiments.^{9,18} It should be noted that the immobile peak of the B marker layer occurs for B concentrations above approximately $1\times10^{19}/\text{cm}^3$, which are somewhat higher than those observed in other experiments.¹⁸ Although the 800 °C iRTP anneal was insufficient to result in any diffusion due to TED in Figure 4-4a, the observation of TED during the 800 °C iRTP anneal for the shallowest B marker layer may very well be due to the fact that the interstitial flux from the EOR damage is approximately an order of magnitude greater into the substrate than toward the surface.²⁰⁵ The decrease in the interstitial flux toward the surface was attributed to the EOR damage acting as interstitial traps, which prevent a significant fraction of the interstitials from diffusing toward the substrate surface. Figure 4-25 shows the SIMS results for the B marker layer approximately 275 nm below the substrate surface both before and after iRTP annealing at 800, 900, and 1000 °C. The most significant result of this data is that the B marker layer undergoes no measurable diffusion during the 800 °C iRTP anneal. This shows that

the interstitials responsible for producing the diffusion enhancement observed during the 800 °C iRTP anneal in Figure 4-25 are not available to produce a similar enhancement for the second deepest B marker layer. This provides sound evidence that interstitial injection from the EOR damage produced by the 80 keV pre-amorphization implant is the cause for the diffusion enhancement observed for the 800 °C iRTP anneal in Figure 4-24 (as opposed to the dissolution of unstable sub-microscopic interstitial clusters). It can therefore be said that a similar interstitial injection mechanism from the EOR damage is the most likely cause for the additional diffusion observed for the 900 °C iRTP anneal in Figure 4-4a (when compared to the 760 and 800 °C iRTP anneals). This thought is supported by Figure 4-26, which shows the SIMS results for the deepest B marker layer (located approximately 360 nm below the substrate surface) both before and after iRTP annealing at 800, 900, and 1000 °C. Similar to the data in Figure 4-25, these results show that the 800 °C iRTP anneal is insufficient to produce any measurable diffusion; however, the 900 and 1000 °C iRTP anneals increase the x_j (at a concentration of $1 \times 10^{17}/\text{cm}^3$) approximately 12 and 53 nm, respectively. Both FLOOPS simulations and calculations based on an Arrhenius equation that describes intrinsic diffusivity of B in Si estimate that approximately 40 min at 900 and 1000 °C are required to produce the observed increase in x_j (at a concentration of $1 \times 10^{17}/\text{cm}^3$) for the 900 and 1000 °C iRTP anneals.²⁶ This increase in the B diffusion behavior is much greater than what would be expected under equilibrium conditions, presumably because interstitial injection from the EOR damage produced by the 80 keV pre-amorphization implant. This shows that interstitials injected from the EOR damage region are capable of diffusing up to at least 200 nm during a 900 °C iRTP anneal, which is the approximate distance between the

interstitial profile produced by the 80 keV pre-amorphization implant and the B atoms in the deepest B marker layer. This is consistent with other data that showed interstitial diffusion over approximately $0.6 \mu\text{m}$ within the first 15 s of annealing at 700°C .¹¹³ Much lower values for interstitial diffusivity were obtained for similar experiments using material grown by molecular beam epitaxy (MBE), presumably due to the relatively high concentration of C trapping centers in the material which reduce interstitial diffusion.⁹⁸ It was noted earlier that, if the additional diffusion observed for the 900°C iRTP anneal in Figure 4-4a was due to interstitial injection from the EOR damage, it may be possible to produce an interstitial profile at a depth such that the 900°C iRTP anneal may result in a profile similar to those produced by the 760 and 800°C iRTP anneals for the 48 keV pre-amorphization implant in Figure 4-4a; however, it can now be said that, although interstitial injection from the EOR damage is the most likely cause for the additional diffusion observed for the 900°C iRTP anneal in Figure 4-4a (when compared to the 760 and 800°C iRTP anneals), the Si interstitials are capable of diffusing over significant distances during annealing. This may make placing the interstitial profile at a depth such that the 900°C iRTP anneal may result in a profile similar to those produced by the 760 and 800°C iRTP anneals for the 48 keV pre-amorphization implant in Figure 4-4a difficult.

Figure 4-4 showed that the 1100°C iRTP anneal has improved junction abruptness compared to the 1000°C iRTP anneal. The junction abruptness for the 1000 and 1100°C iRTP anneals are 10.1 and 8.7 nm/dec and 15.0 and 11.0 nm/dec for the 48 keV and 5 keV pre-amorphization implants, respectively. This improvement in junction abruptness may be due to either or a combination of CED and/or field enhanced

diffusion. Concentration enhanced diffusion is the thermodynamic consideration responsible for reducing any chemical potential differences within the system.⁹² This causes the diffusivity to vary with concentration, with the higher concentration regions diffusing faster in order to decrease the concentration gradient of the as-implanted profile.² A more noticeable example of CED is shown in Figure 4-27, which shows the SIMS results for three different B implant conditions both before and after a 1050 °C refined spike anneal. The refined spike refers to an optimized thermal profile that decreases the amount of time the wafer spends within 50 °C of the peak temperature in order to reduce the amount of diffusion that occurs during the thermal process. As can be seen, the junction abruptness after the 1050 °C refined spike anneal is approximately 19.5, 14.4 and 9.6 nm/dec for the 2×10^{14} , 5×10^{14} , and $1 \times 10^{15}/\text{cm}^2$ B⁺ implants, respectively. This shows that junction abruptness can be significantly affected by the amount of CED that occurs during post-implant thermal processing. Field enhanced diffusion is associated with higher annealing temperatures due to the fact that B activation must take place in order for it to occupy substitutional sites and become negatively charged. This negative charge creates the internal electric field, which enhances dopant diffusion at high concentrations. The field arises from the higher mobility of the holes compared to the B atoms. When the holes diffuse ahead of the B profile an electric field is created with the negatively charged B atoms.² This field is capable of increasing the B diffusion behavior into the bulk of the Si substrate.

Figure 4-6a shows that the 760 and 800 °C intermediate temperatures results in similar profiles after the 1200 °C fRTP anneal, and that the 900 °C intermediate temperature results in a degraded junction abruptness and increased x_j because the

diffusion that occurred during the intermediate temperature for the 48 keV pre-amorphization implant. Additional FLOOPS simulations and calculations based on the Arrhenius equation that describes intrinsic diffusivity of B in Si requires approximately 3 and 13 ms at 1200 °C to produce the observed 0.6 and 1.2 nm increase in x_j for both the 760 and 800 °C and 900 °C intermediate temperatures, respectively.²⁶ Since the T-t profiles for the fRTP anneals are unavailable, it is unclear whether the 1.2 nm increase in x_j for the 900 °C intermediate temperature is due to TED. Although these time scales are similar to those used during the fRTP anneal, it is not known whether interstitial recombination within the bulk or a lack of thermal energy prevented significant diffusion during the anneal. It is reasonable to assume that the time duration of the fRTP anneal is too short to allow enough interstitials to diffuse toward the surface to cause a significant diffusion enhancement.² Similar comments can be made for the diffusion behavior observed for the 1350 °C fRTP anneal presented in Figure 4-8a for the 48 keV pre-amorphization implant. It should be noted that the 760 and 800 °C intermediate temperatures did not result in similar profiles after the 1350 °C fRTP anneal; the 760 °C intermediate temperature resulted in a slightly shallower profile. In addition, the diffusion behavior after the 1350 °C fRTP anneal is greater for the 800 °C intermediate temperature than that observed for the 900 °C intermediate temperature. Since an increase in interstitial interaction with the B would effect the 900 °C intermediate temperature profile more than the 800 °C intermediate temperature, the increase in x_j for the 800 °C intermediate temperature is expected to occur because the fact that the system measured a peak temperature of 1372 °C, as opposed to the desired 1350 °C, and that this increase in temperature was sufficient for producing the increase in

diffusion behavior. Figure 4-6b shows a diffusion enhancement for the 760 and 800 °C intermediate temperatures after the 1200 °C fRTP anneal for the 5 keV pre-amorphization implant when compared to the 48 keV pre-amorphization implant. In addition, the 800 °C intermediate temperature shows increased diffusion behavior compared to the 760 °C intermediate temperature. These results are consistent with the suggestion that the interstitial flux into the substrate is significantly greater than that toward the substrate surface, and that increasing the intermediate temperature results in an increase in the diffusion enhancement. It should be noted that the difference in the profiles may be exaggerated because the fact the system measured a peak temperature of 1218 °C for the 800 °C intermediate temperature. The fact that the 900 °C intermediate temperature resulted in no additional diffusion enhancement after the 1200 °C fRTP anneal suggests that the interstitial flux into the substrate is complete during the 900 °C iRTP anneal. This is supported by the SIMS results in Figure 4-8b, which show that the 1350 °C fRTP anneal resulted in similar profiles independent of the intermediate anneal temperature for the 5 keV pre-amorphization implant.

The TEM results of the EOR damage produced by the 48 keV pre-amorphization implant after the 1200 °C fRTP anneal in Figure 4-7 show that, depending on the intermediate temperature, the defect clusters produced by the iRTP anneals evolve into defect structures consisting of larger defect clusters, {311} defects, and/or dislocation loops. Although the final defect structure depends on the intermediate temperature, the defects have not evolved into a stable morphology (e.g., dislocation loops), and may further evolve during subsequent thermal processing, releasing interstitials that would presumably result in a diffusion enhancement. It can be seen in Figure 4-9c that the

900 °C intermediate temperature with the 1350 °C fRTP anneal produces a defect structure that consists of large dislocation loops. This image shows a defect morphology that more closely resembles a stable defect structure; one that may result in little enhanced diffusion during subsequent thermal processing and would be expected to result in the least amount of junction leakage due to having the lowest dislocation line length per unit area (when compared to all other samples within this study).¹¹⁸ The TEM images for the 1350 °C fRTP anneal clearly show that although the images for the corresponding iRTP anneals in Figure 4-5 appear to be similar in morphology, they differ in their evolution so as to produce a more stable defect structure with increasing intermediate anneal temperature for a given fRTP anneal temperature. These results show that the intermediate temperature plays a significant role not only in terms of the diffusion characteristics, but also the interstitial evolution as it relates to the final defect structure after a fRTP anneal.

Earlier, it was presumed that the plateau concentration defines the concentration level above which inactive B cluster formation or precipitation occurs.⁹ This can be tested by comparing the measured R_s values to those obtained through a theoretical calculation that compensates for the inactive fraction by truncating the concentrations above the plateau concentration. The measured and calculated R_s values for the 48 keV pre-amorphization implant, as well as the measured R_s values for the 5 keV pre-amorphization implant are shown in Figure 4-28. The calculated data for the 5 keV pre-amorphization implant were not included due to the inability in accurately determining the appropriate plateau concentration. The calculated values were

determined by use of the following empirical mobility equation of Caughey and Thomas for Si²⁰⁸

$$\mu(x) = \frac{\mu_a}{\left\{1 + \left[\frac{n(x)}{n_r}\right]^\alpha\right\}} + \mu_b , \quad (4.5)$$

where $\mu(x)$ and $n(x)$ are the mobility and carrier concentration as a function of depth, respectively, and μ_a , μ_b , n_r , and α are constants which depend on the carriers of interest.

The resulting $\mu(x)$ values were converted into R_s by

$$R_s = \frac{1}{\sum_{i=1}^{\infty} [\Delta x_{i-1} \mu(x_i) n(x_i) q]} , \quad (4.6)$$

where Δx is the difference in depth between two carrier concentration values obtained from the SIMS profile, and q is the charge of a free electron. As can be seen in Figure 4-28, the 48 keV pre-amorphization implant resulted in lower R_s values compared to the 5 keV pre-amorphization implant for each annealing condition used in this study. Both implant conditions show that, although it is presumed that most of the activation occurs due to solute trapping during SPER of the implantation-induced amorphous layer, the empirical data suggests that the f RTP anneal significantly improves the R_s .¹⁷⁹ It should be noted that the R_s is relatively independent of both the intermediate and peak f RTP temperature for the 48 keV pre-amorphization implant. The 5 keV pre-amorphization implant shows a larger dependence on the peak f RTP temperature in that the R_s decreases as the f RTP temperature increases. The disagreement with the calculated results for the 48 keV pre-amorphization implant shows that the active B concentrations are greater than those used in the calculation. Further work is required to

better understand why the calculated results do not predict the improvement in the R_s after a fRTP anneal.

Conclusions

Novel high-power arc lamp design has enabled UHT annealing as an alternative to conventional RTP for B ultra-shallow junction formation. This technique heats the wafer to an intermediate temperature (e.g., 800 °C) before discharging a capacitor bank into flash lamps, which anneals the device side of the wafer at a relatively high temperature (e.g., 1200 °C) for a few milliseconds. Here, the Ge^+ pre-amorphization implant energy was varied to investigate the effect of the 1.0 eV activation energy associated with the defect dissolution kinetics of low energy Ge implantation. Two 200 mm (100) n-type CZ grown Si wafers were pre-amorphized with either 48 keV or 5 keV Ge^+ implantation to $5 \times 10^{14}/\text{cm}^2$, and subsequently implanted with 3 keV BF_2^+ molecular ions to $6 \times 10^{14}/\text{cm}^2$. The wafers were sectioned and annealed under various conditions to investigate the effects of the UHT annealing technique on the resulting junction characteristics. The SIMS results show B diffusion in α -Si during SPER of the implantation-induced amorphous layer produced by the 48 keV pre-amorphization implant. No B diffusion in α -Si was observed for the sample that received the 5 keV pre-amorphization implant, presumably because the high local concentration of Si interstitials and B atoms, which participate in immobile BIC formation. The activation energy for B diffusion in α -Si was found to be 2.2 ± 0.26 eV. Although it was shown that both interstitial and vacancy point-defects exist in α -Si, these point-defects do not have a significant effect on the diffusion behavior of P or Sb in α -Si. These differences in diffusion behavior during recrystallization of an implantation-induced amorphous layer makes defining interstitial

and vacancy point-defect mediated diffusion mechanisms in α -Si difficult. Additional SIMS results show a temperature range in which the diffusion characteristics produced by the iRTP anneal result in equivalent dopant profiles, and that the junction abruptness and x_j are improved for the 48 keV pre-amorphization implant. It can be said that interstitial injection from the EOR damage is the most likely cause for the additional diffusion observed for iRTP anneal temperatures above this range. It was shown that the 1100 °C iRTP anneal produces a profile with junction abruptness of 8.7 nm/dec for the 48 keV pre-amorphization implant, which is comparable to that produced by a conventional RTP anneal. This can be compared to the 760 and 900 °C iRTP anneals, which produced profiles with junction abruptness of 3.2 and 5.5 nm/dec, respectively. The junction abruptness of the 760 and 900 °C intermediate temperatures change to 3.4 and 4.4 nm/dec and 5.9 and 5.8 nm/dec after a 1200 and 1350 °C fRTP anneal, respectively. These results show that the UHT annealing technique is capable of producing junctions with the profile characteristics significantly improved over conventional RTP. The increased diffusion enhancement observed for the 5 keV pre-amorphization implant is presumed to be due to an increased interstitial flux into the substrate due to the BIC's obstructing interstitial backflow toward the surface. The TEM results show that the EOR defect structure produced by the 48 keV pre-amorphization implant is dependent on both the intermediate and fRTP anneal temperatures, and that no observable defects form for the 5 keV pre-amorphization implant. This latter result is consistent with BIC formation in that they cannot be directly observed by TEM because of their small size (e.g., 3 to 8 atom clusters). Although the defect structures that result after the 760, 800, and 900 °C iRTP anneals for the wafer that received the 48 keV pre-amorphization implant are

similar in morphology, they result in significantly different defect structures after a 1350 °C fRTP anneal. These results show that the intermediate temperature plays a significant role not only in terms of the diffusion characteristics, but also the interstitial evolution as it relates to the final defect structure after a fRTP anneal. Four-point probe measurements show decreased R_s with the introduction of the fRTP anneal when compared to the corresponding iRTP anneal temperature, which is not reflected though the empirical mobility equation used to calculate the theoretical R_s for each processing condition; this needs to be understood further. This UHT annealing technique is capable of producing junctions with improved characteristics over those obtained through RTP due to the ability of the iRTP anneal to maintain highly abrupt junctions, and the time duration of the fRTP anneal, which limits dopant diffusion.

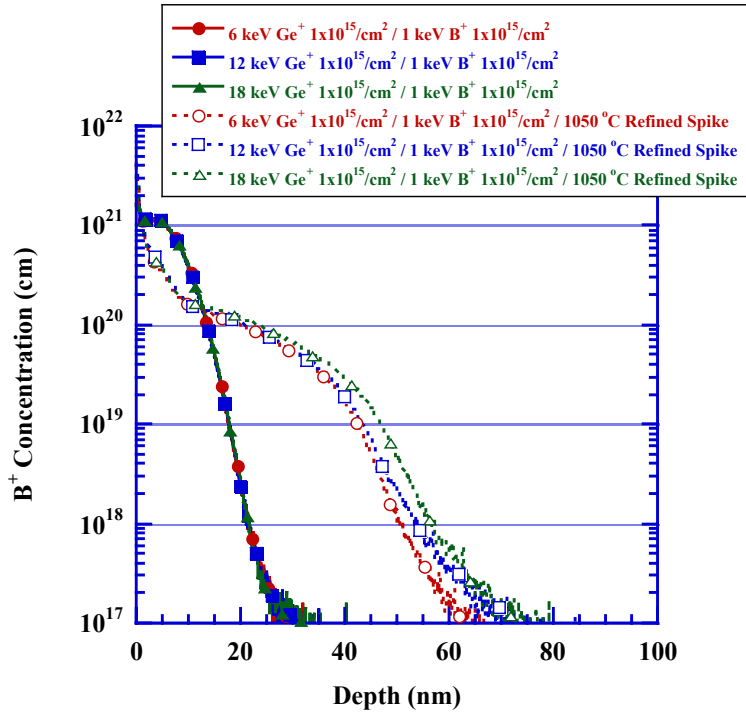


Figure 4-1 Concentration profiles for a 1 keV B⁺ implant to $1 \times 10^{15}/\text{cm}^2$ before and after a 1050 °C refined spike anneal for a substrate pre-amorphized with varying energies of Ge⁺ each to $1 \times 10^{15}/\text{cm}^2$. Note that decreasing the Ge⁺ pre-amorphization implant energy from 18 to 6 keV results in improved junction abruptness and shallower x_j . The symbols are for identifications purposes only.

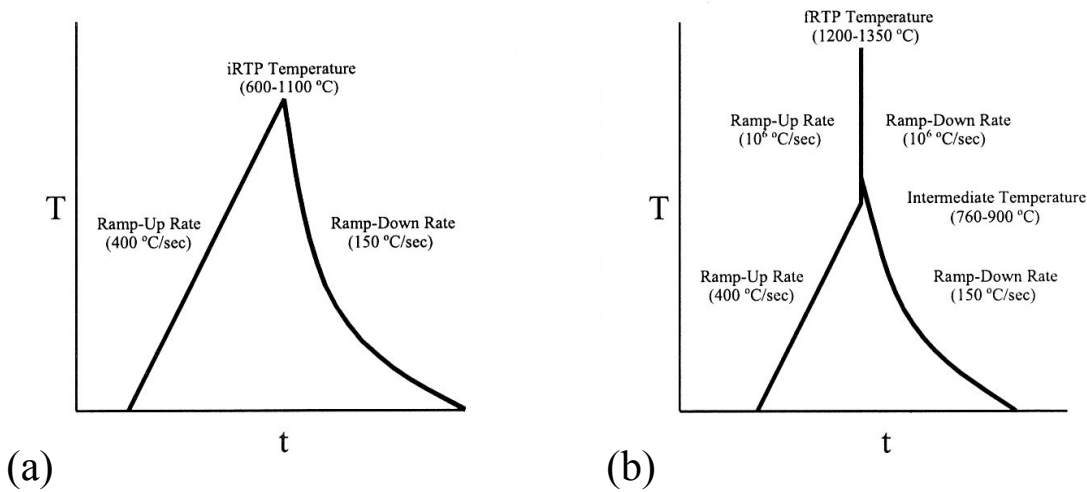


Figure 4-2 Representative T-t profiles of the (a) iRTP and (b) fRTP anneal processes and the UHT annealing conditions used throughout this work.

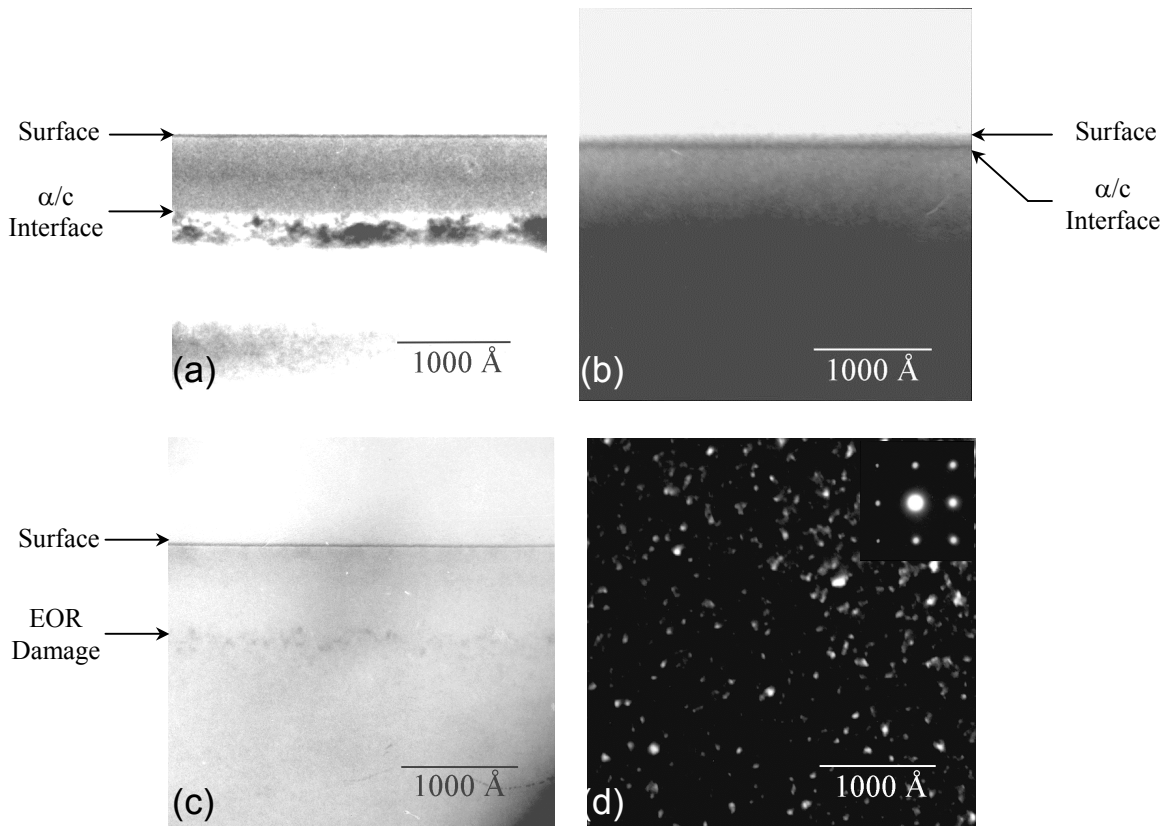


Figure 4-3 Bright field XTEM images showing the (a) continuous amorphous layer produced with the 48 keV and (b) 5 keV Ge^+ pre-amorphization implants to $5 \times 10^{14}/\text{cm}^2$, (c) 48 keV Ge^+ pre-amorphization implant to $5 \times 10^{14}/\text{cm}^2$ after a 585 °C furnace anneal for 45 min, and (d) PTEM image of the 48 keV Ge^+ pre-amorphization implant to $5 \times 10^{14}/\text{cm}^2$ after a 585 °C furnace anneal for 45 min under a WBDF \mathbf{g}_{220} two-beam imaging condition with the corresponding diffraction pattern in the image inset.

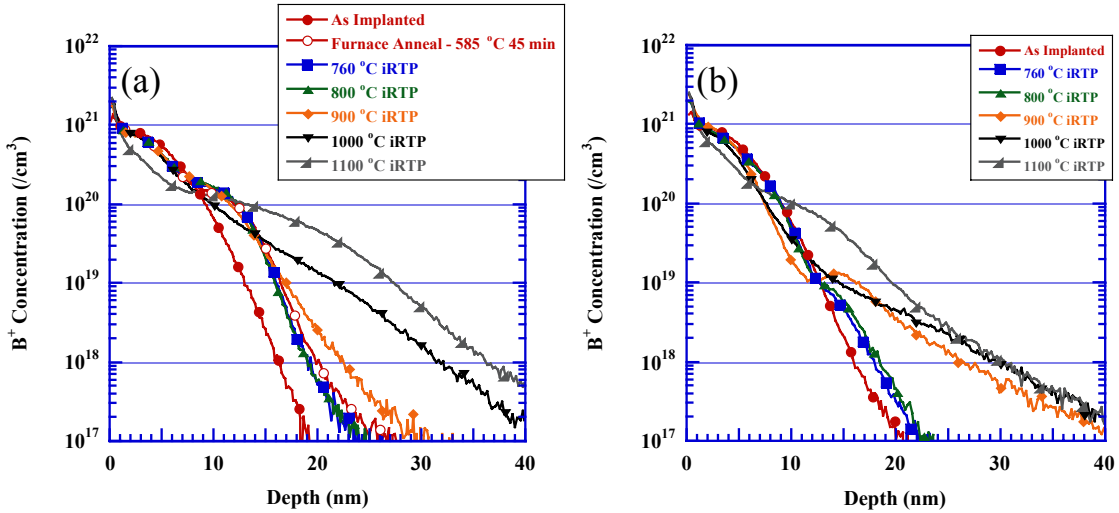


Figure 4-4 Concentration profiles showing the B^+ concentration as a function of depth for the 3 keV BF_2^+ implant to $6 \times 10^{14}/cm^2$ after each iRTP anneal temperature used in this study for the (a) 48 keV and (b) 5 keV Ge^+ pre-amorphization implants to $5 \times 10^{14}/cm^2$. The symbols are for identifications purposes only.

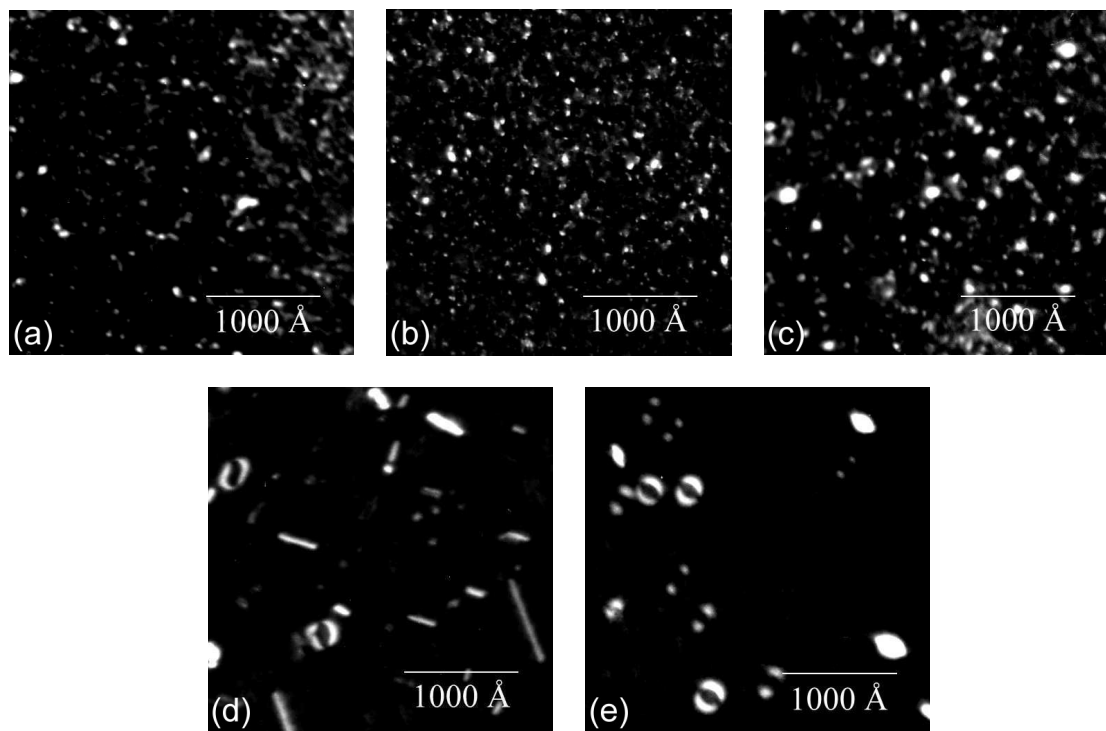


Figure 4-5 Plan-view TEM images of the damage produced by the 48 keV Ge^+ pre-amorphization implant to $5 \times 10^{14}/\text{cm}^2$ under a WBDF \mathbf{g}_{220} two-beam imaging condition after a (a) 760 (b) 800 (c) 900 (d) 1000 and (e) 1100 °C iRTP anneal.

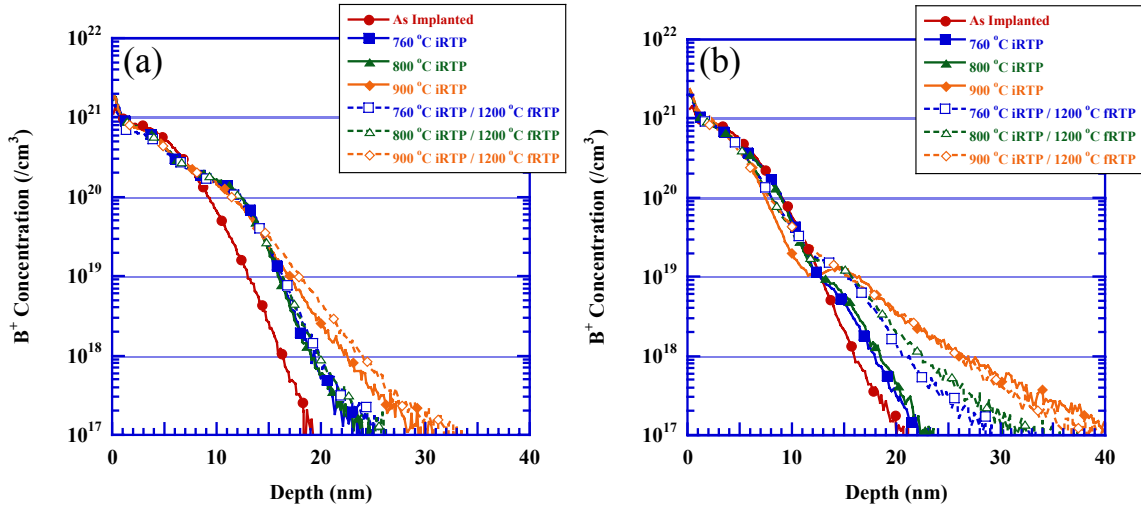


Figure 4-6 Concentration profiles showing the B^+ concentration as a function of depth for the 3 keV BF_2^+ implant to $6 \times 10^{14}/\text{cm}^2$ before and after the 1200 °C fRTP for the (a) 48 keV and (b) 5 keV Ge^+ pre-amorphization implants to $5 \times 10^{14}/\text{cm}^2$. The symbols are for identifications purposes only.

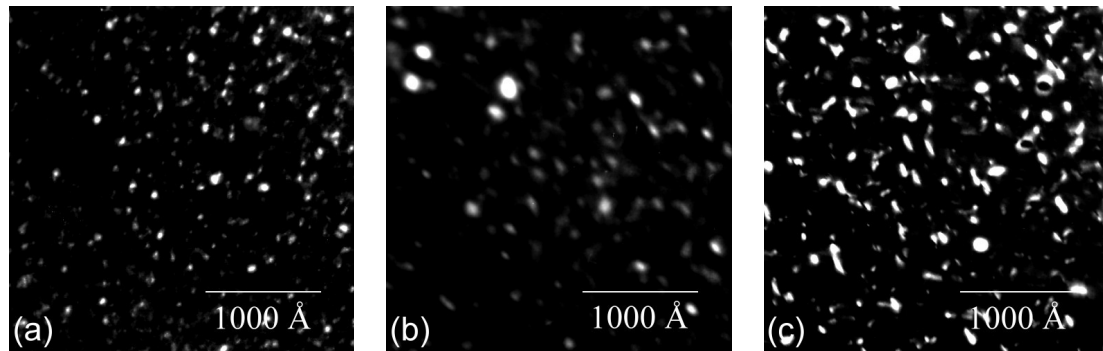


Figure 4-7 Plan-view TEM images of the damage produced by the 48 keV Ge^+ pre-amorphization implant to $5 \times 10^{14}/\text{cm}^2$ under a WBDF \mathbf{g}_{220} two-beam imaging condition for the 1200 °C fRTP using an (a) 760 (b) 800 and (c) 900 °C intermediate temperature.

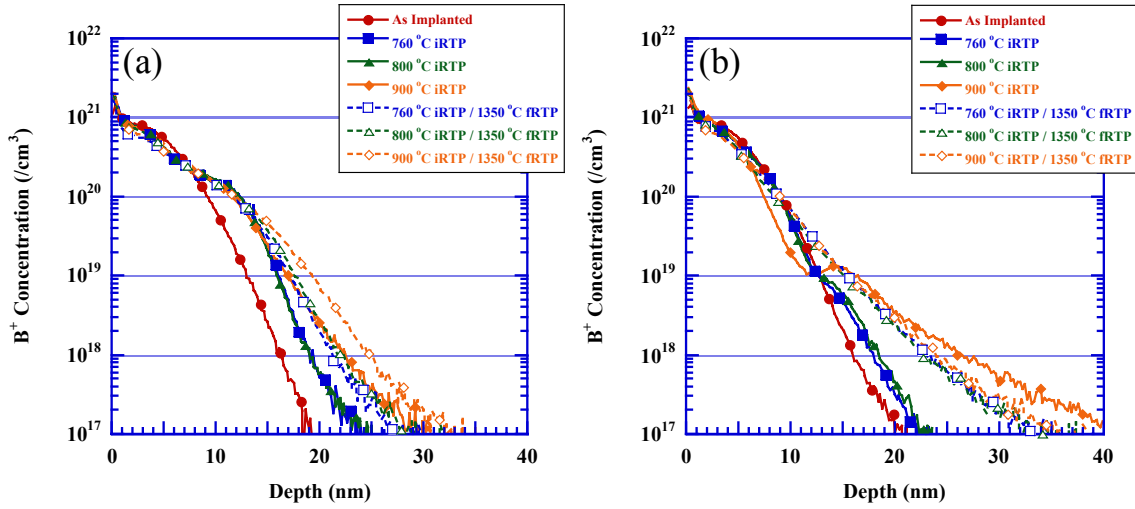


Figure 4-8 Concentration profiles showing the B^+ concentration as a function of depth for the $3 \text{ keV } BF_2^+$ implant to $6 \times 10^{14}/\text{cm}^2$ before and after the 1350°C fRTP for the (a) 48 keV and (b) 5 keV Ge^+ pre-amorphization implants to $5 \times 10^{14}/\text{cm}^2$. The symbols are for identifications purposes only.

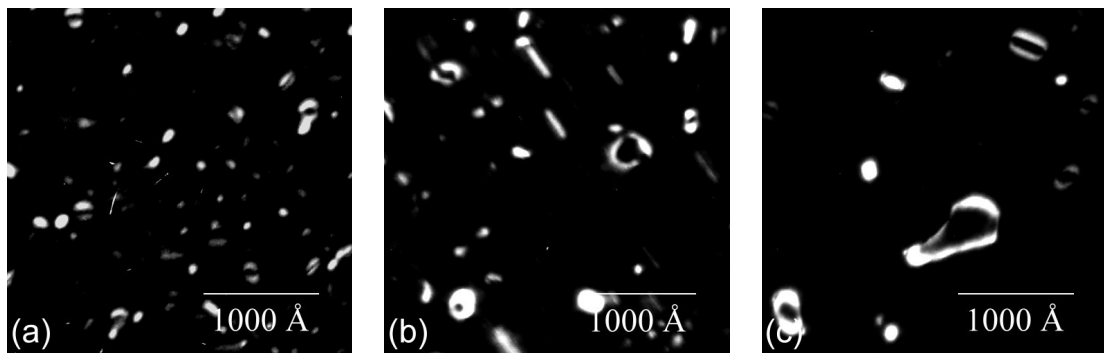


Figure 4-9 Plan-view TEM images of the damage produced by the 48 keV Ge^+ pre-amorphization implant to $5 \times 10^{14}/\text{cm}^2$ under a WBDF \mathbf{g}_{220} two-beam imaging condition for the 1350 °C fRTP using a (a) 760 (b) 800 and (c) 900 °C intermediate temperature.

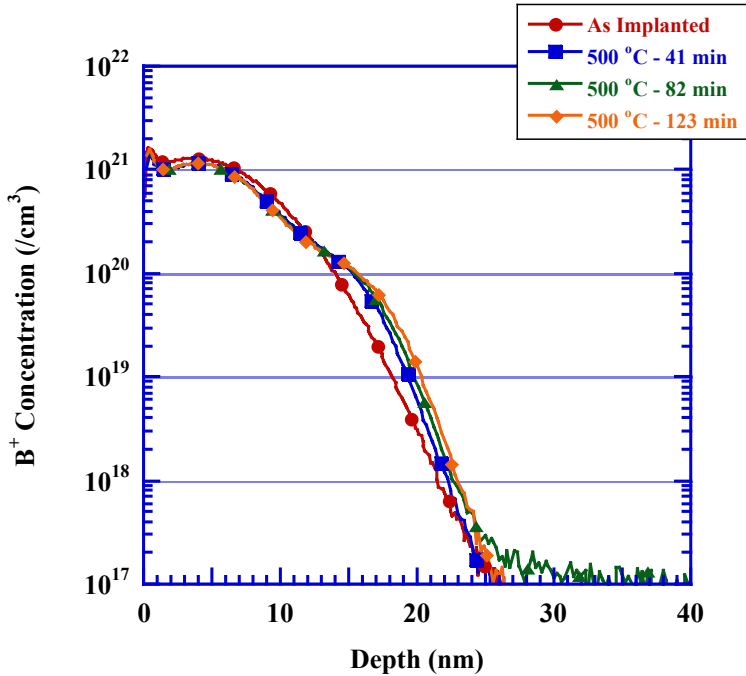


Figure 4-10 Concentration profiles showing the B⁺ concentration as a function of depth for the 1 keV B⁺ implant to $1 \times 10^{15}/\text{cm}^2$ before and after furnace annealing at 500 °C at various times for a substrate pre-amorphized with an 80 keV Ge⁺ implant to $1 \times 10^{15}/\text{cm}^2$. The symbols are for identifications purposes only.

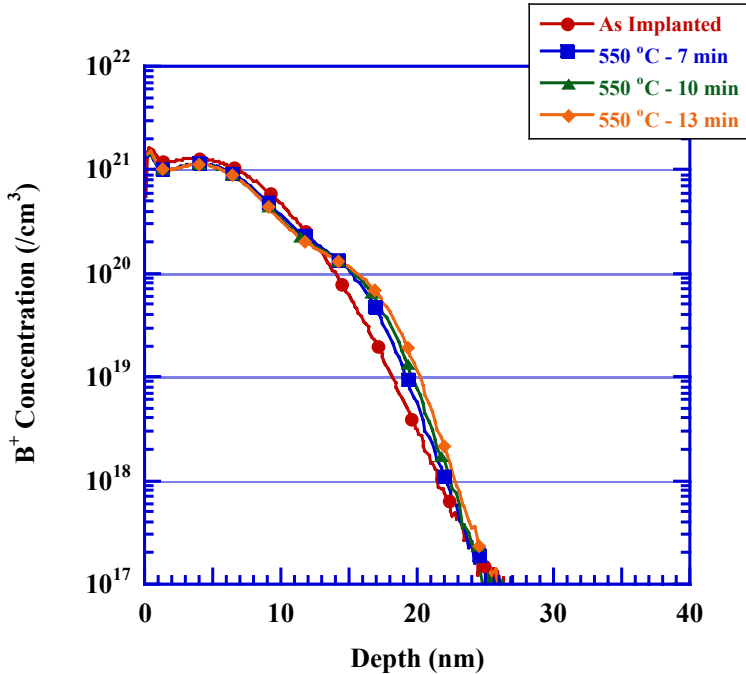


Figure 4-11 Concentration profiles showing the B^+ concentration as a function of depth for the 1 keV B^+ implant to $1 \times 10^{15}/\text{cm}^2$ before and after furnace annealing at $550\text{ }^\circ\text{C}$ at various times for a substrate pre-amorphized with an 80 keV Ge^+ implant to $1 \times 10^{15}/\text{cm}^2$. The symbols are for identifications purposes only.

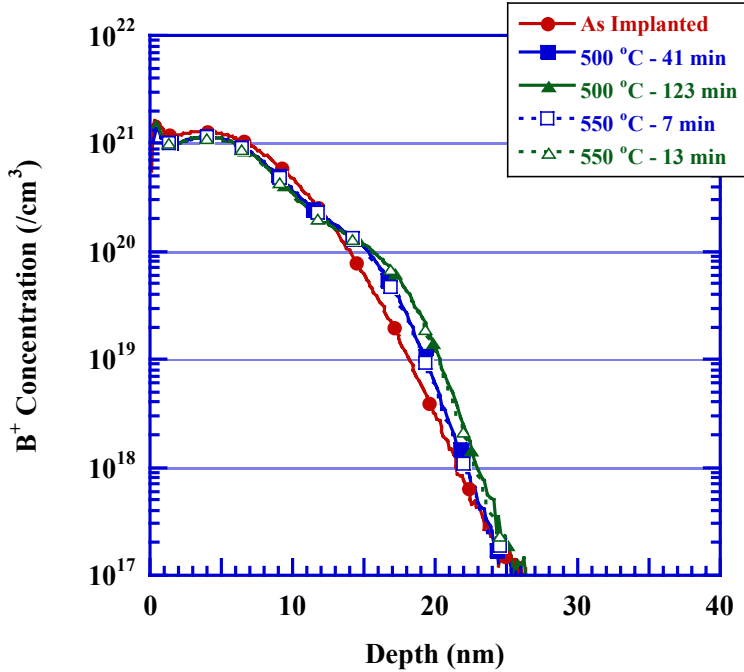


Figure 4-12 Concentration profiles showing the B^+ concentration as a function of depth for the 1 keV B^+ implant to $1 \times 10^{15}/\text{cm}^2$ before and after furnace annealing at either 500 or 550 °C at various times for a substrate pre-amorphized with an 80 keV Ge^+ implant to $1 \times 10^{15}/\text{cm}^2$. The symbols are for identifications purposes only.

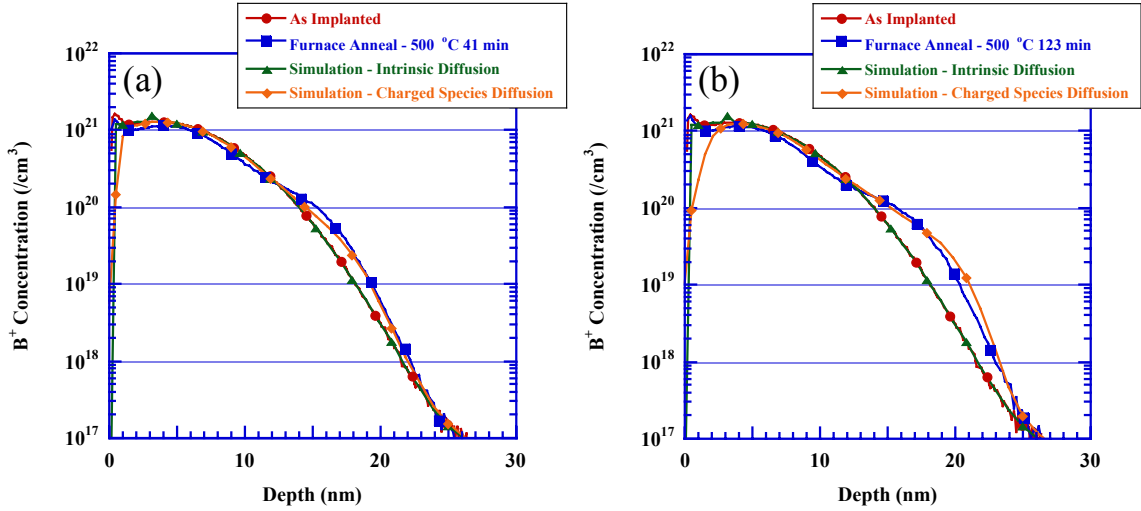


Figure 4-13 Concentration profiles showing the B^+ concentration as a function of depth for the 1 keV B^+ implant to $1 \times 10^{15}/cm^2$ before and after furnace annealing at $500\text{ }^\circ\text{C}$ for (a) 41 and (b) 123 min for a substrate pre-amorphized with an 80 keV Ge^+ implant to $1 \times 10^{15}/cm^2$. The symbols are for identifications purposes only. Note that the FLOOPS simulations closely match the SIMS data only when charged species diffusion is taken into account.

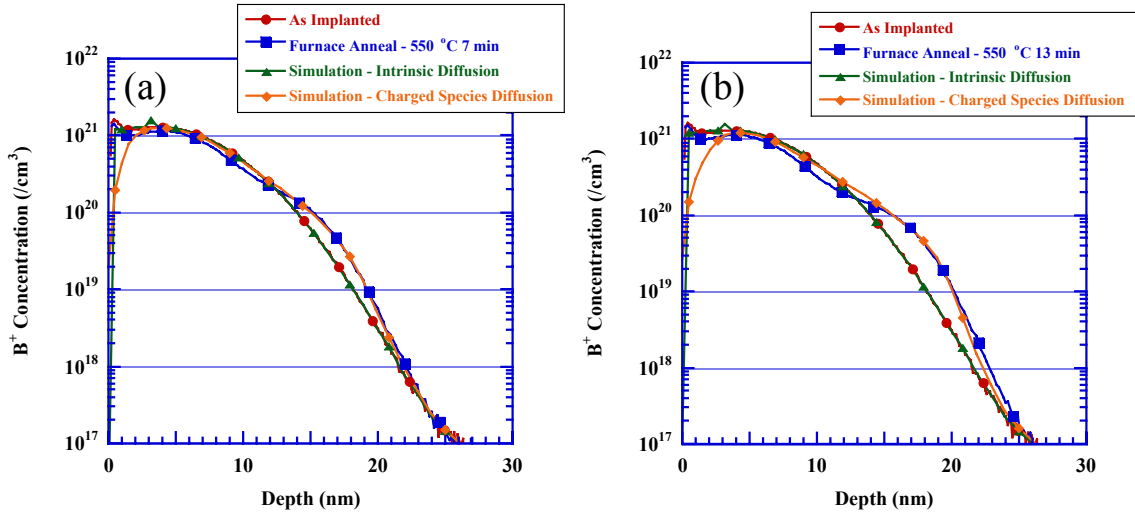


Figure 4-14 Concentration profiles showing the B^+ concentration as a function of depth for the 1 keV B^+ implant to $1 \times 10^{15}/\text{cm}^2$ before and after furnace annealing at $550\text{ }^\circ\text{C}$ for (a) 7 and (b) 13 min for a substrate pre-amorphized with an 80 keV Ge^+ implant to $1 \times 10^{15}/\text{cm}^2$. The symbols are for identifications purposes only. Note that the FLOOPS simulations closely match the SIMS data only when charged species diffusion is taken into account.

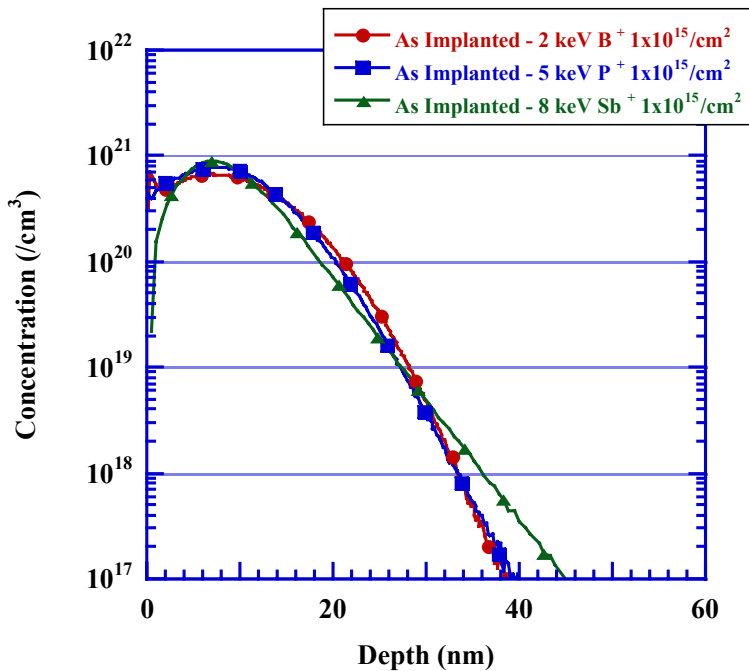


Figure 4-15 Concentration profiles showing the as-implanted dopant concentration as a function of depth for the 2 keV B⁺, 5 keV P⁺, and 8 keV Sb⁺ implants each to $1 \times 10^{15}/\text{cm}^2$ into a Si substrate pre-amorphized with a 80 keV Ge⁺ implant to $1 \times 10^{15}/\text{cm}^2$. The symbols are for identifications purposes only.

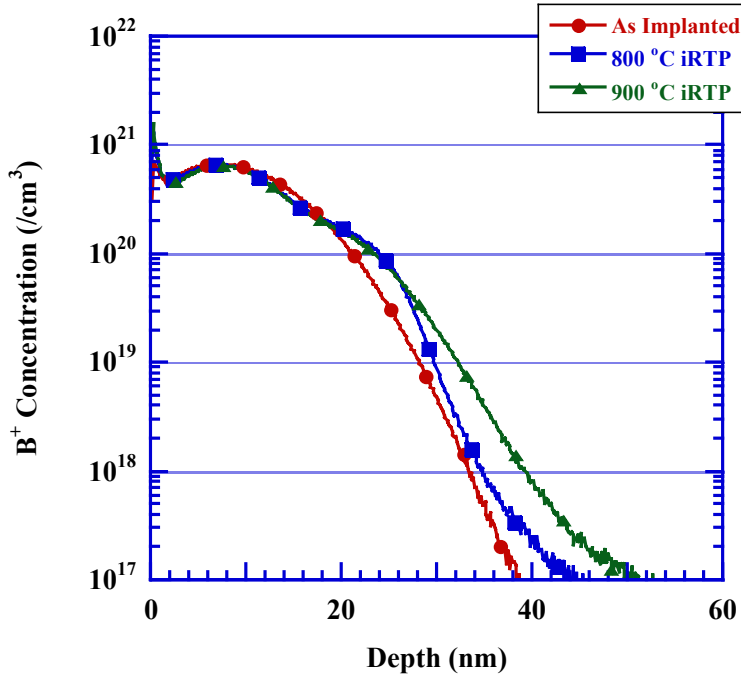


Figure 4-16 Concentration profiles showing the B^+ concentration as a function of depth for the 2 keV B^+ implant to $1 \times 10^{15}/\text{cm}^2$ before and after iRTP annealing at 800 and $900\text{ }^\circ\text{C}$ for a substrate pre-amorphized with an 80 keV Ge^+ implant to $1 \times 10^{15}/\text{cm}^2$. The symbols are for identifications purposes only.

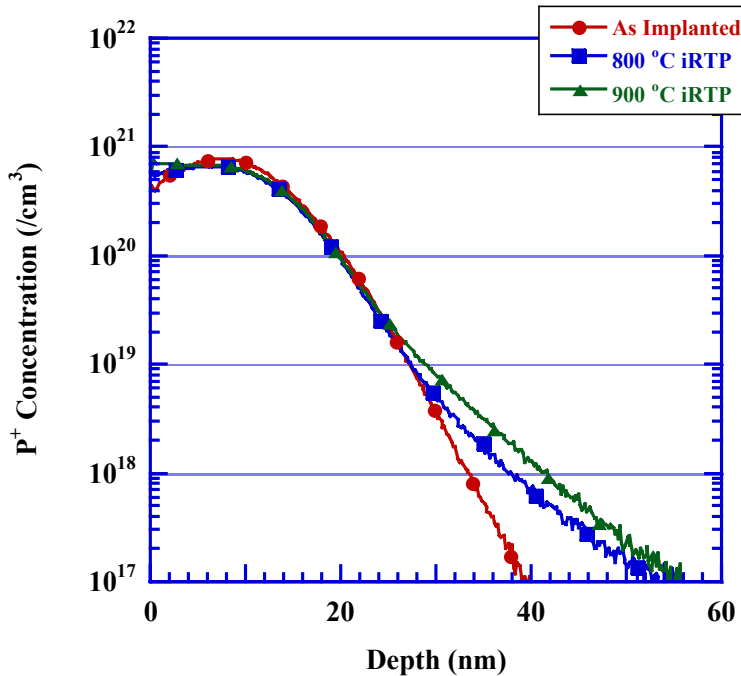


Figure 4-17 Concentration profiles showing the P^+ concentration as a function of depth for the 5 keV P^+ implant to $1 \times 10^{15}/\text{cm}^2$ before and after iRTP annealing at 800 and 900 $^\circ\text{C}$ for a substrate pre-amorphized with an 80 keV Ge^+ implant to $1 \times 10^{15}/\text{cm}^2$. The symbols are for identifications purposes only.

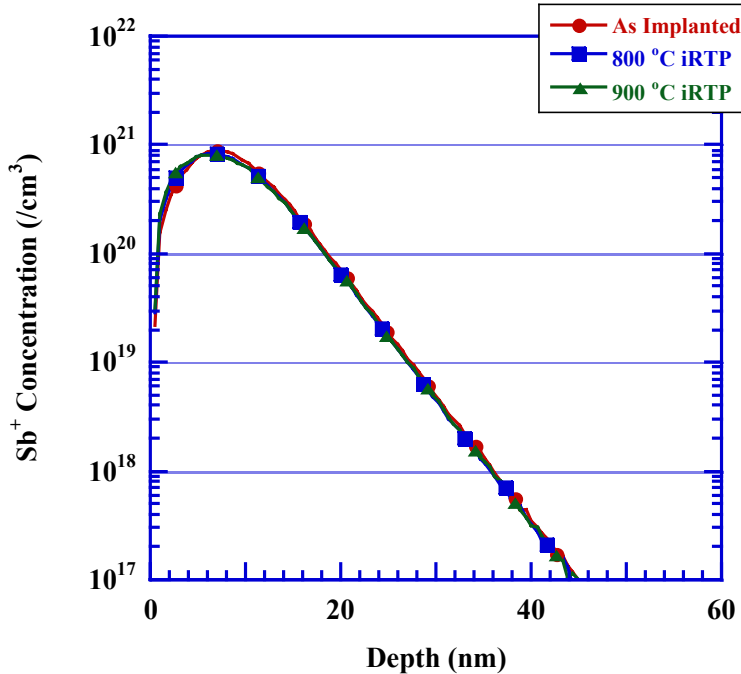


Figure 4-18 Concentration profiles showing the Sb^+ concentration as a function of depth for the 8 keV Sb^+ implant to $1 \times 10^{15}/\text{cm}^2$ before and after iRTP annealing at 800 and $900\text{ }^\circ\text{C}$ for a substrate pre-amorphized with a 80 keV Ge^+ implant to $1 \times 10^{15}/\text{cm}^2$. The symbols are for identifications purposes only.

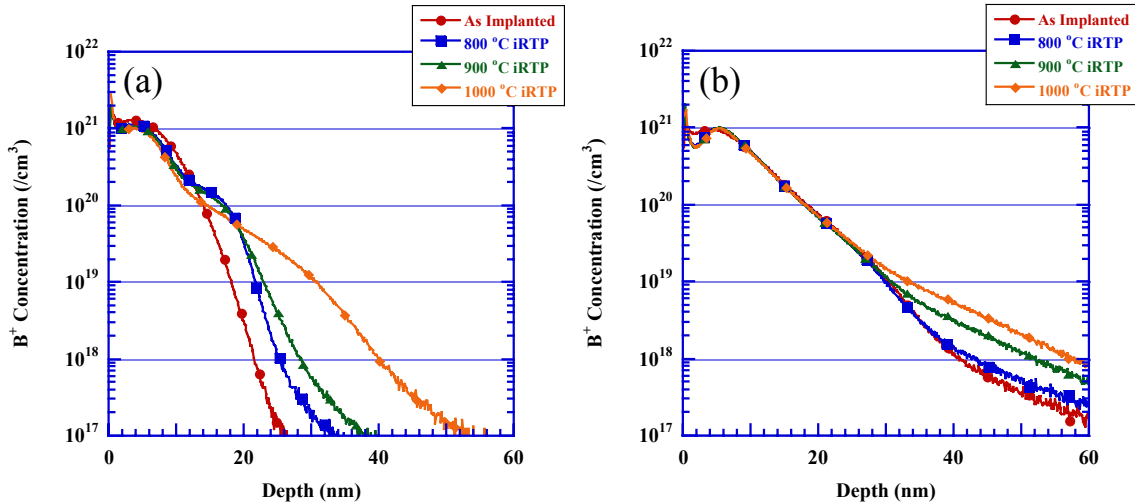


Figure 4-19 Concentration profiles showing the B^+ concentration as a function of depth for the 1 keV B^+ implant to $1 \times 10^{15}/\text{cm}^2$ before and after 800, 900, and 1000 °C iRTP annealing for the wafer (a) with and (b) without the 80 keV Ge^+ pre-amorphization implant to $1 \times 10^{15}/\text{cm}^2$. The symbols are for identifications purposes only.

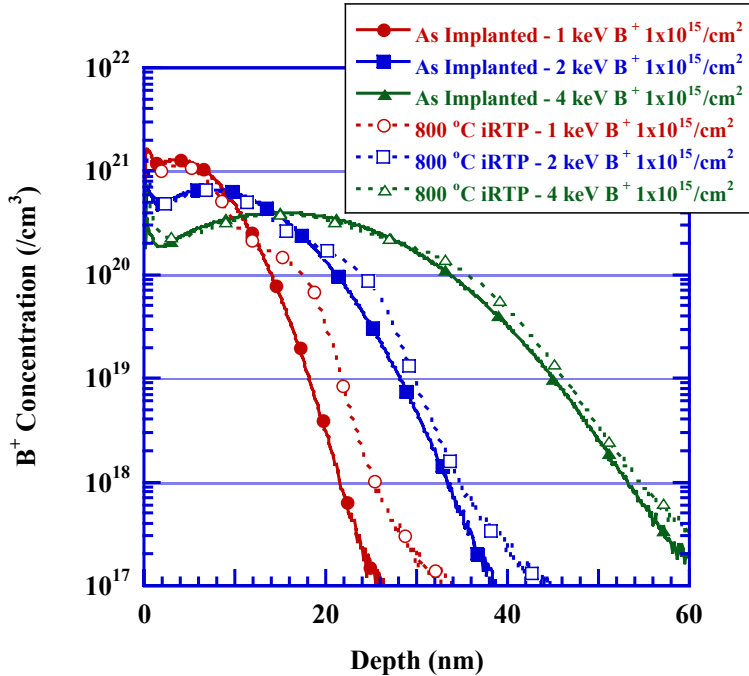


Figure 4-20 Concentration profiles showing the B⁺ concentration as a function of depth for the 1, 2, and 4 keV B⁺ implants each to $1 \times 10^{15}/\text{cm}^2$ before and after iRTP annealing at 800 °C for a substrate pre-amorphized with an 80 keV Ge⁺ implant to $1 \times 10^{15}/\text{cm}^2$. The symbols are for identifications purposes only.

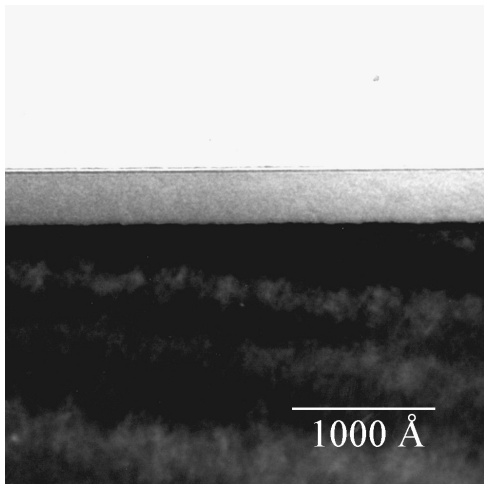


Figure 4-21 Bright field XTEM image showing the 30 nm continuous amorphous layer produced with an 18 keV Ge^+ pre-amorphization implant to $1 \times 10^{15}/\text{cm}^2$.

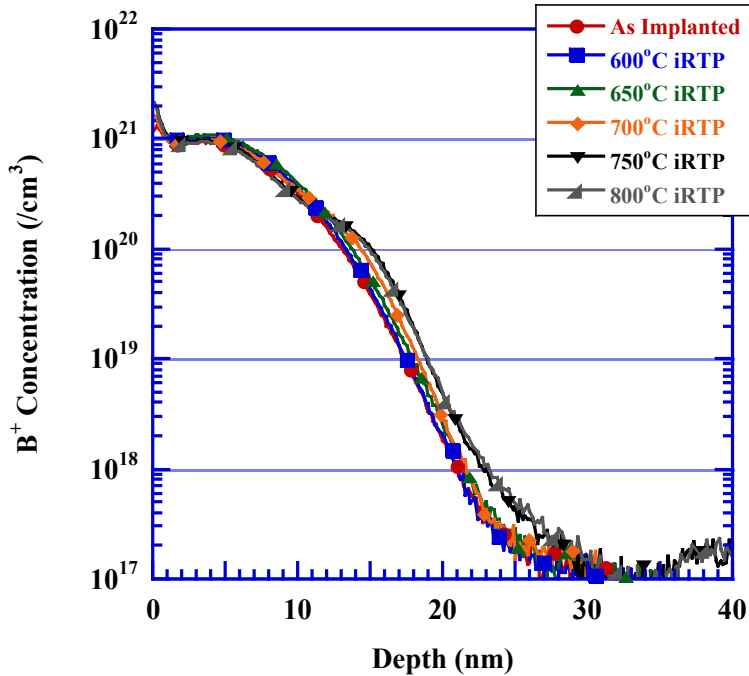


Figure 4-22 Concentration profiles showing the B^+ concentration as a function of depth for the 1 keV B^+ implant to $1 \times 10^{15}/\text{cm}^2$ before and after iRTP annealing over the temperature range of 600-800 °C for a substrate pre-amorphized with an 18 keV Ge^+ implant to $1 \times 10^{15}/\text{cm}^2$. The symbols are for identifications purposes only.

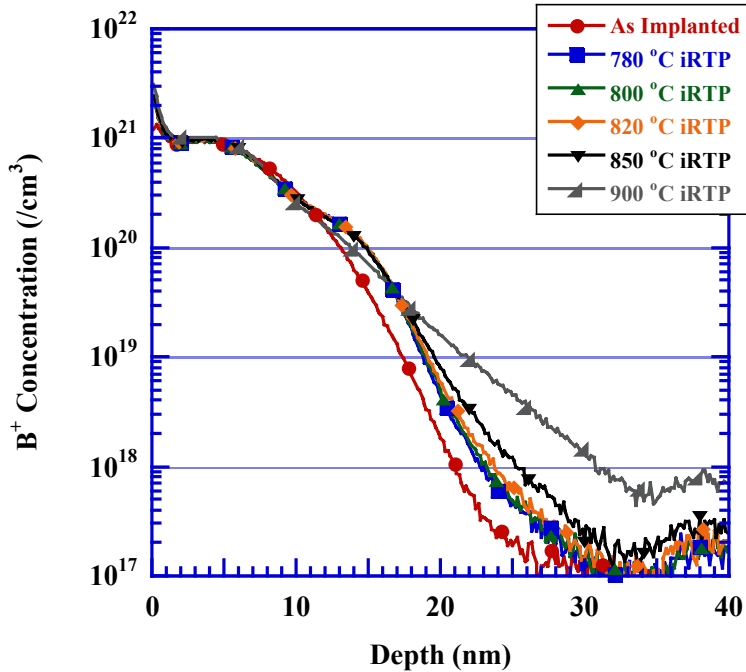


Figure 4-23 Concentration profiles showing the B⁺ concentration as a function of depth for the 1 keV B⁺ implant to $1 \times 10^{15}/\text{cm}^2$ before and after iRTP annealing over the temperature range of 780-900 °C for a substrate pre-amorphized with an 18 keV Ge⁺ implant to $1 \times 10^{15}/\text{cm}^2$. The symbols are for identifications purposes only.

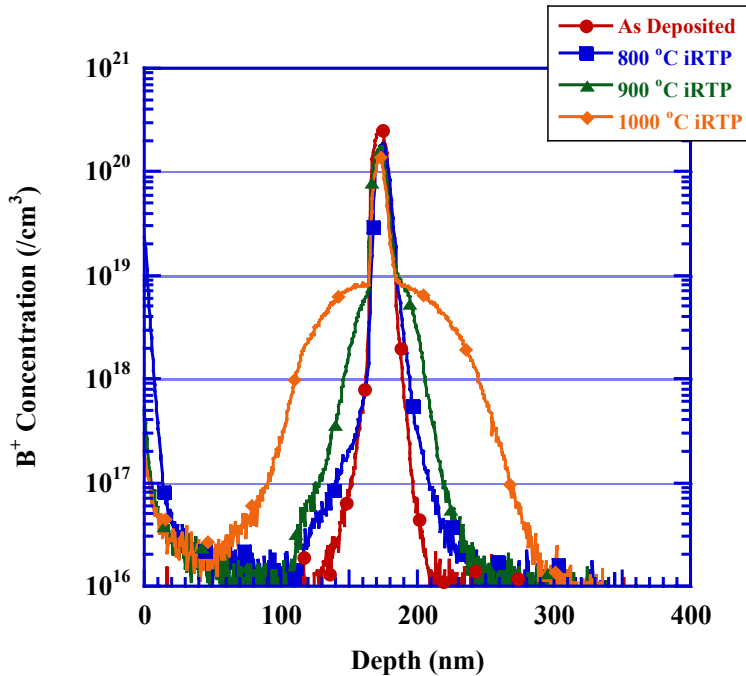


Figure 4-24 Concentration profiles showing the B^+ concentration as a function of depth for the shallowest B marker layer before and after iRTP annealing over the temperature range of 800–1000 °C. The deposition conditions were chosen to result in a B marker layer with a peak concentration of approximately $2 \times 10^{20}/\text{cm}^3$. The intrinsic Si layer thickness was targeted to be 100 nm. The 80 keV Ge^+ pre-amorphization implant to $1 \times 10^{15}/\text{cm}^2$ produced a continuous amorphous layer extending approximately 110 nm below the substrate surface. Note that the 800 °C iRTP anneal results in an appreciable amount of diffusion.

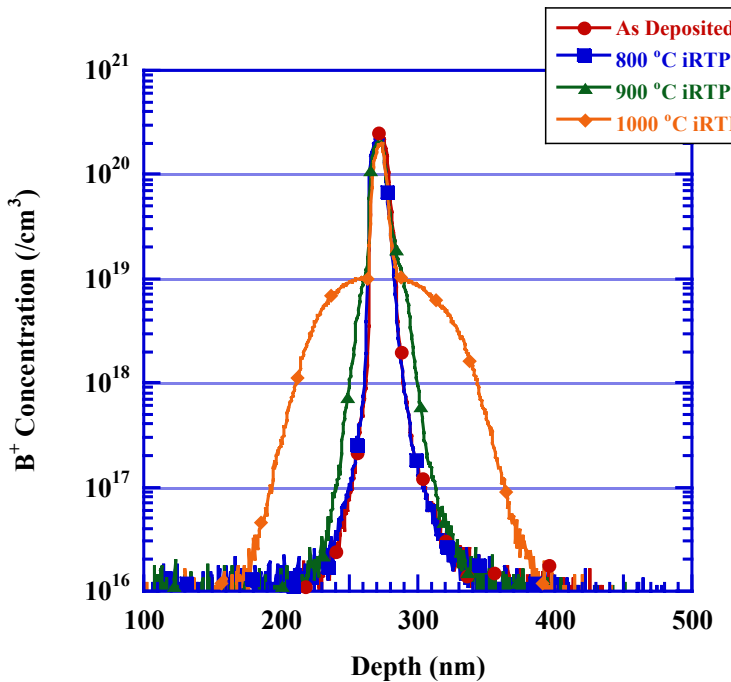


Figure 4-25 Concentration profiles showing the B^+ concentration as a function of depth for the second deepest B marker layer before and after iRTP annealing over the temperature range of 800-1000 °C. The deposition conditions were chosen to result in a B marker layer with a peak concentration of approximately $2 \times 10^{20}/cm^3$. The intrinsic Si layer thickness was targeted to be 200 nm. The 80 keV Ge^+ pre-amorphization implant to $1 \times 10^{15}/cm^2$ produced a continuous amorphous layer extending approximately 110 nm below the substrate surface. Note that the 800 °C iRTP anneal results in no measurable amount of diffusion.

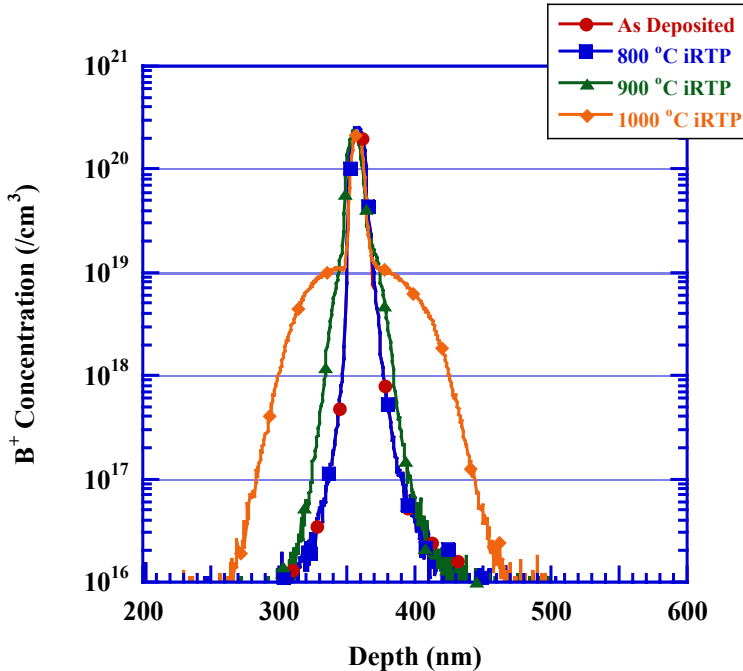


Figure 4-26 Concentration profiles showing the B^+ concentration as a function of depth for the deepest B marker layer before and after iRTP annealing over the temperature range of 800–1000 °C. The deposition conditions were chosen to result in a B marker layer with a peak concentration of approximately $2 \times 10^{20}/\text{cm}^3$. The intrinsic Si layer thickness was targeted to be 300 nm. The 80 keV Ge^+ pre-amorphization implant to $1 \times 10^{15}/\text{cm}^2$ produced a continuous amorphous layer extending approximately 110 nm below the substrate surface. Note that the 800 °C iRTP anneal results in no measurable amount of diffusion.

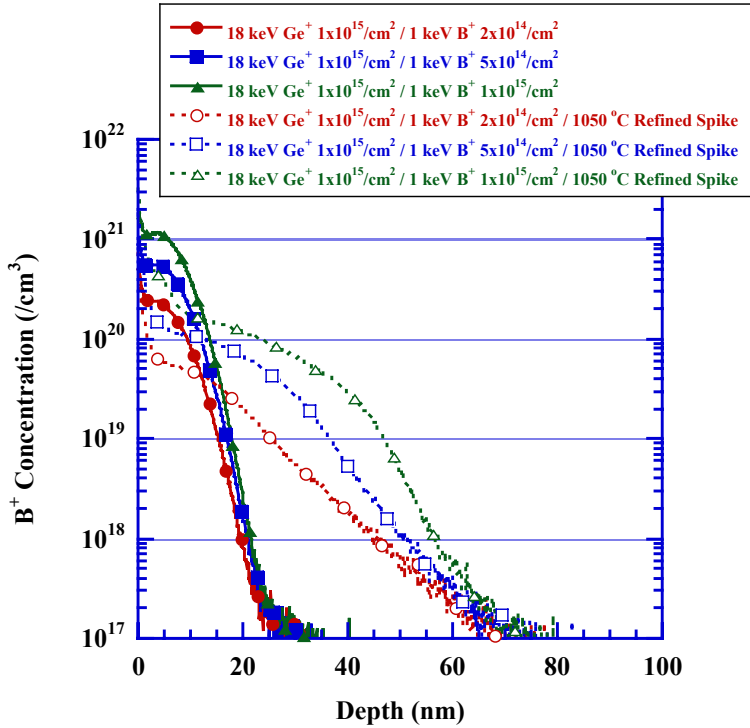


Figure 4-27 Concentration profiles for a 1 keV B^+ implant to $1 \times 10^{15}/\text{cm}^2$ before and after a 1050°C refined spike anneal for a substrate pre-amorphized with an 18 keV Ge^+ implant to $1 \times 10^{15}/\text{cm}^2$. Note that increasing the B^+ dose from $2 \times 10^{14}/\text{cm}^2$ to $1 \times 10^{15}/\text{cm}^2$ results in improved junction abruptness. The symbols are for identifications purposes only.

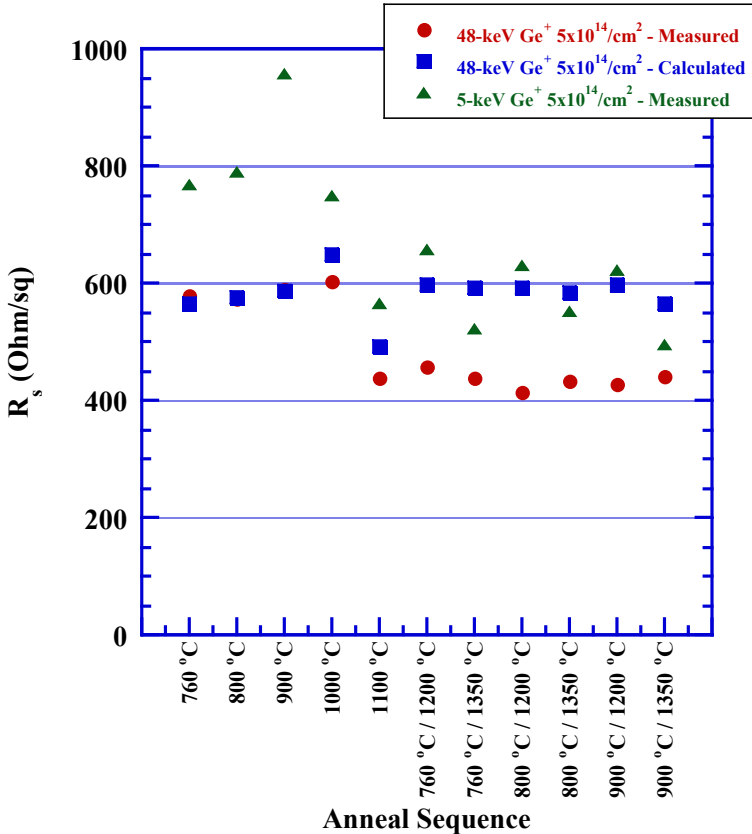


Figure 4-28 Graph of the measured (\bullet) and calculated (\blacksquare) R_s values obtained for the 48 keV Ge^+ pre-amorphization implant to $5 \times 10^{14}/\text{cm}^2$ and the measured (\blacktriangle) values obtained for the 5 keV Ge^+ pre-amorphization implant to $5 \times 10^{14}/\text{cm}^2$.

CHAPTER 5

EFFECT OF SOLID-PHASE EPITAXIAL REGROWTH BEFORE ULTRA-HIGH TEMPERATURE ANNEALING FOR BORON ULTRA-SHALLOW JUNCTION FORMATION OF ION-IMPLANTED SILICON

Introduction

Ion-implantation is commonly used to introduce a controlled amount of dopant into a Si substrate.³ This process is known to create a large amount of interstitial-vacancy (Frenkel) pairs due to the nuclear collisions associated with the primary ions and recoiled atoms. Many of these Frenkel pairs recombine during relaxation of the collision cascade of the implanted ion due to elementary diffusion steps on the time scale of 10^{-9} s, after which the primary damage generated by the incident ion can be considered stable.^{2,40} The probability of the recombination of a Frenkel pair is dependent on the separation distance of the interstitial and vacancy, temperature, and the concentration of point-defect traps. For non-amorphizing implants, the stable damage is primarily small defect clusters, dopant-defect complexes, and some isolated Frenkel pairs.² It is well known that continuous amorphous layers can be formed by ion-implantation and that these layers are capable of preventing ion channeling associated with the implantation of low mass species (e.g., B⁺ and C⁺).^{2,177} These layers extend from the substrate surface down to a depth dependent on the implant conditions. When considering amorphous Si (α -Si) it can be said that the lattice maintains some short range order, although it is significantly disordered and consists of atoms with unsatisfied bonds that exhibit large tetrahedral-bond-angle distortions.¹⁹⁸ The threshold damage density for the formation of an amorphous layer is often taken to be 10% of the Si lattice density.⁴⁶ After an

amorphous state is reached, the damage accumulation saturates.² It was shown that α -Si has a melting temperature and atomic density of approximately 225 ± 50 °C and $1.8 \pm 0.1\%$ below that of crystalline Si (c-Si), respectively.⁴⁷⁻⁴⁹ In addition, it was shown that α -Si consists of a covalently bonded continuous random network (CRN) that can exist as either an as-implanted or structurally relaxed state.⁵⁰⁻⁵⁵ The structurally relaxed α -Si differs from the as-implanted case in that the number of large-angle bond distortions and defect complexes produced during the pre-amorphization implant are reduced and annihilated, respectively, typically by a low temperature relaxation anneal (e.g., 500 °C for 60 min).¹⁹⁴ Regardless of the structural state of the α -Si, a significant amount of excess interstitials are transmitted through the α -Si layer and remain below the original amorphous/crystalline (α/c) interface.

Post implant thermal processing is required to induce solid-phase epitaxial regrowth (SPER) of the amorphous layer, which repairs the lattice damage accumulated during the implantation process as well as activates the implanted dopants by establishing them on substitutional sites where they are able to contribute their holes (electrons) to the valence (conduction) band. During SPER of an implantation-induced amorphous layer, the excess interstitials coalesce into small defect clusters.^{9,64} During subsequent thermal processing these small defect clusters, which are located just below the original α/c interface termed the end-of-range (EOR) region, evolve into either {311} defects or dislocation loops. The {311} defect is an extrinsic row of interstitials lying on the {311} habit plane, elongated in the $\langle 110 \rangle$ direction. Two different types of dislocation loops have been observed: so-called perfect prismatic loops with a Burgers vector $b = a/2\langle 110 \rangle$ and faulted Frank loops with a Burgers vector $b = a/3\langle 111 \rangle$.⁶⁴ Dislocation loops are more

stable than {311} defects.²³ During post implant thermal annealing, these defects release interstitials and these interstitials give rise to transient enhanced diffusion (TED), which significantly increases the diffusion behavior of dopants such as B and P which diffuse primarily or in part by an interstitial(cy) mechanism.⁹⁴ It was shown that the amount of TED observed during an anneal decreases with increasing temperature.^{3,27,73,209} This observation influenced the development of single-wafer thermal processes which are capable of producing a high temperature ambient with ramp rates on the order of 50-200 °C/s, and fast switching times to insulate the dopant from a high degree of TED.²⁸

Rapid thermal processing (RTP) has proven successful in producing junctions with the performance characteristics necessary for the continued scaling of complementary metal-oxide-semiconductor (CMOS) technology to date.²⁹ Its ability to satisfy these requirements is associated with improved equipment capability in the form of spike annealing, which decreases the effective thermal budget, allowing for higher annealing temperatures to improve activation and reduce the amount of diffusion of the dopant during the thermal process.^{30,31} A spike anneal is characterized as a short thermal-anneal cycle that can be achieved by increasing the ramp-up and ramp-down rates and by minimizing the dwell time at the temperature of interest. One process limitation associated with RTP is that a significant amount of TED occurs during the early stages of annealing, which promotes diffusion, resulting in a profile with lack of abruptness and an unacceptable increase in junction depth (x_j).^{9,66,210} This initial interstitial injection mechanism occurs because of either the dissolution and evolution of unstable sub-microscopic interstitial clusters, or the inability of the extended defects in capturing the entire interstitial population during their formation.^{94,113,114} In addition, although

increased spike sharpness enhances the ability to increase the annealing temperature to achieve higher activation levels and improve junction abruptness,¹¹⁵ the amount of diffusion that occurs during the thermal process is still unacceptable. As the spike anneal approaches time durations on the order of 1-2 s within 50 °C of the peak temperature, the advantages offered by annealing at higher temperatures are cancelled by the lack of concentration enhanced diffusion (CED) that takes place during the thermal process, which results in a profile with an unacceptable x_j because of the characteristics produced by TED during the early stages of annealing.¹¹⁶ This illustrates the need to investigate novel annealing technologies that may be able to produce junctions without being subject to a significant amount of TED.

Novel high-power arc lamp design has enabled ultra-high temperature (UHT) annealing as an alternative to conventional RTP for B ultra-shallow junction formation.³³ This technique heats the wafer to an intermediate temperature (e.g., 800 °C) before discharging a capacitor bank into flash lamps, which anneals the device side of the wafer at a relatively high temperature (e.g., 1200 °C) for a few milliseconds.³⁴⁻³⁶ The UHT anneal heats the surface of interest while increasing the bulk wafer temperature not more than 50 °C of the intermediate temperature, allowing for conductive heat loss through the substrate. This quality resolves one of the limiting issues associated with conventional RTP techniques. In addition to developing this novel UHT annealing technique, recent attention has been given to low temperature SPER of an implantation-induced amorphous layer due to its ability to activate dopants well above their solid solubility levels while minimizing the amount of diffusion that occurs during the thermal process.¹¹⁸ The most significant disadvantage of this annealing technique is that a considerable amount of

damage remains below the original α /c interface, which can give rise to a large amount of leakage current. It is well known that defects in the space-charge region contribute to leakage current in bipolar transistors.^{11,12} According to the International Technology Roadmap for Semiconductors (ITRS), junction leakage should only contribute a small amount to the total leakage during the off-state of metal-oxide-semiconductor field-effect-transistors (MOSFETs).¹³ It was shown in Chapter 4 that the UHT annealing technique is capable of evolving implant damage without being subject to a significant amount of dopant diffusion.^{118,226} The focus of this experiment is to use a low temperature SPER anneal to obtain above solid solubility activation levels, and then use the UHT annealing technique to evolve the residual damage without being subject to a significant amount of additional diffusion or dopant deactivation.

Experimental Design

Two 200 mm 3-5 $\Omega\cdot\text{cm}$ (100) n-type Czochralski (CZ) grown Si wafers were pre-amorphized with 48 keV implantation to $5\times 10^{14}/\text{cm}^2$, and subsequently implanted with 3 keV BF_2^+ molecular ions to $6\times 10^{14}/\text{cm}^2$. The implants were carried out in the drift mode and performed at room temperature with the ion beam normal to the surface plane using an Applied Materials Leap-II system. The implant parameters were monitored to ensure they remained within predetermined limits. One of the wafers was subject to a 585 °C furnace anneal for 45 min to regrow the amorphous layer before UHT annealing. The wafers were then sectioned and annealed at Vortek Industries to investigate the effects of the UHT annealing technique on the resulting junction characteristics. Representative temperature-time (T-t) profiles of the two UHT annealing techniques as well as the processing conditions used were shown in Figure 4-2. The impulse anneal

(iRTPTM) is produced by arc lamp irradiation of the front surface of the wafer and is responsible for producing the bulk wafer temperature, known as the intermediate temperature, at which the flash anneal (fRTPTM) is to be introduced. The fRTP anneal is produced by discharging a capacitor bank into flash lamps which increases the temperature of the surface of interest while increasing the bulk wafer temperature not more than 50 °C of the intermediate temperature, allowing for conductive heat loss through the substrate. The iRTP anneal provides a means to better understand the advantages gained by the fRTP anneal. All of the anneals were carried out in a N₂ ambient with less than 10 ppm O₂. The iRTP and fRTP anneal temperatures were determined by a radiometer, which determined the wafer emissivity through a reflectance calculation that expresses the temperature of the system. In this experiment, iRTP anneals were performed over the range of 760 to 1100 °C using a ramp-up rate of 400 °C/s, and a ramp-down rate which was estimated to be approximately 150 °C/s at 900 °C. The ramp-down rate was determined by an instantaneous derivative of the radiation-cooling curve for a gray body with an emissivity and thickness comparable to the Si substrate. It should be noted that the ramp-down rate for conventional RTP is limited to 50-80 °C/s because of radiative cooling of the substrate to the ambient.^{3,117} The ramp-down rate is greater than that obtained through conventional techniques because of absorbing chamber technology, which reduces radiation return to the substrate, providing the improved cooling rate.¹¹⁷ The fRTP anneals were performed over the range of 1200 to 1350 °C using ramp-up and ramp-down rates on the order of 10⁶ °C/s.

Dynamic secondary ion mass spectrometry (SIMS) was used to quantify dopant concentration as a function of depth. The $^{10}\text{B}^+$ and $^{11}\text{B}^+$ counts were obtained on a CAMECA IMS-6f analytical tool using an O_2^+ primary beam with a nominal beam current of 50-70 nA and a net impact energy of 800 eV directed 50° from the sample normal. The depth profile was established by continuously rastering a 200 by 200 μm area, and collected from a centered circular area 30-60 μm in diameter under an isobaric O_2 ambient, which provided an adequate condition for complete oxidation of the Si surface during analysis. The system was configured so as to maintain a sputtering rate of 0.08-0.1 nm/s. Variable angle spectroscopic ellipsometry (VASE) was used to determine the thickness of the implantation-induced amorphous layer. The VASE measurements were performed on a J. A. Woollam Co., Inc. multi-wavelength ellipsometer with the 75 W Xe light source tilted 20° from the surface plane. The system was calibrated by fitting a known oxide thickness from a control Si substrate, and each subsequent measurement assumed a 2 nm native oxide above the continuous amorphous layer in order to more accurately measure the amorphous layer thickness. Cross-sectional transmission electron microscopy (XTEM) was used to verify the thickness of the amorphous layer measured by VASE, and image the depth of the EOR defect layer produced by the 48 keV pre-amorphization implant. The XTEM samples were thinned by 5 kV Ar^+ ion milling, with the plasma sources tilted 12° from the surface plane. All XTEM images were captured on a JEOL 200 CX TEM operating at 200 kV under a bright field imaging condition with the objective aperture centered over the transmitted beam. Plan-view TEM (PTEM) was used to investigate the EOR defect evolution and morphology as a function of the two UHT annealing techniques. The PTEM sample

surfaces and backside periphery were insulated from the 3:1 HNO₃:49% HF solution used to introduce an electron transparent edge surrounding an interstice. The PTEM images were captured on a JEOL 200 CX TEM operating at 200 kV in **g.3g** centered weak-beam dark-field (WBDF) using a **g**₂₂₀ two-beam imaging condition.¹⁷³ A Prometrics RS-20 four-point probe was used to measure the sheet resistance (R_s) for each anneal condition. The sample geometric correction factor is negligible for the wafer sections, which have surface areas greater than those below which edge effects reduce measurement accuracy.

Results

The 48 keV pre-amorphization implant to $5 \times 10^{14}/\text{cm}^2$ generated a continuous amorphous layer extending 76 nm below the substrate surface as determined by VASE and verified through XTEM, an image of which was shown in Figure 4-3a. Figure 4-3c showed an XTEM image of the wafer that received the 48 keV pre-amorphization implant followed by the 585 °C furnace anneal for 45 min. Not only does this anneal allow us to investigate the ability to obtain above solid solubility activation levels but it also serves as a control sample for the wafer that did not receive the furnace anneal, as this relatively low temperature anneal allows sufficient time for proper microstructural reconstruction during SPER in order to monitor any regrowth related defects associated with the iRTP anneals that may be introduced as a result of the roughness of the α/c interface produced by the high energy Ge⁺ implant.¹⁸³ It was shown that a combination of 400 keV and 30 keV Ge⁺ pre-amorphization implants to $5 \times 10^{14}/\text{cm}^2$ with a subsequent 5 keV BF₂⁺ implant to $5 \times 10^{14}/\text{cm}^2$ resulted in hairpin dislocation formation after both a 800 °C anneal for 30 min and a 900 °C anneal for 10 s.¹⁸³ These defects may in turn provide easy diffusion paths, via pipe diffusion, for the B to segregate toward the

substrate surface.¹²⁰ As can be seen in Figure 4-3c, the 585 °C furnace anneal for 45 min is sufficient to completely regrow the amorphous layer and produce a visible EOR defect band without forming any regrowth related defects. Although it is difficult to determine the morphology of the defects from the XTEM image, they are located below the original a/c interface, which is consistent with EOR defect formation.³ The corresponding PTEM image of the sample that received the furnace anneal is shown in Figure 4-3d. The diffraction pattern in the image inset confirms that the anneal is sufficient to completely regrow the amorphous layer and results in high quality single crystalline Si. This image shows that the defect structure that forms as a result of the furnace anneal consists of defect clusters approximately 4 to 12 nm in diameter, a morphology which is typical of low temperature-short time thermal processing.^{9,184} Additional XTEM results (not shown) were similar to Figure 4-3c and showed that the 760 °C iRTP anneal was sufficient to completely recrystallize the amorphous layer produced by the 48 keV pre-amorphization implant and was free of hairpin dislocations. It is presumed that hairpin dislocation formation did not occur for any of the iRTP or intermediate temperature anneals used in this study due to the fact that they should form during regrowth of the amorphous layer.

Figures 5-1a and b show the SIMS results for each of the iRTP anneals used in this study for the wafer without and with the 585 °C furnace anneal before UHT annealing, respectively. The B profile after the 585 °C furnace anneal is included in Figure 5-1b to serve as a reference. Each profile shows an increase in x_j when compared to the as-implanted profile, which has a junction abruptness of 3.3 nm/dec and a x_j of 16.3 nm. Junction abruptness is defined as the inverse slope of the SIMS profile between the

concentration range of 1×10^{18} and $1\times10^{19}/\text{cm}^3$, and the x_j is defined as the depth of the profile at a dopant concentration of $1\times10^{18}/\text{cm}^3$. Figure 5-1a shows that the 760 and 800 °C iRTP anneals display similar profiles with 3.2 nm/dec junction abruptness and a 19.3 nm x_j , which is a 3.0 nm increase in x_j when compared to the as-implanted profile. The SIMS profile for the 585 °C furnace anneal in Figure 5-1b shows that the 3.7 nm increase in x_j is associated with B diffusion during SPER of the amorphous layer produced by the 48 keV pre-amorphization implant.¹⁸⁵⁻¹⁸⁸ Figure 5-1b shows that the 760 and 800 °C iRTP anneals result in no additional diffusion other than that observed during the 585 °C furnace anneal and produce profiles with 3.6 nm/dec junction abruptness and 20.0 nm x_j , which is approximately a 0.4 nm/dec and 0.7 nm degradation in junction abruptness and increase in x_j , respectively, when compared to the 760 and 800 °C iRTP anneals for the wafer without the 585 °C furnace anneal before UHT annealing.

Figure 5-1 shows that the 900 °C iRTP anneal produces profiles with 5.5 and 5.4 nm/dec junction abruptness and a 22.5 and 22.4 nm x_j for the wafer without and with the 585 °C furnace anneal before UHT annealing, respectively. This shows that the effect of the 585 °C furnace anneal on the B diffusion behavior during UHT annealing is dependent on the iRTP anneal temperature; the 760 and 800 °C iRTP anneals result in shallower x_j without the furnace anneal before UHT annealing, whereas the 900 °C iRTP anneal results in similar x_j independent of the furnace anneal. Further increasing the iRTP anneal temperature results in a degradation of the junction abruptness and increase in x_j independent of the 585 °C furnace anneal before UHT annealing.

The 1000 and 1100 °C iRTP anneals produce profiles with 10.6 and 8.7 nm/dec junction abruptness and a 32.1 and 36.1 nm x_j , respectively, for the wafer without the 585 °C furnace anneal before UHT annealing. The 1000 and 1100 °C iRTP anneals produce profiles with 11.3 and 10.5 nm/dec junction abruptness and a 32.7 and 37.8 nm x_j , respectively, for the wafer with the 585 °C furnace anneal before UHT annealing. This shows an increase in the B diffusion behavior during the 1000 and 1100 °C iRTP anneals when the 585 °C furnace anneal is performed before UHT annealing. It should be noted that the 1100 °C iRTP anneal has improved junction abruptness compared to the 1000 °C iRTP anneal independent of the 585 °C furnace anneal before UHT annealing. Although this characteristic applies to both graphs in Figure 5-1, the junction abruptness is more degraded for the wafer that received the 585 °C furnace anneal before UHT annealing.

Figure 5-1a shows that the iRTP anneals produce profiles with plateau concentrations on the order of $1.4\text{-}1.8 \times 10^{20}/\text{cm}^3$ for the wafer without the 585 °C furnace anneal before UHT annealing. The plateau concentration is defined as the concentration at which the anneal produces an inflection point. These profiles show inflection points between 7-8 nm below the substrate surface. These inflection points correspond to the concentration levels above which inactive B cluster formation or precipitation occurs and the B remains immobile.^{5,9,98} Figure 5-1b shows that the 585 °C furnace anneal produces a profile with a plateau concentration on the order of $1.5 \times 10^{20}/\text{cm}^3$, and that the subsequent iRTP anneals result in plateau concentrations ranging between $1.2\text{-}1.5 \times 10^{20}/\text{cm}^3$. It should be noted that the 1100 °C iRTP anneal dissociated of some of

the initially inactive dopant near the Si surface independent of the 585 °C furnace anneal before UHT annealing.

Figure 5-2 shows the PTEM images of the EOR damage produced by the 48 keV pre-amorphization implant after each of the iRTP anneals used in this study. The first row of images correspond to the wafer without the 585 °C furnace anneal before UHT annealing. As can be seen by the images, the 760, 800, and 900 °C iRTP anneals produce a high density defect structure consisting of defect clusters.^{9,184} These defect clusters are approximately 4 to 12 nm and 6 to 18 nm in diameter for the 760 and 900 °C iRTP anneals, respectively. Although the morphology of the defects appears independent of the iRTP anneal over this temperature range, the average size of these defects increases and the defect density decreases with increasing iRTP anneal temperature which suggests that defect coarsening is occurring.^{9,184} The PTEM image for the 1000 °C iRTP anneal shows that it is sufficient to produce a defect structure consisting mainly of {311} defects and dislocation loops.⁶⁴ The {311} defects range from 29 to 88 and average 60 nm in length and the dislocation loops range from 21 to 29 and average 26 nm in diameter. Increasing the iRTP anneal temperature to 1100 °C results in a defect structure consisting only of dislocation loops, which shows that {311} defect dissolution is complete between 1000 and 1100 °C. The dislocation loops range from 24 to 32 and average 29 nm in diameter. The second row of images correspond to the wafer with the 585 °C furnace anneal before UHT annealing. As can be seen by the images, the 760 and 800 °C iRTP anneals produce a high density defect structure consisting of defect clusters, which are similar to those observed for the wafer that without the 585 °C furnace anneal before UHT annealing.^{9,184} The 900 °C iRTP anneal, however, was sufficient to produce small

dislocation loops in addition to the defect clusters. This shows that the 585 °C furnace anneal is sufficient to produce differences in the final defect structure after UHT annealing. These defect clusters are approximately 4 to 12 nm and 4 to 18 nm in diameter for the 760 and 900 °C iRTP anneals, respectively, which are similar in size to those observed for the wafer without the 585 °C furnace anneal. The dislocation loops observed after the 900 °C iRTP anneal range from 9 to 13 and average 11 nm in diameter. Similar to the case without the 585 °C furnace anneal before UHT annealing, the average size of these defect clusters increases and the defect density decreases with increasing iRTP anneal temperature which suggests that defect coarsening is occurring.^{9,184} The PTEM image for the 1000 °C iRTP anneal shows that it is sufficient to produce a defect structure consisting mainly of {311} defects and dislocation loops.⁶⁴ The {311} defects range from 15 to 27 and average 22 nm in length and the dislocation loops range from 18 to 27 and average 22 nm in diameter. It should be noted that the {311} defects and dislocation loops are shorter in length and smaller in diameter than those observed for the wafer without the 585 °C anneal before UHT annealing, respectively. This provides additional evidence that the 585 °C furnace anneal is sufficient to produce differences in the final defect structure after UHT annealing. Increasing the iRTP anneal temperature to 1100 °C results in a defect structure consisting only of dislocation loops, which shows that {311} defect dissolution is complete between 1000 and 1100 °C independent of the 585 °C furnace anneal before UHT annealing. The dislocation loops range from 24 to 29 and average 26 nm in diameter, which are on average slightly smaller in diameter to those observed for the wafer without the 585 °C furnace anneal before UHT annealing.

Figures 5-3a and b show the SIMS results for a collective subset of intermediate temperatures with a 1200 °C fRTP anneal for the wafer without and with the 585 °C furnace anneal before UHT annealing, respectively. As can be seen in Figure 5-3a, the 760 and 800 °C intermediate temperatures produce similar profiles with 3.4 nm/dec junction abruptness and 19.9 nm x_j after the 1200 °C fRTP anneal. The 0.6 nm of diffusion that occurs during the fRTP anneal shows that most the overall diffusion occurs during SPER of the amorphous layer. As was shown in Figure 5-1, the 900 °C iRTP anneal produced a profile with degraded junction abruptness and an increased x_j compared to the 760 and 800 °C iRTP anneals. These characteristics remain when 900 °C is used as the intermediate temperature during the 1200 °C fRTP anneal, which produces a profile with 5.9 nm/dec junction abruptness and 23.7 nm x_j . It should be noted that the diffusion behavior for each of the profiles is much less than would be expected from a conventional RTP anneal. Figure 5-3 shows that the 760 °C intermediate temperature produces similar diffusion behavior during the 1200 °C fRTP anneal, independent of the 585 °C furnace anneal before UHT annealing; however, the 800 °C intermediate temperature produces an increase in diffusion behavior during the 1200 °C fRTP anneal for the wafer with the 585 °C furnace anneal before UHT annealing. As can be seen in Figure 5-3b, the 760 and 800 °C intermediate temperatures produce profiles with 3.9 and 4.5 nm/dec junction abruptness and 20.4 and 21.4 nm x_j , respectively. This shows that the 800 °C intermediate temperature produces a 1.0 nm increase in x_j compared to the 760 °C intermediate temperature, which was not observed for the wafer without the 585 °C furnace anneal before UHT annealing in Figure 5-3a.

These results were confirmed by performing multiple SIMS measurements; the results were reproducible. It should be noted that the 900 °C intermediate temperature produces a profile with 5.9 and 6.1 nm/dec junction abruptness and 23.7 and 23.7 nm x_j for the wafer without and with the 585 °C furnace anneal before UHT annealing, respectively. This shows that the 900 °C intermediate temperature produces similar diffusion behavior during the 1200 °C fRTP anneal, independent of the 585 °C furnace anneal before UHT annealing (considering the 900 °C iRTP anneal resulted in 22.5 and 22.4 nm x_j for the wafer without and with the 585 °C furnace anneal before UHT annealing, respectively). This was not observed when the 760 and 800 °C intermediate temperatures were used.

Figure 5-4 shows the PTEM images of the EOR damage produced by the 48 keV pre-amorphization implant after the 1200 °C fRTP anneal. The first row of images correspond to the wafer without the 585 °C furnace anneal before UHT annealing. The 760 and 800 °C intermediate temperatures result in defect structures consisting of defect clusters and possibly small dislocation loops; it is unclear whether the areas of large contrast are dislocation loops or large defect clusters. For the 760 °C intermediate temperature, these defects are approximately 4 to 12 nm in diameter which are similar to those produced by the corresponding iRTP anneal in Figure 5-2. The 800 °C intermediate temperature produces defects approximately 9 to 22 nm in diameter, which are on average larger than those produced by the corresponding iRTP anneal in Figure 5-2. It can be seen that the 800 °C intermediate temperature produces a defect structure with the defects increasing in size and decreasing in density when compared to the 760 °C intermediate temperature. The 900 °C intermediate temperature is sufficient

to produce a defect structure consisting of defect clusters, {311} defects, and dislocation loops. The {311} defects range from 21 to 29 and average 25 nm in length and the dislocation loops range from 13 to 19 and average 17 nm in diameter. The second row of images correspond to the wafer with the 585 °C furnace anneal before UHT annealing. Similar to the case for the wafer without the 585 °C furnace anneal before UHT annealing, the 760 and 800 °C intermediate temperatures result in defect structures consisting of defect clusters and possibly small dislocation loops. For the 760 °C intermediate temperature, these defects are approximately 4 to 12 nm in diameter, which are similar to those produced by the corresponding iRTP anneals in Figure 5-2. The 800 °C intermediate temperature produces defects approximately 9 to 18 nm in diameter, which are on average larger than those produced by the corresponding iRTP anneal in Figure 5-2 and somewhat smaller than the defects observed for the wafer without the 585 °C furnace anneal before UHT annealing. It can be seen that the 800 °C intermediate temperature produces a defect structure with the defects increasing in size and decreasing in density when compared to the 760 °C intermediate temperature, independent of the 585 °C furnace anneal before UHT annealing. The 900 °C intermediate temperature is sufficient to produce a defect structure consisting of defect clusters, {311} defects, and dislocation loops. The {311} defects range from 16 to 25 and average 20 nm in length and the dislocation loops range from 13 to 18 and average 16 nm in diameter. It should be noted that the average {311} defect is approximately 5 nm shorter in length for the wafer with the 585 °C furnace anneal before UHT annealing when compared to the wafer without the furnace anneal (whereas the average dislocation loop diameter is relatively independent of the furnace anneal). Although these images show subtle differences in the

final defect structure, it is unclear whether the intermediate anneal temperature significantly effects the final defect structure after a fRTP anneal.

Figures 5-5a and b show the SIMS results for various intermediate temperatures with a 1350 °C fRTP anneal for the wafer without and with the 585 °C furnace anneal before UHT annealing, respectively. As can be seen in Figure 5-5a, the 760 and 800 °C intermediate temperatures produce profiles with 4.4 and 4.9 nm/dec junction abruptness and 21.3 and 22.4 nm x_j after the 1350 °C fRTP anneal for the wafer without the 585 °C furnace anneal before UHT annealing. This shows that the 760 °C intermediate temperature results in a slightly shallower profile with the introduction of the 1350 °C fRTP anneal when compared to the 800 °C intermediate temperature, which was not observed after the 1200 °C fRTP anneal shown in Figure 5-3a. The 900 °C intermediate temperature produces a profile with 5.8 nm/dec junction abruptness and 25.0 nm x_j . As can be seen in Figure 5-5b, the 760 and 800 °C intermediate temperatures produce profiles with 4.8 and 5.0 nm/dec junction abruptness and 22.1 and 23.0 nm x_j after the 1350 °C fRTP anneal for the wafer with the 585 °C furnace anneal before UHT annealing. This shows that the 760 °C intermediate temperature results in a slightly shallower profile with the introduction of the 1350 °C fRTP anneal when compared to the 800 °C intermediate temperature, independent of the 585 °C furnace anneal before UHT annealing. The 900 °C intermediate temperature produces a profile with a 5.4 nm/dec junction abruptness and 25.1 nm x_j . This supports the suggestion that the effect of the 585 °C furnace anneal on the B diffusion behavior during UHT annealing is dependent on the intermediate anneal temperature; the 760 and 800 °C intermediate temperatures

result in shallower x_j without the furnace anneal before UHT annealing, whereas the 900 °C intermediate temperature results in similar x_j independent of the furnace anneal. It should be noted that the diffusion enhancement produced by the 900 °C intermediate temperature causes the degraded junction characteristics compared to the 760 and 800 °C intermediate temperatures. Also, the x_j produced by the 1350 °C fRTP anneal are somewhat deeper than those produced by the 1200 °C fRTP anneal, showing that the diffusion characteristics are dependent on the fRTP anneal temperature.

To better illustrate the effect of the 585 °C furnace anneal on the B diffusion behavior during UHT annealing, Figures 5-6a and 5-6b show the SIMS results for the 800 and 900 °C iRTP anneals and intermediate temperatures, respectively, both without and with the 585 °C furnace anneal before UHT annealing. The B profile after the 585 °C furnace anneal is included to serve as a reference. As can be seen by Figure 5-6a the 585 °C furnace anneal results in increased diffusion behavior during UHT annealing, independent of the peak anneal temperature (when compared to the wafer without the 585 °C furnace anneal before UHT annealing). A similar, but less obvious, trend is observed when plotting the data corresponding to the 760 °C intermediate temperature (not shown). Figure 5-6b shows similar diffusion behavior for each peak annealing temperature independent of the 585 °C furnace anneal before UHT annealing, showing that the effect of the 585 °C furnace anneal is dependent on the intermediate temperature and is only observed when the intermediate temperature is sufficiently low.

Figure 5-7 shows the PTEM images of the EOR damage produced by the 48 keV pre-amorphization implant after the 1350 °C fRTP anneal. The first row of images

correspond to the wafer without the 585 °C furnace anneal before UHT annealing. The 760 °C intermediate temperature produces a defect structure consisting of defect clusters, {311} defects, and dislocation loops. The {311} defects range from 19 to 29 and average 25 nm in length and the dislocation loops range from 18 to 24 and average 19 nm in diameter. The 800 °C intermediate temperature produces a defect structure consisting mainly of {311} defects and dislocation loops. The {311} defects range from 19 to 43 and average 32 nm in length and the dislocation loops range from 19 to 59 and average 32 nm in diameter. The 900 °C intermediate temperature produces a defect structure consisting only of dislocation loops. The dislocation loops range from 24 to 115 and average 62 nm in diameter. The most marked difference between these images is the size and overall evolution of the dislocation loops, which increases with the intermediate annealing temperature. The largest dislocation loops in each of the images are approximately 24, 59, and 115 nm in diameter for the 760, 800 and 900 °C intermediate temperatures, respectively. The second row of images correspond to the wafer with the 585 °C furnace anneal before UHT annealing. The 760 °C intermediate temperature produces a defect structure consisting of defect clusters, {311} defects, and dislocation loops. The {311} defects range from 18 to 35 and average 26 nm in length and the dislocation loops range from 18 to 24 and average 20 nm in diameter. The 800 °C intermediate temperature produces a defect structure mainly consisting of {311} defects and dislocation loops. The {311} defects range from 19 to 32 and average 24 nm in length and the dislocation loops range from 19 to 24 and average 21 nm in diameter. The 900 °C intermediate temperature produces a defect structure consisting only of dislocation loops, similar to those observed for the 900 °C intermediate temperature for

the wafer without the 585 °C furnace anneal before UHT annealing. The dislocation loops range from 24 to 85 and averaged 47 nm in diameter. The largest dislocation loops in each of the images are approximately 24, 29, and 85 nm in diameter for the 760, 800 and 900 °C intermediate temperatures, respectively. It should be noted that, although the dislocation loops are similar in size for the lower intermediate temperatures, the dislocation loops are much larger for the wafer without the 585 °C furnace anneal before UHT annealing when higher intermediate temperatures are used. It can be seen that the defect density decreases and the defect size generally increases with increasing intermediate anneal temperature, independent of the 585 °C furnace anneal before UHT annealing. When comparing these images, it can be seen that the resulting defect structure after a fRTP anneal is significantly dependent on the intermediate temperature at which it is introduced; this shows that both the intermediate and fRTP anneal temperatures should be considered when using the UHT annealing technique.

Discussion

Although the 760 and 800 °C iRTP anneals increase the x_j of the B profile in Figure 5-1a, these anneals produce profiles with slightly improved junction abruptness when compared to the as-implanted profile for the wafer without the 585 °C furnace anneal before UHT annealing. The as-implanted profile has a junction abruptness of 3.3 nm/dec, whereas both the 760 and 800 °C iRTP anneals have junction abruptness of 3.2 nm/dec. The B profiles after the 760 and 800 °C iRTP anneals in Figure 5-1a show approximately 3 nm of diffusion up to a concentration of $1.8 \times 10^{20}/\text{cm}^3$, above which inactive B cluster formation or precipitation occurs and the B remains immobile. The diffusion that occurs during these iRTP anneals is due to B diffusion in α -Si, and was

discussed in greater detail throughout Chapter 4. Since additional XTEM results (not shown) revealed that the 76 nm continuous amorphous layer completely recrystallized during the 760 °C iRTP anneal for the wafer without the 585 °C furnace anneal before UHT annealing, it can be said that the 760 and 800 °C iRTP anneals result in similar dopant profiles due to the fact that the B remains in α -Si the same amount of time before complete recrystallization of the implantation-induced amorphous layer. Even though the 760 and 800 °C iRTP anneals produce profiles with slightly improved junction abruptness compared to the as-implanted profile for the wafer without the 585 °C furnace anneal before UHT annealing, it can be seen in Figure 5-1b that the furnace anneal results in a profile with a junction abruptness of 3.6 nm/dec and a x_j of 20.0 nm, which is degraded compared to the 3.2 nm/dec junction abruptness and 19.3 nm x_j produced by the 760 and 800 °C iRTP anneals in Figure 5-1a. The differences between the profiles are presumed to be due to the time duration of the respective anneals. The PTEM image in Figure 4-3d showed that the 585 °C furnace anneal is sufficient to evolve the EOR damage produced by the 48 keV pre-amorphization implant into defect clusters, which were similar in density and size to those observed for the 760 and 800 °C iRTP anneals in Figure 5-2 (for the wafer without the 585 °C furnace anneal before UHT annealing). It is not likely that the time duration of the furnace anneal was sufficient to allow a fraction of the excess interstitials to be released from the EOR damage region, causing the additional diffusion observed for the wafer with 585 °C furnace anneal before UHT annealing. Instead, it is expected that the relatively slow regrowth velocity of the α/c interface during the 585 °C furnace anneal (e.g., 30 nm/min)¹⁹³ increases the amount of time available for B diffusion in α -Si; therefore, allowing for more diffusion compared to the

760 and 800 °C iRTP anneals for the wafer without the 585 °C furnace anneal before UHT annealing. This is supported by calculations in Chapter 4 that estimate approximately 3.5-4.0 nm of B diffusion in α -Si during the 585 °C furnace anneal. In addition, as can be seen in Figure 5-1b, the SIMS results for the 760 and 800 °C iRTP anneals for the wafer with the 585 °C furnace anneal before UHT annealing show no additional diffusion other than that observed during the 585 °C furnace anneal. If the 585 °C furnace anneal was sufficient to allow some of the excess interstitials to be released from the EOR damage region, one would expect the 760 and 800 °C iRTP anneals to result in an additional diffusion enhancement; which is not observed. It is believed that the 760 and 800 °C iRTP anneals are insufficient to evolve the excess interstitials to the point where TED begins to influence the overall diffusion profile, independent of the 585 °C furnace anneal before UHT annealing.

The observation of similar dopant profiles for the 760 and 800 °C iRTP anneals in Figure 5-1 suggests that there is a temperature range in which the iRTP anneal will result in equivalent dopant profiles, independent of the 585 °C furnace anneal before UHT annealing. Indeed, it was shown in Chapter 4 that a iRTP temperature of approximately 750-800 °C can be used without any additional diffusion other than that observed due to B diffusion in α -Si (for a 18 keV Ge^+ pre-amorphization to $1\times 10^{15}/\text{cm}^2$). Using an iRTP anneal within this temperature range will result in junctions with improved characteristics, as this temperature range defines the lower limit associated with the junction abruptness and x_j for the 48 keV pre-amorphization implant. It should be noted

that this temperature range may be lower for the wafer with the 585 °C furnace anneal before UHT annealing because of the possible evolution of some excess interstitials.

Figure 5-1 shows that each profile for an iRTP anneal temperature above 800 °C display increased diffusion behavior in addition to that observed during SPER of the implantation-induced amorphous layer, independent of the 585 °C furnace anneal before UHT annealing. The 900 °C iRTP anneal increased the x_j from 19.3 to 22.5 nm and from 20.0 to 22.4 nm when compared to the 760 and 800 °C iRTP anneals for the wafer without and with the 585 °C furnace anneal before UHT annealing, respectively. It is unclear why the 900 °C iRTP anneal produces less of a diffusion enhancement for the sample with the 585 °C furnace anneal before UHT annealing. Both Florida Object Oriented Process Simulator (FLOOPS) simulations and calculations based on an Arrhenius equation that describes intrinsic diffusivity of B in Si estimate that approximately 2 min at 900 °C are required to produce the observed increase in x_j for the 900 °C iRTP anneal.²⁶ Since the 900 °C iRTP anneal was complete on the order of 8-10 s, the observed diffusion enhancement is presumably due to TED, independent of the 585 °C furnace anneal before UHT annealing. The PTEM results in Figure 5-2 showed that the 760, 800, and 900 °C iRTP anneals produced defect structures consisting mainly of a high density of defect clusters (although the 900 °C iRTP anneal was sufficient to also produce small dislocation loops for the wafer with the 585 °C furnace anneal before UHT annealing). These images suggest that either interstitial cluster dissolution and evolution or a non-conservative defect coarsening process of the EOR damage is responsible for the diffusion enhancement observed in the corresponding SIMS profiles for the 900 °C iRTP anneals in Figure 5-1. Additional experiments

performed in Chapter 4 provided conclusive evidence that interstitial injection from the EOR damage is responsible for the initial diffusion enhancement observed for the 900 °C iRTP anneal, and presumably also causes the diffusion enhancement observed for the wafer with the 585 °C furnace anneal before UHT annealing.

While the 1000 °C iRTP anneal increased the x_j from 19.3 to 32.1 nm and from 20.0 to 32.7 nm when compared to the 760 and 800 °C iRTP anneals for the wafer without and with the 585 °C furnace anneal before UHT annealing, respectively, the 1100 °C iRTP anneal increased the x_j from 19.3 to 36.1 nm and from 20.0 to 37.8 nm when compared to the 760 and 800 °C iRTP anneals for the wafer without and with the 585 °C furnace anneal before UHT annealing, respectively. It is believed that the increase in x_j for the 1000 and 1100 °C iRTP anneals is associated with TED, as both FLOOPS simulations and calculations based on an Arrhenius equation that describes intrinsic diffusivity of B in Si for each of these anneal temperatures estimates that approximately 2 min at 1000 °C and 20 s at 1100 °C are required to produce the corresponding increase in x_j .²⁶ Since these iRTP anneals were complete within approximately 8-10 s, the increased diffusion behavior is believed to be due to additional interstitial injection from the EOR damage. The observation that the 1100 °C iRTP anneal only requires 20 s at 1100 °C to be described in terms of intrinsic diffusivity suggests that the diffusion enhancement is decaying.

Figure 5-1a shows that the 900, 1000, and 1100 °C iRTP anneals increase the x_j 3.2, 12.8, and 16.8 nm, respectively, compared to the 760 and 800 °C iRTP anneals for the wafer without the 585 °C furnace anneal before UHT annealing. Figure 5-1b shows

that the 900, 1000, and 1100 °C iRTP anneals increase the x_j 2.4, 12.7, and 17.8 nm, respectively, compared to the 760 and 800 °C iRTP anneals for the wafer with the 585 °C furnace anneal before UHT annealing. These results show that the largest difference in the diffusion behavior is observed for the 1000 °C iRTP anneal, independent of the 585 °C furnace anneal before UHT annealing. This increase in diffusion behavior could be because a significant fraction of the interstitial flux toward the surface, which is capable of reaching the B profile during the 1000 °C iRTP anneal but is less pronounced for the 900 °C iRTP anneal. Such a significant pulse of TED was shown to occur for 40 keV Si⁺ implants to both $2 \times 10^{13}/\text{cm}^2$ and $5 \times 10^{13}/\text{cm}^2$, which are below the amorphization threshold, during the first 15 s of annealing at 700 °C.¹¹³ This pulse of TED was shown to be in excess of the enhancement caused by {311} defect dissolution, suggesting a different source of interstitials was responsible for the observed diffusion enhancement.¹¹³ Although a similar mechanism may be causing such a large diffusion enhancement for the 1000 °C iRTP anneal in Figure 5-1, it is also expected that interstitial injection from the extended defects in the EOR damage region is also contributing to the diffusion behavior during the 1000 °C iRTP anneal.

The PTEM images for the 1000 °C iRTP anneals in Figure 5-2 showed that they are sufficient for producing a defect structure mainly consisting of {311} defects and dislocation loops. The corresponding SIMS profiles in Figure 5-1 showed a diffusion enhancement with respect to the 900 °C iRTP anneals suggesting that, in addition to any interstitial pulse that may have occurred during early stages of annealing, the extended defects may have released some of the interstitials required to produce the observed diffusion enhancement. The diffusion enhancement could have been caused by a

combination of {311} defect dissolution, non-conservative dislocation loop formation, and/or dislocation loop ripening and dissolution.³ The PTEM images for the 1100 °C iRTP anneals in Figure 5-2 showed that {311} defect dissolution is complete between 1000 and 1100 °C; therefore, the diffusion enhancement observed in the corresponding SIMS profiles in Figure 5-1 can be associated with interstitial injection from {311} defect dissolution and possibly dislocation loop ripening and dissolution.³ The stability of the dislocation loops after the 1100 °C iRTP anneals is not known, and an additional diffusion enhancement may occur during subsequent thermal processing because of dislocation loop dissolution.

Figure 5-3a showed that the 760 and 800 °C intermediate temperatures result in similar profiles after the 1200 °C fRTP anneal, and that the 900 °C intermediate temperature results in a degraded junction abruptness and increased x_j because of the diffusion that occurred during the intermediate temperature anneal for the wafer without the 585 °C furnace anneal before UHT annealing. Both FLOOPS simulations and calculations based on an Arrhenius equation that describes intrinsic diffusivity of B in Si estimate that approximately 3 and 13 ms at 1200 °C are required to produce the observed 0.6 and 1.2 nm increase in x_j for both the 760 and 800 °C and 900 °C intermediate temperatures, respectively.²⁶ Since the T-t profiles for the fRTP anneals are unavailable, it is unclear whether the 1.2 nm increase in x_j for the 900 °C intermediate temperature is due to TED. Although these time scales are similar to those used during the fRTP anneal, it is not known whether interstitial recombination within the bulk or a lack of thermal energy prevented significant diffusion during the anneal. It is reasonable to assume that the time duration of the fRTP anneal is too short to allow enough interstitials to diffuse

toward the surface to cause a significant diffusion enhancement.² Similar comments can be made for the diffusion behavior observed during the 1350 °C fRTP anneal shown in Figure 5-5a for the wafer without the 585 °C furnace anneal before UHT annealing. It should be noted that the 760 and 800 °C intermediate temperatures did not result in similar profiles after the 1350 °C fRTP anneal; the 760 °C intermediate temperature resulted in a slightly shallower profile. It should be noted that the diffusion behavior during the 1350 °C fRTP anneal is greater for the 800 °C intermediate temperature than for the 900 °C intermediate temperature. Since an increase in interstitial interaction would presumably affect the profile for the 900 °C intermediate temperature more than that corresponding to the 800 °C intermediate temperature, the increase in x_j for the 800 °C intermediate temperature is expected to be due to the fact that the system measured a peak temperature of 1372 °C (as opposed to the desired 1350 °C) and that this increase in temperature was sufficient for producing the observed increase in diffusion behavior. Figure 5-3 showed that the 760 °C intermediate temperature produced a similar diffusion enhancement after the 1200 °C fRTP anneal, independent of the 585 °C furnace anneal before UHT annealing; however, Figure 5-3b showed that the 800 °C intermediate temperature produced an increase in diffusion behavior during the 1200 °C fRTP anneal for the wafer with the 585 °C furnace anneal before UHT annealing. This was not observed for the wafer without the 585 °C furnace anneal before UHT annealing in Figure 5-3a. This provides some evidence that the 585 °C furnace anneal is capable of evolving the interstitials to a point where they are able to increase the diffusion behavior during UHT annealing. Similar to Figure 5-5a, Figure 5-5b showed

that the 760 and 800 °C intermediate temperatures did not result in similar profiles after the 1350 °C fRTP anneal; the 760 °C intermediate temperature resulted in a slightly shallower profile. Similar to what was observed in Figure 5-5a, the diffusion behavior during the 1350 °C fRTP anneal is somewhat greater for the 800 °C intermediate temperature than that observed for the 900 °C intermediate temperature in Figure 5-5b. The increase in x_j for the 800 °C intermediate temperature is expected to be due to the fact that the system measured a peak temperature of 1365 °C (as opposed to the desired 1350 °C) and that this increase in temperature was sufficient for producing the observed increase in diffusion behavior.

The thought that the 585 °C furnace anneal is capable of evolving the excess interstitials to a point where they are able to increase the diffusion behavior during UHT annealing is supported by Figure 5-6, which shows the SIMS data for each sample using an iRTP or intermediate temperature of 800 or 900 °C, respectively, without and with the 585 °C furnace anneal before UHT annealing. As can be seen in Figure 5-6a, the wafer with the 585 °C furnace anneal before UHT annealing results in increased diffusion behavior when compared to the wafer without the 585 °C furnace anneal before UHT annealing with an iRTP or intermediate temperature of 800 °C, independent of the peak annealing temperature. This shows that the 585 °C furnace anneal consistently produces profiles with deeper x_j when an intermediate temperature of 800 °C is used during UHT annealing, supporting the suggestion that the 585 °C furnace anneal is capable of evolving the excess Si interstitials to a point where they are able to increase the diffusion behavior during UHT annealing. A similar, but less obvious, trend was observed when

plotting the data corresponding to the 760 °C intermediate temperature (not shown). It should be noted that the profile produced by the 800 °C iRTP anneal for the wafer with the 585 °C furnace anneal before UHT annealing is similar to that after the 585 °C furnace anneal only. This suggests that the difference between the profiles produced by the 800 °C iRTP anneal without and with the 585 °C furnace anneal before UHT annealing is due to the relatively slow regrowth velocity of the α /c interface during the 585 °C furnace anneal, which increases the amount of time available for B diffusion in α -Si. In other words, the difference between the two profiles corresponding to the 800 °C iRTP anneals is due to additional B diffusion in α -Si and not TED. The differences between the profiles that were subject to an fRTP anneal, however, are presumed to be due to TED. Figure 5-6b shows the SIMS data for each sample using an iRTP or intermediate temperature of 900 °C without and with the 585 °C furnace anneal before UHT annealing. As can be seen, annealing with an iRTP or intermediate temperature of 900 °C results in similar profiles independent of the 585 °C furnace anneal before UHT annealing. This shows that the 585 °C furnace anneal is capable of resulting in an observable difference in the diffusion behavior during UHT annealing only when the intermediate temperature is sufficiently low; the 760 and 800 °C intermediate temperatures consistently result in increased diffusion behavior when the 585 °C furnace anneal is performed before UHT annealing; however, the 900 °C intermediate temperature results in similar profiles independent of the 585 °C furnace anneal before UHT annealing. This observation is the focus of the following discussion.

Oxidation experiments used to inject excess interstitials into a Si substrate have shown that B diffuses primarily by the following kick-out reaction



where I is a Si self-interstitial, B_s is a substitutional B atom, and B_i is an interstitial B atom.²¹¹ It was shown that the forward reaction is significantly exothermic (~ 1 eV), with a reaction barrier less than 0.3 eV.²¹¹ It has been reported that most dopants diffuse irregularly, switching between a fast migrating intermediate species (such as a B_i) and a less rapidly diffusing species (such as B_s).²¹² When an intermediate migrating species is formed by an exothermic reaction, a certain amount of thermal energy (in addition to the migration energy) is required to end the migration.²¹³ As a result, the migration distance increases as the diffusion temperature is reduced according to

$$\lambda = \lambda_0 \exp\left(\frac{E_\lambda}{kT}\right), \quad (5.2)$$

where λ is the mean projected path length between the formation of B_i and its return to a substitutional site, λ_0 is the jump distance between adjacent low-energy interstitial sites, E is the activation energy of the process, k is Boltzmann's constant, and T is temperature.²¹³ It should be noted that Equation 5.2 implies that a dopant atom in an interstitial site will migrate over significant distances at low temperature.²¹³ Cowern *et al.* reported the value of λ for B in Si which was found to increase from approximately 5 nm at 800 °C to about 10 nm at 625 °C, consistent with $\lambda_0 \approx 0.05$ nm and $E \approx 0.4$ eV.²¹¹ To date, three different forms of TED have been observed and each form is known to function on its own time scale.¹¹³ For low damage levels (e.g., implantation doses less than $1 \times 10^{11}/\text{cm}^2$) and low annealing temperatures (i.e., less than 600 °C), an ultra-fast diffusion pulse was observed.^{113,114} In Ref. 213, molecular beam epitaxy (MBE) was used to prepare two B doped layers with a width of about 7 nm

and a peak B concentration of approximately $6 \times 10^{17}/\text{cm}^3$ at depths of 75 and 480 nm below the substrate surface.²¹³ These wafers were subsequently implanted with 50 keV Si⁺ to either 1×10^{10} or $1 \times 10^{11}/\text{cm}^2$, which are below the amorphization threshold, at room temperature using a tilt angle of 5° to minimize channeling effects. It should be noted that these implant doses are below the threshold for {311} defect formation, which is approximately $5 \times 10^{12}/\text{cm}^2$.¹⁸ The wafers were then annealed in a N₂ ambient at 450 and 550 °C for times ranging between 30 s and 15 min. The corresponding SIMS results showed that the B atoms in the shallow (i.e., closer to the substrate surface) marker layer diffused approximately 100 nm, independent of the annealing time. That was the first time an implantation-induced TED pulse was observed below 600 °C. The pulse of TED was attributed to freely moving Si interstitials emitted from the as-implanted interstitial/vacancy (*I/V*) distribution.^{114,213} Previous studies of TED after high dose implantation showed an activation energy of ~ 4-5 eV, which would suggest a negligibly slow diffusion transient at 450 °C, which was not observed. The slope of the B profile observed through the SIMS results suggested a value of λ around 80 nm, consistent with the temperature trend extrapolated from their earlier studies at high temperature.²¹¹ The increase in λ with decreasing temperature illustrates the increasing difficulty of the B_{*i*} returning to a substitutional site.²¹³ The results of that experiment showed the effect of the kick-out reaction followed by long range dopant diffusion at low temperature.²¹³

Another experiment, using the same MBE grown material as in Ref. 213, was performed to investigate the suggestion that TED is driven by the annealing of implantation-induced interstitial clusters.^{5,214} These wafers were implanted below the amorphization threshold with 50 keV Si⁺ to either 1×10^{11} or $1 \times 10^{14}/\text{cm}^2$, in order to

investigate the transition between the formation of isolated point-defects for the low dose implant to $1 \times 10^{11}/\text{cm}^2$ and the formation of a damaged microstructure for the high dose implant to $1 \times 10^{14}/\text{cm}^2$.¹¹⁴ These wafers were then annealed at 550 °C for 15 min in a N₂ ambient. The SIMS results showed that, for the low dose implant, only the B in the shallow marker layer experiences a significant amount of diffusion. Only the deeper (i.e., further from the substrate surface) marker layer showed a similar diffusion enhancement for the high dose implant, which occurred on the same time scale as that observed for the low dose implant. That similarity was explained by the density of point-defects in the tail region of the high dose implant which was similar to that near the projected range of the low dose implant. It should be noted that no additional diffusion was observed after annealing the samples for 24 hr at 550 °C. That showed that essentially all the free excess point-defects produced by the implantation process recombined within the first 15 min of annealing at 550 °C.¹¹⁴ Additional experiments were performed to investigate the effect of {311} defect evolution and dissolution on B diffusion behavior during thermal annealing at 800 °C for times ranging from 10 s to 30 min. After annealing at 800 °C for 10 s, the SIMS profiles corresponding to the low dose implant were similar to those after 15 min at 550 °C. That observation was consistent with the suggestion that a weakly activated ultra-fast diffusion dominates in regions of low implant damage density. Further annealing of the low dose implant at 800 °C resulted in no additional diffusion enhancement. That result was consistent with the data that showed that no additional diffusion is observed after the ultra-fast diffusion pulse when annealing the samples for 24 hr at 550 °C. The defect evolution and dissolution of the damage produced by the high dose implant resulted in a significant

amount of additional diffusion than was observed for the low dose implant. The SIMS results showed that, after annealing at 800 °C for 10 s, the diffusion behavior observed for the marker layer was similar to the effect already seen at 550 °C; the shallow marker layer shows less of a diffusion enhancement than the deeper marker layer. The lack of diffusion observed for the shallow marker layer after the 800 °C anneal for 10 s was explained by the TEM results, which showed the formation of {311} defects in the region of the shallow marker layer. The formation of {311} defects in that region of the sample illustrates the higher interstitial density for the high dose implant. The growth of these {311} defects involves the capturing of interstitials, thereby reducing the driving force for the reaction described in Equation 5.1 and preventing TED in the region where the {311} defects are formed. Additional SIMS results showed that annealing the high dose implant at 800 °C for 15 min resulted in an additional diffusion enhancement. The corresponding TEM results showed that {311} defect dissolution was complete within 15 min of annealing at 800 °C, showing that the {311} defects are the primary source of interstitials and are the main driving force for the additional diffusion enhancement observed for the high dose implant. This is the second of the three forms of TED and is typically observed when annealing higher implant doses (e.g., 5×10^{12} - $1 \times 10^{14}/\text{cm}^2$) at higher temperatures (e.g., 670-815 °C).^{2,18,40,113} [The third form of TED is observed for higher implant doses (e.g., $> 1 \times 10^{14}/\text{cm}^2$). There, EOR dislocation loops are created which are more stable than {311} defects and result in long-term diffusion enhancements.]^{18,113} These results show that the release of interstitials produced by Si⁺ implantation to doses below the amorphization threshold occurs on two significantly different time scales; an ultra-fast diffusion pulse or the evolution and dissolution of

{311} defects. The release of interstitials from the {311} defects causes a secondary (much slower) diffusion transient. The ultra-fast diffusion pulse controls the overall diffusion behavior at low implantation doses, while at high doses the evolution and dissolution of {311} defects has a more dominating effect.

An additional experiment illustrating the ultra-fast diffusion pulse was recently reported.¹¹³ In that study, nine 20 nm wide B doping spikes were incorporated into epitaxially grown Si layers at 0.1 μm intervals. The peak concentration of the spikes was approximately $5 \times 10^{17}/\text{cm}^3$ in an attempt to minimize the influence of the B spikes on the interstitial indiffusion. These wafers were implanted with 40 keV Si⁺ to either 2×10^{13} or $5 \times 10^{13}/\text{cm}^2$, which are below the amorphization threshold. The wafers were then annealed at 700 °C for times ranging from 15 s to 40 min. The SIMS results showed that the B diffusivity during the first 15 s was considerably higher than during subsequent annealing. The average diffusivity enhancement was about 2×10^5 during the first 15 s of annealing and dropped to approximately 1×10^4 in the period between 15 s and 2 min. It was shown that the pulse of TED was in excess of the enhancement caused by {311} defect dissolution, suggesting a different source of interstitials.¹¹³ As was shown, the dependence of TED on the implant dose was very weak during the early stages of annealing and was only noticeable after longer annealing times. A similar dose independence of the TED enhancement factor, and dose dependence of the TED time scale, was reported by Angellucci *et al.*²¹⁵ It was concluded that the excess interstitials diffused over a distance of at least 0.6 μm in 15 s.¹¹³ It was suggested that this ultra-fast diffusion pulse may occur because a small fraction of excess interstitials that escape capture by {311} defects and diffuse into the structure. It is also possible that the

ultra-fast pulse is itself controlled by submicroscopic defects that are less stable than {311} defects. In either case, the ultra-fast diffusion pulse decays into the slower TED phase as the absorption and emission rates of interstitials to and from {311} defects begin to affect the overall diffusion profile.¹¹³

Thus far, the ultra-fast diffusion pulse has only been discussed in terms of damage produced by Si⁺ implantation and its effect on the diffusion behavior of epitaxially incorporated B doped layers. It is well known that B implantation into c-Si also creates a certain amount of lattice damage, and it is of interest to review data that provides evidence of a similar ultra-fast diffusion pulse when B implantation is used.

Napolitani *et al.* implanted epitaxially grown (100) oriented Si layers with either 0.5 or 1 keV B⁺ to $1 \times 10^{14}/\text{cm}^2$ using 7° tilt and 30° twist, presumably in an attempt to reduce the amount of channeling during the implant.²¹⁶ The wafers were then annealed over the temperature range of 600-750 °C for times ranging between 1 s and 20 min. The SIMS results showed that, for both implant conditions, a significant amount of TED occurred during the 600 °C anneal. It should be noted that the diffusion transient was complete within 10 min of annealing at 600 °C. While the x_j (measured at $1 \times 10^{17}/\text{cm}^2$) of the 0.5 keV implanted wafer gradually increased up to approximately 8 nm over the time range of 10 s to 10 min of annealing at 600 °C, the 1 keV implanted wafer experienced a comparable increase in x_j after only 10 s of annealing at 600 °C. The x_j of the 1 keV implanted wafer increased an additional 9 nm over the time range of 10 s to 10 min, showing that the overall diffusion behavior is dependent on and increases with the B⁺ implant energy. Since the amount of diffusion is directly proportional to the excess interstitial concentration, it was presumed that the 1 keV B implant created a higher

interstitial concentration when compared to the 0.5 keV implant. Additional SIMS results showed that if the portion of the ultra-fast diffusion pulse observed for the 1 keV implant is added to the overall diffusion behavior of the 0.5 keV implant, then the resulting profile resembles the overall diffusion behavior observed for the 1 keV implant. These results showed that there were two different sources releasing the interstitials that caused the observed diffusion enhancements; one independent of the implant energy, and one only observed for the 1 keV implant. It should be noted that the amount of ultra-fast diffusion was almost independent of the anneal temperature in the range investigated (i.e., 600-750 °C), and was assumed to be the effect of the ‘weakly bound excess interstitials’ (WBEI) created by implants with energies higher than 0.5 keV.²¹⁶ It was suggested that B containing interstitial clusters were the favored source of interstitials which cause the corresponding diffusion enhancement.

An additional experiment was performed to better understand the observation that an ultra-fast diffusion pulse that occurs when increasing the B implant energy from 0.5 to 1 keV.²¹⁷ There, Schroer *et al.* used surface-layer removal in order to determine the source of interstitials that produce the two types of diffusion enhancements observed during post-implant thermal processing. In that experiment, an epitaxially grown Si layer was grown on 150 mm (100) Si substrates. This layer was subsequently implanted with either 0.5 or 1 keV B⁺ to $1 \times 10^{14}/\text{cm}^2$ and then sectioned into pieces. The surface layer of some of the samples was removed by repeatedly etching the material in a 3% HF solution (to remove SiO₂ from the substrate surface, thereby making the surface hydrophobic) and a 5% H₂O₂ solution (to re-oxidize the substrate surface, thereby making the surface hydrophilic). The H₂O₂ solution was maintained at 75 °C. After etching the surface

layer, the samples were annealed at 750 °C for times ranging between 1 to 60 s. The 1 s anneal was used to determine the amount of diffusion that occurs because the ultra-fast diffusion pulse (because this is longer than the time constant of the ultra-fast pulse and shorter than the time constant associated with the other transient diffusion processes).²¹⁷ The SIMS results showed that, when the sample with the 1 keV B⁺ implant to $1 \times 10^{14}/\text{cm}^2$ is not etched, a significant amount of diffusion occurred during 1 s of annealing at 750 °C. Additional SIMS results showed that this ultra-fast diffusion pulse was not affected by etching the first 5.8 nm of the substrate surface before annealing; however, after etching 12.8 nm of the substrate surface, the diffusion behavior during subsequent thermal annealing was significantly less than that observed for either the as-implanted sample without etching or the sample that removed 5.8 nm of the substrate surface before post-implant thermal processing. This difference was attributed to the removal of the peak region of the implanted B profile.^{217,218} It was concluded that the source of the TED for the 1 keV B⁺ implant to $1 \times 10^{14}/\text{cm}^2$ is located within the first 6 nm of the substrate surface, which was near the projected range of the B implant. The authors then divided the defect clusters causing the observed diffusion enhancements into two different classes, which are responsible for the two different types of TED. They suggested that the defect clusters causing the ultra-fast diffusion pulse were located beyond the projected range of the B implant, whereas those causing the so-called ‘fast’ diffusion were located closer to the surface.²¹⁷ The authors used qualitative TRansport of Ions in Matter (TRIM) simulations to show that the momentum transfer of the B ions to the displaced Si atoms cause a variation of the ratio of B concentration to the excess interstitial concentration.²¹⁹ They found that this ratio was higher near the surface and

reached a value of approximately 1 for a depth deeper than about 6 nm.²¹⁷ The authors proposed that the shallower clusters have fewer interstitials when compared to the deeper clusters which are rich in interstitials. They concluded that the interstitial-rich clusters can be attributed to the ultra-fast diffusion pulse, and the low interstitial-content clusters correspond to the so-called ‘fast’ TED.²¹⁷

The current discussion suggests that the increase in diffusion behavior observed for the 760 and 800 °C intermediate temperatures with the additional 585 °C furnace anneal before UHT annealing is due to a pulse of TED that occurs during the early stages of annealing. This pulse of TED had no observable effect on the SIMS results when the intermediate temperature was raised to 900 °C presumably because at such a high intermediate temperature the pulse of TED completes during the early stages of annealing and would, therefore, not produce an increase in diffusion behavior due to the fact that once the interstitials recombine at the substrate surface they are no longer able to enhance its diffusion behavior. In other words, the 760 and 800 °C intermediate temperatures are insufficient to complete the initial ultra-fast diffusion pulse and the addition of the 585 °C furnace anneal before UHT annealing provides enough thermal energy to increase its effect on the overall diffusion behavior. The 900 °C intermediate temperature, however, shows no dependence on the 585 °C furnace anneal before UHT annealing presumably because the ultra-fast diffusion pulse is complete during the early stages of annealing. To the author’s knowledge, this is the first time an ultra-fast diffusion pulse was observed when amorphizing conditions were used before post-implant thermal processing. It should be noted that the amount of diffusion observed during the ultra-fast diffusion pulse is significantly less than that observed in Ref. 211, 213, 216, and 217. This may be

attributed to the type of damage created by the pre-amorphization implant and its effect on interstitial injection during subsequent thermal processing. For example, it was shown that the amount of interstitial injection from the EOR damage can be significantly greater into the bulk of the substrate when compared to that toward the surface.²⁰⁵ This difference may account for the observed decrease in diffusion during the ultra-fast diffusion pulse.

It was suggested in Ref. 113 that this ultra-fast diffusion pulse either occurs because a small fraction of excess interstitials that escape capture by {311} defects and diffuse into the B marker layer structure or that the ultra-fast pulse might itself be controlled by submicroscopic defects that are less stable than {311} defects. An additional experiment was performed to better understand the mechanisms controlling the ultra-fast diffusion pulse presumed to be complete during a 900 °C iRTP anneal. For this experiment, three 200 mm 3-5 Ω·cm (100) n-type CZ grown Si wafers were pre-amorphized with an 80 keV Ge⁺ implant to doses of 0.5, 1, and $2 \times 10^{15}/\text{cm}^2$. Each wafer was subsequently implanted with 1 keV B⁺ to $1 \times 10^{15}/\text{cm}^2$. The implants were carried out in the drift mode and performed at room temperature with the ion beam normal to the surface plane using an Applied Materials Leap-II system. The implant parameters were monitored to ensure they remained within predetermined limits. The pre-amorphization energy of the Ge⁺ implant was increased to 80 keV to produce the thickest possible continuous amorphous layer under the available implant capabilities, which was determined to be approximately 110 nm by XTEM imaging (not shown). The pre-amorphization dose was varied to investigate the effect of the excess interstitial population on the diffusion behavior during post-implant thermal processing. Each of the

wafers were then sectioned and subject to 800, 900, and 1000 °C iRTP anneals to investigate the effect of the pre-amorphization dose on the diffusion behavior during UHT annealing. All of the anneals were carried out in a N₂ ambient with less than 10 ppm O₂ using a ramp-up rate of 400 °C/s, and a ramp-down rate which was estimated to be approximately 150 °C/s at 900 °C. It should be noted that XTEM results (not shown) revealed that recrystallization of the implantation-induced amorphous layer was complete during the 800 °C iRTP anneal, independent of the pre-amorphization dose.

Figure 5-8 shows the SIMS results for the 800 °C iRTP anneal for each pre-amorphization dose used in this experiment. As can be seen the as-implanted profile has a junction abruptness and x_j of 3.4 nm/dec and 21.5 nm, respectively. The 800 °C iRTP anneal degrades the junction abruptness and increases the x_j to 3.6 nm/dec and 25.3 nm, respectively, independent of the pre-amorphization dose. This shows that, although the defect complexes associated with α-Si are expected to be similar to point-defects and small point-defect clusters in heavily damaged c-Si (because the fact that both are fourfold coordinated covalently bonded materials), the density of point-defects and small point-defect clusters appears to be independent of the pre-amorphization dose presumably because damage accumulation saturates after an amorphous state is reached.^{2,198} This is assuming of course that such point-defects have an effect on B diffusion in α-Si; however, if B diffusion in Si is inherently faster in the amorphous phase when compared to the crystalline phase (i.e., independent of the number of point-defects complexes in α-Si), then it can be said that the B undergoes the same amount of diffusion due to the fact that it spends approximately the same amount of time in the amorphous phase before complete recrystallization of the implantation-

induced amorphous layer. Figure 5-9 shows the corresponding PTEM images for each of the pre-amorphization doses after the 800 °C iRTP anneal. As can be seen, the 800 °C iRTP anneal produces a high density defect structure consisting of defect clusters.^{9,184} These defect clusters are approximately 4 to 10 nm and 4 to 12 nm in diameter for the 5×10^{14} and $2 \times 10^{15}/\text{cm}^2$ pre-amorphization implants, respectively. Although the morphology of the defects appears independent of the pre-amorphization dose over this implant range, the average density of these defects increases with increasing pre-amorphization dose as would be expected from the greater amount of damage that resides beyond the original α/c interface.¹⁸⁴ The SIMS results for the 900 °C iRTP anneal for each pre-amorphization dose used in this study are shown in Figure 5-10. Similar to the data in Figure 5-1, the 900 °C iRTP anneal produces an increase in diffusion behavior when compared to that observed during the 800 °C iRTP anneal. The junction abruptness degrades to 5.4, 5.5, and 5.5 nm/dec and the x_j increases to 27.5, 28.5, and 29.0 nm for the 0.5, 1, and $2 \times 10^{15}/\text{cm}^2$ pre-amorphization implants, respectively. This shows, quite remarkably, that both the 48 and 80 keV pre-amorphization implants to $5 \times 10^{14}/\text{cm}^2$ result in the same junction abruptness after a 900 °C iRTP anneal. It should be noted that the junction abruptness after a 900 °C iRTP anneal is relatively independent of the pre-amorphization dose. This SIMS data also show that, even though the 800 °C iRTP anneal produced the same profile independent of the pre-amorphization dose, the amount of diffusion that occurs during the 900 °C iRTP anneal increases with increasing pre-amorphization dose. The corresponding PTEM images for each pre-amorphization dose after the 900 °C iRTP anneal are shown in Figure 5-11. As can be seen, the 900 °C iRTP anneal produces a high density defect

structure consisting of defect clusters.^{9,184} These defect clusters are approximately 4 to 14 nm and 4 to 18 nm in diameter for the 5×10^{14} and $2 \times 10^{15}/\text{cm}^2$ pre-amorphization implants, respectively, which are on average slightly larger than those produced during the 800 °C iRTP anneal. The defect morphology that forms during the 900 °C iRTP anneal is independent of the pre-amorphization dose. Although the defect density remains relatively constant, the average defect size increases with increasing pre-amorphization dose. This data, together with the SIMS data in Figure 5-10, provides evidence that the ultra-fast diffusion pulse observed in Figure 5-6 is because a small fraction of excess interstitials that escape capture by the extended defects and diffuse toward the substrate surface. In other words, it was shown that the excess interstitials produced by a pre-amorphization implant tend to form small defects clusters during a 900 °C iRTP anneal. During the formation of these defects, some fraction of excess interstitials were released from the EOR damage region producing the observed diffusion enhancement for the 900 °C iRTP anneal in Figure 5-10. Since an increase in the B diffusion behavior occurred with increasing pre-amorphization dose, it can be said that more interstitials were able to escape capture by the extended defects and cause the observed increase in diffusion behavior. It is also possible that the ultra-fast pulse is itself controlled by submicroscopic defects that are less stable than {311} defects; however, these defects would need to form below the original α/c interface since the corresponding diffusion behavior increases with increasing pre-amorphization dose and the only difference between the three pre-amorphization implants is the interstitial population just beyond the original α/c interface. Figure 5-12 shows the SIMS results for the 1000 °C iRTP anneal for each pre-amorphization dose used in this experiment. As

can be seen, the 1000 °C iRTP anneal degrades the junction abruptness to 9.7, 9.3, and 9.3 nm/dec and increases the x_j to 40.0, 40.0, and 40.0 nm for the 0.5, 1, and $2 \times 10^{15}/\text{cm}^2$ pre-amorphization implants, respectively. The corresponding PTEM images for each of the pre-amorphization doses after the 1000 °C iRTP anneal are shown in Figure 5-13. The 1000 °C iRTP anneal produces a defect structure consisting mainly of {311} defects, and dislocation loops. The {311} defects range from 27 to 73 and average 49 nm in length and the dislocation loops range from 15 to 27 and average 23 nm in diameter for the 80 keV pre-amorphization implant to $5 \times 10^{14}/\text{cm}^2$. For the 80 keV pre-amorphization implant to $2 \times 10^{15}/\text{cm}^2$, the {311} defects range from 47 to 80 and average 62 nm in length and the dislocation loops range from 20 to 47 and average 29 nm in diameter. These results show that the average {311} defect length and dislocation loop diameter increase with increasing pre-amorphization dose. The SIMS data in Figure 5-12 show that, although the pre-amorphization dose increases up to a factor of four for the 80 keV pre-amorphization implants to 5×10^{14} and $2 \times 10^{15}/\text{cm}^2$, the 1000 °C iRTP anneal results in the same profile. Both FLOOPS simulations and calculations based on an Arrhenius equation that describes intrinsic diffusivity of B in Si for each of these anneal temperatures estimates that approximately 3 min at 1000 °C are required to produce the corresponding increase in x_j (when compared to the x_j produced by the 800 °C iRTP anneal).²⁶ Since these iRTP anneals were complete within approximately 8-10 s, the increased diffusion behavior is presumably due to additional interstitial injection from the EOR damage region. As was mentioned for the 1000 °C iRTP anneal in Figure 5-1a, the increase in diffusion behavior for the 1000 °C iRTP anneal is most likely because a significant fraction of the interstitial flux toward the surface which is capable of reaching

the B profile during the 1000 °C iRTP anneal but is less pronounced for the 900 °C iRTP anneal. Such a significant pulse of TED was shown to occur for 40 keV Si⁺ implants to both $2 \times 10^{13}/\text{cm}^2$ and $5 \times 10^{13}/\text{cm}^2$ during the first 15 s of annealing at 700 °C.¹¹³ This pulse of TED was shown to be in excess of the enhancement caused by {311} defect dissolution, suggesting a different source of interstitials.¹¹³ As was shown, the dependence of TED on the implant dose was very weak during the early stages of annealing and was only noticeable after longer annealing times. A similar dose independence of the TED enhancement factor, and dose dependence of the TED time scale, was reported by Angellucci *et al.*²¹⁵ Although it was suggested earlier that interstitial injection from the extended defects in the EOR damage region may also be contributing to the diffusion behavior during the 1000 °C iRTP anneal, it appears as though the EOR damage has a secondary effect on the diffusion behavior during a 1000 °C iRTP anneal and that a similar dose independent mechanism may be causing such a large diffusion enhancement for the 1000 °C iRTP anneals in Figure 5-12.

The purpose of this experiment was to use a low temperature SPER anneal before UHT annealing in an attempt to obtain above solid solubility activation levels during the SPER process, and evolve the implant damage by using the UHT annealing technique. The TEM results for the wafer without and with the 585 °C furnace anneal before UHT annealing were shown in Figure 5-4 and showed that the defect clusters produced by the iRTP anneals evolve into defect structures consisting of larger defect clusters or dislocation loops during the 1200 °C fRTP anneal, which were a function of the intermediate temperature and not noticeably dependent on the 585 °C furnace anneal before UHT annealing. Although each of the images appeared to be similar in

morphology, the defects did not evolve into stable dislocation loops and may further evolve during subsequent thermal processing (releasing interstitials and resulting in a diffusion enhancement). A similar comment can be made about the defect morphologies that formed during the 1350 °C fRTP anneal when using an intermediate temperatures of either 760 and 800 °C; however, it can be seen in Figure 5-7 that the 1350 °C fRTP anneal produced a defect structure that consists of large dislocation loops when using an intermediate temperature of 900 °C, independent of the 585 °C furnace anneal before UHT annealing. These images show a defect morphology that more closely resembles a stable defect structure; one that may result in little enhanced diffusion during subsequent thermal processing and would be expected to result in least amount of junction leakage due to having the lowest dislocation line length per unit area, when compared to all other samples within this study. The TEM images for the 1350 °C fRTP anneal clearly show that although the images for the corresponding iRTP anneals in Figure 5-2 appeared to be similar in morphology, they differ in their evolution so as to produce a more stable defect structure with increasing intermediate anneal temperature for a given fRTP anneal temperature. These results show that the intermediate temperature plays a significant role not only in terms of the diffusion characteristics, but also the interstitial evolution as it relates to the final defect structure after a fRTP anneal. Although the corresponding SIMS results for the 1100 °C iRTP anneals showed an increase in B diffusion behavior with the additional 585 °C furnace anneal, this difference is negligible when compared to the amount of diffusion that would be expected from a conventional RTP spike anneal. These results clearly demonstrate the ability of the UHT annealing technique to evolve the EOR damage into a defect morphology that more closely resembles a stable defect

structure without significant dopant diffusion. It should be noted, however, that it remains to be seen if this type of defect morphology is acceptable in terms of the amount of junction leakage that results from the defects. If these defects result in too much leakage current, one could try and place the EOR defect band at a depth such that the depletion region remained outside the damaged region thereby further reducing the junction leakage.¹¹⁸

Although it is apparent that this UHT annealing technique is capable of evolving the EOR damage into a defect morphology that closely resembles a stable defect structure without significant dopant diffusion, the effect of subsequent UHT annealing on the dopant activation still needs to be investigated. It was shown in Chapter 4 that the measured R_s after an iRTP anneal can be closely estimated by the use of a theoretical calculation that compensates for the fraction of inactive dopant by truncating the concentrations above the plateau concentration (i.e., the concentration level above which inactive B cluster formation or precipitation occurs and the B remains immobile). The measured and calculated R_s values for the wafer without and with the 585 °C furnace anneal before UHT annealing are shown in Figure 5-14. The calculated values were determined by using Equations 4.5 and 4.6 in Chapter 4.²⁰⁸ It can be seen that the equation used to estimate the R_s is within 50 Ohm/sq of the measured value for most of the iRTP anneals, independent of the 585 °C furnace anneal before UHT annealing. This shows that the R_s can be accurately predicted by Equations 4.5 and 4.6. Although the measured R_s directly after the 585 °C furnace anneal is not available, it can be said with confidence that the anneal resulted in a R_s of approximately 650 Ohm/sq, which was estimated from the measured and calculated values of the 800 °C iRTP anneal for the

wafer with the 585 °C furnace anneal before UHT annealing. As can be seen in Figure 5-14, the 3 keV BF_2^+ implant to $6 \times 10^{14}/\text{cm}^2$ generally results in lower R_s values for the wafer without the 585 °C furnace anneal before UHT annealing. This is inconsistent with the thought that low temperature SPER of an implantation-induced amorphous layer should result in the highest achievable solid solubility-limited activation levels.¹¹⁸ From the calculation used to estimate the R_s , it can be said that the difference between the two sets of data is due to the corresponding plateau concentrations that form during the initial stages of annealing. In order to better illustrate the differences in the plateau concentrations, Figure 5-15 shows the SIMS results for the 800 °C iRTP anneal both without and with the 585 °C furnace anneal before UHT annealing. As can be seen, the 800 °C iRTP anneal (for the wafer without the 585 °C furnace anneal before UHT annealing) results in a profile with a plateau concentration of approximately $1.8 \times 10^{20}/\text{cm}^3$, whereas the 585 °C furnace anneal produces a plateau concentration of approximately $1.5 \times 10^{20}/\text{cm}^3$. In addition, it can be seen that performing an 800 °C iRTP anneal after the 585 °C furnace anneal has no effect on the plateau concentration, which remains approximately $1.5 \times 10^{20}/\text{cm}^3$. This data shows that the plateau concentration that forms during the early stages of annealing has a significant effect on the R_s value during post-implant thermal processing, presumably because this is the concentration below which the B atoms are electrically active. The difference between the plateau concentrations obtained with the 800 °C iRTP anneal (for the wafer without the 585 °C furnace anneal before UHT annealing) and the 585 °C furnace anneal is most likely because the temperature at which recrystallization of the implantation-induced amorphous layer occurred. It can be said that recrystallization occurred at approximately

585 °C during the furnace anneal. This can be compared to a temperature of 700 °C which is the approximate temperature at which the amorphous layer produced by the 48 keV pre-amorphization implant is presumed to completely recrystallize during ramp-up to the 800 °C iRTP anneal temperature. This temperature was estimated by the use of an Arrhenius equation that describes the regrowth velocity of an implantation-induced amorphous layer as a function of ramp rate and temperature. Figure 5-16 shows a plot of the estimated remaining amorphous layer thickness as a function of temperature for an anneal with a ramp-up rate of 400 °C/s. As can be seen, the amorphous layer remains at the original amorphous layer thickness produced by the 48 keV pre-amorphization implant (i.e., 76 nm) until approximately 625 °C where it begins to recrystallize. The recrystallization process increases exponentially with increasing temperature until the amorphous layer completely recrystallizes at a temperature of approximately 700 ± 25 °C. This estimation is consistent with the additional XTEM results (not shown) that revealed that the 760 °C iRTP anneal was sufficient to completely recrystallize the amorphous layer produced by the 48 keV pre-amorphization implant. The improved activation for the 800 °C iRTP anneal for the wafer without the 585 °C furnace anneal before UHT annealing is presumably thought to be because higher activation levels can be achieved at higher recrystallization temperatures. This idea explains why a noticeable improvement in R_s is not observed for the 800 °C iRTP anneal for the wafer with the 585 °C furnace anneal before UHT annealing; complete recrystallization of the implantation-induced amorphous layer already occurred during the 585 °C furnace anneal. The concept that higher activation levels can be achieved at higher recrystallization temperatures is the focus of Chapter 6.

It should be noted that the data in Figure 5-14 shows that the fRTP anneal significantly improves the R_s , independent of the 585 °C furnace anneal before UHT annealing. The disagreement with the calculated results shows that the active B concentrations are greater than those used in the calculation. The wafer with the 585 °C furnace anneal before UHT annealing shows that the R_s consistently decreases when the 1350 °C fRTP anneal is used compared to the 1200 °C fRTP anneal. This is not observed for the wafer without the 585 °C furnace anneal before UHT annealing, which in some cases shows that the R_s increases for the 1350 °C fRTP anneal. It should be noted that the R_s is relatively independent of the intermediate temperature for the wafer with the 585 °C furnace anneal before UHT annealing, whereas some variability remains for the wafer without the 585 °C furnace anneal before UHT annealing. Additional work is required to better understand why the calculated results do not predict the improvement in the R_s after a fRTP anneal.

Conclusion

Novel high-power arc lamp design has enabled UHT annealing as an alternative to conventional RTP for B ultra-shallow junction formation. This technique heats the wafer to an intermediate temperature (e.g., 800 °C) before discharging a capacitor bank into flash lamps, which anneals the device side of the wafer at a relatively high temperature (e.g., 1200 °C) for a few milliseconds. In addition to developing this novel UHT annealing technique, recent attention has been given to low temperature SPER of an implantation-induced amorphous layer because of its ability to activate dopants well above their solid solubility levels while minimizing the amount of diffusion that occurs during the thermal process. The most significant disadvantage of this annealing

technique is that a considerable amount of damage remains below the original α/c interface, which may give rise to a large amount of leakage current. It was shown in Chapter 4 that the UHT annealing technique is capable of evolving implant damage without being subject to a significant amount of dopant diffusion.^{118,226} The focus of this experiment is to use a low temperature SPER anneal to obtain above solid solubility activation levels, and then use the UHT annealing technique to evolve the residual damage without being subject to a significant amount of additional diffusion or dopant deactivation. Two 200 mm (100) n-type CZ grown Si wafers were pre-amorphized with 48 keV Ge⁺ implantation to $5 \times 10^{14}/\text{cm}^2$, and subsequently implanted with 3 keV BF₂⁺ molecular ions to $6 \times 10^{14}/\text{cm}^2$. One of the wafers was then subject to a 585 °C furnace anneal for 45 min to completely recrystallize the amorphous layer before UHT annealing. The wafers were sectioned and annealed under various conditions to investigate the effects of the UHT annealing technique on the resulting junction characteristics. The SIMS results showed that the 585 °C furnace anneal was sufficient to evolve the excess interstitials to a point where they increased the B diffusion behavior during UHT annealing when compared to the wafer without the furnace anneal, and that this was only observed when the intermediate temperature was sufficiently low (i.e., 760 and 800 °C). These results suggest that an ultra-fast diffusion pulse occurs during the early stages of annealing and is only noticeable when a low intermediate temperature is used, presumably due to the fact that the ultra-fast diffusion pulse is complete when higher intermediate temperatures are used (e.g., 900 °C). Additional SIMS results showed that this diffusion behavior increased with increasing pre-amorphization dose. This ultra-fast diffusion pulse is presumably because a small fraction of excess interstitials that escape

capture by the extended defects during their formation and diffuse toward the substrate surface. Since an increase in B diffusion behavior occurred with increasing pre-amorphization dose, it can be said that a larger population of interstitials escaped capture by the extended defects and caused the corresponding increase in diffusion behavior. It is also possible that the ultra-fast pulse is itself controlled by submicroscopic defects that are less stable than {311} defects; however, these defects would need to form below the original α/c interface since the only difference between the three pre-amorphization implants is the interstitial population just beyond the original α/c interface. It should be noted that the amount of diffusion that occurs during the ultra-fast diffusion pulse is significantly less than the values reported in the literature, presumably due to the fact that (under pre-amorphizing conditions) interstitial injection from the EOR damage is significantly greater into the bulk of the substrate when compared to that toward the surface. Although the TEM results show subtle differences in the EOR defect structure produced by the 48 keV pre-amorphization implant when the wafer is subject to a 585 °C furnace anneal before UHT annealing, defect morphology is relatively independent of the furnace anneal. Although it is well known that low temperature SPER of an implantation-induced amorphous layer activates dopants well above their solid solubility levels, the four-point probe results show that the 3 keV BF_2^+ implant to $6 \times 10^{14}/cm^2$ generally results in lower R_s values for the wafer without the 585 °C furnace anneal before UHT annealing. It can be said that the difference between the two sets of data is because the corresponding plateau concentrations that form during the initial stages of annealing. For example, the 800 °C iRTP anneal (for the wafer without the 585 °C furnace anneal before UHT annealing) resulted in a profile with a plateau

concentration of approximately $1.8 \times 10^{20}/\text{cm}^3$, whereas the 585 °C furnace anneal produced a plateau concentration of approximately $1.5 \times 10^{20}/\text{cm}^3$. In addition, performing an 800 °C iRTP anneal after the 585 °C furnace anneal had no effect on the plateau concentration and remained approximately $1.5 \times 10^{20}/\text{cm}^3$. The improved activation for the 800 °C iRTP anneal for the wafer without the 585 °C furnace anneal before UHT annealing is presumably thought to be because higher activation levels can be achieved at higher recrystallization temperatures. It can be said that recrystallization occurred at approximately 585 °C during the furnace anneal. This can be compared to a temperature of 700 °C, which is the approximate temperature at which the amorphous layer produced by the 48 keV pre-amorphization implant is presumed to completely recrystallize during ramp-up to the 800 °C iRTP anneal temperature. This thought offers an explanation why a noticeable improvement in R_s was not observed for the 800 °C iRTP anneal for the wafer with the 585 °C furnace anneal before UHT annealing; complete recrystallization of the implantation-induced amorphous layer already occurred during the 585 °C furnace anneal. The concept that higher activation levels can be achieved at higher recrystallization temperatures is the focus of Chapter 6.

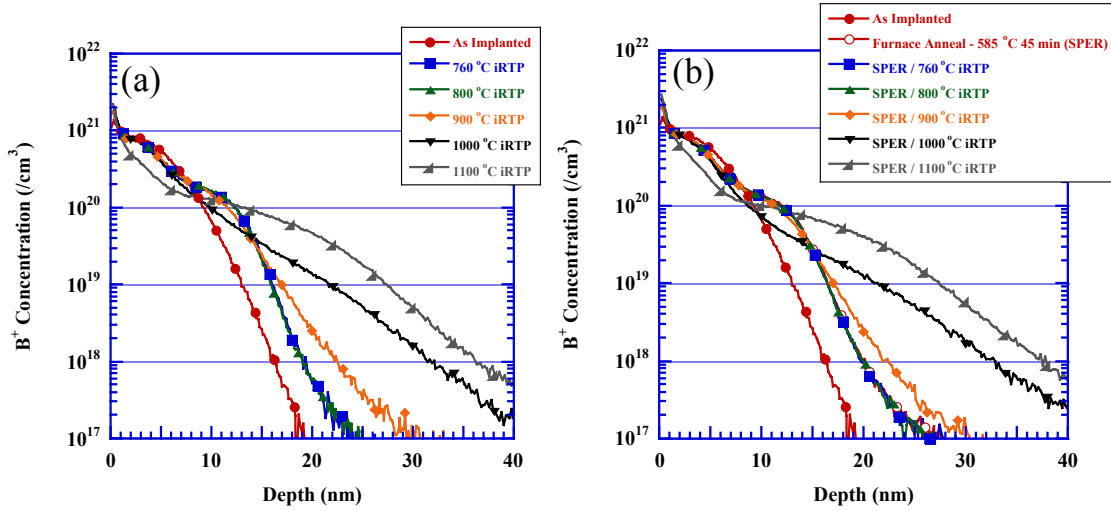


Figure 5-1 Concentration profiles showing the B^+ concentration as a function of depth for the 3 keV BF_2^+ implant to $6 \times 10^{14}/\text{cm}^2$ after each iRTP anneal temperature used in this study for the 48 keV Ge^+ pre-amorphization implant to $5 \times 10^{14}/\text{cm}^2$ (a) without and (b) with the 585°C furnace anneal for 45 min before UHT annealing. The symbols are for identifications purposes only.

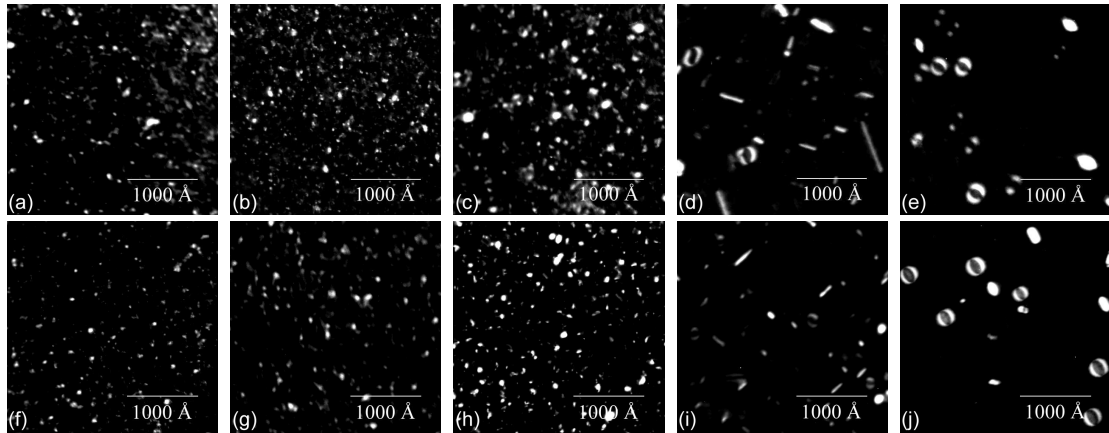


Figure 5-2 Plan-view TEM images of the damage produced by the 48 keV Ge^+ pre-amorphization implant to $5 \times 10^{14}/\text{cm}^2$ under a WBDF \mathbf{g}_{220} two-beam imaging condition after the (a)(f) 760 (b)(g) 800 (c)(h) 900 (d)(i) 1000 and (e)(j) 1100 °C iRTP anneals for the wafer without and with the 585 °C furnace anneal for 45 min before UHT annealing, respectively.

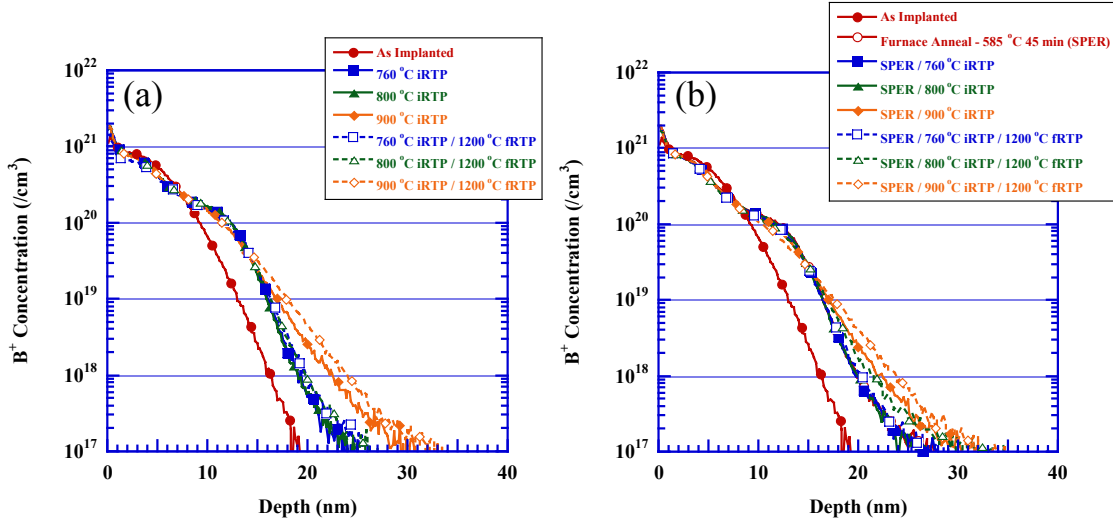


Figure 5-3 Concentration profiles showing the B^+ concentration as a function of depth for the 3 keV BF_2^+ implant to $6 \times 10^{14}/cm^2$ before and after the $1200\text{ }^\circ\text{C}$ fRTP anneal for the 48 keV Ge^+ pre-amorphization implant to $5 \times 10^{14}/cm^2$ (a) without and (b) with the $585\text{ }^\circ\text{C}$ furnace anneal for 45 min before UHT annealing. The symbols are for identifications purposes only.

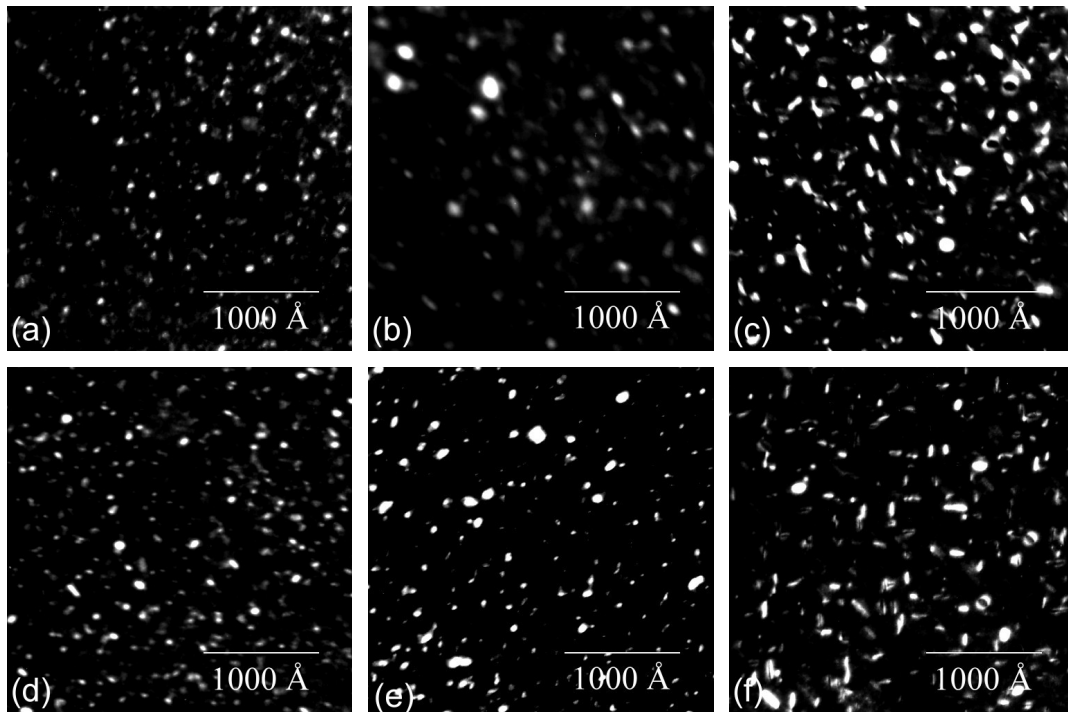


Figure 5-4 Plan-view TEM images of the damage produced by the 48 keV Ge^+ pre-amorphization implant to $5 \times 10^{14}/\text{cm}^2$ under a WBDF \mathbf{g}_{220} two-beam imaging condition for the 1200 °C fRTP anneal using a (a)(d) 760 (b)(e) 800 and (c)(f) 900 °C intermediate temperature for the wafer without and with the 585 °C furnace anneal for 45 min before UHT annealing, respectively.

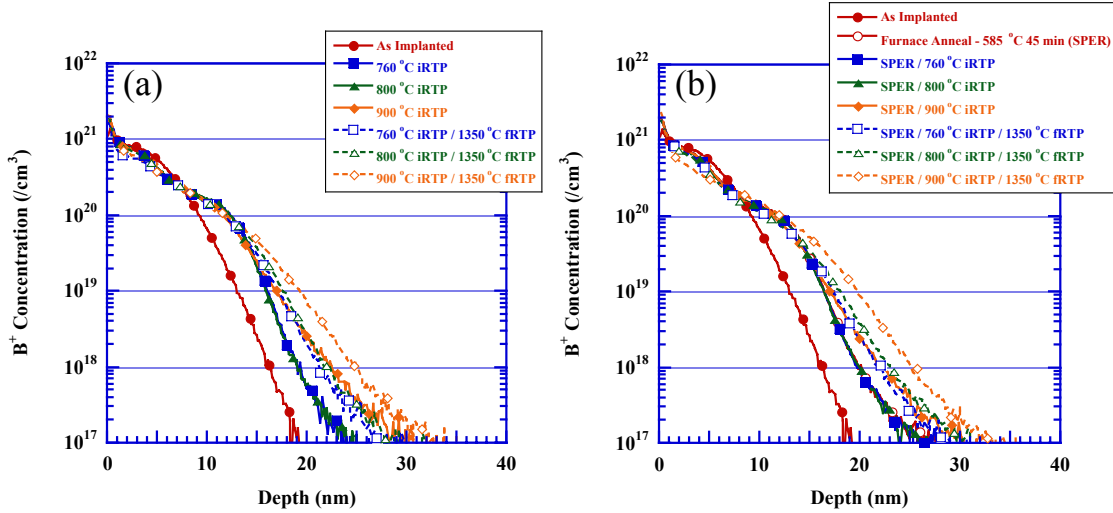


Figure 5-5 Concentration profiles showing the B^+ concentration as a function of depth for the 3 keV BF_2^+ implant to $6 \times 10^{14}/\text{cm}^2$ before and after the $1350\text{ }^\circ\text{C}$ fRTP anneal for the 48 keV Ge^+ pre-amorphization implant to $5 \times 10^{14}/\text{cm}^2$ (a) without and (b) with the $585\text{ }^\circ\text{C}$ furnace anneal for 45 min before UHT annealing. The symbols are for identifications purposes only.

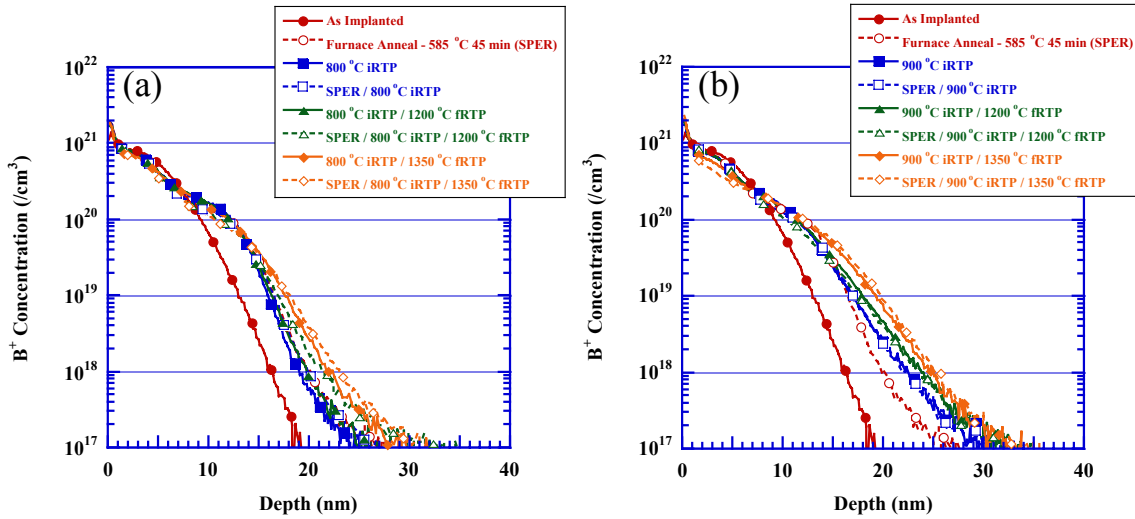


Figure 5-6 Concentration profiles showing the B^+ concentration as a function of depth for the 3 keV BF_2^+ implant to $6 \times 10^{14}/\text{cm}^2$ before and after UHT annealing with an iRTA or intermediate temperature of (a) 800°C and (b) 900°C . The profile for the 585°C furnace anneal is included to serve as a reference. Note that the furnace anneal has no effect on the diffusion behavior when an iRTA or intermediate temperature of 900°C is used. The symbols are for identifications purposes only.

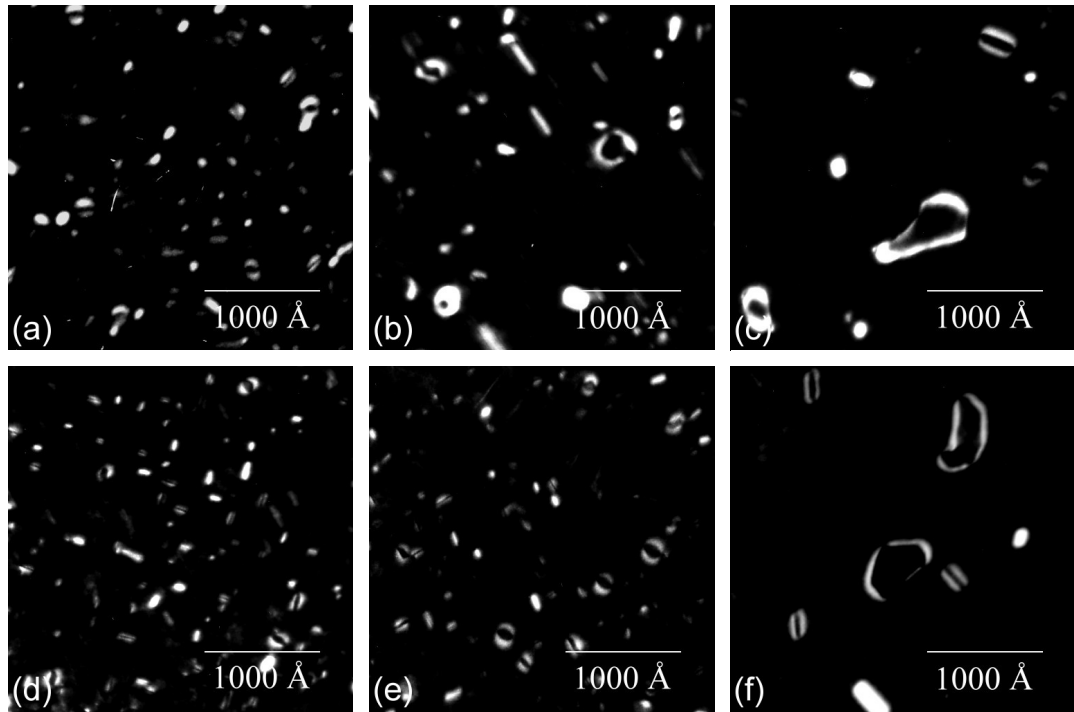


Figure 5-7 Plan-view TEM images of the damage produced by the 48 keV Ge^+ pre-amorphization implant to $5 \times 10^{14}/\text{cm}^2$ under a WBDF \mathbf{g}_{220} two-beam imaging condition for the 1350 °C fRTP anneal using a (a)(d) 760 (b)(e) 800 and (c)(f) 900 °C intermediate temperature for the wafer without and with the 585 °C furnace anneal for 45 min before UHT annealing, respectively.

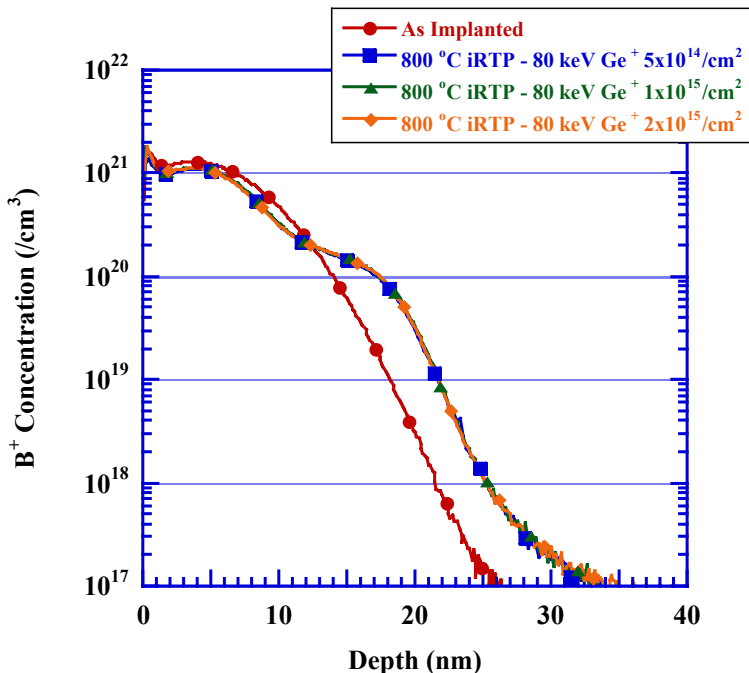


Figure 5-8 Concentration profiles showing the B⁺ concentration as a function of depth for the 1 keV B⁺ implant to $1 \times 10^{15}/\text{cm}^2$ before and after iRTP annealing at 800 °C for a substrate pre-amorphized with an 80 keV Ge⁺ implant to various doses. The symbols are for identifications purposes only.

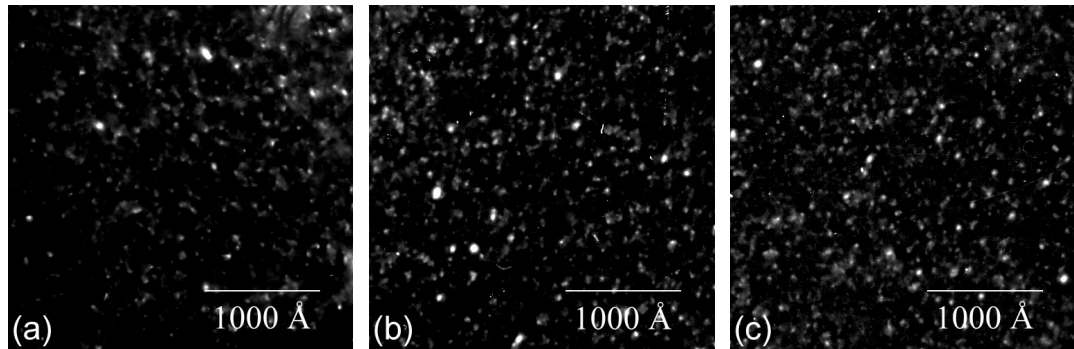


Figure 5-9 Plan-view TEM images of the damage produced by the 80 keV Ge^+ pre-amorphization implant to (a) 5×10^{14} (b) 1×10^{15} and (c) $2 \times 10^{15}/\text{cm}^2$ under a WBDF \mathbf{g}_{220} two-beam imaging condition for the 800 °C iRTP anneal.

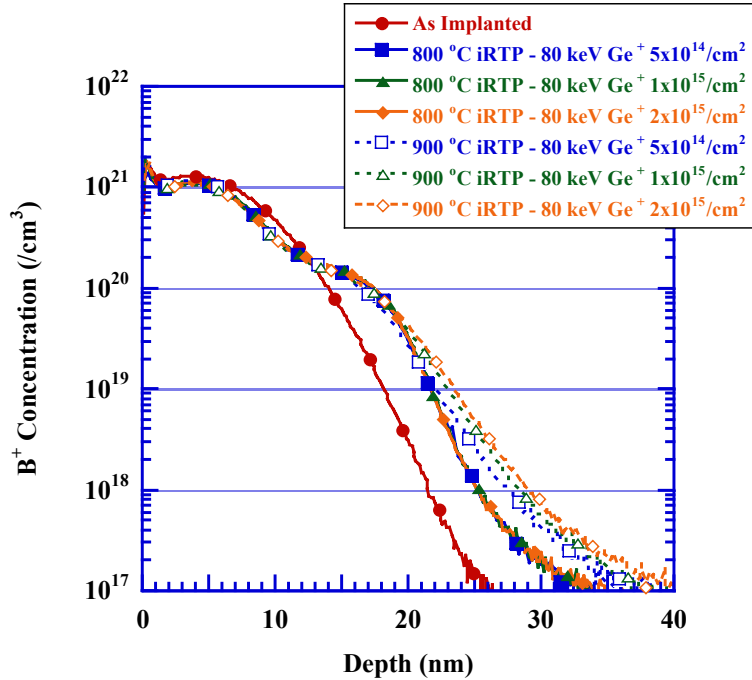


Figure 5-10 Concentration profiles showing the B⁺ concentration as a function of depth for the 1 keV B⁺ implant to $1 \times 10^{15}/\text{cm}^2$ before and after iRTP annealing at 800 and 900 °C for a substrate pre-amorphized with an 80 keV Ge⁺ implant to various doses. The symbols are for identifications purposes only.

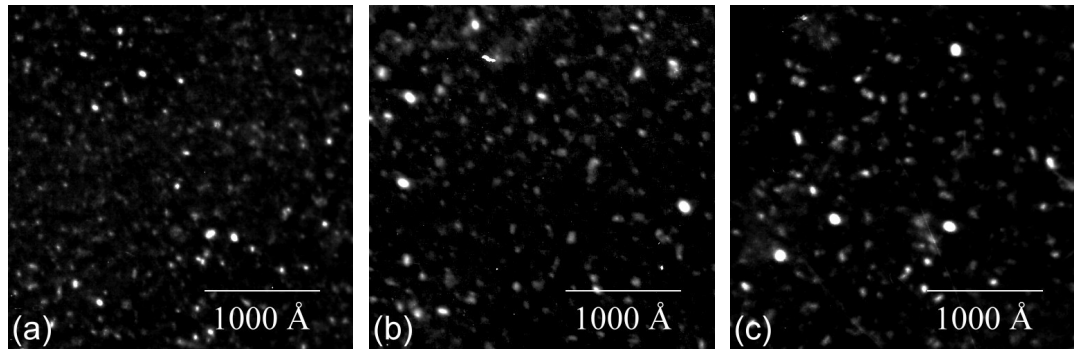


Figure 5-11 Plan-view TEM images of the damage produced by the 80 keV Ge^+ pre-amorphization implant to (a) 5×10^{14} (b) 1×10^{15} and (c) $2 \times 10^{15}/\text{cm}^2$ under a WBDF \mathbf{g}_{220} two-beam imaging condition for the 900 °C iRTP anneal.

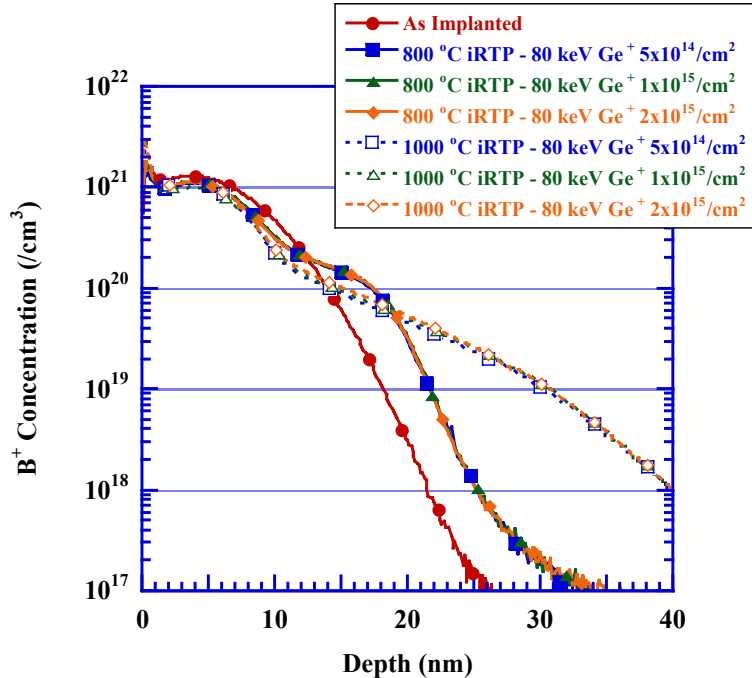


Figure 5-12 Concentration profiles showing the B^+ concentration as a function of depth for the 1 keV B^+ implant to $1 \times 10^{15}/\text{cm}^2$ before and after iRTP annealing at 800 and 1000 °C for a substrate pre-amorphized with an 80 keV Ge^+ implant to various doses. The symbols are for identifications purposes only.

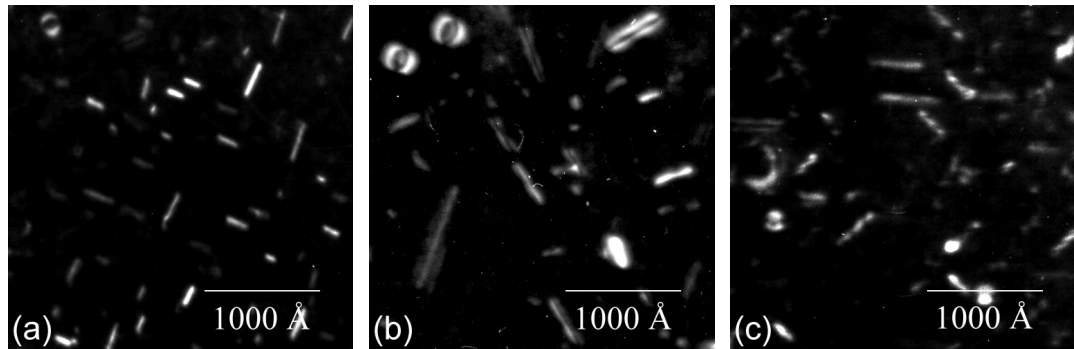


Figure 5-13 Plan-view TEM images of the damage produced by the 80 keV Ge^+ pre-amorphization implant to (a) 5×10^{14} (b) 1×10^{15} and (c) $2 \times 10^{15}/\text{cm}^2$ under a WBDF \mathbf{g}_{220} two-beam imaging condition for the 1000 °C iRTP anneal.

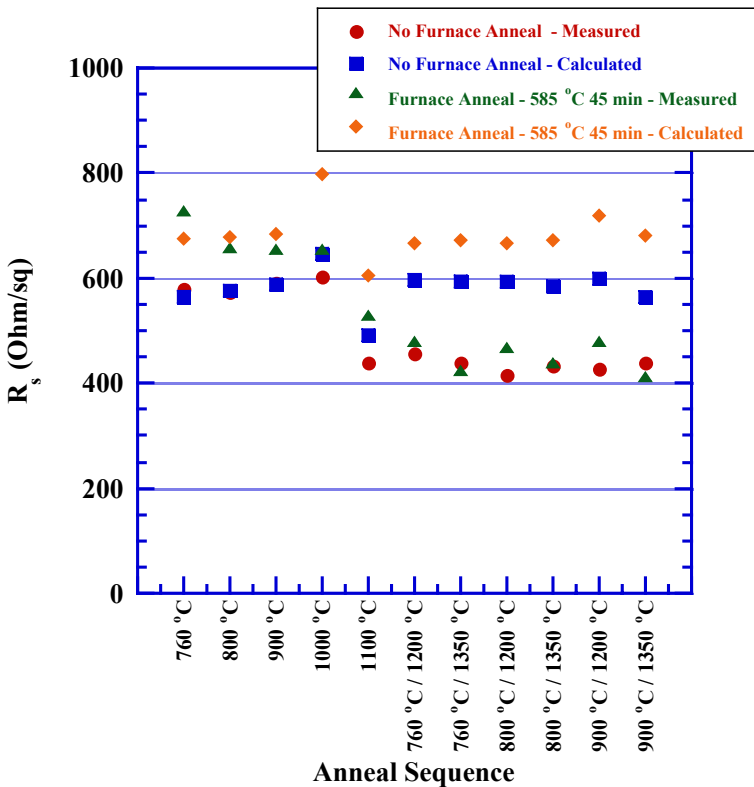


Figure 5-14 Graph of the measured (\bullet)(\blacktriangle) and calculated (\blacksquare)(\blacklozenge) R_s values obtained for the 48 keV Ge^+ pre-amorphization implant to $5 \times 10^{14}/\text{cm}^2$ without and with the 585 °C furnace anneal before UHT annealing, respectively.

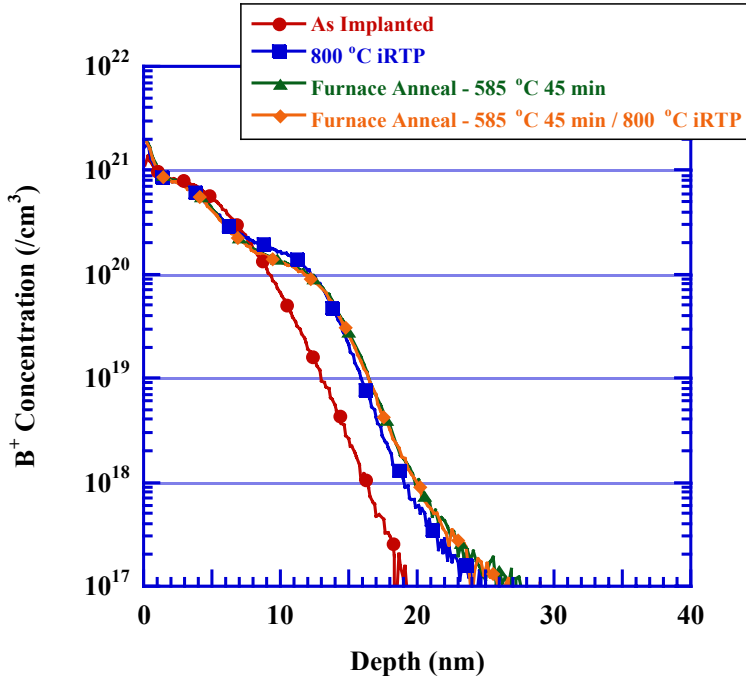


Figure 5-15 Concentration profiles showing the B^+ concentration as a function of depth for the 3 keV BF_2^+ implant to $6 \times 10^{14}/cm^2$ before and after the $800\text{ }^\circ\text{C}$ iRTP anneal both without and with the $585\text{ }^\circ\text{C}$ furnace anneal before UHT annealing for a substrate pre-amorphized with an 48 keV Ge^+ implant to $5 \times 10^{14}/cm^2$. The profile for the $585\text{ }^\circ\text{C}$ furnace anneal is included to serve as a reference. Note that the profile for the $800\text{ }^\circ\text{C}$ iRTP anneal (for the wafer without the $585\text{ }^\circ\text{C}$ furnace anneal) has a higher plateau concentration when compared to the profile for the $585\text{ }^\circ\text{C}$ furnace anneal even after an additional $800\text{ }^\circ\text{C}$ iRTP anneal. The symbols are for identifications purposes only.

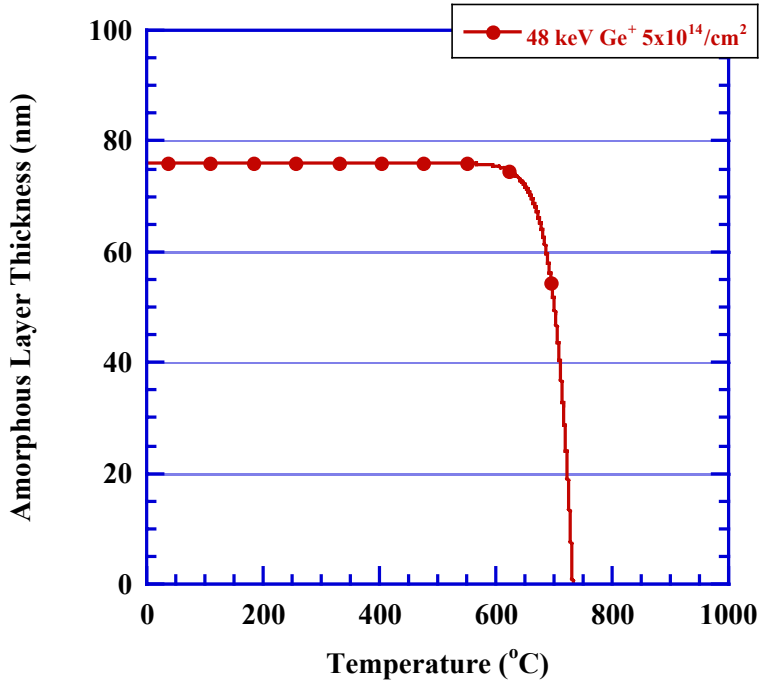


Figure 5-16 Plot of the estimated remaining amorphous layer thickness as a function of temperature for an anneal with a ramp-up rate of 400 °C/s. Note that the amorphous layer remains at the original amorphous layer thickness produced by the 48 keV pre-amorphization implant (i.e., 76 nm) until approximately 625 °C where it begins to recrystallize. The recrystallization process increases exponentially with increasing temperature until the amorphous layer completely recrystallizes at a temperature of approximately 700 ± 25 °C.

CHAPTER 6

EFFECT OF RECRYSTALLIZATION TEMPERATURE ON BORON ULTRA-SHALLOW JUNCTION FORMATION DURING ULTRA-HIGH TEMPERATURE ANNEALING OF ION-IMPLANTED SILICON

Introduction

Ion-implantation is currently used in complementary metal-oxide-semiconductor (CMOS) technology to introduce dopants into the source/drain extension (SDE) region of the device. It is well known that this process results in a perturbation in the equilibrium point-defect population as a result of the nuclear collisions between the primary ions and recoiled atoms with the lattice atoms of the substrate.² These nuclear collisions produce a number of interstitial-vacancy (Frenkel) pairs, many of which recombine during the relaxation of the collision cascade, leaving a population of excess interstitials similar to the implanted dose.

There are three possible primary implant damage morphologies that may exist directly after ion-implantation.⁴⁵ The first morphology consists of a surface with a damage structure such that the entire profile remains below the amorphization threshold. It should be noted that, although the entire profile remains below the amorphization threshold, it may include isolated amorphous regions within the crystalline Si (c-Si) lattice. In this case, the damage density profile is similar to the implant profile and most of the point-defects are located near the projected range (R_p) of the implant (where most of the nuclear collisions occur). For non-amorphizing implants, the stable damage is primarily small defect clusters, dopant-defect complexes, and some isolated Frenkel pairs.² The second morphology consists of the formation of a buried amorphous layer

centered around the peak of the damage profile with c-Si above and below the amorphous region. This type of morphology is typically avoided in CMOS processing due to the defect structure that forms during post-implant thermal processing. The third possible morphology consists of a continuous amorphous layer that extends from the substrate surface to a depth determined by the implant conditions.

When considering continuous surface amorphous layers, most of point-defects are located just below the amorphous/crystalline (α/c) interface produced by the implant (since the amorphous phase is inherently composed of crystallographic imperfections and is assumed to be structurally uniform).² The threshold damage density for the first order phase transition and formation of an amorphous layer is often taken to be 10% of the Si lattice density.⁴⁶ After an amorphous state is reached, the damage accumulation saturates.² Although amorphous Si (α -Si) no longer exhibits long-range order, short-range order still exists between nearest neighbors due to bond bending and the formation of 5- and 7-member rings. It was shown that α -Si has a melting temperature and atomic density approximately 225 ± 50 °C and $1.8 \pm 0.1\%$ below that of c-Si, respectively.⁴⁷⁻⁴⁹ In addition, it was shown that α -Si consists of a covalently bonded continuous random network (CRN) that can exist as either an as-implanted or structurally relaxed state.⁵⁰⁻⁵⁵ The structurally relaxed α -Si differs from the as-implanted case in that the number of large-angle bond distortions produced during the pre-amorphization implant are reduced, typically by a low temperature relaxation anneal (e.g., 500 °C for 60 min).⁵⁶⁻⁶² Regardless of the primary implant damage condition, post-implant thermal processing is required to repair the lattice damage accumulated during the implantation

process as well as activate dopants by establishing them on substitutional sites where they are able to contribute their holes (electrons) to the valence (conduction) band.

It is assumed that the effective mobility of point-defects at room temperature is relatively low due to trapping of the point-defects at a number of sites with a higher capture-cross section than the complementary component of the Frenkel pair, and that any Frenkel defects that survive the initial interstitial-vacancy (*I-V*) recombination process remain until post-implant thermal processing.⁶³ During post-implant thermal processing the corresponding point-defect mobility increases and the interstitial and vacancy populations decrease as a result of recombination in the bulk or at the substrate surface. This recombination process reduces the free energy of the system by attempting to adjust the interstitial concentration, C_i , and vacancy concentration, C_v , to equilibrium values (i.e., C_i^* and C_v^*). The fraction of point-defects that do not participate in the recombination process form intermediate clusters with point-defects or dopant atoms to obtain a more favorable energy state. The two most common self interstitial clusters that form after high temperature annealing of continuous surface amorphous layers are the {311} rod-like defect and dislocation loop.

The {311} defect is an extrinsic row of interstitials lying on the {311} habit plane, elongated in the ⟨110⟩ direction with a Burgers vector $b = a/25\langle 116 \rangle$.⁷⁰⁻⁷² Two different types of dislocation loops have been observed: so-called perfect prismatic loops with a Burgers vector $b = a/2\langle 110 \rangle$ and faulted Frank loops with a Burgers vector $b = a/3\langle 111 \rangle$. The Frank loop consists of an extra {111} plane bound by a dislocation line.⁶⁴ It should be noted that for higher thermal budgets, dislocation loops of both types are observed, whereas for the highest temperatures (e.g., 900 °C for 400 s) only faulted dislocation

loops are present.⁶⁴ A number of experiments have been performed and show that the dissolution kinetics of {311} defects (with an activation energy of approximately 3.7 eV)^{3,72} match the time scale of the effect known as transient enhanced diffusion (TED).^{77,78} Transient enhanced diffusion significantly increases the diffusion behavior of dopants such as B and P which diffuse primarily or in part by an interstitial(cy) mechanism.^{2,22} The main source of TED is the release of excess interstitials from the {311} defect.¹⁷ Although dislocation loops are more stable than {311} defects and, therefore, exist at higher annealing temperatures, the annealing temperature is usually high enough so that the relative enhancement, C_l/C_l^* , is not as large as the effect from {311} dissolution at lower temperatures.¹⁸ It is well known that the amount of TED observed during an anneal decreases when the defects are annealed out at a higher temperature.^{3,9,27} This observation influenced the development of single-wafer thermal processes which are capable of producing a high temperature ambient with ramp rates on the order of 50-200 °C/s, and fast switching times to insulate the dopant from a high degree of TED.²⁸

Rapid thermal processing (RTP) has proven successful in producing junctions with the performance characteristics necessary for the continued scaling of CMOS technology to date.²⁹ Its ability to satisfy these requirements is associated with improved equipment capability in the form of spike annealing, which decreases the effective thermal budget, allowing for higher annealing temperatures to improve activation and reduce the amount of diffusion of the dopants during the thermal process.^{30,31} A spike anneal is characterized as a short thermal-anneal cycle that can be achieved by increasing the ramp-up and ramp-down rates and by minimizing the dwell time at the temperature of

interest. The inability of this technique to produce junctions with the performance characteristics required by future technology nodes is in the cycle time of the thermal process, which results in an unacceptable amount of dopant diffusion. The minimum cycle times in conventional RTP techniques are limited by the maximum power delivered to the wafer, which determines the ramp-up rate, and the minimum response time of the relatively large thermal mass incandescent tungsten lamps, which determines both the soak time and the ramp-down rate. Without being able to minimize the soak time and the ramp-down rate, increasing the ramp-up rate above 100 °C/s results in no additional improvement in terms of forming a highly-activated ultra-shallow junction.^{30,32}

Novel high-power arc lamp design has enabled ultra-high temperature (UHT) annealing as an alternative to conventional RTP for B ultra-shallow junction formation.³³ This technique heats the wafer to an intermediate temperature (e.g., 800 °C) before discharging a capacitor bank into flash lamps, which anneals the device side of the wafer at a relatively high temperature (e.g., 1200 °C) for a few milliseconds.³⁴⁻³⁶ The UHT anneal heats the surface of interest while increasing the bulk wafer temperature not more than 50 °C of the intermediate temperature, allowing for conductive heat loss through the substrate. In contrast to tungsten lamp heating technology (i.e., RTP), this technique uses a water-wall arc lamp which provides the means for significantly reducing the heating-cycle time because of its ability to deliver higher power and because of its faster response time.¹⁶³ The arc lamp responds more rapidly than tungsten filament lamps due to the reduced thermal mass of the argon gas used in the arc lamp system. The lamps can be switched off in a few microseconds, allowing greater control and repeatability over the anneal process. The response realized in practice is determined by the power supply and

control system. An approximate value for the response time of the arc lamp system is 50 ms when excited with a 3-phase rectifying bridge supply.³⁴ It should be noted that a switch mode supply is capable of even faster response times. The switching time constant for tungsten incandescent lamps is on the order of 0.5 s.¹⁶³ A second advantage of the arc lamp design is its spectral distribution.³³ Figure 2-17 shows the integrated spectra as a function of wavelength and shows that over 95% of the arc radiation is below the 1.2 μm band gap absorption of Si at room temperature (compared to 40% for tungsten).³³ It should be noted that as the electrical power is reduced the spectra from tungsten sources shift to longer wavelengths and absorption drops below 40%. In contrast, the arc lamp spectral output is constant with electrical power and the absorption characteristics do not change.³³ Arc lamp radiation is strongly absorbed in Si due to band-to-band transitions with very low transmission through the wafer.¹⁶⁴

It was shown in Chapter 5 that higher activation levels can be achieved by using this annealing technique directly after implantation as opposed to performing a low temperature solid-phase epitaxial regrowth (SPER) anneal before UHT annealing. This improved activation was presumably thought to be because higher activation levels can be achieved at higher recrystallization temperatures. In other words, higher activation levels can be achieved when recrystallization (and presumably activation) occurs during ramp-up of an UHT anneal (e.g., approximately 700 °C), as opposed to a low temperature (i.e., 585 °C) furnace anneal. In order to test this idea, an experiment was designed in an attempt to reduce the regrowth velocity of the amorphous/crystalline (α/c) interface such that complete recrystallization of the implantation-induced amorphous layer would occur at even higher temperatures (e.g., 1000 °C). It is well known that F⁺ implantation to a

concentration of approximately $10^{18}/\text{cm}^3$ reduces the regrowth velocity of the α/c interface during SPER of an implantation-induced amorphous layer.^{140,141,196,220} Implanting F^+ to concentrations much greater than $10^{18}/\text{cm}^3$ may be sufficient to allow recrystallization to occur during the UHT anneal, thereby resulting in higher activation levels. The focus of this experiment is to use F co-implantation in an attempt to reduce the regrowth velocity of the α/c interface such that complete recrystallization of the implantation-induced amorphous layer would occur during the UHT anneal.

Experimental Design

Two 200 mm 3-5 $\Omega\cdot\text{cm}$ (100) n-type Czochralski (CZ) grown Si wafers were pre-amorphized with 48 keV Ge^+ implantation to $5\times 10^{14}/\text{cm}^2$. One of the wafers was subject to a 12 keV F^+ implant to $1.5\times 10^{15}/\text{cm}^2$ and both wafers were then implanted with 3 keV BF_2^+ molecular ions to $6\times 10^{14}/\text{cm}^2$. The implants were carried out in the drift mode and performed at room temperature with the ion beam normal to the surface plane using an Applied Materials Leap-II system. The implant parameters were monitored to ensure they remained within predetermined limits. The wafers were then sectioned and annealed at Vortek Industries to investigate the effects of the UHT annealing technique on the resulting junction characteristics. Representative temperature-time (T-t) profiles of the two UHT annealing techniques as well as the processing conditions that were used are shown in Figure 4-2. The impulse anneal (iRTPTM) is produced by continuous wave mode arc lamp irradiation of the front surface of the wafer and is responsible for producing the bulk wafer temperature, known as the intermediate temperature, at which the flash anneal (fRTPTM) is to be introduced. The fRTP anneal is produced by discharging a capacitor bank into flash lamps which increases the temperature of the

surface of interest while increasing the bulk wafer temperature not more than 50 °C of the intermediate temperature, allowing for conductive heat loss through the substrate. The iRTP anneal provides a means to better understand the advantages gained by the fRTP anneal. All of the anneals were carried out in a N₂ ambient with less than 10 ppm O₂. The iRTP and fRTP anneal temperatures were determined by a radiometer, which determined the wafer emissivity through a reflectance calculation that expresses the temperature of the system. In this experiment, iRTP anneals were performed over the range of 760 to 1100 °C using a ramp-up rate of 400 °C/s, and a ramp-down rate which was estimated to be approximately 150 °C/s at 900 °C. The ramp-down rate was determined by an instantaneous derivative of the radiation-cooling curve for a gray body with an emissivity and thickness comparable to the Si substrate. It should be noted that the ramp-down rate for conventional RTP is limited to 50-80 °C/s due to radiative cooling of the substrate to the ambient.^{3,117} The ramp-down rate is greater than that obtained through conventional techniques because of the use of absorbing chamber technology, which reduces radiation return to the substrate, providing the improved cooling rate.¹¹⁷ The fRTP anneals were performed over the range of 1200 to 1350 °C using ramp-up and ramp-down rates on the order of 10⁶ °C/s.

Dynamic secondary ion mass spectrometry (SIMS) was used to quantify dopant concentration as a function of depth. The ¹⁰B⁺ and ¹¹B⁺ counts were obtained on a CAMECA IMS-6f analytical tool using an O₂⁺ primary beam with a nominal beam current of 50-70 nA and a net impact energy of 800 eV directed 50° from the sample normal. The depth profile was established by continuously rastering a 200 by 200 μm area, and collected from a centered circular area 30-60 μm in diameter under an isobaric

O_2 ambient, which provided an adequate condition for complete oxidation of the Si surface during analysis. The system was configured so as to maintain a sputtering rate of 0.08-0.1 nm/s. Variable angle spectroscopic ellipsometry (VASE) was used to determine the thickness of the implantation-induced amorphous layer. The VASE measurements were performed on a J. A. Woollam Co., Inc. multi-wavelength ellipsometer with the 75 W Xe light source tilted 20° from the surface plane. The system was calibrated by fitting a known oxide thickness from a control Si substrate, and each subsequent measurement assumed a 2 nm native oxide above the continuous amorphous layer in order to more accurately measure the amorphous layer thickness. Cross-sectional transmission electron microscopy (XTEM) was used to verify the thickness of the amorphous layer measured by VASE, and image the depth of the EOR defect layer for the 48 keV pre-amorphization implant. The XTEM samples were thinned by 5 kV Ar^+ ion milling, with the plasma sources tilted 12° from the surface plane. All XTEM images were captured on a JEOL 200 CX TEM operating at 200 kV under a bright field imaging condition with the objective aperture centered over the transmitted beam. Plan-view TEM (PTEM) was used to investigate the EOR defect evolution and morphology as a function of the two UHT annealing techniques. The PTEM sample surfaces and backside periphery were insulated from the 3:1 HNO_3 :49% HF solution used to introduce an electron transparent edge surrounding an interstice. The PTEM images were captured on a JEOL 200 CX TEM operating at 200 kV in \mathbf{g}_{220} centered weak-beam dark-field (WBDF) using a \mathbf{g}_{220} two-beam imaging condition.¹⁷³ A Prometrics RS-20 four-point probe was used to measure the sheet resistance (R_s) for each anneal condition. The

sample geometric correction factor is negligible for the wafer sections, which have surface areas greater than those below which edge effects reduce measurement accuracy.

Results

The 48 keV pre-amorphization implant to $5 \times 10^{14}/\text{cm}^2$ generated a continuous amorphous layer extending 76 nm below the substrate surface as determined by VASE and verified through XTEM, an image of which was shown in Figure 4-3a. It is well known that regrowth related defects may be introduced during recrystallization of an implantation-induced amorphous layer as a result of the roughness of the α/c interface produced by high energy Ge^+ implantation.¹⁸³ It was shown that a combination of 400 keV and 30 keV Ge^+ pre-amorphization implants to $5 \times 10^{14}/\text{cm}^2$ with a subsequent 5 keV BF_2^+ implant to $5 \times 10^{14}/\text{cm}^2$ resulted in hairpin dislocation formation after both a 800 °C anneal for 30 min and a 900 °C anneal for 10 s.¹⁸³ These defects may in turn provide easy diffusion paths, via pipe diffusion, for the B to segregate toward the substrate surface.¹²⁰ Additional XTEM results in Figure 6-1a show that, for the wafer without the additional 12 keV F^+ implant to $1.5 \times 10^{15}/\text{cm}^2$, the 760 °C iRTP anneal is sufficient to completely regrow the amorphous layer produced by the 48 keV pre-amorphization implant. It can be seen that the substrate surface is free of hairpin dislocations and that the anneal reveals in a contrast band associated with the EOR damage, which is located approximately 78 nm below the substrate surface. Figure 6-1b shows that the additional 12 keV F^+ implant to $1.5 \times 10^{15}/\text{cm}^2$ reduces the regrowth velocity of the α/c interface such that the 800 °C iRTP anneal is unable to completely regrow the amorphous layer produced by the 48 keV pre-amorphization implant; approximately 22 nm of $\alpha\text{-Si}$ remains near the substrate surface after the 800 °C iRTP

anneal. Although the amorphous layer did not completely regrow during an 800 °C iRTP anneal, it can still be seen that no hairpin dislocations formed. It should be noted that additional contrast can be seen in the portion of the material that recrystallized during the 800 °C iRTP anneal for the XTEM image of the wafer with the additional F⁺ implant in Figure 6-1b. It is presumed that hairpin dislocation formation did not occur for any of the iRTP or intermediate anneals used in this study. Additional XTEM results (not shown) revealed that the 900 °C iRTP anneal was sufficient to completely regrow the amorphous layer produced by the 48 keV pre-amorphization implant for the wafer with the additional F⁺ implant.

The SIMS results for the 12 keV F⁺ implant to $1.5 \times 10^{15}/\text{cm}^2$ before and after iRTP annealing are shown in Figure 6-2. The as-implanted profile displays a Gaussian distribution which is slightly broadened beyond a depth of 76 nm, presumably due to ion channeling associated with alignment along atomic rows where the ions experience a slower rate of energy loss thereby producing a profile with an asymmetric distribution; one that is Gaussian towards the substrate surface but supplemented by a characteristic broadening at lower concentrations into the bulk of the substrate. It should be noted that the increase in F⁺ concentration near the substrate surface is due to the 3 keV BF₂⁺ implant to $6 \times 10^{14}/\text{cm}^2$. The R_p of the 12 keV F⁺ implant to $1.5 \times 10^{15}/\text{cm}^2$ is approximately 24.5 nm below the substrate surface which is almost 6.0 nm shallower than the R_p estimated by a TRansport of Ions in Matter (TRIM) simulation. As can be seen, the 760 and 900 °C iRTP anneals produce the same F profile with a peak concentration of approximately $2-3 \times 10^{20}/\text{cm}^3$ in the first 40 nm below the substrate surface. The only noticeable difference between the two profiles is the peak that forms

approximately 70 nm below the substrate surface, which remains during the 760 °C iRTP anneal but is no longer present after the 900 °C iRTP anneal. These results and the corresponding XTEM results in Figure 6-1 show that a F concentration of approximately $3 \times 10^{20}/\text{cm}^3$ is sufficient to prevent complete recrystallization of the implantation-induced amorphous layer during the 800 °C iRTP anneal.

Figure 6-3 shows the SIMS results for the as-implanted profiles of each wafer without and with the additional 12 keV F⁺ implant to $1.5 \times 10^{15}/\text{cm}^2$. As can be seen, the as-implanted profile for the wafer without the 12 keV F⁺ implant to $1.5 \times 10^{15}/\text{cm}^2$ shows a typical Gaussian distribution with a junction abruptness of 3.3 nm/dec and a junction depth (x_j) of 16.3 nm. Junction abruptness is defined as the inverse slope of the SIMS profile between the concentration range of $1 \times 10^{18}/\text{cm}^3$ and $1 \times 10^{19}/\text{cm}^3$, and the x_j is defined as the depth of the profile at a dopant concentration of $1 \times 10^{18}/\text{cm}^3$ (for the wafer that did not receive the additional F⁺ implant). The as-implanted profile for the wafer with the additional 12 keV F⁺ implant to $1.5 \times 10^{15}/\text{cm}^2$ has a junction abruptness of 11.9 nm/dec and a x_j of 25.6 nm, which is significantly degraded when compared to the wafer without F⁺ implant. It can be seen that the two as-implanted profiles are similar down to a concentration of approximately $1 \times 10^{19}/\text{cm}^2$, below which the as-implanted profile for the wafer with the additional F⁺ implant decreases exponentially as a function of depth. It is this exponential decrease that produces such a large difference between the as-implanted junction abruptness and x_j . Additional SIMS results will show that, although dopant diffusion occurs at higher concentrations, the profiles for the wafer with the 12 keV F⁺ implant to $1.5 \times 10^{15}/\text{cm}^2$ maintain a x_j of approximately 25.6 nm for most of the annealing conditions used in this study; because of this, the x_j for the wafer with

the additional F⁺ implant will be defined as the depth of the profile at a dopant concentration of $1\times10^{19}/\text{cm}^3$ in order to distinguish between a measurable difference in dopant diffusion. The as-implanted x_j at a dopant concentration of $1\times10^{19}/\text{cm}^3$ is 13.7 nm for the wafer with the additional 12 keV F⁺ implant to $1.5\times10^{15}/\text{cm}^2$. It should be noted that these implant conditions were repeated on an additional set of wafers to ensure that this characteristic is real; the results were reproducible.

Figures 6-4a and b show the SIMS results for each of the iRTP anneals used in this study for the wafer without and with the 12 keV F⁺ implant to $1.5\times10^{15}/\text{cm}^2$, respectively. Each profile shows an increase in x_j when compared to the as-implanted profile. Figure 6-4a shows that the 760 and 800 °C iRTP anneals display similar profiles with junction abruptness of 3.2 nm/dec and x_j of 19.3 nm (measured at $1\times10^{18}/\text{cm}^3$), which is a 3.0 nm increase in x_j when compared to the as-implanted profile. Figure 6-4b shows that the 760 °C iRTP anneal results in a profile with junction abruptness of 7.7 nm/dec and x_j of 18.6 nm (measured at $1\times10^{19}/\text{cm}^3$), which is a 4.9 nm increase in x_j when compared to the as-implanted profile. It should be noted that, although the profile for the 760 °C iRTP anneal in Figure 6-4b undergoes diffusion at higher concentrations (e.g., $1\times10^{19}/\text{cm}^3$), the profile is similar to the as-implanted profile below a concentration of approximately $2\times10^{18}/\text{cm}^3$ illustrating the need to define the x_j at $1\times10^{19}/\text{cm}^2$ to distinguish between differences in dopant diffusion. Although the SIMS profile for the 800 °C iRTP anneal is unavailable for the wafer with the additional F⁺ implant, additional SIMS results put forward that this anneal produces a profile similar to the 760 °C iRTP anneal.

Figure 6-4 shows that the 900 °C iRTP anneal produces profiles with junction abruptness of 5.5 and 5.4 nm/dec and x_j of 22.5 (measured at $1\times10^{18}/\text{cm}^3$) and 20.4 (measured at $1\times10^{19}/\text{cm}^3$) nm for the wafer without and with the 12 keV F⁺ implant to $1.5\times10^{15}/\text{cm}^2$, respectively. This shows that, with respect to their individual 760 °C iRTP anneals, the junction abruptness degrades for the wafer without the 12 keV F⁺ implant to $1.5\times10^{15}/\text{cm}^2$ whereas it improves for the wafer with the additional F⁺ implant. The profile for the 900 °C iRTP anneal in Figure 6-4a shows that the junction abruptness degrades due to B diffusion in the low concentration region of the profile (e.g., $1\times10^{18}/\text{cm}^3$). Figure 6-4b shows improved junction abruptness due to diffusion at higher concentrations while maintaining the same x_j at a concentration of $1\times10^{18}/\text{cm}^3$. Further increasing the iRTP anneal temperature results in a degradation of the junction abruptness and increase in x_j independent of the 12 keV F⁺ implant to $1.5\times10^{15}/\text{cm}^2$.

The 1000 and 1100 °C iRTP anneals produce profiles with junction abruptness of 10.1 and 8.7 nm/dec and x_j of 31.7 and 36.1 nm (measured at $1\times10^{18}/\text{cm}^3$), respectively, for the wafer without the 12 keV F⁺ implant to $1.5\times10^{15}/\text{cm}^2$. The 1000 and 1100 °C iRTP anneals produce profiles with 5.8 and 5.7 nm/dec junction abruptness and a 22.1 and 26.2 nm x_j (measured at $1\times10^{19}/\text{cm}^3$), respectively, for the wafer with the 12 keV F⁺ implant to $1.5\times10^{15}/\text{cm}^2$. This shows a significant increase in B diffusion behavior during the 1000 °C iRTP anneal for the wafer without the additional F⁺ implant. The 1000 °C iRTP profile in Figure 6-4b shows that it is sufficient to ‘unpin’ the dopant at a concentration of $1\times10^{18}/\text{cm}^3$. It is interesting to note that the difference in x_j between the 1000 and 1100 °C iRTP anneals are similar independent of the 12 keV F⁺ implant to

$1.5 \times 10^{15}/\text{cm}^2$, which is approximately 4 nm. It should be noted that the 1100°C iRTP anneal has improved junction abruptness compared to the 1000°C iRTP anneal independent of the additional F^+ implant. Although this characteristic applies to both graphs in Figure 6-4, the junction abruptness is more degraded for the wafer without the 12 keV F^+ implant to $1.5 \times 10^{15}/\text{cm}^2$.

Figure 6-4a shows that the iRTP anneals produce profiles with plateau concentrations on the order of $1.4\text{-}1.8 \times 10^{20}/\text{cm}^3$ for the wafer without the 12 keV F^+ implant to $1.5 \times 10^{15}/\text{cm}^2$. The plateau concentration is defined as the concentration at which the anneal produces an inflection point. These profiles show inflection points between 7-8 nm below the substrate surface. These inflection points correspond to the concentration levels below which B is diffusing and presumed to be active and above which inactive B cluster formation or precipitation occurs and the B remains immobile.^{5,9,98} Figure 6-4b shows that the iRTP anneals produce profiles with plateau concentrations on the order of $1.6\text{-}1.8 \times 10^{20}/\text{cm}^3$ for the wafer with the additional F^+ implant. It should be noted that the 1100°C iRTP anneal dissociated of some of the initially inactive dopant near the Si surface independent of the 12 keV F^+ implant to $1.5 \times 10^{15}/\text{cm}^2$.

Figure 6-5 shows the PTEM images of the EOR damage produced by the 48 keV pre-amorphization implant after each of the iRTP anneals used in this study. The first row of images correspond to the wafer without the 12 keV F^+ implant to $1.5 \times 10^{15}/\text{cm}^2$. As can be seen by the images, the 760 , 800 , and 900°C iRTP anneals produce a high density defect structure consisting of defect clusters.^{9,184} These defect clusters are approximately 4 to 12 nm and 6 to 18 nm in diameter for the 760 and 900°C iRTP

anneals, respectively. Although the morphology of the defects appears independent of the iRTP anneal over this temperature range, the average size of these defects increases and the defect density decreases with increasing iRTP anneal temperature, which suggests that defect coarsening is occurring.⁹ The PTEM image for the 1000 °C iRTP anneal shows that it is sufficient to produce a defect structure mainly consisting of {311} defects and dislocation loops.⁹ The {311} defects range from 29 to 88 and average 60 nm in length and the dislocation loops range from 21 to 29 and average 26 nm in diameter. Increasing the iRTP anneal temperature to 1100 °C results in a defect structure consisting only of dislocation loops, which shows that {311} defect dissolution is complete between 1000 and 1100 °C. The dislocation loops range from 24 to 32 and average 29 nm in diameter. The second row of images correspond to the wafer with the additional 12 keV F⁺ implant to $1.5 \times 10^{15}/\text{cm}^2$. As can be seen by the images, the 760, 800, and 900 °C iRTP anneals produce a high density defect structure consisting of defect clusters, which are similar to those observed for the wafer without the 12 keV F⁺ implant to $1.5 \times 10^{15}/\text{cm}^2$.^{9,184} These defect clusters are approximately 3 to 8 nm and 5 to 14 nm in diameter for the 760 and 900 °C iRTP anneals, respectively, which are similar in size to those observed for the wafer without the additional F⁺ implant. The average size of these defect clusters increases and the defect density decreases with increasing iRTP anneal temperature, which suggests that defect coarsening is occurring.⁹ The PTEM image for the 1000 °C iRTP anneal shows that it is sufficient to produce a defect structure mainly consisting of {311} defects and dislocation loops.⁹ The {311} defects range from 6 to 50 and average 32 nm in length and the dislocation loops range from 14 to 34 and average 22 nm in diameter. Increasing the iRTP anneal temperature to 1100 °C results in a defect

structure consisting only of dislocation loops, which shows that {311} defect dissolution is complete between 1000 and 1100 °C independent of the 12 keV F⁺ implant to $1.5 \times 10^{15}/\text{cm}^2$. The dislocation loops range from 14 to 40 and average 26 nm in diameter, which are on average similar in diameter to those observed for the wafer without the additional F⁺ implant.

Figures 6-6a and b show the SIMS results for the 760 °C intermediate temperature with both 1200 and 1350 °C fRTP anneals for the wafer without and with the 12 keV F⁺ implant to $1.5 \times 10^{15}/\text{cm}^2$, respectively. As can be seen in Figure 6-6a, the 760 °C intermediate temperature produces profiles with junction abruptness of 3.4 and 4.4 nm/dec and x_j of 19.9 and 21.3 nm (measured at $1 \times 10^{18}/\text{cm}^3$) after a 1200 and 1350 °C fRTP anneal, respectively. The 0.6 nm of diffusion during the 1200 °C fRTP anneal shows that most the overall diffusion occurs during SPER of the amorphous layer. Although the 1350 °C fRTP anneal resulted in an additional 1.4 nm of diffusion when compared to the 1200 °C fRTP anneal, the diffusion behavior for each of the profiles is much less than would be expected from a conventional RTP anneal. The plateau concentration for each of these annealing conditions remains constant at approximately $1.8 \times 10^{20}/\text{cm}^3$, suggesting that any additional activation that may occur during the UHT anneal is not directly observed by an increase in the plateau concentration of the SIMS profile. Figure 6-6b shows that the 760 °C intermediate temperature produces profiles with junction abruptness of 7.3 and 7.8 nm/dec and x_j of 18.0 and 18.6 nm (measured at $1 \times 10^{19}/\text{cm}^3$) after a 1200 and 1350 °C fRTP anneal, respectively. This shows that no significant degradation of the junction abruptness or increase in x_j occurs during UHT annealing of the wafer with the 12 keV F⁺ implant to $1.5 \times 10^{15}/\text{cm}^2$. In fact, the 1350 °C

fRTP anneal results in a profile with the same x_j as the profile produced by the 760 °C iRTP anneal with only a 0.1 nm/dec degradation in junction abruptness. This is a noticeable improvement when compared to the wafer without the additional F⁺ implant, which resulted in 1.2 nm/dec degradation in junction abruptness and 2.0 nm increase in x_j for the same annealing condition. The seeming improvement in both junction abruptness and x_j for the 1200 °C fRTP anneal (when compared to the 760 °C iRTP anneal) is presumably due to the noise in the raw data and the values that were used to represent the junction abruptness and x_j . Figure 6-4 showed that the 760 °C iRTP anneal resulted in a plateau concentration of approximately $1.8 \times 10^{20}/\text{cm}^3$ independent of the 12 keV F⁺ implant to $1.5 \times 10^{15}/\text{cm}^2$. Although the plateau concentration does not change during UHT annealing of the wafer without the additional F⁺ implant, it increases with increasing peak temperature during UHT annealing of the wafer with the 12 keV F⁺ implant to $1.5 \times 10^{15}/\text{cm}^2$. The plateau concentration increases from $1.8 \times 10^{20}/\text{cm}^3$ to 2.6×10^{20} and $2.9 \times 10^{20}/\text{cm}^3$ for the 1200 and 1350 °C fRTP anneals, respectively. Linear plots of the SIMS data are included in Figure 6-6 to better illustrate this difference in the plateau concentration region.

Figure 6-7 shows the PTEM images of the EOR damage produced by the 48 keV pre-amorphization implant for each of the fRTP anneals when using an intermediate temperature of 760 °C. The first row of images correspond to the wafer without the 12 keV F⁺ implant to $1.5 \times 10^{15}/\text{cm}^2$. The 1200 °C fRTP anneal results in a defect structure consisting of defect clusters and possibly small dislocation loops; it is unclear whether the areas of large contrast are dislocation loops or large defect clusters. These defects are approximately 4 to 12 nm in diameter, which are similar to those produced by

the corresponding iRTP anneal in Figure 6-5. The 1350 °C fRTP anneal produces a defect structure consisting of defect clusters, {311} defects, and dislocation loops. The {311} defects range from 19 to 29 and average 25 nm in length and the dislocation loops range from 18 to 24 and average 19 nm in diameter. This shows that the fRTP anneal is capable of evolving the EOR damage and that the final EOR defect structure is dependent on the peak UHT annealing temperature. The second row of images correspond to the wafer with the 12 keV F⁺ implant to $1.5 \times 10^{15}/\text{cm}^2$. Similar to the wafer without the additional F⁺ implant, the 1200 °C fRTP anneal results in a defect structure consisting of defect clusters and possibly small dislocation loops. These defects are approximately 5 to 18 nm in diameter, which are slightly larger than those produced by the corresponding iRTP anneal in Figure 6-5. The 1350 °C fRTP anneal produces a defect structure consisting of defect clusters, {311} defects, and dislocation loops. The {311} defects range from 20 to 27 and average 23 nm in length and the dislocation loops range from 20 to 34 and average 26 nm in diameter. This supports the suggestion that the fRTP anneal is capable of evolving the EOR damage and that the final EOR defect structure is dependent on the peak UHT annealing temperature.

The SIMS results for the 800 °C intermediate temperature with both 1200 and 1350 °C fRTP anneals for the wafer without and with the 12 keV F⁺ implant to $1.5 \times 10^{15}/\text{cm}^2$ are shown in Figures 6-8a and b, respectively. As can be seen in Figure 6-8a, the 800 °C intermediate temperature produces profiles with junction abruptness of 3.4 and 4.9 nm/dec and x_j of 19.9 and 22.4 nm (measured at $1 \times 10^{18}/\text{cm}^3$) for the 1200 and 1350 °C fRTP anneals, respectively. This shows that although both the 760 and 800 °C intermediate temperatures result in similar profiles after the 1200 °C

fRTP anneal, the 1350 °C fRTP anneal results in a more abrupt and slightly shallower profile when the 760 °C intermediate temperature is used. Similar to the 760 °C intermediate temperature, the plateau concentration for each of these annealing conditions remains constant at approximately $1.8 \times 10^{20}/\text{cm}^3$ when the 800 °C intermediate temperature is used. As can be seen in Figure 6-8b, the 800 °C intermediate temperature produces profiles with junction abruptness of 7.4 and 7.4 nm/dec and x_j of 18.7 and 18.8 nm x_j (measured at $1 \times 10^{19}/\text{cm}^3$) for the 1200 and 1350 °C fRTP anneals, respectively, for the wafer with the 12 keV F⁺ implant to $1.5 \times 10^{15}/\text{cm}^2$. The SIMS profile for the 760 °C iRTP anneal is included in Figure 6-8b to serve as a reference (since the depth profile for the 800 °C iRTP anneal is expected to appear similar to the 760 °C iRTP anneal). Similar to the 760 °C intermediate temperature, a negligible amount of diffusion occurs during the 1350 °C fRTP anneal (when compared to the profile for the 760 °C iRTP anneal) showing that the additional F⁺ implant is capable of preventing diffusion at a peak temperature of 1350 °C. It should be noted that using the SIMS profile of the 760 °C iRTP anneal as a reference for the 800 °C iRTP anneal is reasonable considering the slight difference between the SIMS profiles corresponding to the 1200 and 1350 °C fRTP anneals and the 760 °C iRTP anneal. Figure 6-8b shows that the 760 °C iRTP anneal results in a plateau concentration of approximately $1.8 \times 10^{20}/\text{cm}^3$, which is comparable to the plateau concentration observed for the 800 °C iRTP anneal in Figure 6-8a. Similar to the data for the 760 °C intermediate temperature in Figure 6-6, the plateau concentration remains constant during UHT annealing of the wafer without the 12 keV F⁺ implant to $1.5 \times 10^{15}/\text{cm}^2$ and increases with increasing peak temperature

during UHT annealing of the wafer with the additional F⁺ implant. The plateau concentration increases from $1.8 \times 10^{20}/\text{cm}^3$ to 2.5×10^{20} and $2.8 \times 10^{20}/\text{cm}^3$ for the 1200 and 1350 °C fRTP anneals, respectively. Linear plots of the SIMS data are included in Figure 6-8 to better illustrate this difference in the plateau concentration region. It should be noted that this increase in plateau concentration is less than that observed during UHT annealing for the wafer with the additional F⁺ implant when 760 °C is used as the intermediate temperature.

The PTEM images of the EOR damage produced by the 48 keV pre-amorphization implant for each of the fRTP anneals when using an intermediate temperature of 800 °C are shown in Figure 6-9. The first row of images correspond to the wafer without the 12 keV F⁺ implant to $1.5 \times 10^{15}/\text{cm}^2$. The 1200 °C fRTP anneal results in a defect structure consisting of defect clusters and possibly small dislocation loops; it is unclear whether the areas of large contrast are dislocation loops or large defect clusters. The defect structure is assumed to be predominantly defect clusters, due to the fact that the reverse transformation of a dislocation loop into a {311} defect has never been observed and {311} defects were observed to form for the 1350 °C fRTP anneal.⁶⁴ The 800 °C intermediate temperature produces defects 9 to 22 nm in diameter, which are on average larger than those produced by the 1200 °C fRTP anneal when 760 °C is used as the intermediate temperature (as shown in Figure 6-7). It should be noted that these defects are also on average larger than those produced by the corresponding 800 °C iRTP anneal in Figure 6-5. The 1350 °C fRTP anneal produces a defect structure mainly consisting of {311} defects and dislocation loops. The {311} defects range from 19 to 43 and average 32 nm in length and the dislocation loops range from 19 to 59 and average 32 nm in

diameter. These images provide some evidence that the final EOR defect structure is dependent on both the intermediate temperature and peak UHT annealing temperature. The second row of images correspond to the wafer with the 12 keV F⁺ implant to $1.5 \times 10^{15}/\text{cm}^2$. Similar to the wafer without the additional F⁺ implant, the 1200 °C fRTP anneal results in a defect structure consisting of defect clusters and possibly small dislocation loops. The 800 °C intermediate temperature produces defects 7 to 22 nm in diameter, which are on average slightly larger than those produced by the 1200 °C fRTP anneal when 760 °C is used is the intermediate temperature (as shown in Figure 6-7). It should be noted that these defect are also on average larger than those produced by the corresponding 800 °C iRTP anneal in Figure 6-5. The 1350 °C fRTP anneal produces a defect structure mainly consisting of {311} defects and dislocation loops. The {311} defects range from 20 to 33 and average 27 nm in length and the dislocation loops range from 23 to 53 and average 34 nm in diameter. These images support the idea that the final EOR defect structure is dependent on both the intermediate temperature and peak UHT annealing temperature.

Figures 6-10a and b show the SIMS results for the 900 °C intermediate temperature with both 1200 and 1350 °C fRTP anneals for the wafer without and with the 12 keV F⁺ implant to $1.5 \times 10^{15}/\text{cm}^2$, respectively. As can be seen in Figure 6-10a, the 900 °C intermediate temperature produces profiles with junction abruptness of 5.9 and 5.8 nm/dec and x_j of 23.7 and 25.0 nm (measured at $1 \times 10^{18}/\text{cm}^3$) for the 1200 and 1350 °C fRTP anneals, respectively. When compared to the 760 and 800 °C intermediate temperatures, which result in similar profiles after the 1200 °C fRTP anneal, the 900 °C intermediate temperature degrades the junction abruptness 2.4 nm/dec and increases the

x_j 3.8 nm during the 1200 °C fRTP anneal. This degradation is in part due to the diffusion that occurs during the intermediate anneal, as the 900 °C iRTP anneal degraded the junction abruptness 2.3 nm/dec and increased the x_j 3.2 nm compared to both the 760 and 800 °C iRTP anneals. Similar to both the 760 and 800 °C intermediate temperatures, the plateau concentration for each of these annealing conditions remains constant at approximately $1.8 \times 10^{20}/\text{cm}^3$ when the 900 °C is used as the intermediate temperature. As can be seen in Figure 6-10b, the 900 °C intermediate anneal produces profiles with junction abruptness of 5.5 and 6.5 nm/dec and x_j of 20.5 and 22.6 nm (measured at $1 \times 10^{19}/\text{cm}^3$) for the 1200 and 1350 °C fRTP anneals, respectively, for the wafer with the 12 keV F⁺ implant to $1.5 \times 10^{15}/\text{cm}^2$. The improvement in junction abruptness (compared to the lower intermediate temperatures) is due to dopant diffusion at higher concentrations while maintaining the same x_j at a concentration of $1 \times 10^{18}/\text{cm}^3$. It can be seen in Figure 6-10b that the 1200 and 1350 °C fRTP anneals increase the x_j 0.1 and 2.2 nm when compared to the 900 °C iRTP anneal, respectively. This shows that the 12 keV F⁺ implant to $1.5 \times 10^{15}/\text{cm}^2$ is only capable of preventing an additional diffusion enhancement (other than that observed during SPER) for the 1350 °C fRTP anneal when the intermediate temperature is sufficiently low (e.g., 800 °C). It should be noted that the 1200 °C fRTP anneal resulted in no appreciable diffusion enhancement independent of the intermediate temperatures used here. Figures 6-6 and 6-8 showed that, for the 760 and 800 °C intermediate temperatures, the plateau concentration remains constant for the wafer without the 12 keV F⁺ implant to $1.5 \times 10^{15}/\text{cm}^2$ independent of the peak UHT annealing temperature whereas it increases with increasing peak UHT temperature for the

wafer with the additional F⁺ implant. This is not observed for the 900 °C intermediate temperature; the plateau concentration remains approximately $1.9 \times 10^{20}/\text{cm}^3$ independent of the peak UHT annealing temperature. Linear plots of the SIMS data are included in Figure 6-10 to better illustrate this difference in the plateau concentration region.

The PTEM images of the EOR damage produced by the 48 keV pre-amorphization implant for each of the fRTP anneals when using an intermediate temperature of 900 °C are shown in Figure 6-11. The first row of images correspond to the wafer without the 12 keV F⁺ implant to $1.5 \times 10^{15}/\text{cm}^2$. The 1200 °C fRTP anneal is sufficient to produce a defect structure consisting of defect clusters, {311} defects, and dislocation loops. The {311} defects range from 21 to 29 and average 25 nm in length and the dislocation loops range from 13 to 19 and average 17 nm in diameter. The 1350 °C fRTP anneal produced a defect structure consisting only of dislocation loops. The dislocation loops range from 24 to 115 and averaged 62 nm in diameter. The most marked difference between the images corresponding to each of the 1350 °C fRTP anneals is the size and overall evolution of the dislocation loops, which increases with the intermediate annealing temperature. The largest dislocation loops in each of the images are approximately 24, 59, and 115 nm in diameter for the 760, 800 and 900 °C intermediate temperatures, respectively. These images support the suggestion that, not only is the final EOR defect structure dependent on the peak UHT annealing temperature, but it is also dependent on the intermediate anneal temperature. The second row of images correspond to the wafer with the 12 keV F⁺ implant to $1.5 \times 10^{15}/\text{cm}^2$. Similar to the wafer without the additional F⁺ implant, the 1200 °C fRTP anneal is sufficient to produce a defect structure consisting of defect clusters, {311} defects, and dislocation loops. The {311} defects range from 23

to 47 and average 33 nm in length and the dislocation loops range from 20 to 33 and average 23 nm in diameter. The 1350 °C fRTP anneal produced a defect structure consisting only of dislocation loops. The dislocation loops range from 20 to 70 and averaged 38 nm in diameter. Similar to the wafer without the 12 keV F⁺ implant to $1.5 \times 10^{15}/\text{cm}^2$, the size and overall evolution of the dislocation loops is the most noticeable difference between each of the intermediate temperatures used in this study. As can be seen in Figure 6-11, the largest dislocation loops in each of the images corresponding to the wafer with the additional F⁺ implant are approximately 34, 53, and 70 nm in diameter for the 760, 800 and 900 °C intermediate temperatures, respectively. After reviewing all the PTEM data, it can be said that the defect evolution and morphology is relatively independent of the 12 keV F⁺ implant to $1.5 \times 10^{15}/\text{cm}^2$ for each annealing condition used here.

Discussion

As can be seen in Figure 6-3, the as-implanted profile for the wafer without the 12 keV F⁺ implant to $1.5 \times 10^{15}/\text{cm}^2$ shows a typical Gaussian distribution with a junction abruptness of 3.3 nm/dec and x_j of 16.3 nm (measured at $1 \times 10^{18}/\text{cm}^3$). Although the additional 12 keV F⁺ implant to $1.5 \times 10^{15}/\text{cm}^2$ was not expected to affect the as-implanted profile, it resulted in a junction abruptness of 11.9 nm/dec and x_j of 25.6 nm (measured at $1 \times 10^{18}/\text{cm}^3$) which is significantly degraded when compared to the wafer without the additional F⁺ implant. It can be seen that the two as-implanted profiles are similar down to a concentration of $1 \times 10^{19}/\text{cm}^2$, below which the as-implanted profile for the wafer with the additional F⁺ implant decreases exponentially as a function of depth. It is this exponential decrease that produces such a large difference between the as-implanted

junction abruptness and x_j . In order to best explain this observation, a brief overview of structural defects in α -Si is given.

It is well known that ion-implanted α -Si contains a number of structural imperfections such as large-angle bond distortions and defect complexes.^{194,198,199} In α -Si, short range order is maintained by directional covalent bonding; however, long range order is suppressed by distortions of the ideal tetrahedral bond-angle (i.e., bond bending).³⁷ Estimations made from computer modeling suggest that the 11.3° average bond-angle distortion ($\Delta\theta$) observed in the as-implanted state is almost twice as large as the lowest possible average bond distortion in any CRN, which is approximately 6.6°.^{37,221-223} The defect complexes associated with α -Si are expected to be similar to point-defects and small point-defect clusters in heavily damaged c-Si due to the fact that both are fourfold coordinated covalently bonded materials.¹⁹⁸ Additional work has shown that structural defects in α -Si may also be thought of as broken and highly strained Si-Si bonds.^{195,224} It should be noted that defects in c-Si produce deep levels in the band gap and act as carrier trapping and recombination centers.^{223,225} This was also expected for α -Si. Indeed, low intensity pump-probe experiments revealed that the carrier lifetime in α -Si is roughly inversely proportional to the defect density.^{223,225} The carrier lifetime in α -Si at low plasma densities (e.g., $10^{18}/\text{cm}^3$) is determined by the capture of mobile carriers at defect-related electronic states in the band gap.²²³

The high density of defects in the α -Si network causes the difference in the effective diffusion coefficients between α - and c-Si.³⁷ Previous work suggested that, although the diffusion mechanisms in c-Si are similar in α -Si (i.e., interstitial diffusers in c-Si also diffuse by an interstitial mechanism in α -Si) impurity diffusion in α -Si is much

slower than that in c-Si.^{37,199,200} This slower diffusion was explained by frequent trapping of the diffusing impurity at structural defects intrinsic to the amorphous structure.^{37,199,200}

Evidence for trap-retarded diffusion of transition metals in α -Si was drawn from the observation that their diffusivities increase when their concentrations become comparable to the trap concentration.³⁷ This is due to the fact that the filled traps have no effect on the diffusing atoms.³⁷ It should be noted that B has an influence on the trapping properties of these defects.²²⁴ Also, it was shown that these traps can act as sinks for interstitials.³⁷ Although there is evidence of slower diffusion in α -Si when compared to c-Si, it has also been shown that a number of impurities (e.g., Au, B, and Pt), which diffuse via the kick-out mechanism in c-Si, diffuse much faster in α -Si than in c-Si.^{43,190,226} In fact, it was shown that even slow diffusers in c-Si diffuse fast in α -Si when their concentration is sufficiently high.²²⁷

The diffusion of such fast diffusing species in α -Si was modeled as an interstitial mechanism mediated by defect trapping.^{37, 194,195,199,223} It should be noted that fast diffusing impurities can also be trapped at defect sites in c-Si.¹⁹⁴ It was shown that electrical defects are associated with the structural imperfections in ion-implanted α -Si and may influence the diffusion behavior of transition metals since these electrical defects are located at the same sites as the structural defects that serve as trapping sites for fast-diffusing metal atoms (e.g., Cu and Pd).^{37,194,195,198,199,204,228} For this reason, defects controlling impurity diffusion in α -Si should also serve as midgap levels in the electronic density of states.^{223,224} It was shown that the density of these states is so high in pure α -Si (e.g., $\sim 10^{20}/\text{cm}^3$ eV) that they pin the Fermi level and dominate electronic transport.²²⁹ Electronic transport in pure α -Si is dominated by a hopping mechanism

through the large density of deep lying states in the gap which pin the Fermi level.^{229,230} This pinning of the Fermi level also prevents doping of the material.²²⁴ Past work has shown that H, implanted at concentrations of 2 at. %, can passivate these defects and prevent them from acting as trapping sites for transition metals (e.g., Cu and Pd).^{195,224} The trapping defects must, therefore, be identified with those defects which produce deep lying states in the band gap.^{195,224}

Although the as-implanted defect concentration of α -Si saturates at approximately 1-2 at. %, the saturation density of electrical defects in α -Si at room temperature is 0.3-0.6 at. % (because most of the defects in α -Si introduced by implantation anneal out when raised to room temperature).^{37,223,231} At the saturation defect density, it becomes more energetically favorable to eliminate defects at the expense of locally inserting strained regions in the α -Si network.²²³ As a result, excess defects will raise the overall network strain (due to local rearrangements involving bond angle distortions) without increasing the defect density.^{223,232} It should be noted that the degree of network strain in α -Si is not solely determined by the strain field associated with defects. It was shown that defects and tetrahedral bond angle distortions in α -Si are independent from one another, which is an important distinction from the earlier concept¹⁹⁸ that the overall network strain in α -Si is entirely controlled by defects.²²³

It was shown that low temperature (i.e., 500 °C) annealing causes a reduction in the trap defect concentration and a concomitant increase in the transition metal diffusion coefficients.^{194,195,198,199} This type of annealing induces structural relaxation of the α -Si by defect annihilation, which is consistent with the model that impurity diffusion in α -Si can be explained by frequent trapping of the diffusing impurity at structural defects

intrinsic to the amorphous structure.^{37,199,200} It should be noted that structural relaxation of the α -Si reduces the average $\Delta\theta$ from approximately 11.3° to 9° .²²³ Structural relaxation refers to an intrinsic network rearrangement which is not typical just of α -Si, but also occurs in heavily damaged c-Si where it has long been known as defect annihilation.^{198,223,233,234} It should be noted that α -Si releases an amount of heat equal to about 5 kJ/mol when it is first brought to 500°C . The fact that the density of α -Si remains unchanged upon structural relaxation suggests mutual annihilation of low- and high-density defects.^{198,204} The simplest form of such a process is vacancy-interstitial recombination which probably already occurs at very low temperatures and only has a small effect on the atomic density.^{232,235} For completion, it is noted that α -Si expands (0.1%) upon heating from room temperature to 250°C and then contracts (0.1%) on heating further to 500°C .^{236,237}

In addition to defect trapping sites, positron annihilation spectroscopy (PAS) studies have shown that a large variety of stable vacancies and small vacancy clusters are present in α -Si.²⁰¹⁻²⁰⁴ Although both vacancy and interstitial defects may exist in α -Si, positron trapping is most likely to occur only at vacancy-type defects.²⁰⁴ It was shown that the vacancy type defects that were able to trap positrons no longer serve as such traps after the dangling bonds have been passivated with H.²⁰⁴ This passivation, which reduces the density of states in the gap by several orders of magnitude, is due to either the chemical bonding of H to dangling bonds or the removal of highly strained Si bonds.^{224,238} This suggests that the H atoms are occupying vacancies and that dangling bonds are associated with vacancy type defects.²⁰⁴ The mean void size was estimated to be approximately 5 vacancies.²⁰¹ It was shown that the average defect cross section is

similar to the capture cross sections for dangling bonds in α -Si, which are discussed presently.²²³

It is also well known that ion-implanted α -Si results in the formation of an isolated threefold-coordinated topological bulk defect commonly referred to as a dangling bond.^{204,239} This defect occurs at sites where it becomes more energetically favorable to form an unsatisfied bond than to increase the stress in local bonds required by fourfold coordination.²³⁹ For completion, it should be noted that the dangling bond is also believed to be the dominant paramagnetic defect at the Si-SiO₂ interface, and is referred to as the P_b center.^{240,241} In α -Si, the Fermi level cannot be easily moved by doping because of the large density of defects such as dangling bonds.²⁴² When attempting to dope α -Si, the carriers are trapped on these dangling bond sites, thereby charging them; however, if a doping concentration on the order of the concentration of dangling bonds is introduced, it is possible to shift the Fermi level.²⁴² Earlier studies showed that the conductivity of ion-implanted α -Si can be substantially changed when the dopant concentrations are comparable to these high defect concentrations.²²⁴ It should be noted that charged dangling bonds are important in the recrystallization process.²⁴²

Some have proposed that the dangling bond in α -Si is mobile (i.e., a floating bond).^{243,244} It was shown that this so-called ‘overcoordinated’ floating bond (i.e., fivefold coordination) is very likely to occur and to have a significant effect on many of the properties of α -Si.²⁴⁵⁻²⁴⁸ For atoms that are fourfold coordinated, it is convenient to replace the four *s* and *p* orbitals with four *sp*₃ hybrids pointing in the directions of the four neighbors. When two neighboring Si atoms are fourfold coordinated, bonding and antibonding combinations form. The net result is that the basis

set consists entirely of bonding and antibonding orbitals that yield the valence and conduction bands, respectively. A point-defect in such a system represents an unsatisfied bonding-antibonding combination. In the case of threefold coordination (i.e., dangling bonds), the principle set consists of four *s* and *p* orbitals on the central atom in addition to three hybrids pointing toward it. The resulting system yields three bonding combinations in the valence bands, a dangling bond in the gap, and three antibonding states in the conduction bands. The fivefold-coordination (i.e., floating bond) condition differs from threefold coordination (i.e., dangling bond) in that the principle set consists of four *s* and *p* orbitals on the central atom plus five hybrids pointing toward it. The resulting system yields four bonding combinations in the valence bands, a nonbonding state in the gap, and four antibonding states in the conduction bands. The principle part of the nonbonding state (i.e., the floating bond) is completely localized on the five hybrids with negligible amplitude on the four orbitals of the central atom. Although subsequent work found little direct indication for such mobility in α -Si,²⁴⁹ additional experiments showed evidence of a temperature dependent line shape that was most likely associated with a highly mobile paramagnetic defect in α -Si.²⁴⁴

Electron paramagnetic resonance (EPR) [or electron spin resonance (ESR)] studies have shown that the concentration of dangling bonds in α -Si is on the order of 0.02-0.10 at. %,^{223,250,251} which is considerably lower than the concentration of structural defects determined by such techniques as differential scanning calorimetry (DSC),¹⁹⁸ optical-absorption spectroscopy,²²³ and positron annihilation.²⁵² This indicates that most of the structural defects are not paramagnetic and shows that EPR has a very limited sensitivity and is incapable of detecting the majority of defects in α -Si.^{198,204,223} This

sensitivity arises because EPR detects unpaired dangling bonds which have a large formation energy of several eV.¹⁹⁸ This could imply that the major fractions of dangling bond centers are not occupied by a single electron.²²³ It should be noted that most of the dangling bonds are expected to exchange electrons in pairs and become either positively or negatively charged, thereby losing its EPR activity.¹⁹⁸ It was postulated that the charging of the defects will modify their trapping properties.²²⁴ Indeed, it was shown that the defects are preferentially charged positively in the presence of B, and that positively charged traps are less efficient than neutral traps.²²⁴ The difference in the trapping efficiency can be explained by variations in the enthalpy and entropy of the system with the addition of dopants.²²⁴ It should be noted that α -Si could also contain electrical defects different from dangling bonds, such as uncharged vacancies and/or vacancy complexes surrounded by reconstructed Si bonds, which introduce non-paramagnetic electronic levels in the band gap.²²³ This difference in the defect concentrations suggests that, either there are dangling bond configurations that are not paramagnetic, or structural defects do not necessarily have to embody broken or dangling bonds. The latter situation would entail Si-Si strained bonds. It should be noted that various types of defects are found to contribute to the EPR spectra of c-Si.²²³

This brief overview of defects in α -Si, together with the following discussion based on impurity trapping and gettering, will provide a description of the physical mechanism believed to be causing the anomalous diffusion enhancement observed for the wafer that received the additional 12 keV F⁺ implant to $1.5 \times 10^{15}/\text{cm}^2$. It was shown that implanted Cu⁺, which diffuses interstitially in α -Si, exhibits a partitioning between the two different structural states of α -Si.^{37,194} This was done by creating a 2.2 μm thick

amorphous layer by use of overlapping 0.5, 1.0 and 2.0 MeV Si⁺ implants each to $5 \times 10^{15}/\text{cm}^2$. The implants were performed at -196 °C. Two of the three resulting sections were annealed at 500 °C for 1 hr at a base pressure below 10^{-7} Torr to bring the α-Si to a structurally relaxed state. One of the annealed samples was then implanted with 5.5 MeV Si⁺ to $1.6 \times 10^{15}/\text{cm}^2$ to bring the α-Si back to a structurally unrelaxed state, similar to the as-implanted case. All three samples were then implanted with 200 keV Cu⁺ to $5.5 \times 10^{15}/\text{cm}^2$ and subsequently annealed at various temperatures ranging from 150 to 270 °C, for times between 10 min and 104 hr. Backscattering (BS) spectra showed a significant amount of Cu in-diffusion for the unannealed sample after a 221 °C anneal for 4 hr. However, for the annealed sample, a high uniform Cu concentration is observed in an approximately 300 nm thick surface layer (i.e., the unannealed portion of the layer) while a low concentration Cu tail is observed in the deeper lying annealed layer. The interface between the two concentration regions corresponds to the EOR of the Cu⁺ implant, which returned the first 300 nm of α-Si to a structurally unrelaxed state. The higher Cu concentration in the 300 nm surface layer suggests that during the anneal, Cu is partially reflected at the interface between annealed and unannealed α-Si, which is characteristic of solute partitioning at a phase boundary. The ratio between the Cu levels in the two structural states of α-Si can be thought of in terms of a partitioning coefficient (k), which is approximately $k = 9 \pm 1$. It should be noted that the Cu diffusion profile in the sample that received both the 500 °C anneal and 5.5 MeV Si⁺ implant to $1.6 \times 10^{15}/\text{cm}^2$ was similar to that observed for the unannealed sample. Additional data showed that the partition coefficient is independent of Cu concentration and both diffusion time and temperature in the temperature range investigated. This data showed for the first time

that defects in unannealed α -Si are capable of trapping and gettering impurities in α -Si. It should be noted that this impurity trapping resulted in an extremely high solubility of Cu in α -Si; this will be discussed later. Also, although the diffusion coefficient in annealed α -Si is a factor of 2-5 higher than in unannealed α -Si (presumably due to the decrease in defect concentration with the additional 500 °C anneal), the activation energies for diffusion in both types of α -Si are identical within experimental error, indicating that the structurally relaxed state of α -Si is still highly defective and that diffusion in both cases is defect dominated.

Another experiment performed by Coffa *et al.* demonstrated the ability of the defects within unannealed α -Si to trap and getter impurities.¹⁹⁹ Similar to the previous experiment, a 2.2 μm thick α -Si layer was produced by overlapping 0.5, 1.0, and 2.0 Si⁺ implants to $5 \times 10^{15}/\text{cm}^2$. These implants were also performed at -196 °C. The as prepared α -Si was subsequently implanted at -196 °C with 500 keV Pd⁺ to $2 \times 10^{15}/\text{cm}^2$. It should be noted that Pd diffuses interstitially in α -Si.³⁷ The material was then annealed at 500 °C for 1 hr at a base pressure of 10^{-6} mbar (7.5×10^{-7} Torr) to bring the α -Si to a structurally relaxed state as well as completely redistribute the Pd to a uniform concentration of $1 \times 10^{19}/\text{cm}^3$ throughout the amorphous layer. The near surface region of the α -Si layer was subsequently implanted at -196 °C with 200 keV Si⁺ to doses ranging from 1×10^{12} - $5 \times 10^{15}/\text{cm}^2$. These implants were done to bring the first 400 nm of α -Si to varying degrees of the structurally unrelaxed state, while the rest of the α -Si remained in the structurally relaxed state. The samples were then annealed at 250 °C for 36 hr. This anneal was done to investigate the Pd diffusion behavior without annealing a significant

amount of the implantation-induced structural defects. Rutherford backscattering spectrometry (RBS) measurements show that, after annealing at 250 °C for 36 hr, the Pd is gettered from the bulk of the material to the Si⁺ implanted surface region. It was shown that the amount of trapped Pd increased with increasing Si⁺ dose up to $5 \times 10^{12}/\text{cm}^2$; above $5 \times 10^{12}/\text{cm}^2$ a saturation was observed, which was characterized by the same Pd signal height for doses of 1×10^{13} and $5 \times 10^{15}/\text{cm}^2$, for example. It appeared as though the low dose Pd profiles were associated with the defects produced by Si⁺ implantation which getter the Pd atoms. Indeed, TRIM simulations confirmed that the concentration of displaced atoms compare quite well with the measured profiles of the Pd atoms for the low dose Si⁺ implants. This experiment confirmed that, in fact, defects in α-Si are capable of gettering impurities such as Cu and Pd when in the unannealed (i.e., as-implanted) state.

An additional experiment by Coffa and Poate was performed to better understand the effect of defect concentration on the diffusion behavior of both Cu and Pd in α-Si.¹⁹⁵ Once again, overlapping 0.5, 1.0, and 2.0 Si⁺ implants to $5 \times 10^{15}/\text{cm}^2$ were used to generate a $2.2 \mu\text{m}$ thick α-Si layer. These implants were performed at -196 °C. The as-prepared α-Si was subsequently implanted at -196 °C with 500 keV Pd⁺ to $2 \times 10^{15}/\text{cm}^2$. The material was then annealed under vacuum at 500 °C for 1 hr in order to bring the α-Si to a structurally relaxed state as well as completely redistribute the Pd throughout the amorphous layer. These samples were then implanted at -196 °C with 80 keV H⁺ to doses between $1.4-7.0 \times 10^{16}/\text{cm}^2$. The peak concentration of these implants was in the range 1-5 at. %. In order to achieve a uniform concentration of defects in the amorphous layer, the samples were further implanted with 2 MeV Si⁺ to $5 \times 10^{15}/\text{cm}^2$.

This implant produced a saturation value in the defect concentration throughout the entire α -Si layer. Vacuum annealing was then performed over the temperature range of 250-500 °C. The time at each anneal temperature was chosen so as to allow complete redistribution of the Pd in the sample (e.g., 350 °C for 2 hr). Rutherford backscattering spectrometry was used to measure the depth distribution of the Pd atoms, whereas the H depth distribution was obtained by measuring the resistivity of the α -Si layer as a function of depth using the spreading-resistance technique. These measurements showed that Pd was depleted or rejected from the region containing the implanted H. The authors noted that this depletion was partial for the lower H⁺ dose of $1.4 \times 10^{16}/\text{cm}^2$; however, appeared to be complete for the higher H⁺ dose of $7 \times 10^{16}/\text{cm}^2$. The depletion or rejection of Pd during the anneal was explained by the following discussion. The as-implanted H and diffused Pd occupied traps or defect states in the amorphous layer. During the anneal, a thermodynamic equilibrium was established between the free and trapped impurity atoms. Since the Pd diffusion length during a 350 °C anneal for 2 hr was comparable to the thickness of the α -Si layer, the post-annealing Pd depth profiles are presumed to reflect the distribution of traps which were available to the Pd atoms throughout the amorphous layer. The fact that the Pd is rejected from the H containing region indicates not only that the Pd and H occupy the same traps but also that H is more strongly bonded to these traps (a concentration of which the authors estimate to be approximately 2.2 at. % in pure α -Si). Additional RBS results showed that the region from which Pd was depleted became larger with higher annealing temperatures, presumably due to H diffusion. In other words, at a higher annealing temperature, the broadening of the H concentration profile caused a saturation of the traps and induced

de-trapping of Pd over a larger region. In addition to Pd, the authors performed a similar experiment with implanted Cu⁺. It should be noted that both Pd and Cu diffuse interstitially in α -Si.³⁷ In that experiment, 220 keV Cu⁺ was-implanted to $2.5 \times 10^{15}/\text{cm}^2$ and completely redistributed throughout the α -Si layer by annealing at 300 °C for 1 hr. The wafer was then implanted with 50 keV H⁺ to $4 \times 10^{16}/\text{cm}^2$ and subsequently annealed at 350 °C for 1 hr. The corresponding RBS profiles showed that the Cu is fully depleted from the region which contains H. It should be noted that the diffusion of both Pd and Cu through the passivated α -Si is enhanced by a factor of 5 when compared to the non-passivated case. This is consistent with their model that considers transition metal diffusion in α -Si to be similar to an interstitial mechanism mediated by defect trapping. It should be noted that the higher activation enthalpy (1.5 eV) for H diffusion in α -Si compared to Pd (1.1 eV) is consistent with the H being more strongly bonded to the trapping defects in α -Si. The most noteworthy result of this experiment is that additional results (not shown) revealed that implanted F⁺ was as efficient as H in de-trapping Cu or Pd.

The results of these experiments offer a possible explanation for the difference observed between the as-implanted profiles in Figure 6-3. It was already shown through the literature that impurities such as H and F can passivate the trapping sites in α -Si by forming highly-favored bonding arrangements. When these trapping sites are occupied, interstitially diffusing species such as Pd and Cu are rejected from the passivated regions presumably due to there being no structural defects capable of preventing their motion. It is reasonable to put forward that the 12 keV F⁺ implant to $1.5 \times 10^{15}/\text{cm}^2$ is sufficient to passivate the α -Si trapping sites therefore allowing B, which is presumed to diffuse

interstitially in α -Si, to diffuse into the substrate to a depth consistent with the distribution of available trapping sites. It should be noted that the F concentration at the depth where B begins to form the exponentially decreasing profile is approximately $3 \times 10^{20}/\text{cm}^3$ (i.e., 0.6 at. %). This is significantly less than the 80 keV H^+ implant to $7 \times 10^{16}/\text{cm}^2$ used in Ref. 195 to de-trap the Pd and Cu, which resulted in a peak concentration of approximately 5 at. %; however, it is remarkably close to the value reported by Stolk *et al.* for the saturation defect density in α -Si at room temperature (i.e., 0.5 at. %).²²³ The most notable difference between the literature and the present experiment is that, here, the B underwent a significant diffusion enhancement without any additional thermal annealing procedure. The experiments described earlier observed impurity de-trapping or gettering after some additional thermal processing, which was used to promote impurity diffusion in α -Si.

It should be noted that the data in Ref. 196 show a similar exponentially decreasing profile as a function of depth for the wafer with the additional F^+ implant. There, two Si substrates were pre-amorphized with 70 keV Si^+ implantation to $1 \times 10^{15}/\text{cm}^2$, which generated a 180 nm continuous amorphous layer. These wafers were then implanted with 0.5 keV B^+ to $1 \times 10^{15}/\text{cm}^2$. One of the wafers was subsequently implanted with 6 keV F^+ to $2 \times 10^{15}/\text{cm}^2$. The SIMS results showed that the as-implanted junction abruptness and x_j for the wafer without the 6 keV F^+ implant to $2 \times 10^{15}/\text{cm}^2$ was approximately 4 nm/dec and 15 nm at a concentration $1 \times 10^{18}/\text{cm}^3$, respectively. This can be compared to the as-implanted junction abruptness and x_j for the wafer with the additional F^+ implant, which degrades to approximately 13 nm/dec and increases to 28 nm at a concentration of $1 \times 10^{18}/\text{cm}^3$, respectively. This data goes against any argument that puts forward the F,

which was-implanted first in the current experiment, had time to establish a certain type of equilibrium with the trapping defects in α -Si before the B^+ implant, and that this allowed for the observed increase in x_j . This independence of implant sequence needs to be better understood. It should be noted that, although the degradation in junction abruptness is similar for each of the wafers that received the additional F^+ implant (i.e., approximately 9 nm/dec), the increase in x_j is about 3.5 nm greater for the data presented in Ref. 196. This increase in x_j could be a result of either the higher F^+ dose (i.e., $2 \times 10^{15}/\text{cm}^2$ compared to $1.5 \times 10^{15}/\text{cm}^2$), which may occupy more trapping defects and therefore increase the B diffusion behavior, or the fact that the F implant in Ref. 196 was performed after the B implant and was sufficient to redistribute the B profile due to the nuclear collisions between the B atoms in the amorphous layer and the transmitted F ions. It should be noted that, based on the current discussion, the effect of the F from the BF_2^+ implant is not known.

A number additional experiments were performed to better understand the effect of F^+ co-implantation on the differences observed between the as-implanted junction abruptness and x_j for the wafer without and with the 12 keV F^+ implant to $1.5 \times 10^{15}/\text{cm}^2$. The first experiment was designed to investigate whether the observed diffusion behavior was similar to that produced by ion channeling. It is well known that implant profiles into c-Si can be significantly different than a Gaussian profile due to ion channeling. This occurs when the ion trajectory is aligned along atomic rows where it experiences a slower rate of energy loss, thereby producing a profile with an asymmetric distribution; one that is Gaussian towards the substrate surface but supplemented by a characteristic broadening at lower concentrations into the bulk of the substrate. Ion channeling can be

eliminated by implanting a heavy mass ion (e.g., Si⁺ or Ge⁺) before dopant incorporation to bring the substrate surface to an amorphous state. Amorphization of the substrate surface effectively prevents the possibility of the ions aligning along atomic rows where they can travel for distances greater than expected. It should be noted that ion channeling can be partially prevented by pre-damaging the substrate surface before dopant incorporation; pre-damaging the substrate refers to a damage profile that is below the amorphization threshold, however, sufficient to reduce the effect of ion channeling. For this experiment, two 200 mm 3-5 Ω·cm (100) n-type CZ grown Si wafers were either pre-damaged or pre-amorphized with an 80 keV Ge⁺ implant to 3×10^{13} or $1 \times 10^{15}/\text{cm}^2$, respectively. These two wafers as well as an undamaged control wafer were subsequently implanted with 1 keV B⁺ to $1 \times 10^{15}/\text{cm}^2$. The implants were carried out in the drift mode and performed at room temperature with the ion beam normal to the surface plane using an Applied Materials Leap-II system. The implant parameters were monitored to ensure they remained within predetermined limits. The energy of the Ge⁺ implant was increased to 80 keV to create a sufficient amount of damage for the low dose implant and produce the thickest possible continuous amorphous layer under the available implant capabilities for the high dose implant, which was determined to be approximately 110 nm by XTEM imaging (not shown). The control wafer was not pre-damaged to determine the effect of ion channeling on the as-implanted profile of the 1 keV B⁺ implant to $1 \times 10^{15}/\text{cm}^2$. It should be noted that the effect of ion channeling could have been minimized without pre-damaging the substrate by performing the B implant at an angle to the substrate surface, which reduces alignment with the atomic rows. Figure 6-12 shows the SIMS results for the three as-implanted profiles

corresponding to the different damage conditions established before the 1 keV B⁺ implant to $1 \times 10^{15}/\text{cm}^2$. As can be seen, the implant conditions result in as-implanted profiles with junction abruptness of 10.5, 7.0, and 3.4 nm/dec and x_j of 40.8, 35.6, and 21.5 nm for the control wafer and the wafers that received the 80 keV Ge⁺ implant to 3×10^{13} and $1 \times 10^{15}/\text{cm}^2$, respectively. This shows that the effect of pre-damaging the substrate surface before dopant incorporation is sufficient to improve the as-implanted junction abruptness and x_j . Figure 6-13 shows the SIMS data for the as-implanted profile for the wafer without any pre-damage in Figure 6-12 together with the SIMS profiles of the two as-implanted profiles used in the original experiment shown in Figure 6-3. As can be seen, the effect of ion channeling degrades the junction abruptness and increases the x_j much more significantly than the effect observed with the 12 keV F⁺ implant to $1.5 \times 10^{15}/\text{cm}^2$. It should be noted that the differences between the B implant conditions (i.e., the lower B⁺ energy and dose for the original experiment) are not expected to make difficult the conclusion that ion channeling does not cause the degradation in junction abruptness and increase in x_j observed for the as-implanted profile in Figure 6-3 for the wafer with the additional F⁺ implant.

The second additional experiment was designed to investigate the effect of the F from the BF₂⁺ implant as well as the effect of implanting the 12 keV F⁺ implant to $1.5 \times 10^{15}/\text{cm}^2$ before or after the B⁺ implant on the as-implanted junction abruptness and x_j for the wafer without and with the 12 keV F⁺ implant to $1.5 \times 10^{15}/\text{cm}^2$. The equivalent B⁺ implant energy will be used to compare the effect of the F from the BF₂⁺ implant. The equivalent B⁺ implant energy can be determined by the using the ionic mass ratio between the B and F ions. In the case of BF₂⁺ molecular ions, the dissociated B⁺ has

approximately 22% (i.e., 11:49) of the total ion energy. For a 3 keV BF_2^+ implant, this results in an equivalent B^+ energy of approximately 0.67 keV. It is well known that as the energy required to produce the SDE decreases, the loss of beam current due to the reduced electric field between the anode and cathode becomes a significant issue. Lower beam current requires more time to complete a low energy implant, which is of great importance in an environment such as a manufacturing facility. One of the most significant advantages of using BF_2^+ for the p-type SDE is the increased beam current associated with the higher partial pressure of BF_2 when compared to that of B .⁶³ The higher number of BF_2 molecules leads to a higher number of BF_2 ions that are accelerated by the voltage plates of the system, resulting in a higher beam current. Although a 0.67 keV B^+ implant to $1 \times 10^{15}/\text{cm}^2$ is not as manufacturable as a 3 keV BF_2^+ implant to $1 \times 10^{15}/\text{cm}^2$ for the p-type SDE, it will be used here to better understand the effect of the F from the BF_2^+ implant on the as-implanted junction abruptness and x_j for the wafer without and with the 12 keV F^+ implant to $1.5 \times 10^{15}/\text{cm}^2$. For this experiment, six 200 mm 3-5 $\Omega\cdot\text{cm}$ (100) n-type CZ grown Si wafers were pre-amorphized with a 60 keV Ge^+ implant to $1 \times 10^{15}/\text{cm}^2$. The six wafers were then divided into two sets of three wafers each. For each set of wafers, one wafer received the B^+ implant (i.e., either the 0.67 keV B^+ or 3 keV BF_2^+ implant to $1 \times 10^{15}/\text{cm}^2$) without any additional F^+ implant and the other two wafers of each set were subject to a 12 keV F^+ implant to $1.5 \times 10^{15}/\text{cm}^2$ either before or after their respective B^+ implant. The implants were carried out in the drift mode and performed at room temperature with the ion beam normal to the surface plane using an Applied Materials Leap-II system. The implant parameters were monitored to ensure they remained within predetermined limits. The energy of the Ge^+

implant was increased to 60 keV to produce the thickest possible continuous amorphous layer under the available implant capabilities. Figure 6-14 shows the SIMS results for the six as-implanted profiles corresponding to the different implant conditions used in this study. As can be seen, the as-implanted profiles have junction abruptness of approximately 3.3, 13.2, and 15.7 nm/dec and x_j of 17.3, 27.8, and 32.7 nm for the control wafer without the additional F⁺ implant and the wafers that received the 12 keV F⁺ implant to $1.5 \times 10^{15}/\text{cm}^2$ before and after the B⁺ implant, respectively. These results show that the additional F⁺ implant significantly degrades the junction abruptness and increases the x_j when compared to the profiles without the 12 keV F⁺ implant to $1.5 \times 10^{15}/\text{cm}^2$, independent of the additional F⁺ implant being performed before or after the B⁺ or BF₂⁺ implant. The observation that the same as-implanted profile forms for the wafers that received the 12 keV F⁺ implant to $1.5 \times 10^{15}/\text{cm}^2$ after their respective B⁺ implants supports the earlier suggestion that the F does not establish a certain type of equilibrium with the trapping defects in α -Si when the F⁺ is implanted before the B⁺ implant. It should be noted that the as-implanted profiles for the wafers that received either the B⁺ implant without any additional F⁺ implant or the 12 keV F⁺ implant to $1.5 \times 10^{15}/\text{cm}^2$ before the respective B⁺ implants are similar down to a concentration of approximately $1 \times 10^{19}/\text{cm}^2$, below which the as-implanted profile for the wafer with the additional F⁺ implant decreases exponentially as a function of depth; consistent with the as-implanted profiles of the original experiment shown in Figure 6-3. It is this exponential decrease that produces such a large difference between the as-implanted junction abruptness and x_j . The most interesting result of this experiment is that the F from the BF₂⁺ implant does not affect the as-implanted profile for any of the conditions

used in this study. In other words, the F from the BF_2^+ implant is insufficient to degrade the junction abruptness and increase the x_j for any of the as-implanted profiles. The most notable independence is that observed for the 3 keV BF_2^+ implant to $1\times 10^{15}/\text{cm}^2$ without the additional F^+ implant. That data shows that, although the F from the 12 keV F^+ implant to $1.5\times 10^{15}/\text{cm}^2$ affects the as-implanted B profile, the F from the 3 keV BF^+ implant to $1\times 10^{15}/\text{cm}^2$ has no such effect. One possible explanation for this observation is that the mechanism causing the degradation in junction abruptness and increase in x_j with the 12 keV F^+ implant to $1.5\times 10^{15}/\text{cm}^2$ (i.e., diffusion of freely moving B atoms due to F passivation of the trapping sites in the amorphous phase) at relatively low B concentrations no longer affects low temperature diffusion when the B and F atoms are present at relatively the same concentration. The equivalent F^+ implant energy for the 3 keV BF^+ implant to $1\times 10^{15}/\text{cm}^2$ is calculated to be approximately 1.16 keV. Additional TRIM simulations estimate that the R_p and vertical straggle (ΔR_p) for the equivalent implant energy of the B (i.e., 0.67 keV) and F (i.e., 1.16 keV) ions are approximately 4.5 and 4.7 nm and 2.3 and 2.4 nm, respectively. This shows that the equivalent implant energy will place the F profile near the substrate surface where it will closely overlap the B profile. It should be noted that the F concentration is expected to be twice as high as the B concentration in any particular region due to the stoichiometry of the BF_2 molecular ion. The observation that the F from the 3 keV BF^+ implant to $1\times 10^{15}/\text{cm}^2$ has no effect on the as-implanted B profile may be due to the relatively high concentration of unoccupied trapping sites near the substrate surface. In other words, although the F may be detrappling the B atoms from defect sites near the substrate surface, the relatively high concentration of unoccupied trapping sites would most likely trap the mobile atoms near

their original position; resulting in a Gaussian profile. The B atoms that remain immobile in α -Si independent of the 12 keV F^+ implant to $1.5 \times 10^{15}/\text{cm}^2$ may either be clustering with each other at high concentrations or binding with Si interstitials which form immobile B clusters. In order to remain consistent with the current postulate regarding submicroscopic cluster formation, the atoms that participate in cluster formation must be B atoms and Si interstitials. This is an interesting result considering the high local concentration of both B and Si atoms is enough to affect the B diffusion behavior in α -Si at room temperature. This explanation is consistent with the rest of the data in Figure 6-14 in that B clustering at high concentrations should have no effect on the part of the as-implanted profile that undergoes an increase in diffusion behavior at low temperatures and the presumed passivation of the trapping sites in the amorphous phase only occurs with the addition of the 12 keV F^+ implant to $1.5 \times 10^{15}/\text{cm}^2$. Another interesting result of this data is that the two profiles corresponding to the wafers that received the 12 keV F^+ implant to $1.5 \times 10^{15}/\text{cm}^2$ after their respective B^+ implants are deeper than the two profiles with the additional F^+ implant before the B^+ implants. A similar difference was observed when comparing the as-implanted profiles in Figure 6-3 to those in Ref. 196. It was noted that this increase in x_j could be a result of either the higher F^+ dose (i.e., $2 \times 10^{15}/\text{cm}^2$ compared to $1.5 \times 10^{15}/\text{cm}^2$), which may occupy more trapping defects and therefore increase the B diffusion behavior, or the fact that the F^+ implant in Ref. 196 was performed after the B implant and was sufficient to redistribute the B profile due to the nuclear collisions between the B atoms in the amorphous layer and the transmitted F ions. The data of this experiment show that the increase in x_j is not due to the higher F^+ dose. In order to test the idea that nuclear collisions between the B

atoms in the amorphous layer and the transmitted F ions produce the increase in x_j when the 12 keV F⁺ implant to $1.5 \times 10^{15}/\text{cm}^2$ is performed after either the B⁺ or BF₂⁺ implant, the following experiment was performed: for this experiment, four 200 mm 3-5 Ω·cm (100) n-type CZ grown Si wafers were pre-amorphized with a 60 keV Ge⁺ implant to $1 \times 10^{15}/\text{cm}^2$. The four wafers were then divided into two sets of two wafers each. One set of wafers was subject to a 0.67 keV B⁺ implant to $1 \times 10^{15}/\text{cm}^2$, while the other set of wafers was subject to a 3 keV BF₂⁺ implant to $1 \times 10^{15}/\text{cm}^2$. One wafer from each set was then subject to either a 46 keV Ge⁺ implant to $1.5 \times 10^{15}/\text{cm}^2$ or a 58 keV GeF⁺ molecular ion implant to $1.5 \times 10^{15}/\text{cm}^2$. It should be noted that the energy of the GeF⁺ molecular ion implant was chosen to result in an equivalent implant energy of approximately 12 keV for the F ions; the energy of the Ge⁺ implant is the equivalent implant energy of the 58 keV GeF⁺ molecular ion implant. These implants were performed to determine the effect of ion mass on the profile broadening observed in Figure 6-14 for the wafers that received the 12 keV F⁺ implant to $1.5 \times 10^{15}/\text{cm}^2$ after either the B⁺ or BF₂⁺ implant. The implants were carried out in the drift mode and performed at room temperature with the ion beam normal to the surface plane using an Applied Materials Leap-II system. The implant parameters were monitored to ensure they remained within predetermined limits. The energy of the Ge⁺ implant was increased to 60 keV to produce the thickest possible continuous amorphous layer under the available implant capabilities. Figure 6-15 shows the SIMS results for four of the as-implanted profiles shown in Figure 6-14 together with the SIMS profiles of the four as-implanted profiles used in this experiment. As can be seen, the as-implanted profiles have junction abruptness of approximately 34.3 and 35.2 nm/dec and x_j of 53.2 and 56.0 nm for the wafers that received the 46 keV Ge⁺

implant to $1.5 \times 10^{15}/\text{cm}^2$ and 58 keV GeF⁺ molecular ion implant to $1.5 \times 10^{15}/\text{cm}^2$ after their respective B⁺ implants. These results show that the x_j increases with increasing mass of the implanted ion. The increase in x_j is most likely due to the increase in momentum transfer between the B atoms in the amorphous layer and the subsequently implanted heavier ions. It is presumed that this so-called ‘knock-on’ effect produces the difference between the as-implanted profiles with the 12 keV F⁺ implant to $1.5 \times 10^{15}/\text{cm}^2$ observed in Figure 6-14. It can be seen that the F from 3 keV BF₂⁺ implant to $1 \times 10^{15}/\text{cm}^2$ does not affect the as-implanted profiles. This supports the idea that the B atoms are either clustering with each other or binding with Si interstitials which form immobile B clusters. It should be noted that this ‘knock-on’ effect is capable of increasing the depth of the B profile at B concentrations as high as $1 \times 10^{20}/\text{cm}^3$.

Another experiment was performed to better understand the effect of F⁺ co-implantation on the differences observed between the as-implanted profiles for the wafer without and with the 12 keV F⁺ implant to $1.5 \times 10^{15}/\text{cm}^2$. This experiment was designed to investigate the suggestion that F passivation of the trapping sites in the amorphous phase produces the observed degradation in junction abruptness and increase in x_j for the as-implanted profiles in Figure 6-3. It is well known that B diffusion is suppressed in SiGe when compared to intrinsic c-Si.²⁵³⁻²⁶⁰ In particular, B was observed to pileup in SiGe layers adjacent to intrinsic c-Si films.²⁵⁹ This was done by growing a 100 nm buffer layer of epitaxial Si on {100} float zone (FZ) Si by low-pressure chemical vapor deposition (LPCVD) at 850 °C using a mixture of SiH₄ and H₂ gas, followed by the growth of an undoped 40 nm Si_{0.9}Ge_{0.1} layer using a mixture of SiH₄, GeH₄, and H₂ gas. A 250 nm Si layer containing B was then grown using B₂H₆ to concentrations of 3×10^{18} ,

6×10^{18} , and $1.5 \times 10^{19}/\text{cm}^3$. This was followed by the growth of a second undoped 40 nm $\text{Si}_{0.9}\text{Ge}_{0.1}$ layer and a capping layer of 100 nm of undoped Si. After growth of the epitaxial layers, 40 nm of SiO_2 and 160 nm of Si_3N_4 were deposited to form a barrier against the diffusion of O_2 or water vapor, which might be present in trace amounts during the subsequent heat treatments. These heat treatments were at 850 °C in an N_2 ambient for periods of 4, 24, or 96 hr for each of the three B concentrations. It should be noted that the SiGe layer thickness was chosen to avoid relaxation during post-deposition thermal processing. The SIMS results showed a pileup of B in the SiGe layers. The corresponding simulation results suggest that the difference between the total B concentration and the active mobile B concentration after diffusion can be explained by a simple pairing mechanism due to the formation of an immobile complex which forms due to B trapping at Ge atom sites through the reaction,



The authors note that by assuming that the complex GeB is immobile, a simple mechanism can be implied for reducing the diffusion of B when Ge is present. It should be noted that the adjustable parameter used in their model was found to be independent of concentration for all three B concentrations used in the experiment (for both the 24 and 96 hr anneals at 850 °C). The pairing of B and Ge atoms is consistent with the fact that the two atoms compensate strain.²⁵³ It was suggested that, since Ge diffuses much slower compared to B in Si, an attraction between Ge and B might slow B diffusion in SiGe alloys.²⁶¹ It should be noted that B diffusion in SiGe was shown to be predominantly a function of Ge content rather than biaxial strain.²⁵⁶ It is possible, however, that the local strain could increase the interstitial formation energy thereby affecting diffusion.²⁵⁶

Since it was shown through the literature that B diffusion is retarded in SiGe alloys, presumably due to B trapping at Ge atom sites, it is of interest to see if the addition of Ge to the amorphous material has any measurable effect on the low temperature diffusion behavior observed for the as-implanted profiles in Figure 6-14. In other words, adding Ge to the amorphous layer may reduce the amount of diffusion observed with the addition of the 12 keV F⁺ implant to $1.5 \times 10^{15}/\text{cm}^2$ due to trapping of B at Ge atom sites. For this experiment, two 200 mm 3-5 Ω·cm (100) n-type CZ grown Si wafers were pre-amorphized with a 60 keV Ge⁺ implant to $1 \times 10^{15}/\text{cm}^2$. The wafers were then subject to a 58 keV GeF⁺ implant to $1.5 \times 10^{15}/\text{cm}^2$ and subsequently implanted with either 0.67 keV B⁺ or 3 keV BF₂⁺ molecular ions to $1 \times 10^{15}/\text{cm}^2$. The implants were carried out in the drift mode and performed at room temperature with the ion beam normal to the surface plane using an Applied Materials Leap-II system. The implant parameters were monitored to ensure they remained within predetermined limits. The energy of the Ge⁺ implant was increased to 60 keV to produce the thickest possible continuous amorphous layer under the available implant capabilities. Figure 6-16 shows the SIMS results for four of the as-implanted profiles shown in Figure 6-14 together with the SIMS profiles of the two as-implanted profiles used in this experiment. As can be seen, the as-implanted profiles have junction abruptness of approximately 7.7 nm/dec and average x_j of 21.5 nm for the wafers that received the 58 keV GeF⁺ molecular ion implant to $1.5 \times 10^{15}/\text{cm}^2$ before their respective B⁺ implants. These results show that the additional $1.5 \times 10^{15}/\text{cm}^2$ of Ge is sufficient to reduce the low temperature diffusion behavior observed with the 12 keV F⁺ implant to $1.5 \times 10^{15}/\text{cm}^2$. It can be seen that the as-implanted profiles for this experiment are similar to those for the wafers without any additional F⁺ or GeF⁺ implants.

down to a concentration of $3 \times 10^{18}/\text{cm}^2$, below which the as-implanted profile for the wafer with the additional GeF^+ implant decreases exponentially as a function of depth. This shows that the GeF^+ implant decreases the concentration level below which low temperature B diffusion is observed; it is this exponential decrease in the B concentration that produces the difference between the as-implanted junction abruptness and x_j for wafers without and with the additional GeF^+ before their respective B^+ implants. Consistent with data from previous experiments, the F from the BF_2^+ implant does not affect the as-implanted profile for any of the conditions used in this study. These results provide evidence of B trapping at Ge atom sites in the amorphous phase, and show that Ge atoms sites are sufficient to compete with the de-trapping that presumably occurs with the addition of the 12 keV F^+ implant to $1.5 \times 10^{15}/\text{cm}^2$. The results of these experiments suggest that F passivation of the trapping sites in the amorphous phase is responsible for the observed degradation in junction abruptness and increase in x_j for the as-implanted profiles in Figure 6-3.

It is well known that ion-implanted α -Si results in the formation of an isolated threefold-coordinated topological bulk defect commonly referred to as a dangling bond.^{204,239} This defect occurs at sites where it becomes more energetically favorable to form an unsatisfied bond than to increase the stress in local bonds required by fourfold coordination.²³⁹ In α -Si, the Fermi level cannot be easily moved by doping because of the large density of defects such as dangling bonds.²⁴² When attempting to dope α -Si, the carriers are trapped on these dangling bond sites, thereby charging them; however, if a doping concentration on the order of the concentration of dangling bonds is introduced, it is possible to shift the Fermi level.²⁴² In other words, doping the material can be done

when the number of trapping sites is reduced. Electron paramagnetic resonance studies have shown that the concentration of dangling bonds (i.e., D centers) in α -Si is on the order of 0.02-0.10 at. %,^{223,250,251} which is considerably lower than the concentration of structural defects determined by such techniques as DSC,¹⁹⁸ optical-absorption spectroscopy,²²³ and positron annihilation.²⁵⁰ This indicates that most of the structural defects are not paramagnetic and shows that EPR has a very limited sensitivity and is incapable of detecting the majority of defects in α -Si.^{198,204,223} This sensitivity arises because EPR detects unpaired dangling bonds which have a large formation energy of several eV.¹⁹⁸ It should be noted that α -Si could also contain electrical defects different from dangling bonds, such as uncharged vacancies and/or vacancy complexes surrounded by reconstructed Si bonds, which introduce non-paramagnetic electronic levels in the band gap.²²³ This difference in the defect concentrations suggests that, either there are dangling bond configurations that are not paramagnetic, or structural defects do not necessarily have to embody broken or dangling bonds. The latter situation would entail Si-Si strained bonds. It is interesting to note that the dangling bond concentration reported in earlier EPR studies was found to be approximately $1-5 \times 10^{19}/\text{cm}^3$ (i.e., 0.02-0.10 at. %),^{223,250,251} which is remarkably close to the concentration level below which the increase in low temperature diffusion behavior was found to occur for the as-implanted profiles in Figure 6-14; therefore, it is of interest to investigate the effect of F^+ co-implantation on the resulting EPR signal to better understand the mechanisms controlling the low temperature diffusion behavior observed for the as-implanted profiles in Figure 6-14. For this experiment, three 200 mm 50-70 $\Omega\cdot\text{cm}$ (100) n-type CZ grown Si wafers were pre-amorphized with a 60 keV Ge^+ implant to $1 \times 10^{15}/\text{cm}^2$. It should be

noted that the wafer resistivity used in this experiment was increased to enhance the EPR signal measured from the paramagnetic defects in α -Si. Two of the wafers were then subject to 12 keV F⁺ implantation to either 1.5×10^{15} or $3.0 \times 10^{15}/\text{cm}^2$. The 12 keV F⁺ implant to $3.0 \times 10^{15}/\text{cm}^2$ was performed to better understand the effect of F⁺ co-implantation on the as-implanted EPR signal. The implants were carried out in the drift mode and performed at room temperature with the ion beam normal to the surface plane using an Applied Materials Leap-II system. The implant parameters were monitored to ensure they remained within predetermined limits. The energy of the Ge⁺ implant was increased to 60 keV to produce the thickest possible continuous amorphous layer under the available implant capabilities. The wafers were then sectioned and annealed in a conventional tube furnace under a N₂ ambient at 500 °C for 60 min. This anneal was performed to bring the amorphous material to a structurally relaxed state⁵⁶⁻⁶² as well as investigate the thermal behavior of the co-implanted F⁺ on the resulting EPR signal. The EPR spectra were measured by using a Bruker Elexsys E580 spectrometer with a Super High-Q Cavity and the sample held at near liquid He temperatures (i.e., 15.6 ± 0.5 K) under the following system settings: 0.3165 mW of microwave power at a frequency of 9.343 ± 0.002 GHz with an attenuation of 28 dB, a modulation frequency of 100 kHz and modulation amplitude of 0.5 G with a receiver gain of 53 dB. The exact settings for each measurement can be found in Appendix B. Figure 6-17 shows three EPR spectra for the wafers that were pre-amorphized with a 60 keV Ge⁺ implant to $1 \times 10^{15}/\text{cm}^2$; two of the spectra correspond to the wafers that were subject to subsequent 12 keV F⁺ implantation to either 1.5×10^{15} or $3.0 \times 10^{15}/\text{cm}^2$. As can be seen, each of the implant conditions used in this study produce EPR spectra with a center field

of approximately 3326 G. The most interesting result of this data is that the EPR spectra corresponding to the wafer without any additional F⁺ implant and the wafer with the 12 keV F⁺ implant to $1.5 \times 10^{15}/\text{cm}^2$ have almost the same signal; each showing an intensity of approximately 11 (on an arbitrary scale). This is consistent with the literature and shows that the additional F⁺ implant has a negligible effect on the as-implanted paramagnetic defect concentration as measured by EPR.^{262,263} It should be noted that the signal intensity slightly increases with the addition of the 12 keV F⁺ implant to $1.5 \times 10^{15}/\text{cm}^2$. In theory, there is a linear dependence between the EPR signal intensity and the number of paramagnetic centers in a sample; however, this increase in intensity for the wafer with the additional F⁺ implant is expected to be due to the 10-20% error associated with the measurement and not an increase in the concentration of paramagnetic defects. When comparing the EPR spectra for the wafer without any additional F⁺ implant to that for the wafer with the 12 keV F⁺ implant to $3.0 \times 10^{15}/\text{cm}^2$, it can be seen that the signal for the wafer with the additional F⁺ implant has an intensity of approximately 9 (on an arbitrary scale) which is lower than the intensity for either of the other two EPR spectra in Figure 6-17. Although some of the decrease in intensity may be due to the relatively high F⁺ dose interacting with a fraction of the paramagnetic defects in the amorphous layer, this decrease is not significant and presumed to be due to in part by the 10-20% error associated with the measurement. It should be noted that the peak F concentration used in Ref. 263 was estimated to be approximately $1 \times 10^{22}/\text{cm}^3$, and the corresponding EPR results showed spin densities comparable to those reported in the literature for implanted α -Si prepared by different ion species; this concentration is much greater than the peak F concentration produced by the 12 keV F⁺ implant to

$3.0 \times 10^{15}/\text{cm}^2$, which is expected to be approximately $4 \times 10^{20}/\text{cm}^2$. These results suggest that, in general, it can be said that F has a negligible effect on the as-implanted concentration of paramagnetic defects over the concentration range used in this study. It can be said that the as-implanted F^+ does not increase the low temperature diffusion behavior of B by passivation of the trapping sites in $\alpha\text{-Si}$ by forming highly-favored bonding arrangements with paramagnetic defects in the amorphous layer; however, that can only be said for the *measurable* paramagnetic defects. It is well known that the saturation defect density in $\alpha\text{-Si}$ at room temperature is approximately 0.5 at. % and that a majority of these defects are not paramagnetic,²²³ making EPR incapable of detecting these defects; therefore, it is reasonable to assume that the F is capable of interacting with a fraction of the non-paramagnetic defects which are responsible for trapping the B atoms. The increase in low temperature diffusion behavior observed for the as-implanted profiles in Figure 6-14 is, therefore, presumably due to the co-implanted F occupying these non-paramagnetic defect states thereby de-trapping the B atoms. The preferential interaction between F and the non-paramagnetic traps or defect states in the amorphous layer would imply that the F is more strongly bonded to these traps than the paramagnetic defects. Figure 6-18 shows the EPR spectra for the three wafers shown in Figure 6-17, however, after a 500 °C relaxation anneal for 60 min. Structural relaxation refers to an intrinsic network rearrangement which is not typical just of $\alpha\text{-Si}$, but also occurs in heavily damaged c-Si where it has long been known as defect annihilation.^{198,223,233,234} The fact that the density of $\alpha\text{-Si}$ remains unchanged upon structural relaxation suggests mutual annihilation of low- and high-density defects.^{198,204} It should be noted that structural relaxation of the $\alpha\text{-Si}$ reduces the average $\Delta\theta$ from approximately 11.3° to

9° .²²³ As can be seen in Figure 6-18, the intensity of each EPR signal is much less than what was observed for the corresponding spectra in Figure 6-17. This shows that the 500 °C relaxation anneal is capable of significantly reducing the concentration of paramagnetic defects, independent of the additional F⁺ implant. Although approximately 13 nm of regrowth is expected to occur during the relaxation anneal,¹⁴² somewhat reducing the concentration of paramagnetic defects, the reduction of the EPR signal is expected to be dominated by defect annihilation in the amorphous layer. When comparing the EPR spectra for the wafer without any additional F⁺ implant to that for the wafer with the 12 keV F⁺ implant to $1.5 \times 10^{15}/\text{cm}^2$, it can be seen that the signal for the wafer with the additional F⁺ implant has an intensity of approximately 0.4 (on an arbitrary scale) which is lower than the 0.9 (on an arbitrary scale) intensity for the EPR spectra corresponding to the wafer without any additional F⁺ implant. A similar comment can be made when comparing the EPR spectra for the wafer without any additional F⁺ implant to that for the wafer with the 12 keV F⁺ implant to $3.0 \times 10^{15}/\text{cm}^2$. This shows that, although the 500 °C relaxation anneal is capable of significantly reducing the concentration of paramagnetic defects, the additional F⁺ implant has an added effect on reducing the paramagnetic defect concentration. Since increasing the dose from $1.5 \times 10^{15}/\text{cm}^2$ to $3.0 \times 10^{15}/\text{cm}^2$ resulted in no measurable difference between the EPR spectra, it can be said that this effect is independent of the F concentration range used in this study. Although the 10-20% error associated with the measurement may complicate interpretation of the results, the fact that the EPR spectra is similar for both wafers with the 12 keV F⁺ implant suggests qualitatively that the effect is the same for both implant conditions. This shows that a F concentration of approximately $3 \times 10^{20}/\text{cm}^3$

is sufficient to saturate the effect on the paramagnetic defects in the amorphous material. The effect of implanted F⁺ on the spin density of amorphous layers has been previously investigated.²⁶³ For that experiment, a 10-20 Ω·cm ⟨111⟩ n-type Si wafer was pre-amorphized with a 60 keV F⁺ implant to $2 \times 10^{17}/\text{cm}^2$. It should be noted that the relatively high F⁺ dose was used to prevent recrystallization of the implantation-induced amorphous layer during post implant thermal processing. The wafer was then subject to 150 keV BF₂⁺ implantation to $5.0 \times 10^{15}/\text{cm}^2$ and annealed in a N₂ ambient for 2 hr at various temperatures. Electron spin resonance measurements were performed with a JEOL JES-FE3X ESR spectrometer to determine the spin density as a function of post-implant thermal processing. The ESR measurements were carried out at room temperature with a field modulation frequency of 100 kHz. The spin densities were estimated by comparing the ESR signal with that of a standard α-Si sample with a known total spin. It should be noted that the lack of a standard sample with a known spin density prevented quantitative analysis for the data in Figures 6-17 and 6-18. The data in Ref. 263 showed that the ESR spin density for the as-implanted sample was approximately $2.6 \times 10^{19}/\text{cm}^3$ which is similar to the value of $2 \times 10^{19}/\text{cm}^3$ reported for implanted α-Si samples, independent of the incident ion species.²⁶² The data also showed that the ESR spin density decreases with increasing annealing temperature; however, while the spin density in Ref. 262 was reported to decrease by a factor of 2 or 3 after annealing at 500 °C for 2 hr, the spin density in Ref. 263 was found to decrease by an order of magnitude under similar annealing conditions. The authors suggest that the difference between the two sets of data was due to the effectiveness of the F atoms serving as dangling bond terminators in Ref. 263. It should be noted that Ref. 263 did not

take into consideration the effect of structural relaxation on the resulting ESR spin density. It was shown in Figures 6-17 and 6-18 that a 500 °C anneal for 60 min is capable of significantly reducing the concentration of paramagnetic defects, independent of an additional F⁺ implant. For better comparison, the effect of the structural relaxation anneal on the resulting EPR spectra without an additional F⁺ implant is shown in Figure 6-19. As can be seen the 500 °C anneal for 60 min reduces the EPR signal intensity from approximately 11 (on an arbitrary scale) to 0.9 (on an arbitrary scale), which is similar to the order of magnitude decrease in spin density observed for a 500 °C anneal for 2 hr in Ref. 263; however, without the additional F⁺ implant. Although it is reasonable to assume that the implanted F⁺ affects the ESR spin density during post-implant thermal annealing, the decrease in spin density from structural relaxation of the implantation-induced amorphous layer must be taken into consideration.

As can be seen in Figure 6-4, the 760 °C iRTP anneal produced an increase in x_j independent of the 12 keV F⁺ implant to $1.5 \times 10^{15}/\text{cm}^2$. The 760 °C iRTP increased the x_j 3.0 (measured at $1 \times 10^{18}/\text{cm}^3$) and 4.9 nm (measured at $1 \times 10^{19}/\text{cm}^3$) for the wafer without and with the additional F⁺ implant, respectively. It is presumed that the diffusion that occurs during this iRTP anneal is associated with B diffusion in α-Si, and was discussed in Chapter 4. The increase in B diffusion behavior for the wafer with the 12 keV F⁺ implant to $1.5 \times 10^{15}/\text{cm}^2$ can be explained by the difference in the amount of time the B spends in α-Si before complete recrystallization of the implantation-induced amorphous layer. The XTEM results in Figure 6-1 revealed that, although the 760 °C iRTP anneal was sufficient to completely recrystallize the amorphous layer for the wafer without the 12 keV F⁺ implant to $1.5 \times 10^{15}/\text{cm}^2$, the additional F⁺ implant was capable of reducing the

regrowth velocity of the α/c interface such that the 800 °C iRTP anneal is unable to completely regrow the amorphous layer produced by the 48 keV pre-amorphization implant and leaves approximately 22 nm of α -Si near the substrate surface. Considering no appreciable regrowth of the amorphous layer is expected to occur during ramp-up to the iRTP anneal temperature until approximately 600 °C (which was estimated from an Arrhenius equation used to describe the regrowth velocity of an implantation-induced amorphous layer as a function of ramp rate and temperature), it can be said that the B remains in α -Si for approximately 1-2 s before complete recrystallization of the amorphous layer for the wafer without the 12 keV F^+ implant to $1.5 \times 10^{15}/\text{cm}^2$. However, since the 800 °C iRTP anneal was unable to completely recrystallize the amorphous layer produced by the 48 keV pre-amorphization implant for the wafer with additional F^+ implant, it can be said that the B spends a prolonged amount of time in α -Si when compared to the wafer without the 12 keV F^+ implant to $1.5 \times 10^{15}/\text{cm}^2$. In fact, since approximately 22 nm of α -Si remained near the substrate surface after the 800 °C iRTP anneal, it can be said that the active (i.e., diffusing) B resides in α -Si throughout the entire anneal. This could result in the B spending an additional 1-2 s in α -Si above 600 °C, considering the entire anneal cycle consists of ramping-up to 800 °C and subsequently ramping-down to room temperature. It is presumed that this time difference is enough to account for the increase in x_j for the wafer with the additional F^+ implant.

It has recently been shown that B diffusion in α -Si is enhanced in the presence of F.¹⁹⁶ This enhanced diffusion was suggested to occur due to the F interactions with Si dangling bonds in the amorphous material. It was proposed that the F decreases the dangling bond concentration, thereby reducing the formation energy required for B

diffusion. The XTEM results from Ref. 196 showed that the regrowth velocity increases when the α/c interface reaches a B concentration of approximately $10^{18}/\text{cm}^3$ and decreases when it reaches a F concentration of approximately $10^{18}/\text{cm}^3$. The 180 nm implantation-induced amorphous layer generated by the 70 keV Si^+ implant to $1\times 10^{15}/\text{cm}^2$ completely recrystallized after 30 min of annealing at 550 °C for the sample implanted with B^+ alone, and was complete after 130 min of annealing for the sample that was co-implanted with B^+ and F^+ . These results estimate the B diffusivity in α -Si at 550 °C in the presence of F as being approximately $3\times 10^{-17}\text{cm}^2/\text{s}$, which is more than five orders of magnitude larger than the equilibrium diffusivity of B in c-Si.¹⁹⁶ Elliman *et al.* showed that B diffusion in α -Si at 600 °C is enhanced more than five order of magnitude without the presence of F.¹⁹⁰ In addition, it was shown that B from both B^+ and BF_2^+ implants into Si displays similar diffusion behavior during SPER of an implantation-induced amorphous layer at 550 °C.¹⁸⁸ These observations, coupled with the fact that it was shown that the presence of the F decreases the regrowth velocity, suggests that the effect of F on increasing the amount of B diffusion within α -Si may also be due to the additional time available for B diffusion in α -Si for the co-implanted sample.

An additional experiment was performed to better understand the mechanisms controlling B diffusion in α -Si when in the presence of F. This experiment was designed to determine whether the observed increase in B diffusion behavior in α -Si when in the presence of F is due to F interactions with Si dangling bonds in the amorphous material or, more simply, due to a reduction in the regrowth velocity of the α/c interface. It was shown that the degradation in the junction abruptness and the increase in x_j observed for

the as-implanted profile in Figure 6-14 is due to the 12 keV F⁺ implant to $1.5 \times 10^{15}/\text{cm}^2$.

Figure 6-17 showed that the as-implanted F had no effect on the concentration of paramagnetic defects in α -Si as measured by EPR; therefore, the effect of the additional F⁺ implant on the observed low temperature diffusion behavior was attributed to F interactions with a fraction of the non-paramagnetic defects in the amorphous material which form highly-favored bonding arrangements and de-trap the B atoms from these defect sites. These non-paramagnetic defects can be isolated from introducing any type of effect on the B diffusion behavior in α -Si by adding different doses of F⁺ to the amorphous material so that different amounts of low temperature diffusion are observed. Additional EPR results showed that structural relaxation of the amorphous layer produces a significant decrease in the concentration of paramagnetic defects. Although the addition of F had an added effect, it was not as significant as the reduction observed during the structural relaxation anneal. This shows that low temperature furnace annealing is not the most ideal situation to investigate the effect of F on dangling bond interactions due to the effect of structural relaxation on the paramagnetic defect concentration. Although shorter times are required for structural relaxation to occur at higher temperatures, it is believed that using a relatively short thermal cycle such as an iRTP anneal is insufficient to induce structural relaxation of the amorphous layer before complete recrystallization of the implantation-induced amorphous layer.²²³ It should be noted that pulsed laser annealing (tuned just below the α -Si melt threshold) can be used to induce large-angle bond relaxation without a significant amount of point-defect annihilation, showing that large-angle bond relaxation can occur on very short time scales when the annealing temperature is sufficiently high.²²³ For this experiment, four 200 mm

3-5 $\Omega\cdot\text{cm}$ (100) n-type CZ grown Si wafers were pre-amorphized with an 80 keV Ge^+ implant to $1\times 10^{15}/\text{cm}^2$. Three of the wafers were then subject to 3 keV F^+ implantation to doses of either 1×10^{14} , 2×10^{14} , or $3\times 10^{14}/\text{cm}^2$. All four wafers were subsequently implanted with 2 keV B^+ to $1\times 10^{15}/\text{cm}^2$. It should be noted that the F^+ and B^+ implant energies were chosen to result in the same R_p to overlap their concentration profiles in an attempt to maximize the interaction between the F atoms and either the dangling bonds or B atoms. The implants were carried out in the drift mode and performed at room temperature with the ion beam normal to the surface plane using an Applied Materials Leap-II system. The implant parameters were monitored to ensure they remained within predetermined limits. The pre-amorphization energy of the Ge^+ implant was increased to 80 keV to produce the thickest possible continuous amorphous layer under the available implant capabilities, which was determined to be approximately 110 nm by XTEM imaging (not shown). Each of the wafers were then sectioned and subject to an 800 and 900 °C iRTP anneals to investigate the effect of F^+ co-implantation on B diffusion in $\alpha\text{-Si}$ during UHT annealing. All of the anneals were carried out in a N_2 ambient with less than 10 ppm O_2 using a ramp-up rate of 400 °C/s. Figures 6-20 and 6-21 show the SIMS results for the as-implanted profiles for each of the B^+ and F^+ implant conditions used in this experiment, respectively. As can be seen in Figure 6-20, the implant conditions result in as-implanted profiles with junction abruptness of 5.2, and 6.1 nm/dec and x_j of 33.3, and 34.2 nm for the control wafer and the wafer that received the 3 keV F^+ implant to $3\times 10^{14}/\text{cm}^2$, respectively. This shows that the co-implanted F^+ does not have a significant effect on the as-implanted junction abruptness and x_j (measured at $1\times 10^{18}/\text{cm}^3$); however, it can be seen that increasing the F^+ concentration increases the

low temperature diffusion behavior of the B profile below a concentration of approximately $1\times10^{18}/\text{cm}^3$. This shows that a F^+ dose as low as $1\times10^{14}/\text{cm}^2$ is sufficient to de-trap the B atoms from the non-paramagnetic defect sites, which is presumably responsible for the corresponding increase in diffusion behavior in Figure 6-20. The fact that the amount of low temperature diffusion increases with increasing F concentration is consistent with the thought that the co-implanted F^+ de-traps the B atoms by forming highly-favored bonding arrangements with non-paramagnetic defect sites in the amorphous layer. Although an increase in the low temperature diffusion behavior is observed with increasing F concentration over the dose range used in this experiment, it is expected that a saturation of this effect will occur once all the non-paramagnetic defects are occupied by F atoms. Figure 6-3 showed that the as-implanted profiles for the original experiment are similar down to a concentration of approximately $1\times10^{19}/\text{cm}^2$, below which the as-implanted profile for the wafer with the additional F^+ implant decreases exponentially as a function of depth. It is interesting to note that the exponential decrease observed for the wafer with the 6 keV F^+ implant to $2\times10^{15}/\text{cm}^2$ in Ref. 196 develops at a similar concentration level, which may very well be near the saturation value. Figure 6-22 shows the SIMS results for the 2 keV B^+ implant to $1\times10^{15}/\text{cm}^2$ after a 800 °C iRTP anneal. As can be seen, the 800 °C iRTP anneal result in profiles with junction abruptness of 5.1, and 6.4 nm/dec and x_j of 34.8, and 35.9 nm for the control wafer and the wafer that received the 3 keV F^+ implant to $3\times10^{14}/\text{cm}^2$, respectively. The most interesting result of this data is that the 800 °C iRTP anneal produced the same (high concentration) diffusion behavior independent of the additional F^+ implant. It can be seen that the low concentration (i.e., below $1\times10^{18}/\text{cm}^3$) region of

the B profile shows an increase in diffusion behavior with increasing F concentration; however, this diffusion is expected to be due to the effect already seen for the as-implanted profiles and not due to interstitial injection from the EOR damage. If the co-implanted F⁺ increased B diffusion in α -Si by interacting with Si dangling bonds then one would expect an increase in B diffusion behavior with an increase in F concentration, which was not observed experimentally. This provides evidence that the effect of F⁺ co-implantation on B diffusion in α -Si is primarily due to a reduction in the regrowth velocity of the α/c interface and not due to F interactions with Si dangling bonds in the amorphous material; similar to recently reported work.²⁶⁴ Figure 6-23 shows the SIMS results for the 2 keV B⁺ implant to $1 \times 10^{15}/\text{cm}^2$ after a 900 °C iRTP anneal. As can be seen, the 900 °C iRTP anneal result in profiles with junction abruptness of 7.1, and 7.0 nm/dec and x_j of 39.2, and 37.0 nm for the control wafer and the wafer that received the 3 keV F⁺ implant to $3 \times 10^{14}/\text{cm}^2$, respectively. This shows that the control wafer undergoes the most diffusion during the 900 °C iRTP anneal when compared to any of the profiles corresponding to the wafers with an additional F⁺ implant. This is consistent with the data in Figure 6-4, which showed that the additional F⁺ implant was sufficient to significantly reduce the diffusion behavior in c-Si during post-implant thermal processing. This data shows that, although F⁺ co-implantation has a negligible effect on B diffusion in α -Si during recrystallization of an implantation-induced amorphous layer (when the F concentration is sufficiently low to not affect the regrowth velocity of the α/c interface), the co-implanted F⁺ has a significant effect on B diffusion behavior during the initial stages after complete recrystallization.

Figure 6-4 showed that the 760 °C iRTP anneal was sufficient to produce an immobile B peak just below the substrate surface, independent of the 12 keV F⁺ implant to $1.5 \times 10^{15}/\text{cm}^2$. It is well known that the pairing between both B atoms and Si interstitials results in the formation of an immobile B complex which is presumed to be inactive.^{9,18} It was shown that this clustering only occurs when the concentration of B atoms and Si interstitials is sufficiently high.⁹ The exact structure (i.e., stoichiometry) of this complex has been the subject of ongoing investigation. Direct observation of these clusters by such techniques as high resolution TEM or x-ray diffraction (XRD) is complicated by their small size (being approximately 3 to 8 atoms clusters). Thus, evidence of these clusters can only be obtained by electrical measurements and theoretical calculations.⁹ Most of the data regarding the formation of such an immobile complex has been obtained by investigating B diffusion behavior in c-Si. Since it was shown that an 800 °C iRTP is unable to completely regrow the amorphous layer produced by the 48 keV pre-amorphization implant, the data in Figure 6-4b shows that immobile B cluster formation or precipitation occurs in α-Si at temperatures as low as 760 °C. This is an interesting result considering the high local concentration of both B and Si atoms is enough to affect the B diffusion behavior in α-Si. In order to remain consistent with the current postulate regarding submicroscopic cluster formation, the atoms that participate in cluster formation must be B atoms and Si interstitials. Although point-defects such as interstitials and vacancies can be defined as locations where the translational symmetry of the lattice is broken in c-Si, a similar definition for α-Si is slightly more complicated due to the inherent random nature of the amorphous phase.²⁶⁵ It is expected that in both α- and c-Si the atoms surrounding a defect slightly change their

positions to accommodate this highly energetically unfavorable state.¹⁹⁸ Assuming that a point-defect leads to local rearrangements of both nearest and next-nearest neighbors, it can be said that these defect concentrations lead to a majority of the large-angle bond distortions. A large fraction of the energy associated with the defect is thought to be stored in these distorted bonds. The heat release observed during defect annihilation during structural relaxation, for example, is therefore expected to be due to the change in structure around the collapsing defect in both α - and c-Si. This interpretation suggests that the population of point-defects in α -Si is similar to that in c-Si. In fact, Roorda *et al.* have shown that defects introduced in α -Si by ion-implantation exhibit close similarities to defects introduced in c-Si under equivalent conditions.²⁶⁶ Therefore, both single vacancies and interstitials as well as small clusters of defects can easily be defined in a fully connected α -Si network without any need for the translational or rotational symmetry exhibited by the c-Si lattice.¹⁹⁸ The possible existence of stable single vacancies and small vacancy clusters in a fourfold covalently bonded CRN had been predicted from calculations based on the Keating potential.^{267,268} Indeed, a number of experiments have been performed and support the idea that such defects exist in α -Si.^{203,204} It should be noted that the data presented in Ref. 196 also show B clustering in α -Si, presuming that the amorphous layer produced by the 70 keV Si⁺ pre-amorphization implant to $1 \times 10^{15}/\text{cm}^2$ does not completely recrystallize until after 130 min of furnace annealing at 550 °C.

There have been reports of impurity precipitation in the amorphous phase after implantation and annealing. Campisano *et al.* observed Sb precipitation in α -Si by studying the effect of Sb concentration on the SPER regrowth velocity of the α/c

interface during post-implant thermal processing. There, 120 or 200 keV Sb⁺ implantation to a concentration of approximately $5 \times 10^{20}/\text{cm}^3$ was followed by annealing in a forming gas [i.e., N₂(90%)/H₂(10%)] at a base pressure of 10⁻⁷ Torr and temperatures of 480 and 500 °C. Both Rutherford scattering and channeling and glancing angle detector geometry were used to determine the amorphous layer thickness, Sb concentration profiles, and Sb substitutionality. It was shown that the regrowth velocity reached a maximum and then slowly decreases at Sb concentration on the order of $5 \times 10^{20}/\text{cm}^3$. The XTEM results showed that the 120 keV Sb⁺ implant to $1 \times 10^{16}/\text{cm}^2$ produced a 160 nm thick amorphous layer, which reduced to approximately 80 nm after a 500 °C anneal for 10 min. These results also showed areas of dark contrast about 5 nm in diameter within the α-Si, which were concluded to be non-crystalline agglomerates of Sb-rich material. These agglomerates were presumably responsible for the decrease in regrowth velocity at higher Sb concentrations, which was further supported by the XTEM results that showed roughening of the α/c interface for samples with Sb concentrations on the order of $5 \times 10^{20}/\text{cm}^3$. The authors suggest that the agglomerates form due to diffusion in α-Si during either implantation or the initial stages of annealing. They note that this precipitation occurred in α-Si at a lower temperature and dose than for c-Si, which may be a result of enhanced diffusion of Sb in α-Si.¹¹⁹ This was the first reported observation of impurity precipitation in the amorphous phase.

Elliman *et al.* also reported evidence of impurity precipitation in α-Si. There, samples were prepared by implanting Cu⁺, As⁺, In⁺, Sb⁺, Au⁺, and Bi⁺ into (100) or (111) Si wafers at energies between 100 and 400 keV and doses between 1×10^{14} - $1 \times 10^{17}/\text{cm}^2$. The implant conditions were chosen to result in the formation of amorphous layers

approximately 200 nm thick. It should be noted that some of the samples were amorphized to depths of 2 μm using Ar^+ implantation at -196 °C. This was done to allow more time for impurity diffusion in α -Si before complete recrystallization of the implantation-induced amorphous layer. The samples were then annealed at a base pressure below 10^{-7} mm Hg to temperatures up to 600 °C. Rutherford backscattering and channeling spectra show that, although a negligible amount of SPER occurred during a 450 °C anneal for 30 min, the implanted Au^+ diffused isotropically within the amorphous layer with a diffusion coefficient of approximately 10^{-13} cm²/s. Similar diffusion profiles were observed for Cu at lower temperatures and times (e.g., 350 °C for 30 min) resulting in a diffusion coefficient of 10^{-12} cm²/s. The horizontal character of the RBS spectra indicated that the diffusing Au and Cu atoms are reflected from the surface and the α/c interface, with no appreciable diffusion into the underlying c-Si. Additional PTEM results of the Au^+ implanted sample showed that the 450 °C anneal for 30 min was sufficient to induce precipitation within the amorphous layer. Selected area diffraction (SAD) showed that these precipitates were pure Au metal concentrated in the upper half of the amorphous layer with a size distribution ranging from 2.5-25 nm. It should be noted that precipitates were not observed in the as-implanted samples or even in samples annealed at 400 °C for similar times. No diffusion in α -Si was observed for the As, In, Sb, or Bi at concentrations less than 1 at. %; however, at higher concentrations a significant amount of diffusion was observed in the temperature range of 500-600 °C. These impurities diffused to give a horizontal character in the RBS spectra similar to that observed for Au. The implanted concentrations above which diffusion was observed for As^+ , In^+ , Sb^+ , and Bi^+ appeared to follow the same trends as equilibrium solubility limits

for these impurities in c-Si. It is well known that both Au and Cu are fast diffusers in c-Si, whereas As, In, Sb, and Bi are considered slow diffusers in c-Si. Since the same trend was observed for α -Si, the increase in diffusion behavior above a certain concentration level was presumed to be due to the ability of these substitutional impurities to be forced into rapid diffusion or interstitial sites. A similar phenomena is not expected to occur c-Si since these impurities cannot be incorporated within the lattice at such high concentrations, which are well above the equilibrium solid solubility levels. This work provided conclusive evidence of impurity precipitation in the amorphous phase after diffusion.

Figure 6-4 showed that the 900 °C iRTP anneal resulted in an additional increase in x_j when compared to the 760 °C iRTP anneal. Chapter 4 showed that this increase in diffusion behavior is most likely TED due to interstitial injection from the EOR damage for the wafer without the 12 keV F⁺ implant to $1.5 \times 10^{15}/\text{cm}^2$. The increase in x_j for the wafer with the additional F⁺ implant, however, is most likely due to additional B diffusion in α -Si. Additional XTEM results (not shown) revealed that, although the 800 °C iRTP anneal was unable to completely regrow the amorphous produced by the 48 keV pre-amorphization implant, the 900 °C iRTP anneal was sufficient to result in a c-Si surface layer. The additional time B spends in α -Si is presumed to be enough to cause the additional diffusion observed for the 900 °C iRTP anneal for the wafer with the 12 keV F⁺ to $1.5 \times 10^{15}/\text{cm}^2$. The thought that the increase in x_j after the 900 °C iRTP anneal is due to additional B diffusion in α -Si is supported by the observation that the profile for the 900 °C iRTP anneal is similar to the 760 °C iRTP anneal below a concentration of approximately $1.5 \times 10^{18}/\text{cm}^3$. This shows that the low concentration

portion of the B profile does not diffuse during the anneal, which is inconsistent with the effect expected from TED. As can be seen in Figure 6-4b, the depth of each profile above 900 °C increases at a concentration of $1\times10^{18}/\text{cm}^3$ showing that interstitial injection from the EOR damage created by the 48 keV pre-amorphization implant only affects the B profile when a iRTP annealing temperatures above 900 °C are used.

One of the most noticeable results in Figure 6-4 is that, after complete recrystallization of the implantation-induced amorphous layer, the 12 keV F⁺ implant to $1.5\times10^{15}/\text{cm}^2$ is sufficient to significantly reduce the B diffusion behavior during post-implant thermal processing. For example, it can be seen that the 1000 °C iRTP anneal degrades the junction abruptness and increases the x_j of the wafer without the additional F⁺ implant from 3.2 nm/dec and 19.3 nm (for the 760 °C iRTP anneal) to 10.1 nm/dec and 31.7 nm (measured at $1\times10^{18}/\text{cm}^3$), respectively. This can be compared to the wafer with the 12 keV F⁺ implant to $1.5\times10^{15}/\text{cm}^2$ which degrades the junction abruptness and increases the x_j from 5.4 nm/dec and 20.4 nm (for the 900 °C iRTP anneal) to 5.8 nm/dec and 22.1 nm (measured at $1\times10^{19}/\text{cm}^3$), respectively. It can be seen that the additional F⁺ implant maintains a highly abrupt junction and prevents a significant amount of diffusion during the 1000 °C iRTP anneal. Figure 6-4a showed that the 900, 1000, and 1100 °C iRTP anneals increased the x_j 3.2, 12.4, and 16.8 nm, respectively, compared to the 760 and 800 °C iRTP anneals for the wafer without the 12 keV F⁺ implant to $1.5\times10^{15}/\text{cm}^2$. These results show that the largest difference in the diffusion behavior is observed for the 1000 °C iRTP anneal. The increase in diffusion behavior for the 1000 °C iRTP anneal is most likely due to a significant fraction of the

interstitial flux toward the surface, which is capable of reaching the B profile during the 1000 °C iRTP anneal but is less pronounced for the 900 °C iRTP anneal. Such a significant pulse of TED was shown to occur for 40 keV Si⁺ implants to both 2×10^{13} and $5 \times 10^{13}/\text{cm}^2$ during the first 15 s of annealing at 700 °C.¹¹³ This pulse of TED was shown to be in excess of the enhancement caused by {311} defect dissolution, suggesting a different source of interstitials.¹¹³ It is presumed that a similar mechanism is causing the diffusion enhancement for the 1000 °C iRTP anneal in Figure 6-4a for the wafer without the 12 keV F⁺ implant to $1.5 \times 10^{15}/\text{cm}^2$, as the PTEM results in Figure 6-5 show that {311} dissolution is incomplete after the 1000 °C iRTP anneal. The results in Figure 6-4b suggest that the additional F⁺ implant is sufficient to bind with the excess interstitials being injected from the EOR damage produced by the 48 keV pre-amorphization implant, thereby preventing their ability to cause a significant amount of TED.⁶³

It is well known that co-implanted F⁺ reduces B diffusion during post-implant thermal processing in part due to a chemical species effect.²⁶⁹ This was done by pre-amorphizing a substrate surface before dopant incorporation to isolate the difference between the damage profiles that would be expected if both B⁺ and BF₂⁺ were implanted into c-Si substrates. The B⁺ implant would presumably be insufficient for producing a continuous surface amorphous layer provided that the implanted dose remained below that shown to induce amorphization of the substrate surface,²⁷⁰ whereas the BF₂⁺ implant would most likely form a continuous amorphous layer from the substrate surface down to a depth consistent with the implant conditions. The difference between these damage profiles would complicate interpretation of the results. Therefore, pre-amorphization of

the substrate surface provided a controllable means of investigating the chemical species effect of co-implanted F⁺ on B diffusion behavior during post-implant thermal processing. The 70 keV Si⁺ pre-amorphization implant to $1 \times 10^{15}/\text{cm}^2$ produced a 145 nm thick amorphous layer, which was subsequently implanted with either 1 keV B⁺ or 5 keV BF₂⁺ to $1 \times 10^{15}/\text{cm}^2$. It was shown that the BF₂⁺ implanted material resulted in the shallower x_j after either a 1000 or 1050 °C spike RTP anneal. This experiment presented conclusive evidence that co-implanted F⁺ has a chemical species effect on B diffusion behavior.

Although co-implanted F⁺ is known to have a chemical species effect, it was suggested here that F is capable of binding with the excess Si interstitials thereby preventing them from having a significant effect on B diffusion during post-implant thermal processing. Robertson noted that in order for the co-implanted F to reduce the enhanced diffusion of implanted B⁺, it must interfere with one or more of the processes which control TED.⁶³ Of the three main processes (i.e., F forming an immobile complex with B, F increasing the trap density thereby decreasing its interstitial diffusion distance, and F binding with excess interstitials thereby reducing the interstitial supersaturation) the idea that F binds with excess interstitials appears to be the most consistent with his data. The only part of the data that does not follow this thought is that all the B profiles with co-implanted F⁺ showed much greater diffusion behavior within the first 15 min of annealing at 750 °C when compared to the annealing period from 15 min to 2 hr. Robertson suggested that the enhancement of B diffusion during the first 15 min of annealing at 750 °C was either due to the co-implanted F⁺ interacting with dangling bonds in the amorphous phase or slowing down the regrowth velocity of the α/c

interface. This work suggests that the increase in B diffusion behavior during the early stages of annealing, when compared to longer annealing times, can most likely be explained by the increase in B diffusivity in α -Si and the ability of F to reduce the regrowth velocity of the α/c interface. In other words, it is believed that the reason for observing such a significant difference in the diffusion behavior during the early stages of annealing is due to B diffusion in α -Si before complete recrystallization of the implantation-induced amorphous layer, and not an interaction between B atoms and the Si interstitials being injected from the EOR damage produced by the pre-amorphization implant. It should be noted that the solubility of B at 750 °C was estimated from the SIMS profiles to be approximately 1×10^{19} and $1\times10^{20}/\text{cm}^3$ for the samples without and with the additional F⁺ implant, respectively. It is well known that electrical activation is limited by the clustering of B atoms with Si interstitials. Assuming that B diffusion in α -Si is the cause for the increase in diffusion behavior during the early stages of annealing, it can be said that the idea of F trapping excess interstitials is consistent with the reduction of TED at longer annealing times and the increase in the B solubility. Indeed, additional experimental data supported this idea. There, a substrate was pre-amorphized by overlapping 150 and 40 keV Si⁺ implantation to $1\times10^{15}/\text{cm}^2$. The wafer was then subject to a 16 keV F⁺ implant to $2\times10^{15}/\text{cm}^2$ which was subsequently annealed at 750 °C for 3 hr to create a F well. The well was then implanted with 25 keV Si⁺ to $1\times10^{14}/\text{cm}^2$, which is well above the threshold for {311} defect formation (i.e., $5\times10^{12}/\text{cm}^2$) and just below the threshold for dislocation loop formation (i.e., $\sim10^{14}/\text{cm}^2$).¹⁸ The R_p of this implant is approximately 39 nm, which was shown to be near the center of the F well. The samples were then annealed at 750 °C for 30 min.

The PTEM results show that the presence of the F well retards the formation of {311} defects, which are easily observed in the sample without the additional F⁺ implant. The fact that F is sufficient to prevent {311} defect formation provided conclusive evidence that F can bind with excess interstitials, which is presumed to be the reason for the difference in B diffusion behavior observed in Figure 6-4 for the 1000 °C iRTP anneal. It should be noted that the PTEM results throughout the current experiment appear to be independent of the 12 keV F⁺ implant to $1.5 \times 10^{15}/\text{cm}^2$, suggesting that the additional F⁺ implant does not affect the evolution of the EOR damage produced by the 48 keV pre-amorphization implant; Robertson also observed a similar independence.⁶³

It was shown in Chapter 5 that higher activation levels can be achieved by using this UHT annealing technique directly after implantation as opposed to performing a low temperature SPER anneal before UHT annealing. This improved activation was presumably thought to be because higher activation levels can be achieved at higher recrystallization temperatures. In other words, higher activation levels can be achieved when recrystallization (and presumably activation) occurs during ramp-up of an UHT anneal (e.g., approximately 700 °C), as opposed to a low temperature (i.e., 585 °C) furnace anneal. This idea is further supported by the data in Figures 6-5 and 6-7 which showed that, for both the 760 and 800 °C intermediate temperatures, the plateau concentration remains constant during UHT annealing of the wafer without the 12 keV F⁺ implant to $1.5 \times 10^{15}/\text{cm}^2$ and increases with increasing peak temperature during UHT annealing of the wafer that received the additional F⁺ implant. The XTEM results in Figure 6-1 showed that, although the 760 °C iRTP anneal is sufficient to completely regrow the amorphous layer produced by the 48 keV pre-amorphization implant for the

wafer without the 12 keV F⁺ implant to $1.5 \times 10^{15}/\text{cm}^2$, the 800 °C iRTP anneal leaves approximately 22 nm of α-Si near the substrate surface for the wafer with the additional F⁺ implant. The corresponding SIMS results in Figure 6-4b show that most of the implanted B is contained within the first 22 nm of material. This shows that complete recrystallization of the amorphous layer occurs during the fRTP anneal, as opposed to ramping-up to the intermediate temperature (as is the case for the wafer without the additional F⁺ implant). Therefore, since recrystallization (and presumably activation) occurred during the fRTP anneal, the plateau concentrations are higher than those corresponding to the annealing conditions that completely recrystallized the amorphous layer during ramp-up to the intermediate temperature. This is consistent with the thought that higher activation levels can be achieved at higher recrystallization temperatures. In addition, it was shown that the plateau concentration for the 900 °C intermediate temperature remains approximately $1.8 \times 10^{20}/\text{cm}^3$ independent of the peak UHT annealing temperature despite of the additional F⁺ implant. Additional XTEM results (not shown) revealed that the 900 °C iRTP anneal was sufficient to result in a c-Si surface layer independent of the 12 keV F⁺ implant to $1.5 \times 10^{15}/\text{cm}^2$. This shows that complete recrystallization of the amorphous layer most likely occurred during ramp-up to the intermediate temperature; therefore, the plateau concentration did not increase with increasing peak annealing temperature presumably because recrystallization was complete before the high temperature (i.e., 1200 or 1350 °C) portion of the fRTP anneal occurred. In other words, the plateau concentrations that were achieved from UHT annealing with an intermediate temperature of 900 °C are representative of those obtained during ramp-up to the intermediate temperature as opposed to those obtained during UHT

annealing at temperatures on the order of 1200 or 1350 °C. This is presumably due to the higher solubility of dopants in α -Si when compared to c-Si, and consistent with the thought that higher activation levels can be achieved at higher recrystallization temperatures.

It is well known that low temperature (e.g., 500-600 °C) furnace annealing is capable of producing above solid solubility activation levels.^{118,271,272} Campisano *et al.* showed that supersaturated solid solutions of Bi can be incorporated into Si after annealing at temperatures as low as 550 °C.²⁷³ This was done by implanting Si substrates with 120 keV Bi⁺ to doses ranging from 5×10^{13} - $2\times10^{15}/\text{cm}^2$. The material was subsequently annealed in a forming gas [N₂(90%)/H₂(10%)] over a temperature range of 550-925 °C. Channeling results showed that the lowest substitutional concentration obtained after SPER of the implantation-induced amorphous layer was at least an order of magnitude higher than the predicted maximum solid solubility of Bi in Si.¹⁴ This shows that low temperature (i.e., 550 °C) furnace annealing is capable of incorporating impurities above their solid solubility levels. Solute trapping at the α/c interface is presumed to be the reason for obtaining such supersaturated solid solutions.^{179,274,275} The authors suggested that the formation of a supersaturated solid solution during SPER is determined by the impurities diffusion coefficient in the solid, and that if the impurity diffusion length is larger than their average separation distance then precipitation of a second phase would occur as opposed to the impurity being incorporated into a supersaturated solid solution. In other words, impurities will be trapped on substitutional sites only if the impurity diffusion length is negligible with respect to the average impurity separation distance. Since the diffusion coefficient of Bi in Si was shown to be

approximately 10^{-25} cm²/s at 550 °C, it can be said that the implanted Bi atoms do not diffuse during the SPER anneal and are trapped at the α /c interface. In order to test their theory based on the competition between impurity incorporation and precipitation, the authors implanted Cu⁺ in Si. Copper has a diffusion coefficient in Si of approximately 10^{-5} cm²/s at 600 °C,²⁷⁶ which is much greater than that corresponding to Bi, and a maximum solid solubility of about $1.5 \times 10^{18}/\text{cm}^3$,¹⁴ which is close to that of Bi in Si. Since the average diffusion length of Bi and Cu is about 10^{-5} and 10^4 nm during recrystallization of one atomic layer at 550 °C, respectively, it can be said that the Cu can easily escape from the α /c interface and eventually precipitate in the amorphous phase. Indeed, channeling measurements showed poly-crystalline (p-Si) formation during SPER of the implantation-induced amorphous layer as opposed to c-Si formation, indicating that any precipitates that presumably formed inhibited regrowth to the point where p-Si formation occurred.

Another study based on the substitutional solid solubility limits obtained during SPER of an implantation-induced amorphous layer suggested that the measured non-equilibrium substitutional solubility limits obtained for low temperature SPER of high dose In⁺ and Sb⁺ can be attributed to local recrystallization effects rather than to impurity diffusion during regrowth.²⁷⁷ This was done by implanting Si substrates at -130 °C with 80 keV In⁺ or Sb⁺ to doses ranging from 1×10^{14} - $1 \times 10^{16}/\text{cm}^2$. The wafers were subsequently annealed in the temperature range of 500-700 °C. Rutherford backscattering and channeling measurements showed that a 580 °C anneal for 30 min was sufficient to completely regrowth the amorphous layer produced by a 80 keV Sb⁺ implant to $5 \times 10^{15}/\text{cm}^2$ and resulted in approximately 97% of the Sb atoms being on or

close to substitutional sites within the Si lattice.²⁷⁷ Additional results showed that the highest achievable substitutional concentration was approximately $1.1 \times 10^{21}/\text{cm}^3$, which is at least an order of magnitude above the equilibrium solubility limit for Sb in Si.¹⁴ It was noted that the addition of any more Sb significantly reduced the regrowth velocity of the α/c interface. Additional measurements showed that a substitutional In concentration of approximately $5 \times 10^{19}/\text{cm}^3$ was achieved after annealing at 555 °C, which is well in excess of the equilibrium solubility limit of $8 \times 10^{17}/\text{cm}^3$. Similar to Sb, a significant reduction in the regrowth velocity was observed when any additional In was added to the system. It should be noted that a significant amount of the In was observed to reside at the advancing α/c interface during SPER. The authors attempted to explain their results based on α/c interfacial processes. The authors put forward that, during bond breaking and atomic rearrangement at the α/c interface, it is reasonable to expect that the differences in the covalent radii between the impurity and Si atoms would give rise to local bond distortion and hence to interfacial strain when impurities are incorporated into substitutional sites. This level of strain would most likely increase with both impurity concentration and mismatch between the covalent radius of the impurity and Si atoms. In fact, the maximum limit of solute concentration is presumably reached when the gain in free energy due to the α - to c-Si transformation is equal to the increase in strain energy associated with c-Si resulting from differences in covalent radii of dopants and the Si lattice.²⁷⁵ Also, the phase transformation from α - to c-Si is accompanied by an increase in the atomic density of approximately 1.8%.⁴⁹ Together, these two effects may account for the observed regrowth behavior in that high levels of strain at the α/c interface may slow bond breaking and thus retard the epitaxial regrowth rate. This interfacial strain

may also provide the driving force for rejection of the In atoms into the less dense amorphous phase rather than their incorporation into substitutional sites. Based on this model, the larger In atoms (covalent radius of 0.144 nm) would be expected to produce higher levels of strain than Sb (covalent radius of 0.136 nm) in the Si lattice (covalent radius of 0.111 nm).²⁷⁸ As a result, the solubility limit should be lower for In when compared to Sb, which was observed experimentally. It should be noted that the difference between the covalent radii of B (covalent radius of 0.82 nm) and Si is 0.29 nm. Although interfacial strain may have some effect on the amount of dopant that can be incorporated onto substitutional sites during SPER of an implantation-induced amorphous layer, it is suggested here that the increase in plateau concentration (and presumably activation) observed with the additional 12 keV F⁺ implant to $1.5 \times 10^{15}/\text{cm}^2$ is due to either increased dopant solubility in α -Si or increased regrowth velocity with higher recrystallization temperatures.

It was shown that impurity solubility in α -Si is significantly greater than that in c-Si.^{37,194,227,279,280} It is well known that the defects responsible for trapping or gettering impurities in c-Si are also responsible for increasing the effective impurity solubility in the crystalline phase.¹⁹⁸ A similar statement can be made about α -Si. The as-implanted defect concentration in α -Si was shown to saturate at approximately 1-2 at. %.^{199,266} It is this large density of defects that leads to the extremely high solubility of transition metals (e.g., Au and Cu) in α -Si.³⁷ Elliman *et al.* offered one of the first suggestions on the possibility of enhanced solubility of impurities in α -Si.²²⁷ There, samples were prepared by implanting Au⁺ and Cu⁺ into (100) or (111) Si wafers. The implant conditions were chosen to result in the formation of amorphous layers approximately 200 nm thick. It

should be noted that some of the samples were amorphized to depths of 2 μm using Ar^+ implantation at -196 °C. This was done to allow more time for impurity diffusion in $\alpha\text{-Si}$ before complete recrystallization of the implantation-induced amorphous layer. The samples were then annealed at a base pressure below 10^{-7} mm Hg to temperatures up to 600 °C. Rutherford backscattering and channeling spectra show that, although a negligible amount of SPER occurred during a 450 °C anneal for 30 min, the implanted Au^+ diffused isotropically within the amorphous layer with a diffusion coefficient of approximately 10^{-13} cm^2/s . Similar diffusion profiles were observed for Cu at lower temperatures and times (e.g., 350 °C for 30 min) resulting in a diffusion coefficient of 10^{-12} cm^2/s . The authors note that the horizontal character of the RBS spectra indicate that the diffusing Au and Cu atoms are reflected from the substrate surface and the α/c interface, with no appreciable diffusion into the underlying c-Si. This observation was said to be due to either a kinetic barrier at the interface or, more plausibly, to a much higher solubility of these impurities in $\alpha\text{-Si}$ as compared to c-Si.

In addition, Polman *et al.* showed that implanted Cu^+ , which diffuses interstitially in $\alpha\text{-Si}$, exhibits a partitioning between the two different structural states of $\alpha\text{-Si}$.^{37,194} This was done by creating a 2.2 μm thick amorphous layer by use of overlapping 0.5, 1.0 and 2.0 MeV Si^+ implants each to $5 \times 10^{15}/\text{cm}^2$. The implants were performed at -196 °C. Two of the three resulting sections were annealed at 500 °C for 1 hr at a base pressure below 10^{-7} Torr to bring the $\alpha\text{-Si}$ to a structurally relaxed state. One of the annealed samples was then implanted with 5.5 MeV Si^+ to $1.6 \times 10^{15}/\text{cm}^2$ to bring the $\alpha\text{-Si}$ back to a structurally unrelaxed state, similar to the as-implanted case. All three samples were then

implanted with 200 keV Cu⁺ to $5.5 \times 10^{15}/\text{cm}^2$ and subsequently annealed at various temperatures ranging from 150 to 270 °C, for times between 10 min and 104 hr. Backscattering spectra show a significant amount of Cu in-diffusion for the unannealed sample after a 221 °C anneal for 4 hr; however, for the annealed sample, a high uniform Cu concentration is observed in an approximately 300 nm thick surface layer (i.e., the unannealed portion of the layer) while a low concentration Cu tail is observed in the deeper lying annealed layer. The interface between the two concentration regions corresponds to the EOR of the Cu⁺ implant, which returned the first 300 nm of α-Si to a structurally unrelaxed state. The higher Cu concentration in the 300 nm surface layer suggests that during the anneal, Cu is partially reflected at the interface between annealed and unannealed α-Si, which is characteristic of solute partitioning at a phase boundary. The Cu concentrations observed in the backscattering spectra for the unannealed α-Si were at least ten orders of magnitude than the (extrapolated) equilibrium solubility in c-Si. This data showed for the first time that defects in unannealed α-Si are capable of trapping and gettering impurities in α-Si.

Calcagno *et al.* gave another report of increased impurity solubility in α-Si.²⁷⁹ There, approximately 450 nm of α-Si was deposited onto polished Si wafers at 450 °C by chemical vapor deposition (CVD). The wafers were then implanted at room temperature with 200 keV Au⁺ to $8 \times 10^{14}/\text{cm}^2$ and subsequently annealed over the temperature range of 400-800 °C for 1-2400 s in a N₂ ambient. The Au concentration profiles were measured by RBS. It should be noted that no Au precipitation was observed within the resolution of the TEM analysis. The RBS spectra show that the Au concentration in the CVD layer is on the order of $3 \times 10^{19}/\text{cm}^3$ after annealing the material at 600 °C. This is

several orders of magnitude greater than the solubility limit extrapolated at 600 °C from measurements performed in crystalline material (i.e., $1.2 \times 10^{13}/\text{cm}^3$). The authors put forward that this enhanced solubility is most likely due to the structure of the amorphous phase where the distorted atom rings can accommodate a large concentration of Au atoms.

Enhanced solubility of B in the amorphous phase is a significant result. This offers the ability to increase the activation level in the p-type SDE by increasing the temperature at which recrystallization of an implantation-induced amorphous layer takes place. It is now of interest to compare these results to those observed for B in c-Si. Michel *et al.* and Cowern *et al.* reported the concentration levels below which B diffusion occurred in c-Si as a function of annealing temperature.^{5,210} The experiment in Ref. 5 performed a temperature dependent diffusion study using one $10 \Omega\cdot\text{cm}$ (100) n-type Si wafer implanted with 60 keV B^+ to $2 \times 10^{14}/\text{cm}^2$. The SIMS results showed that the peak concentration of the B profile was approximately $1.5 \times 10^{19}/\text{cm}^3$, which is well below the solid solubility limit in c-Si. It was shown that the shape of the depth profile had a strong dependence on the anneal temperature. At 800 °C a significant amount of diffusion occurred at relatively low B concentrations whereas a negligible amount of diffusion occurred in the peak of the B profile above a concentration of approximately $2 \times 10^{18}/\text{cm}^3$. The concentration level below which diffusion occurred was shown to increase with increasing annealing temperature until a temperature of 1000 °C where all of the B was shown to diffuse. The authors noted that the concentration level below which B diffusion occurred corresponded very well with the intrinsic carrier concentration at each anneal temperature. The intrinsic carrier concentrations at 800, 900, and 1000 °C were

approximately 2.3, 4.9, and $9.3 \times 10^{18}/\text{cm}^3$, respectively. The observed diffusion behavior and corresponding R_s data provided evidence that the mobile portion of the B profile was electrically active and, therefore, the substitutional component of B. The experiment in Ref. 210 performed a transient diffusion study using bare (111) n-type FZ grown Si wafers implanted with 25 keV B⁺ to $2 \times 10^{14}/\text{cm}^2$. The authors noted that the peak B concentration was well above the intrinsic carrier concentration but below the solubility limit for B in c-Si. The SIMS results showed that a critical concentration, C_{enh} , exists which separates the low concentration region where transient diffusion occurs from the high concentration region where B is immobile. Additional SIMS results showed that the C_{enh} was independent of the B dose and approximately an order of magnitude below the equilibrium solubility limit in c-Si. Spreading-resistance measurements confirmed that the immobile portion of the B profile was electrically inactive. These results were consistent with the idea that the B remains immobile and electrically inactive for concentrations above the intrinsic carrier concentration. For comparison between the values reported throughout the literature and those obtained within this work, the data reported in Ref. 210 is included in Figure 6-24 along with the values for the plateau concentrations observed through the SIMS profiles in Figures 5-15, 6-6, 6-8, and 6-10.²⁸¹⁻²⁸⁴ It should be noted that a temperature of 700 °C was used to plot the data corresponding to any anneal where recrystallization of the implantation-induced amorphous layer was presumed to complete during the ramp-up to the peak temperature (e.g., 800 °C iRTP anneal). Also, since the T-t profiles for the fRTP anneals are unavailable, the temperature at which recrystallization occurred was estimated from the extrapolated fit between the data corresponding to the 585 °C furnace anneal and the

800 °C iRTP anneal. As can be seen in Figure 6-23, the data from the literature show that the concentration level below which diffusion occurs matches very well with the intrinsic carrier concentration (n_i) reported by Morin and Maita.²⁸⁵ It can be seen that this concentration level is approximately an order of magnitude lower than the corresponding solid solubility levels (C_s) estimated by Fair under equilibrium conditions for B in c-Si.²⁸³ The most interesting feature of Figure 6-24 is that the values corresponding to the plateau concentrations of the SIMS data observed in this work when recrystallization of the implantation-induced amorphous layer occurs at relatively low temperatures (e.g., 585 or 700 °C) are more than an order of magnitude greater than the C_s in c-Si. The difference between the plateau concentrations observed through the SIMS data and C_s is less noticeable when recrystallization of an implantation-induced amorphous layer occurs at higher temperatures. It should be noted that extrapolating from the low temperature data results in recrystallization of the amorphous layer occurring at approximately 1060 and 1240 °C for the 760 °C intermediate temperature when a peak UHT temperature of 1200 and 1350 °C is used, respectively. Recrystallization of the amorphous layer is expected to occur at approximately 1010 and 1160 °C for the 800 °C intermediate temperature when a peak UHT temperature of 1200 and 1350 °C is used, respectively. When compared to the data from the literature, it can be seen that increase in plateau concentration has relatively low temperature dependence. Comparison between the C_s and the plateau concentrations observed through the SIMS data supports the idea that B solubility is higher in the amorphous phase.

The idea of achieving high activation levels due to the higher solubility of dopants in α -Si when compared to c-Si, and the thought that higher activation levels can be

achieved at higher recrystallization temperatures should not be exclusive to this UHT annealing technique. Indeed, a similar report based on the rapid recrystallization of pre-amorphized Si with scanned continuous wave (cw) electron-beam (e-beam) and laser annealing showed much higher activation levels after either e-beam or laser annealing when compared to equilibrium C_s activation levels.²⁸⁶ This was done by implanting 100 keV As⁺ to $1\times10^{16}/\text{cm}^2$ into a 10-20 Ω·cm ⟨100⟩ p-type Si substrate. This implantation step was performed at either -100 or 0 °C and produced a continuous amorphous layer extending approximately 100 nm below the substrate surface. Both e-beam²⁸⁷ and laser²⁸⁸ annealing were used to recrystallize this amorphous layer. For the e-beam anneal, the substrate temperature was ~50 °C and the beam energy was 14.0 W (31 kV at 0.45 mA) resulting in a power/radius (*P/r*) ratio of 0.14 W/ μm . The laser anneal was performed with a substrate temperature of 350 °C and a laser beam energy of 6.4 W, resulting in a corrected (reflection coefficient) *P/r* ratio of 0.17 W/ μm . Electrical and/or mechanical scanning were used to provide uniform coverage of large areas. It should be noted that, although the ramp-up rates and peak annealing temperatures were not given, both the e-beam and laser annealing techniques are expected to result in rapid recrystallization of the implantation-induced amorphous layer. A differential van der Pauw technique was used to examine both the electrical activation and carrier mobility, while MeV He⁺ channeling measurements were used to determine the lattice location of the implanted As⁺ and the residual damage within the material. The differential van der Pauw technique showed that the maximum electron concentration exceeds $1\times10^{21}/\text{cm}^3$ for both the e-beam and laser annealed samples. This shows that both the e-beam and laser annealing techniques are capable of achieving much greater activation levels than those

predicted by equilibrium C_s . Although the authors implanted the Si with As^+ instead of B^+ , it is presumed that a similar activation mechanism (i.e., solute trapping at the α/c interface) takes place during recrystallization and is responsible for the high activation levels observed for the e-beam and laser annealing techniques. In other words, although it is expected that the solubility of dopants in $\alpha\text{-Si}$ will be different for different impurities, the solubility of impurities in $\alpha\text{-Si}$ is expected to increase with increasing temperature independent of impurity type (similar to dopant solubility in c-Si).

It was shown in Chapter 5 that higher activation levels can be achieved by using this annealing technique directly after implantation as opposed to performing a low temperature SPER anneal before UHT annealing. This improved activation was presumably thought to be because higher activation levels can be achieved at higher recrystallization temperatures. In other words, higher activation levels can be achieved when recrystallization (and presumably activation) occurs during ramp-up of an UHT anneal (e.g., approximately 700 °C), as opposed to a low temperature (i.e., 585 °C) furnace anneal. Although it was shown that the plateau concentration can be further increased with increasing peak temperature during UHT annealing of the wafer with the 12 keV F^+ implant to $1.5 \times 10^{15}/\text{cm}^2$ (when using intermediate temperatures of either 760 or 800 °C), the effect of additional F^+ implant on the dopant activation still needs to be investigated. It was shown in Chapter 4 that the measured R_s after an iRTP anneal can be closely estimated by the use of a theoretical calculation that compensates for the fraction of inactive dopant by truncating the concentrations above the plateau concentration (i.e., the concentration level above which inactive B cluster formation or precipitation occurs and the B remains immobile). The measured and calculated R_s values for the

wafer without and with the 12 keV F⁺ implant to $1.5 \times 10^{15}/\text{cm}^2$ before UHT annealing are shown in Figure 6-25. The calculated values were determined by using Equations 4.5 and 4.6 in Chapter 4.²⁰⁸ It can be seen that the equation used to estimate the R_s is within 50 Ohm/sq of the measured value for most of the iRTP anneals, independent of the additional F⁺ implant. This shows that the R_s can be accurately predicted by Equations 4.5 and 4.6. It can be seen that, in general, the 12 keV F⁺ implant to $1.5 \times 10^{15}/\text{cm}^2$ resulted in lower R_s values compared to the wafer without the additional F⁺ implant for each annealing condition used in this study. Although it is presumed that most of the activation occurs due to solute trapping during SPER of the implantation-induced amorphous layer, the empirical data suggests that the fRTP anneal significantly improves the R_s independent of the additional F⁺ implant.^{179,274,275} It should be noted that, although the R_s is relatively independent of both the intermediate and peak fRTP temperature for the wafer without the 12 keV F⁺ implant to $1.5 \times 10^{15}/\text{cm}^2$, the wafer with the additional F⁺ implant shows a decrease in the R_s with increasing peak annealing temperature. The R_s shows the largest dependence on the peak annealing temperature when the 760 °C intermediate temperature is used. This dependence is less noticeable for the 800 °C intermediate temperature, and almost negligible when 900 °C is used as the intermediate temperature. This data is consistent with the increase in plateau concentration observed for the different intermediate temperatures in Figures 6-6b, 6-8b, and 6-10b; the 760 °C intermediate temperature resulted in the largest increase in plateau concentration during a fRTP anneal whereas the 800 °C intermediate temperature shows less of an increase and the 900 °C intermediate temperature shows almost no increase in the plateau concentration. The main inconsistency with the data is that, although the 760

and 800 °C intermediate temperatures result in an increase in the plateau concentration with increasing peak annealing temperature, only a slight improvement in R_s is observed when compared to the wafer without the additional F⁺ implant. In other words, the increase in plateau concentration does not appear to have a large effect on the resulting R_s . The corresponding XTEM images for the iRTP anneals in Figure 6-1 showed that, although the only contrast observed for the wafer without the 12 keV F⁺ implant to $1.5 \times 10^{15}/\text{cm}^2$ in Figure 6-1a is due to the EOR damage produced by the 48 keV pre-amorphization implant (which is approximately 78 nm below the substrate surface), additional contrast can be seen in the XTEM image for the wafer with the additional F⁺ implant in Figure 6-1b. This additional contrast is uniformly distributed throughout the region of regrown material and is presumably due to the formation of F precipitates or regrowth related defects associated with the high dose F⁺ implant. Similar defects were observed after annealing a wafer that was pre-amorphized with overlapping 150 and 40 keV Si⁺ implants both to $1 \times 10^{15}/\text{cm}^2$ and subsequently implanted with 16 keV F⁺ to $2 \times 10^{15}/\text{cm}^2$.⁶³ It should be noted that the peak F concentration in Ref. 63 was approximately $1 \times 10^{20}/\text{cm}^3$, whereas the peak F concentration for the current experiment is approximately $3 \times 10^{20}/\text{cm}^3$. It is likely that these defects result in a reduction in carrier mobility, and that this reduction is enough to cancel any improvement in R_s due to the increase in active dose as a result of recrystallization during the fRTP anneal.

Unfortunately, this could not be confirmed by Hall effect measurements due to the amount of sample available for characterization. The disagreement between the measured and calculated results shows that the active B concentrations are greater than

those used in the calculation. Additional work is required to better understand why the calculated results do not predict the improvement in the R_s after a fRTP anneal.

Conclusions

Novel high-power arc lamp design has enabled UHT annealing as an alternative to conventional RTP for B ultra-shallow junction formation. This technique heats the wafer to an intermediate temperature (e.g., 800 °C) before discharging a capacitor bank into flash lamps, which anneals the device side of the wafer at a relatively high temperature (e.g., 1200 °C) for a few milliseconds. It was shown in Chapter 5 that higher activation levels can be achieved by using this annealing technique directly after implantation as opposed to performing a low temperature SPER anneal before UHT annealing. This improved activation was presumably thought to be because higher activation levels can be achieved at higher recrystallization temperatures. In other words, higher activation levels can be achieved when recrystallization (and presumably activation) occurs during ramp-up of an UHT anneal (e.g., approximately 700 °C), as opposed to a low temperature (i.e., 585 °C) furnace anneal. In order to test this idea, an experiment was designed in an attempt to reduce the regrowth velocity of the α/c interface such that recrystallization of the implantation-induced amorphous layer would occur at even higher temperatures (e.g., 1000 °C). It is well known that F^+ implantation to a concentration of approximately $10^{18}/cm^3$ reduces the regrowth velocity of the α/c interface during SPER of an implantation-induced amorphous layer. Implanting F^+ to concentrations much greater than $10^{18}/cm^3$ may be sufficient to allow recrystallization to occur during the UHT anneal, thereby resulting in higher activation levels. Two 200 mm (100) n-type CZ grown Si wafers were pre-amorphized with 48 keV Ge^+ implantation to $5\times 10^{14}/cm^2$. One

of the wafers was subject to a 12 keV F⁺ implant to $1.5 \times 10^{15}/\text{cm}^2$ and both wafers were then implanted with 3 keV BF₂⁺ molecular ions to $6 \times 10^{14}/\text{cm}^2$. The wafers were sectioned and annealed under various conditions to investigate the effects of the UHT annealing technique on the resulting junction characteristics. The SIMS results showed that the as-implanted junction abruptness and x_j for the wafer without the 12 keV F⁺ implant to $1.5 \times 10^{15}/\text{cm}^2$ was approximately 3.3 nm/dec and 16.3 nm, respectively. Additional SIMS results showed that the junction abruptness degraded to 11.9 nm/dec and the x_j increased to approximately 25.6 nm for the wafer with the additional F⁺ implant. It was shown through the literature that impurities such as H and F can passivate the trapping sites in α -Si by forming highly-favored bonding arrangements. When these trapping sites are occupied, interstitially diffusing species such as Pd and Cu are rejected from the passivated regions presumably due to there being no structural defects capable of preventing their motion. It is reasonable to put forward that the 12 keV F⁺ implant to $1.5 \times 10^{15}/\text{cm}^2$ is sufficient to passivate the α -Si trapping sites therefore allowing B, which is presumed to diffuse interstitially in α -Si, to diffuse into the substrate to a depth consistent with the distribution of available trapping sites. Additional experiments showed that the as-implanted F⁺ has no effect on the concentration of paramagnetic defects in α -Si as measured by EPR; therefore, the effect of the additional F⁺ implant on the observed low temperature diffusion behavior was attributed to F interactions with a fraction of the non-paramagnetic defects in the amorphous material which form highly-favored bonding arrangements and de-trap the B atoms from these defect sites. It is well known that the saturation defect density in α -Si at room temperature is approximately 0.5 at. % and that a majority of these defects are

not paramagnetic,²²³ making EPR incapable of detecting these defects; therefore, it is reasonable to assume that the F is capable of interacting with a fraction of the non-paramagnetic defects which are responsible for trapping the B atoms. The preferential interaction between F and the non-paramagnetic traps or defect states in the amorphous layer would imply that the F is more strongly bonded to these traps when compared to paramagnetic defects. It should be noted that the F concentration at the depth where B begins to form the exponentially decreasing profile is approximately $3 \times 10^{20}/\text{cm}^3$ (i.e., 0.6 at. %), which is remarkably close to the value reported by Stolk *et al.* for the saturation defect density in α -Si at room temperature (i.e., 0.5 at. %). Additional SIMS results showed that the amount of B diffusion that occurs during SPER of the implantation-induced amorphous layer increases for the wafer with the additional F^+ implant, presumably due to the F reducing the regrowth velocity of the α/c interface, allowing more time for B to diffuse in α -Si before complete recrystallization of the implantation-induced amorphous layer. Also, the SIMS results show that F^+ co-implantation is capable of preventing any additional diffusion during a 1350 °C UHT anneal when the intermediate temperature is sufficiently low (e.g., 800 °C). The TEM results show that the final EOR defect structure is dependent on both the intermediate and peak temperatures of the thermal process but relatively independent of the 12 keV F^+ implant to $1.5 \times 10^{15}/\text{cm}^2$. Additional TEM results show that the additional F^+ implant is sufficient to slow the regrowth velocity of the α/c interface such that approximately 22 nm of α -Si remains near the substrate surface after the 800 °C iRTP anneal. The SIMS results corresponding to the 760 and 800 °C intermediate temperatures show an increase in plateau concentration with increasing peak temperature during UHT annealing

of the wafer with the 12 keV F⁺ implant to $1.5 \times 10^{15}/\text{cm}^2$, presumably due to the higher solubility of dopants in α -Si when compared to c-Si and the thought that higher activation levels can be achieved at higher recrystallization temperatures. The values corresponding to the plateau concentrations of the SIMS data observed in this work when recrystallization of the implantation-induced amorphous layer occurs at relatively low temperatures (e.g., 585 or 700 °C) are more than an order of magnitude greater than the C_s in c-Si. The difference between the plateau concentrations observed through the SIMS data and C_s is less noticeable when recrystallization of an implantation-induced amorphous layer occurs at higher temperatures. When compared to the data from the literature, it can be seen that increase in plateau concentration has relatively low temperature dependence. Comparison between the C_s and the plateau concentrations observed through the SIMS data supports the idea that B solubility is higher in the amorphous phase. Four-point probe measurements show a decrease in R_s with the introduction of the UHT anneal when compared to the intermediate anneal, and that the R_s is generally lower for the wafer that received the additional F⁺ implant before UHT annealing. The four-point probe measurements only show a slight improvement in R_s for the wafer with the 12 keV F⁺ implant to $1.5 \times 10^{15}/\text{cm}^2$ presumably due to the formation of F precipitates or regrowth related defects associated with the high dose F⁺ implant. It is believed that these defects cause a reduction in the carrier mobility, and that this reduction is enough to cancel any improvement in R_s due to the increase in active dose as a result of recrystallization during the f RTP anneal. The reduction in TED and increase in activation for the co-implanted wafer is presumably due to the F binding with excess Si interstitials so as to reduce point-defect mediated diffusion and the amount of inactive

dopant associated with immobile B cluster formation. The improved activation is also due to F reducing the regrowth velocity of the α/c interface such that recrystallization occurs during the UHT anneal [when the intermediate temperature is sufficiently low (e.g., 800 °C)].

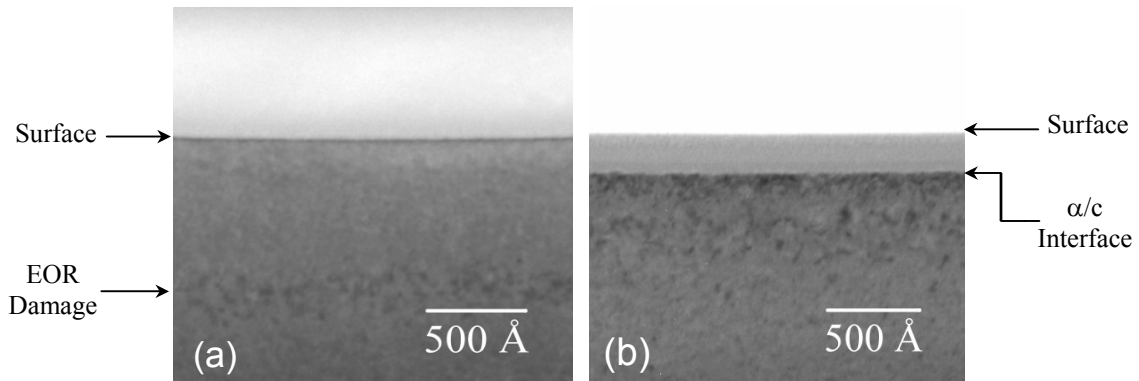


Figure 6-1 Bright field XTEM images showing that the (a) 760 °C iRTP anneal is sufficient to completely recrystallize the amorphous layer produced by the 48 keV Ge⁺ pre-amorphization implant to $5 \times 10^{14}/\text{cm}^2$ and (b) the 12 keV F⁺ implant to $1.5 \times 10^{15}/\text{cm}^2$ is sufficient to reduce the regrowth velocity of the a/c interface such that approximately 22 nm of amorphous material remains near the substrate surface after an 800 °C iRTP anneal.

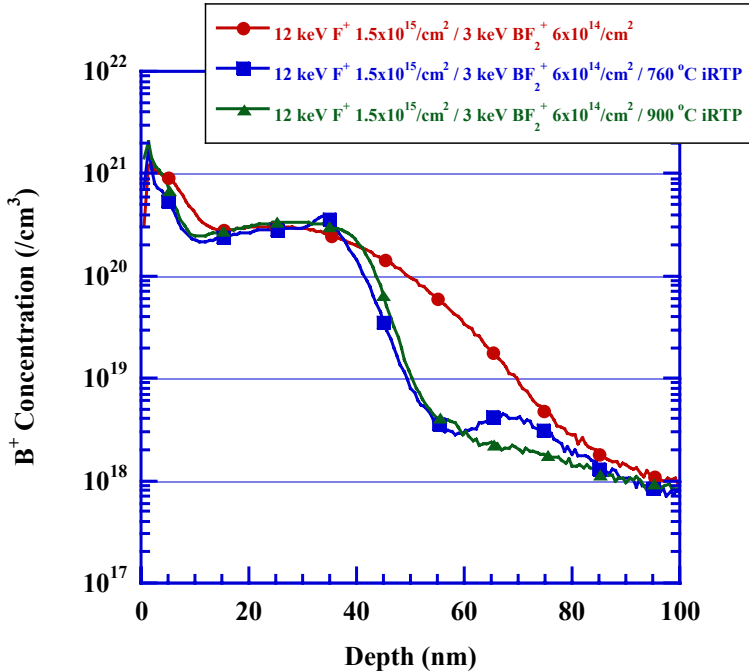


Figure 6-2 Concentration profiles showing the F⁺ concentration as a function of depth for both the 12 keV F⁺ implant to $1.5 \times 10^{15}/\text{cm}^2$ and 3 keV BF₂⁺ implant to $6 \times 10^{14}/\text{cm}^2$ before and after iRTP annealing at 800 and 900 °C for the 48 keV Ge⁺ pre-amorphization implant to $5 \times 10^{14}/\text{cm}^2$. The symbols are for identifications purposes only.

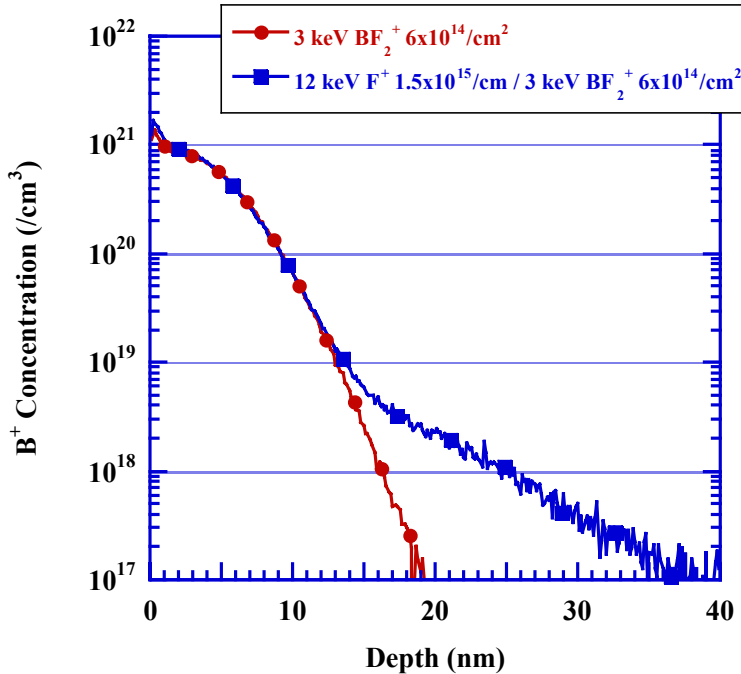


Figure 6-3 Concentration profiles showing the as-implanted B^+ concentration as a function of depth for the 3 keV BF_2^+ implant to $6 \times 10^{14}/\text{cm}^2$ without and with the 12 keV F^+ implant to $1.5 \times 10^{15}/\text{cm}^2$ directly after the 48 keV Ge^+ pre-amorphization implant to $5 \times 10^{14}/\text{cm}^2$. The symbols are for identifications purposes only.

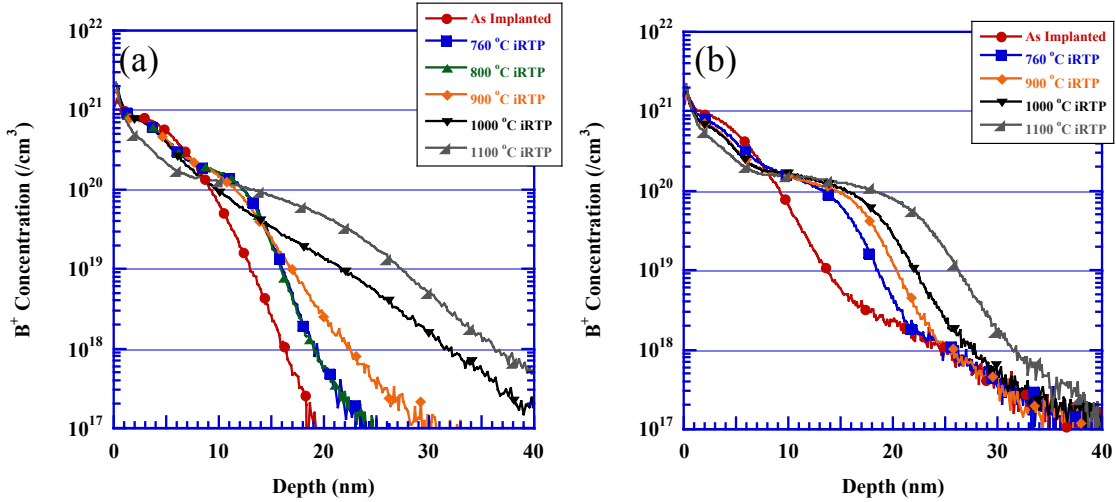


Figure 6-4 Concentration profiles showing the B^+ concentration as a function of depth for the $3 \text{ keV } BF_2^+$ implant to $6 \times 10^{14} \text{ cm}^{-2}$ after each iRTP anneal temperature used in this study for the $48 \text{ keV } Ge^+$ pre-amorphization implant to $5 \times 10^{14} \text{ cm}^{-2}$ (a) without and (b) with the $12 \text{ keV } F^+$ implant to $1.5 \times 10^{15} \text{ cm}^{-2}$. The symbols are for identifications purposes only.

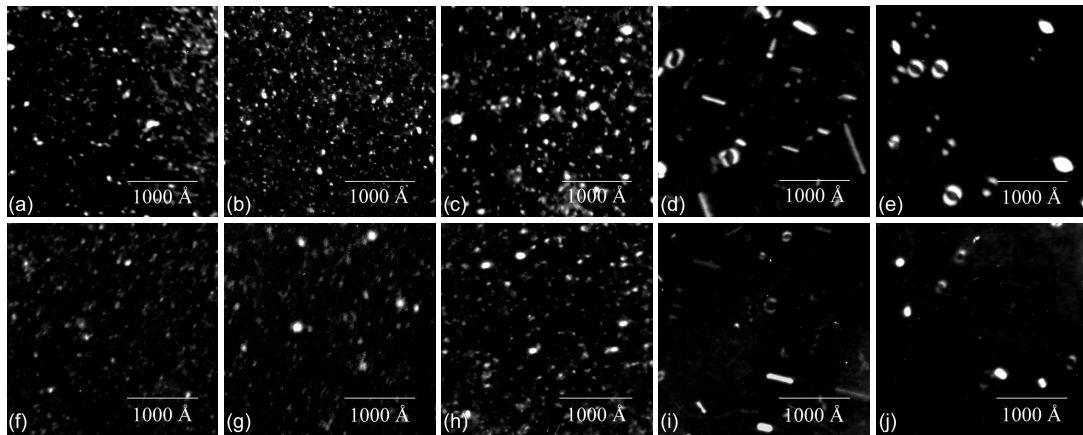


Figure 6-5 Plan-view TEM images of the damage produced by the 48 keV Ge⁺ pre-amorphization implant to $5 \times 10^{14}/\text{cm}^2$ under a WBDF \mathbf{g}_{220} two-beam imaging condition after the (a)(f) 760 (b)(g) 800 (c)(h) 900 (d)(i) 1000 and (e)(j) 1100 °C iRTP anneals for the wafer without and with the 12 keV F⁺ implant to $1.5 \times 10^{15}/\text{cm}^2$, respectively.

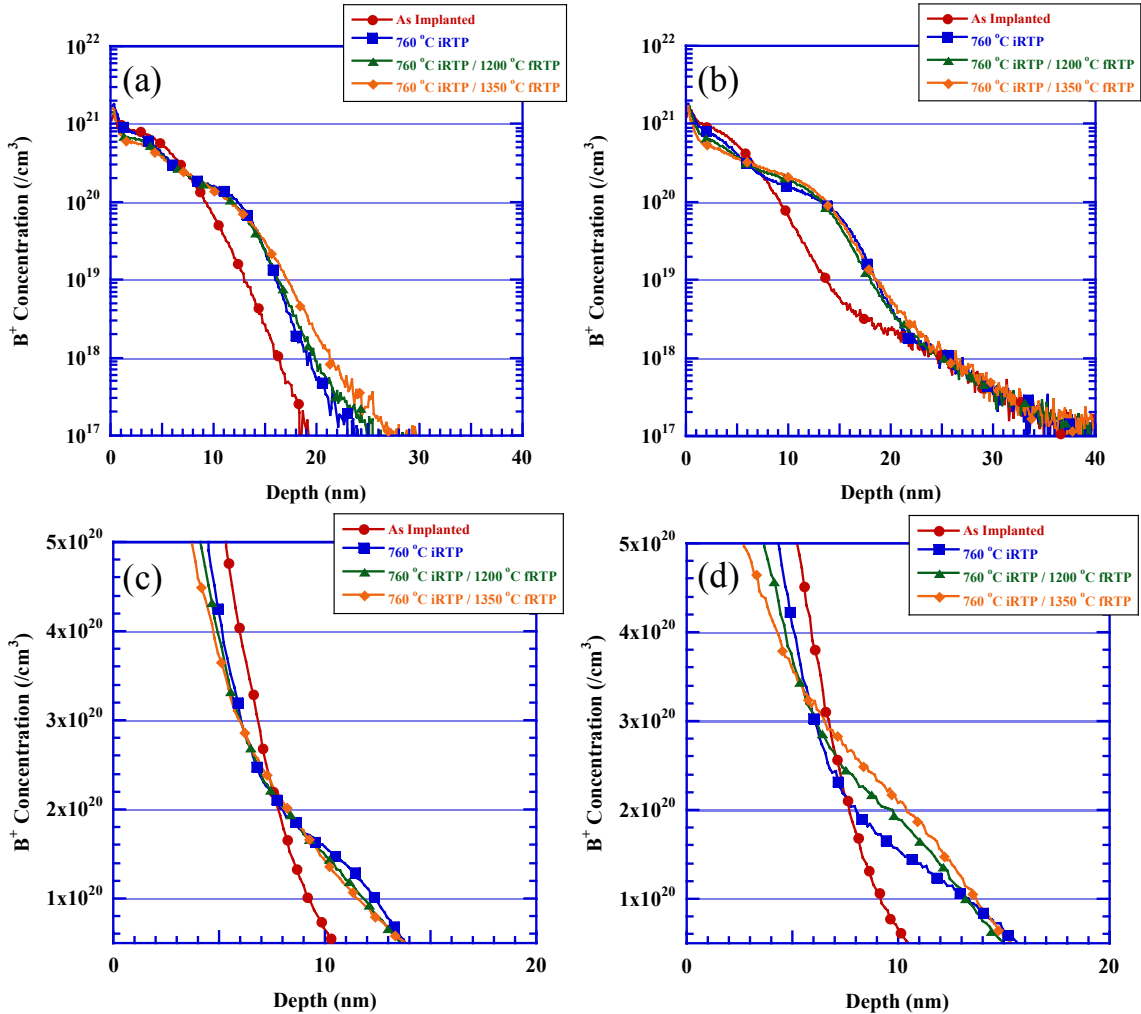


Figure 6-6 Concentration profiles showing the B^+ concentration as a function of depth for the 3 keV BF_2^+ implant to $6 \times 10^{14}/cm^2$ before and after a 1200 or 1350 °C fRTP anneal when using an intermediate temperature of 760 °C for the 48 keV Ge^+ pre-amorphization implant to $5 \times 10^{14}/cm^2$ (a)(c) without and (b)(d) with the 12 keV F^+ implant to $1.5 \times 10^{15}/cm^2$. The symbols are for identifications purposes only.

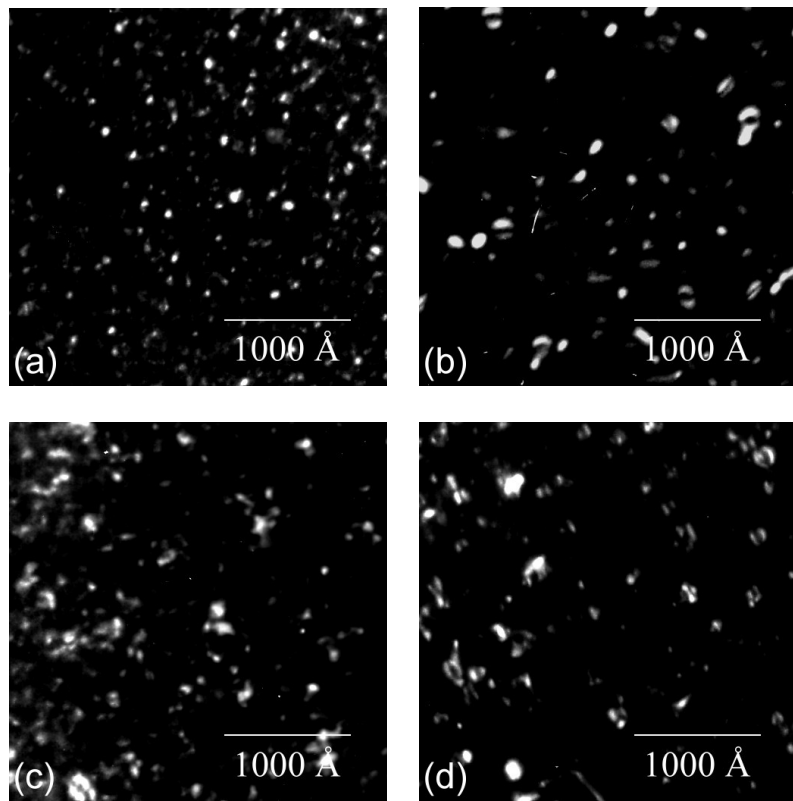


Figure 6-7 Plan-view TEM images of the damage produced by the 48 keV Ge^+ pre-amorphization implant to $5 \times 10^{14}/\text{cm}^2$ under a WBDF \mathbf{g}_{220} two-beam imaging condition for the (a)(c) 1200 and (b)(d) 1350 °C fRTP anneal using an intermediate temperature of 760 °C for the wafer without and with the 12 keV F^+ implant to $1.5 \times 10^{15}/\text{cm}^2$, respectively.

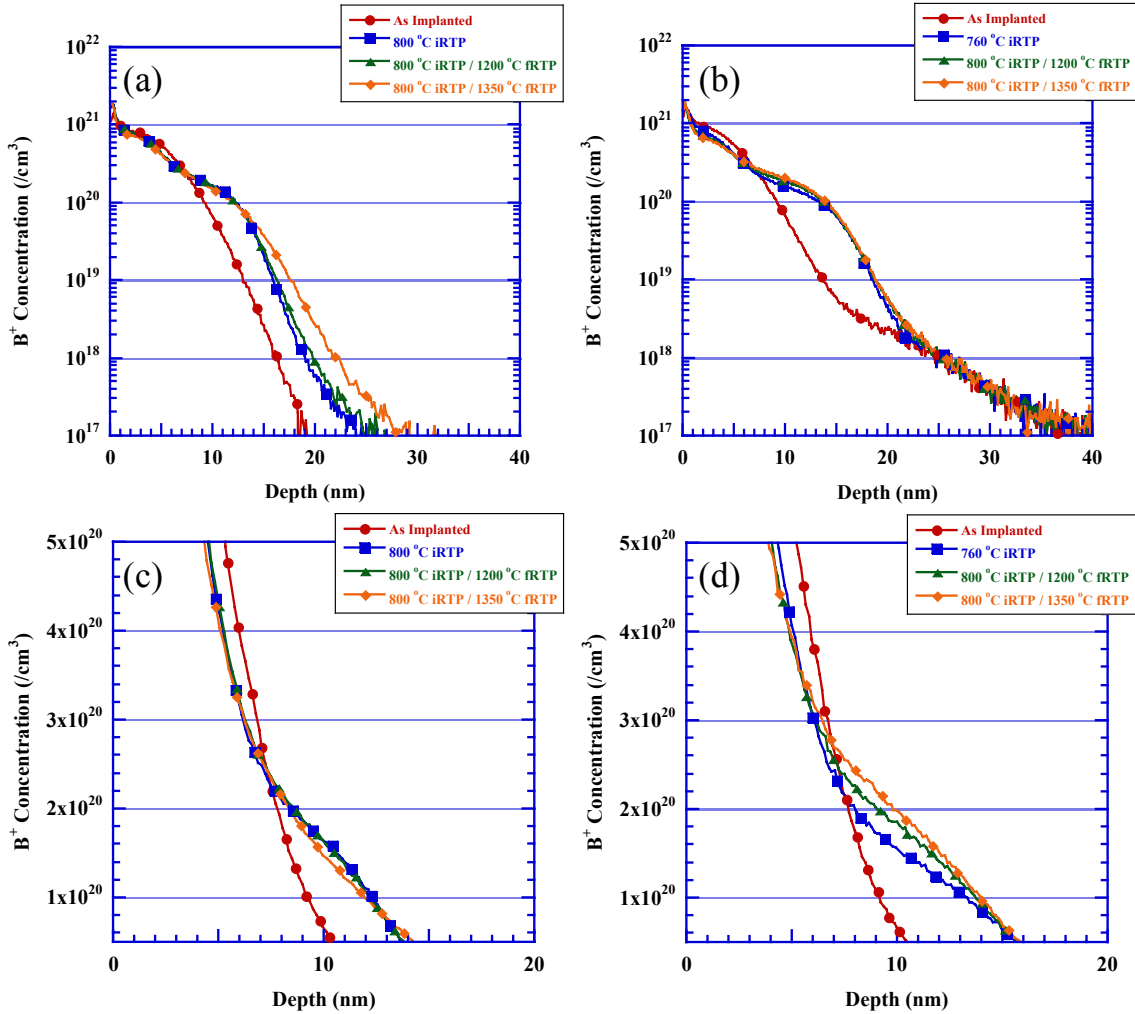


Figure 6-8 Concentration profiles showing the B^+ concentration as a function of depth for the 3 keV BF_2^+ implant to $6 \times 10^{14}/\text{cm}^2$ before and after a 1200 or 1350°C fRTP anneal when using an intermediate temperature of 800°C for the 48 keV Ge^+ pre-amorphization implant to $5 \times 10^{14}/\text{cm}^2$ (a)(c) without and (b)(d) with the 12 keV F^+ implant to $1.5 \times 10^{15}/\text{cm}^2$. The symbols are for identifications purposes only.

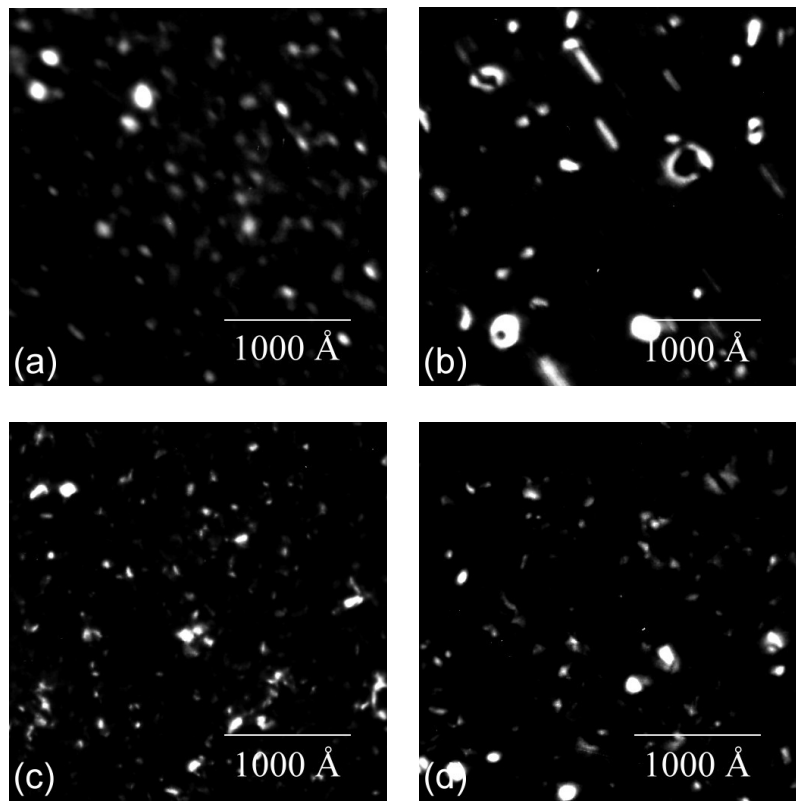


Figure 6-9 Plan-view TEM images of the damage produced by the 48 keV Ge^+ pre-amorphization implant to $5 \times 10^{14}/\text{cm}^2$ under a WBDF \mathbf{g}_{220} two-beam imaging condition for the (a)(c) 1200 and (b)(d) 1350 °C fRTP anneal using an intermediate temperature of 800 °C for the wafer without and with the 12 keV F^+ implant to $1.5 \times 10^{15}/\text{cm}^2$, respectively.

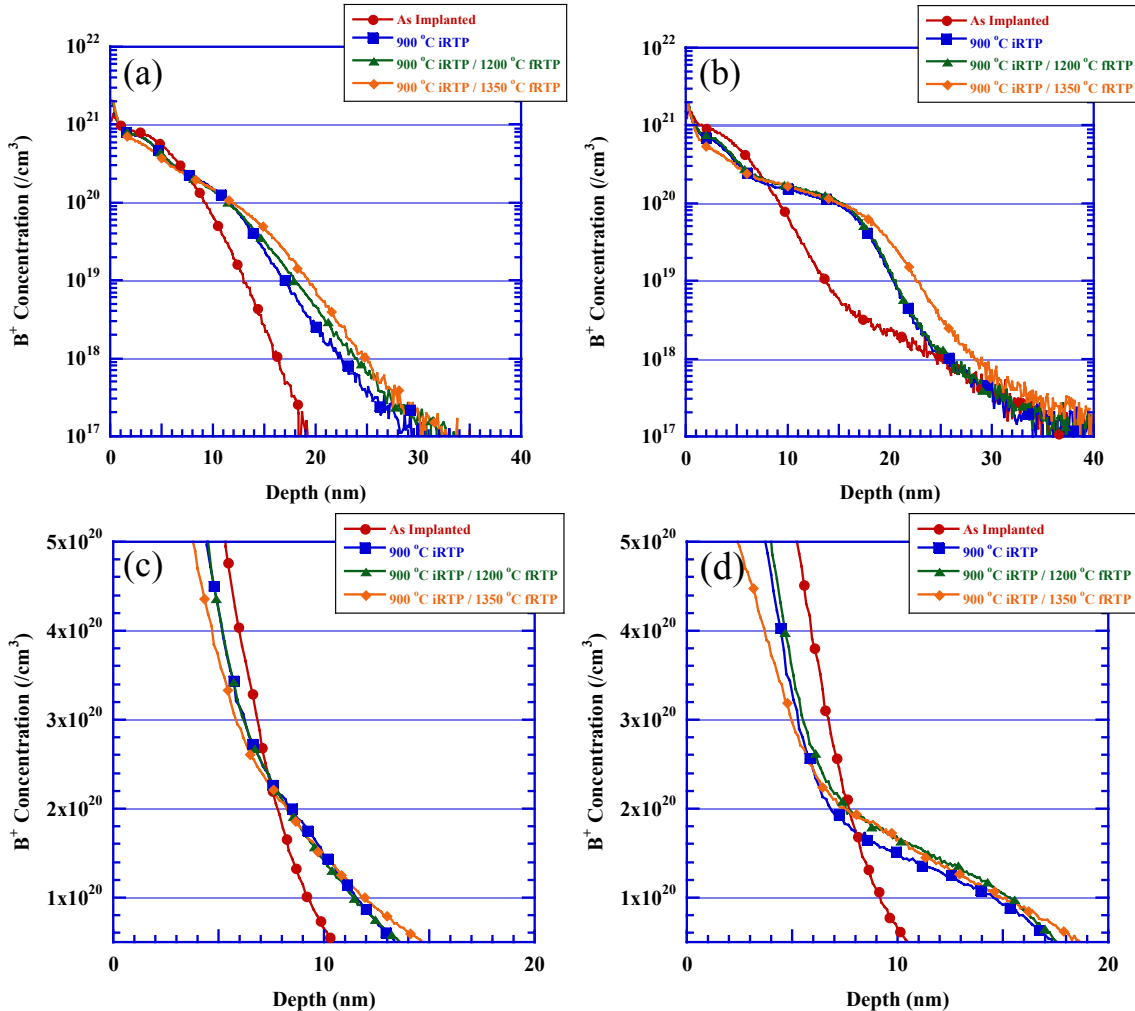


Figure 6-10 Concentration profiles showing the B^+ concentration as a function of depth for the 3 keV BF_2^+ implant to $6 \times 10^{14}/\text{cm}^2$ before and after a 1200 or 1350 °C fRTP anneal when using an intermediate temperature of 900 °C for the 48 keV Ge^+ pre-amorphization implant to $5 \times 10^{14}/\text{cm}^2$ (a)(c) without and (b)(d) with the 12 keV F^+ implant to $1.5 \times 10^{15}/\text{cm}^2$. The symbols are for identifications purposes only.

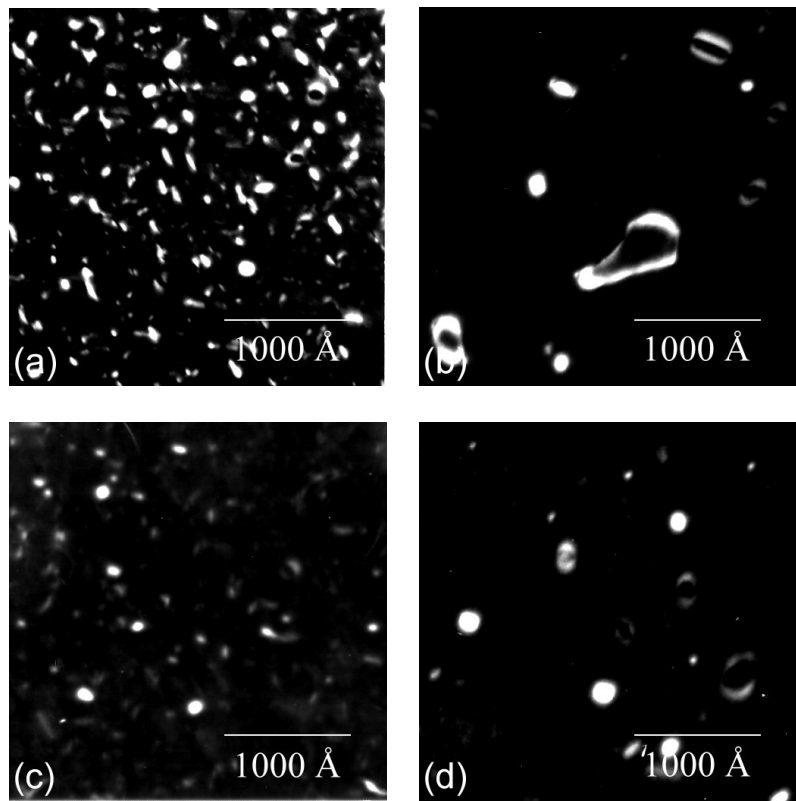


Figure 6-11 Plan-view TEM images of the damage produced by the 48 keV Ge^+ pre-amorphization implant to $5 \times 10^{14}/\text{cm}^2$ under a WBDF \mathbf{g}_{220} two-beam imaging condition for the (a)(c) 1200 and (b)(d) 1350 °C fRTP anneal using an intermediate temperature of 900 °C for the wafer without and with the 12 keV F^+ implant to $1.5 \times 10^{15}/\text{cm}^2$, respectively.

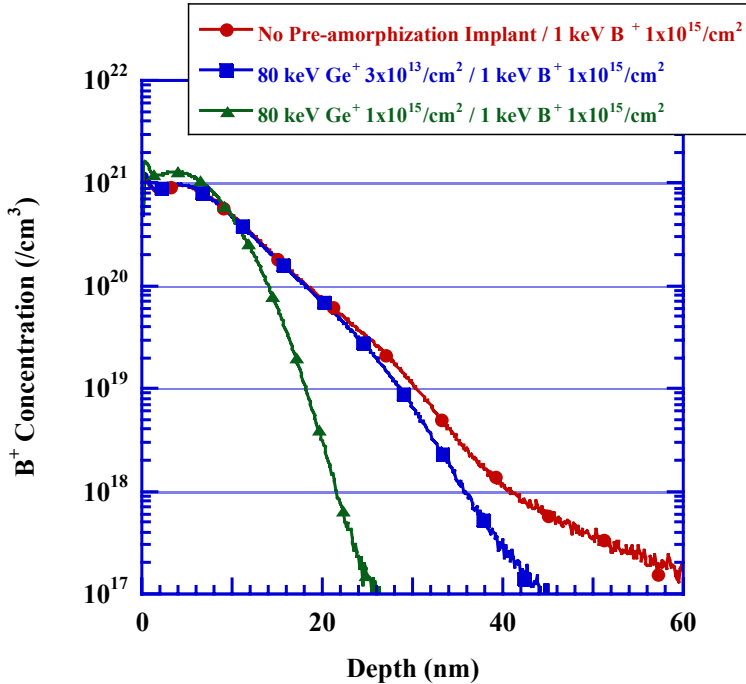


Figure 6-12 Concentration profiles showing the as-implanted B⁺ concentration as a function of depth for the 1 keV B⁺ implant to $1 \times 10^{15}/\text{cm}^2$ before and after pre-damaging or pre-amorphizing the substrate surface with a 48 keV Ge⁺ implant to either $3 \times 10^{13}/\text{cm}^2$ or $1 \times 10^{15}/\text{cm}^2$, respectively. The symbols are for identifications purposes only.

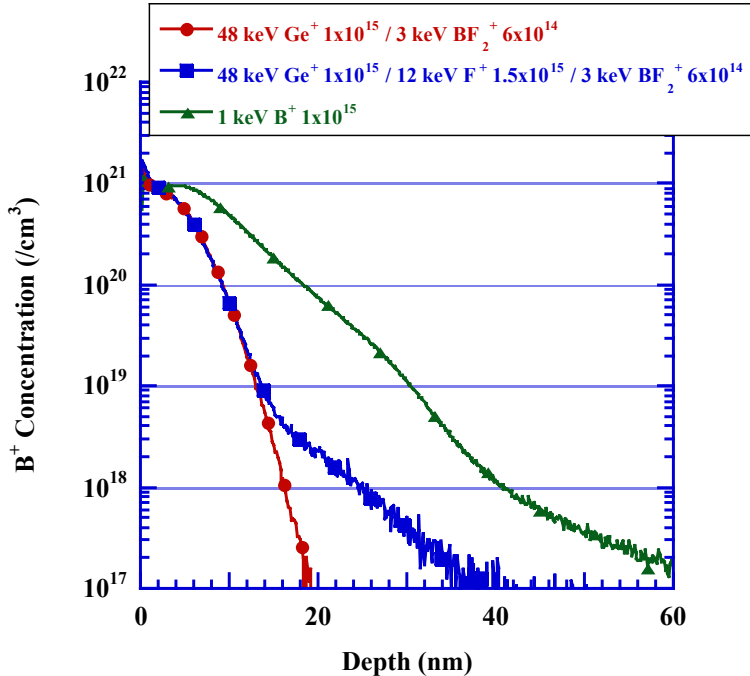


Figure 6-13 Concentration profiles showing the as-implanted B⁺ concentration as a function of depth for the 3 keV BF₂⁺ implant to $6 \times 10^{14}/\text{cm}^2$ without and with the 12 keV F⁺ implant to $1.5 \times 10^{15}/\text{cm}^2$ directly after the 48 keV Ge⁺ pre-amorphization implant to $5 \times 10^{14}/\text{cm}^2$ compared to the as-implanted B⁺ for the 1 keV B⁺ implant to $1 \times 10^{15}/\text{cm}^2$ without any pre-amorphization implant. The symbols are for identifications purposes only.

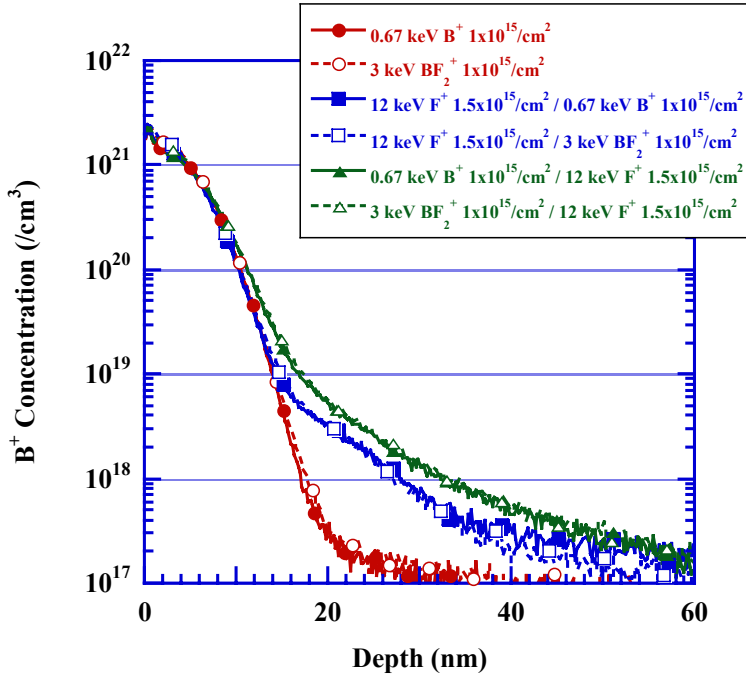


Figure 6-14 Concentration profiles showing the as-implanted B^+ concentration as a function of depth for either a 0.67 keV B^+ implant to $1 \times 10^{15}/\text{cm}^2$ or 3 keV BF_2^+ implant to $1 \times 10^{15}/\text{cm}^2$ without any additional processing and before and after a 12 keV F^+ implant to $1.5 \times 10^{15}/\text{cm}^2$ for wafers with a 60 keV Ge^+ pre-amorphization implant to $1 \times 10^{15}/\text{cm}^2$. The symbols are for identifications purposes only.

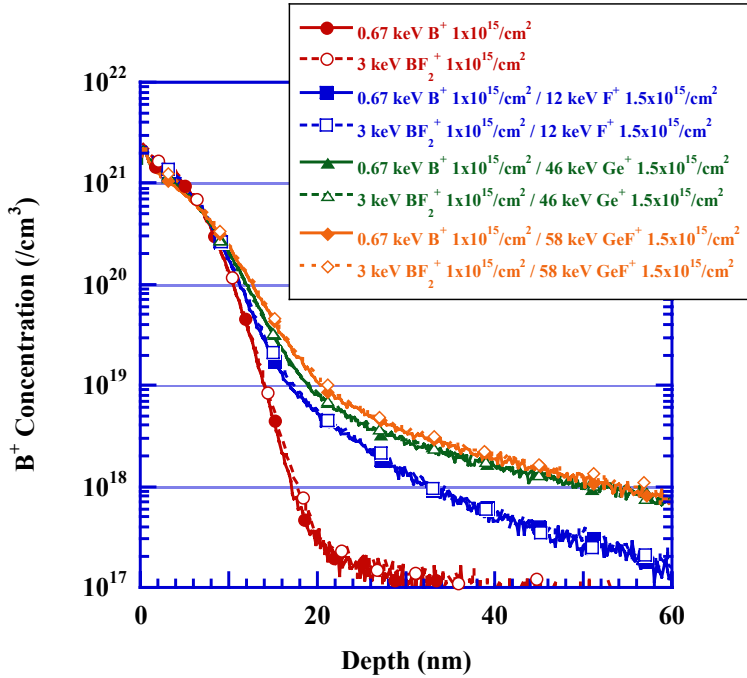


Figure 6-15 Concentration profiles showing the as-implanted B⁺ concentration as a function of depth for either a 0.67 keV B⁺ implant to $1 \times 10^{15}/\text{cm}^2$ or 3 keV BF₂⁺ implant to $1 \times 10^{15}/\text{cm}^2$ without any additional processing and after implantation with either 12 keV F⁺, 46 keV Ge⁺, or 58 keV GeF⁺ each to $1.5 \times 10^{15}/\text{cm}^2$ for wafers with a 60 keV Ge⁺ pre-amorphization implant to $1 \times 10^{15}/\text{cm}^2$. The symbols are for identifications purposes only. Note that the x_j increases with increasing ion mass.

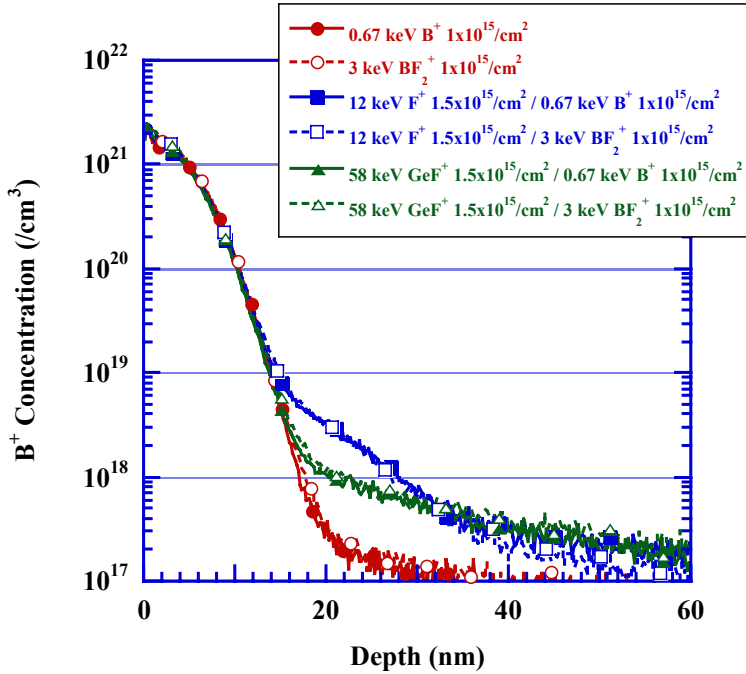


Figure 6-16 Concentration profiles showing the as-implanted B^+ concentration as a function of depth for either a 0.67 keV B^+ implant to $1 \times 10^{15}/\text{cm}^2$ or 3 keV BF_2^+ implant to $1 \times 10^{15}/\text{cm}^2$ without any additional processing and before implantation with either 12 keV F^+ or 58 keV GeF^+ each to $1.5 \times 10^{15}/\text{cm}^2$ for wafers with a 60 keV Ge^+ pre-amorphization implant to $1 \times 10^{15}/\text{cm}^2$. The symbols are for identifications purposes only. Note that the junction abruptness and x_j decreases with the additional Ge^+ implant.

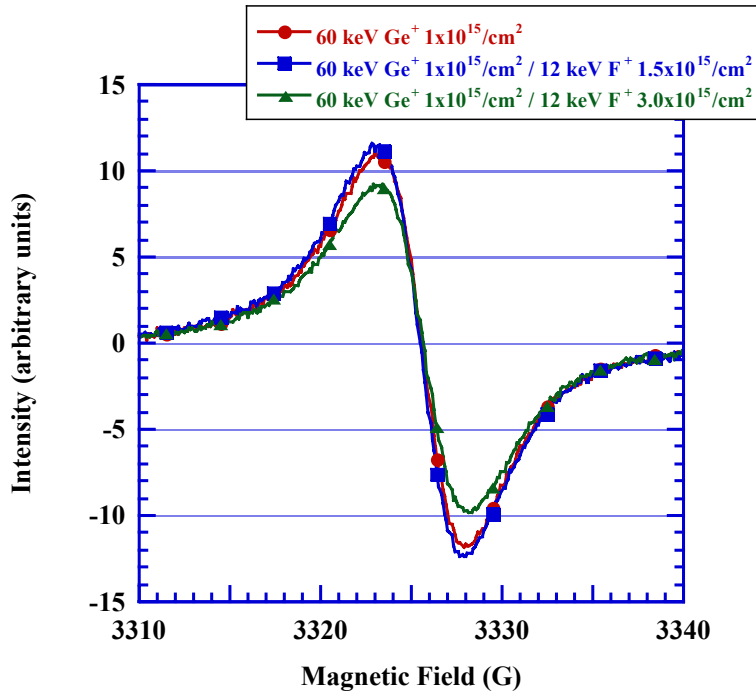


Figure 6-17 Paramagnetic response from wafers pre-amorphized with a 60 keV Ge^+ implant to $1 \times 10^{15}/\text{cm}^2$. In two cases the wafers were subsequently implanted with 12 keV F^+ to either $1.5 \times 10^{15}/\text{cm}^2$ or $3.0 \times 10^{15}/\text{cm}^2$. Note that within the 10-20% error associated with the measurement, the additional F^+ implant has a negligible effect on the EPR spectra.

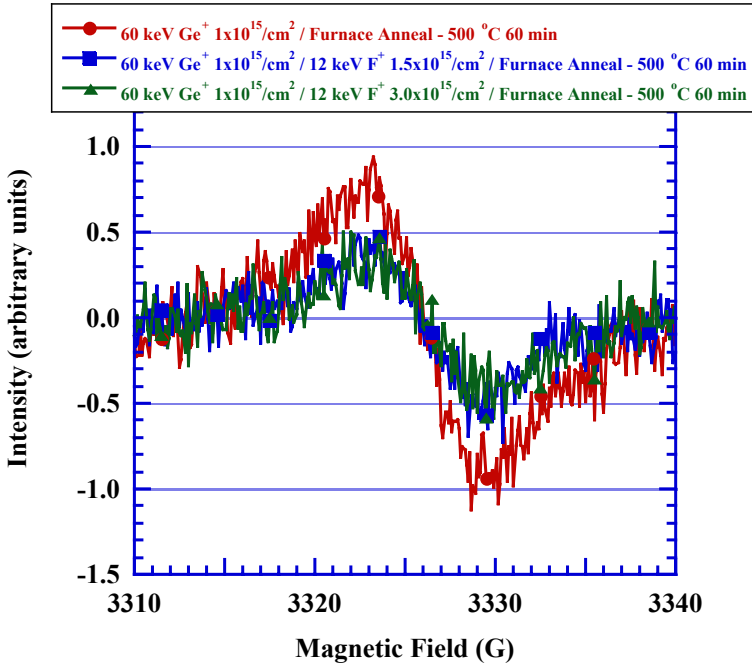


Figure 6-18 Paramagnetic response from wafers pre-amorphized with a 60 keV Ge^+ implant to $1 \times 10^{15}/\text{cm}^2$. In two cases the wafers were subsequently implanted with 12 keV F^+ to either $1.5 \times 10^{15}/\text{cm}^2$ or $3.0 \times 10^{15}/\text{cm}^2$. Each wafer was then subject to a 500 °C structural relaxation anneal for 60 min. Note that the additional F^+ implant has an added effect on reducing the intensity of the EPR spectra.

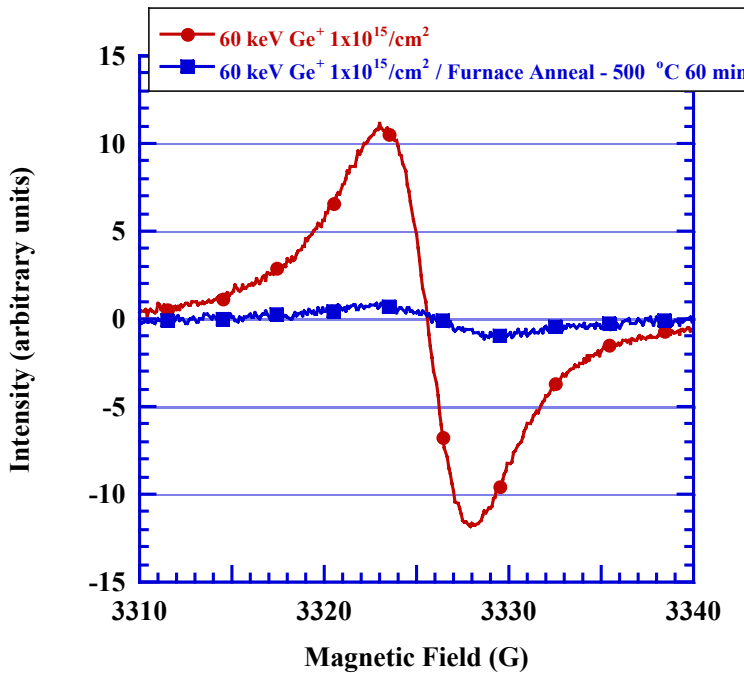


Figure 6-19 Comparison of the paramagnetic response from wafers pre-amorphized with a 60 keV Ge⁺ implant to $1 \times 10^{15}/\text{cm}^2$. One wafer was then subject to a 500 °C structural relaxation anneal for 60 min. Note that the structural relaxation anneal significantly reduces the intensity of the EPR spectra, showing that it decreases the concentration of paramagnetic defects in the amorphous material.

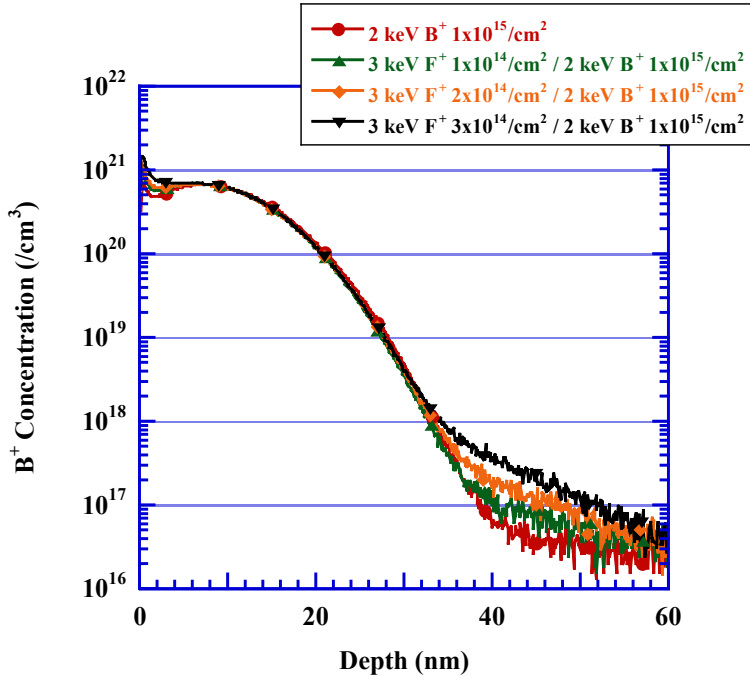


Figure 6-20 Concentration profiles showing the as-implanted B^+ concentration as a function of depth for the 2 keV B^+ implant to $1 \times 10^{15}/\text{cm}^2$ for the 80 keV Ge^+ pre-amorphization implant to $1 \times 10^{15}/\text{cm}^2$. Three of the wafers were previously implanted with 12 keV F^+ to various doses. The symbols are for identifications purposes only.

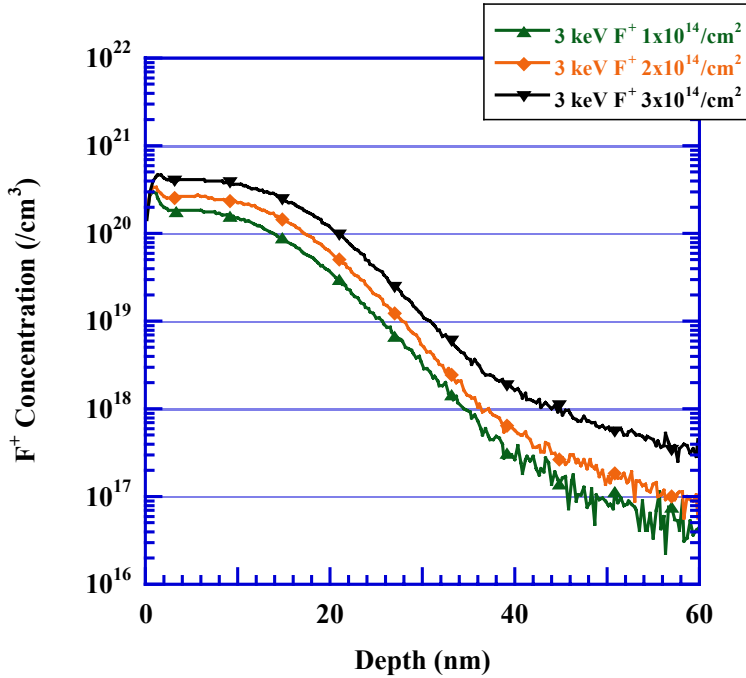


Figure 6-21 Concentration profiles showing the as-implanted F⁺ concentration as a function of depth for the 3 keV F⁺ implant to doses of 1, 2, and $3 \times 10^{14}/\text{cm}^2$ for the 80 keV Ge⁺ pre-amorphization implant to $1 \times 10^{15}/\text{cm}^2$. The symbols are for identification purposes only.

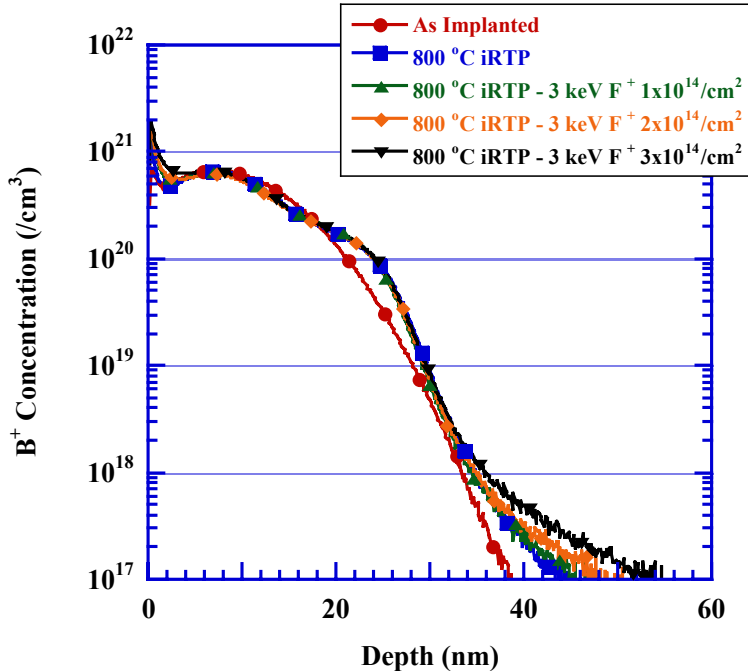


Figure 6-22 Concentration profiles showing the B^+ concentration as a function of depth for the 1 keV B^+ implant to $1 \times 10^{15}/\text{cm}^2$ before and after an 800°C iRTP anneal for the 80 keV Ge^+ pre-amorphization implant to $1 \times 10^{15}/\text{cm}^2$. Three of the wafers were previously implanted with 12 keV F^+ to various doses. The symbols are for identification purposes only.

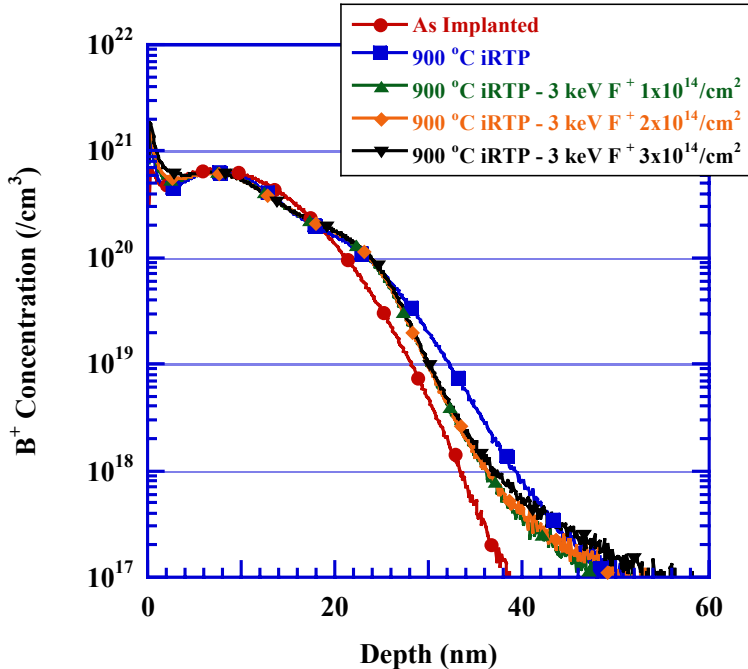


Figure 6-23 Concentration profiles showing the B^+ concentration as a function of depth for the 1 keV B^+ implant to $1 \times 10^{15}/\text{cm}^2$ before and after a 900°C iRTP anneal for the 80 keV Ge^+ pre-amorphization implant to $1 \times 10^{15}/\text{cm}^2$. Three of the wafers were previously implanted with 12 keV F^+ to various doses. The symbols are for identification purposes only.

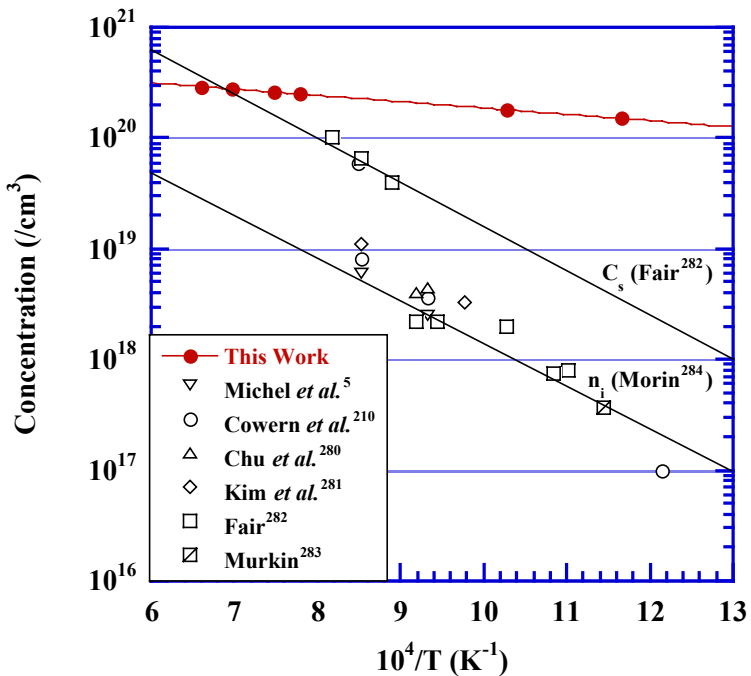


Figure 6-24 Concentration versus inverse temperature. The data corresponding to this work refer to the plateau concentrations observed through the SIMS data. The data from the literature show that the C_{enh} is very well matched by the n_i at the anneal temperature and is approximately an order of magnitude lower than C_s . Note that the plateau concentration values are significantly greater than C_s .

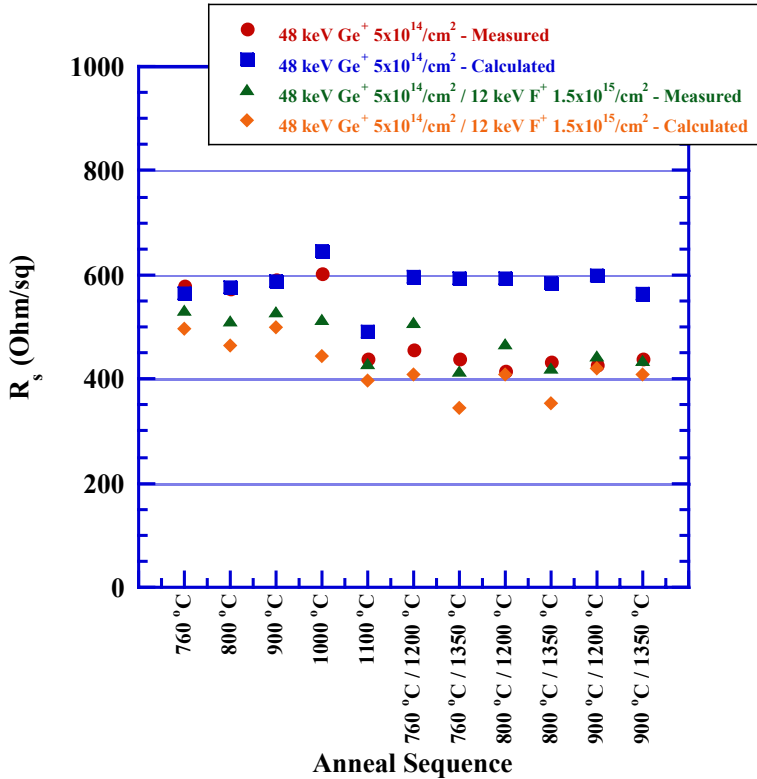


Figure 6-25 Graph of the measured (●)(▲) and calculated (■)(◆) R_s values obtained for the 48 keV Ge^+ pre-amorphization implant to $5 \times 10^{14}/\text{cm}^2$ without and with the 12 keV F^+ implant to $1.5 \times 10^{15}/\text{cm}^2$, respectively.

CHAPTER 7

SUMMARY AND FUTURE WORK

One of the many challenges in successfully scaling the dimensions of the metal-oxide-semiconductor field-effect-transistor (MOSFET) transistor is in maintaining an ultra-shallow low-resistivity p-type source/drain extension (SDE) region under the gate. Figure 1-3 showed the International Technology Roadmap for Semiconductors (ITRS), which represents the sheet resistance (R_s) and junction depth (x_j) required for the SDE to produce devices with the performance characteristics outlined by the individual technology nodes (represented as rectangles).¹³ One difficulty in improving the R_s is the thermodynamic solid solubility of impurities in crystalline-Si (c-Si), which limits the active dopant concentration.¹⁴ Figure 1-4 showed the solid solubility of a number of common impurities in c-Si, which increases as a function of temperature until an upper limit is reached.¹⁵ Aside from solid solubility limiting the amount of active dopant in the substrate, lattice imperfections and ionized impurities may serve as scattering sites which reduce carrier mobility and further increase the R_s .¹⁶ Decreasing the x_j of the SDE is made difficult by the significant amount of diffusion that occurs during post-implant thermal processing, such as the deep source/drain (S/D) activation anneal. During post-implant thermal processing, the Si self-interstitials generated during the implantation process redistribute throughout the lattice^{17,18} and remove the B atoms from their substitutional sites by a so-called kick-out reaction,¹⁹⁻²¹ allowing them to diffuse deep into the substrate through a well documented interstitial mechanism.²²⁻²⁵ The observation that the amount of TED decreases when the damage is annealed out at a higher

temperature influenced the development of single-wafer thermal processes capable of producing a high temperature ambient with ramp rates on the order of 50-200 °C/s, and fast switching times to insulate the dopant from a high degree of TED.^{3,27,28}

Rapid thermal processing (RTP) has proven successful in producing junctions with the performance characteristics necessary for the continued scaling of complementary MOS (CMOS) technology to date.²⁹ Its ability to satisfy these requirements is associated with improved equipment capability in the form of spike annealing, which decreases the effective thermal budget, allowing for higher annealing temperatures to improve activation and reduce the amount of diffusion that takes place during the thermal process.^{30,31} A spike anneal is characterized as a short thermal-anneal cycle that can be achieved by increasing the ramp-up and ramp-down rates and by minimizing the dwell time at the temperature of interest. The inability of this technique to produce junctions with the performance characteristics required by future technology nodes is in the cycle time of the thermal process, which results in an unacceptable amount of dopant diffusion. The minimum cycle times in conventional RTP techniques are limited by the maximum power delivered to the wafer, which determines the ramp-up rate, and the minimum response time of the relatively large thermal mass incandescent tungsten lamps, which determines both the soak time and the ramp-down rate. Without being able to minimize the soak time and the ramp-down rate, increasing the ramp-up rate above 100 °C/s results in no additional improvement in terms of forming a highly-activated ultra-shallow junction.³² This illustrates the need to investigate novel annealing technologies that may be able to produce highly activated junctions without being subject to a significant amount of TED.

Novel high-power arc lamp design has enabled ultra-high temperature (UHT) annealing as an alternative to conventional RTP for B ultra-shallow junction formation.³³ This technique heats the wafer to an intermediate temperature (e.g., 800 °C) before discharging a capacitor bank into flash lamps, which anneals the device side of the wafer at a relatively high temperature (e.g., 1200 °C) for a few milliseconds.³⁴⁻³⁶ This time duration is significantly reduced from those obtained with conventional RTP, which are on the order of 1-2 s within 50 °C of the peak temperature. The UHT anneal heats the surface of interest while increasing the bulk wafer temperature not more than 50 °C of the intermediate temperature, allowing for conductive heat loss through the substrate. In contrast to tungsten lamp heating technology (i.e., RTP), this technique uses a water-wall arc lamp which provides the means for significantly reducing the heating-cycle time because of its ability to deliver higher power and because of its faster response time.³⁷ The arc lamp responds more rapidly than tungsten filament lamps due to the reduced thermal mass of the argon gas used in the arc lamp system. The lamps can be switched off in a few microseconds, allowing greater control and repeatability over the anneal process. Although these qualities resolve the limiting issues associated with conventional RTP techniques, the activation and diffusion mechanisms that take place on these times scales were not well understood and were the subject of this work.

To better understand the effect of the UHT annealing technique on EOR damage evolution, the Ge⁺ pre-amorphization implant energy was varied to investigate the effect of the 1.0 eV activation energy associated with the defect dissolution kinetics of low energy Ge⁺ implantation. Two 200 mm (100) n-type Czochralski (CZ) grown Si wafers were pre-amorphized with either 48 keV or 5 keV Ge⁺ implantation to $5 \times 10^{14}/\text{cm}^2$, and

subsequently implanted with 3 keV BF_2^+ molecular ions to $6 \times 10^{14}/\text{cm}^2$. The wafers were sectioned and annealed under various conditions to investigate the effects of the UHT annealing technique on the resulting junction characteristics. The SIMS results show B diffusion in α -Si during solid-phase epitaxial regrowth (SPER) of the implantation-induced amorphous layer produced by the 48 keV pre-amorphization implant. No B diffusion in α -Si was observed for the sample that received the 5 keV pre-amorphization implant, presumably because of the high local concentration of interstitials and B atoms which participate in immobile B interstitial cluster (BIC) formation. The activation energy for B diffusion in α -Si was found to be 2.2 ± 0.26 eV. Although it was shown that both interstitial and vacancy point-defects exist in α -Si, these point-defects do not have a significant effect on the diffusion behavior of P or Sb in α -Si. These differences in diffusion behavior during recrystallization of an implantation-induced amorphous layer makes difficult defining interstitial and vacancy point-defect mediated diffusion mechanisms in α -Si. Additional SIMS results show a temperature range in which the diffusion characteristics produced by the iRTP anneal result in equivalent dopant profiles, and that the junction abruptness and x_j are improved for the 48 keV pre-amorphization implant. It can be said that interstitial injection from the EOR damage is the most likely cause for the additional diffusion observed for iRTP anneal temperatures above this range. It was shown that the 1100°C iRTP anneal produces a profile with junction abruptness of 8.7 nm/dec for the 48 keV pre-amorphization implant, which is comparable to that produced by a conventional RTP anneal. This can be compared to the 760 and 900°C iRTP anneals, which produced profiles with junction abruptness of 3.2 and 5.5 nm/dec , respectively. The junction

abruptness of the 760 and 900 °C intermediate temperatures change to 3.4 and 4.4 nm/dec and 5.9 and 5.8 nm/dec after a 1200 and 1350 °C fRTP anneal, respectively. These results show that the UHT annealing technique is capable of producing junctions with the profile characteristics significantly improved over conventional RTP. The increased diffusion enhancement observed for the 5 keV pre-amorphization implant is presumed to be due to an increased interstitial flux into the substrate because the BIC's are obstructing interstitial backflow toward the surface. The TEM results show that the EOR defect structure produced by the 48 keV pre-amorphization implant is dependent on both the intermediate and fRTP anneal temperatures, and that no observable defects form for the 5 keV pre-amorphization implant. This latter result is consistent with BIC formation in that they cannot be directly observed by TEM because of their small size (e.g., 3 to 8 atom clusters). Although the defect structures that result after the 760, 800, and 900 °C iRTP anneals for the wafer that received the 48 keV pre-amorphization implant are similar in morphology, they result in significantly different defect structures after a 1350 °C fRTP anneal. These results show that the intermediate temperature plays a significant role not only in terms of the diffusion characteristics, but also the interstitial evolution as it relates to the final defect structure after a fRTP anneal. Four-point probe measurements show decreased R_s with the introduction of the fRTP anneal when compared to the corresponding iRTP anneal temperature, which is not reflected though the empirical mobility equation used to calculate the theoretical R_s for each processing condition; this needs to be understood further. This UHT annealing technique is capable of producing junctions with improved characteristics over those obtained through RTP

because of the ability of the iRTP anneal to maintain highly abrupt junctions, and the time duration of the fRTP anneal, which limits dopant diffusion.

In addition to understanding the effect of UHT annealing on the EOR defect evolution, dopant activation during UHT annealing is of significant interest. Recent attention has been given to low temperature SPER of an implantation-induced amorphous layer because of its ability to activate dopants well above their solid solubility levels while minimizing the amount of diffusion that occurs during the thermal process. The most significant disadvantage of this annealing technique is that a considerable amount of damage remains below the original α/c interface, which can give rise to a large amount of leakage current. It was shown previously that the UHT annealing technique is capable of evolving the implant damage to a point where it is presumed that the junction leakage will be improved over those obtained by SPER only, and that the dopant diffusion during the anneal was significantly reduced compared to what would be expected from a conventional RTP anneal. The focus of this experiment was to use a low temperature SPER anneal before UHT annealing in an attempt to obtain above solid solubility activation levels during the SPER process, and evolve the implant damage to acceptable levels by using the UHT annealing technique. Two 200 mm (100) n-type CZ grown Si wafers were pre-amorphized with 48 keV Ge^+ implantation to $5 \times 10^{14}/\text{cm}^2$, and subsequently implanted with 3 keV BF_2^+ molecular ions to $6 \times 10^{14}/\text{cm}^2$. One of the wafers was then subject to a 585 °C furnace anneal for 45 min to completely recrystallize the amorphous layer before UHT annealing. The wafers were sectioned and annealed under various conditions to investigate the effects of the UHT annealing technique on the resulting junction characteristics. The SIMS results show that the 585 °C furnace anneal

is sufficient to evolve the excess interstitials to a point where they can increase the B diffusion behavior during UHT annealing when compared to the wafer without the furnace anneal, and that this is only observed when the intermediate temperature is sufficiently low (i.e., 760 and 800 °C). These results suggest that an ultra-fast diffusion pulse occurs during the early stages of annealing, and is only observable when a low intermediate temperature is used, presumably thought to be because the ultra-fast diffusion pulse is complete when higher intermediate temperatures are used (e.g., 900 °C). Additional SIMS results show that this diffusion behavior increases with increasing pre-amorphization dose. This ultra-fast diffusion pulse is presumed to be due to a small fraction of excess interstitials that escape capture by the extended defects and diffuse toward the substrate surface. Since an increase in the B diffusion behavior occurred with increasing pre-amorphization dose, it can be said that more interstitials were able to escape capture by the extended defects and cause the observed increase in diffusion behavior. It is also possible that the ultra-fast pulse is itself controlled by submicroscopic defects that are less stable than {311} defects; however, these defects would need to form below the original α/c interface since the corresponding diffusion behavior increases with increasing pre-amorphization dose and the only difference between the three pre-amorphization implants is the interstitial population just beyond the original α/c interface. It should be noted that the amount of diffusion that occurs during the ultra-fast diffusion pulse is less than the values reported in the literature, presumably due to the fact that interstitial injection from the EOR damage is significantly greater into the bulk of the substrate when compared to that toward the surface. Although in some cases the TEM results show subtle differences in the EOR defect structure produced by

the 48 keV pre-amorphization implant when the wafer is subject to a 585 °C furnace anneal before UHT annealing, the defect morphology is relatively independent of this furnace anneal. Although it is well known that low temperature SPER of an implantation-induced amorphous layer activates dopants well above their solid solubility levels, the four-point probe results show that the 3 keV BF_2^+ implant to $6 \times 10^{14}/\text{cm}^2$ generally results in lower R_s values for the wafer without the 585 °C furnace anneal before UHT annealing. It can be said that the difference between the two sets of data is due to the corresponding plateau concentrations that form during the initial stages of annealing. For example, the 800 °C iRTP anneal (for the wafer without the 585 °C furnace anneal before UHT annealing) results in a profile with a plateau concentration of approximately $1.8 \times 10^{20}/\text{cm}^3$, whereas the 585 °C furnace anneal produces a plateau concentration of approximately $1.5 \times 10^{20}/\text{cm}^3$. In addition, performing an 800 °C iRTP anneal after the 585 °C furnace anneal has no effect on the plateau concentration, which remains approximately $1.5 \times 10^{20}/\text{cm}^3$. The improved activation for the 800 °C iRTP anneal for the wafer without the 585 °C furnace anneal before UHT annealing is presumably thought to be because higher activation levels can be achieved at higher recrystallization temperatures. It can be said that recrystallization occurred at approximately 585 °C during the furnace anneal. This can be compared to a temperature of 700 °C which is the approximate temperature at which the amorphous layer produced by the 48 keV pre-amorphization implant is presumed to have completely recrystallized. This idea explains why a noticeable improvement in R_s is not observed for the 800 °C iRTP anneal for the wafer with the 585 °C furnace anneal before UHT annealing; complete recrystallization of the implantation-induced amorphous layer already occurred

during the 585 °C furnace anneal. The concept that higher activation levels can be achieved at higher recrystallization temperatures was the focus of the final experiment.

It was shown previously that higher activation levels can be achieved by using this annealing technique directly after implantation as opposed to performing a low temperature SPER anneal before UHT annealing. This improved activation was presumably thought to be because higher activation levels can be achieved at higher recrystallization temperatures. In other words, higher activation levels can be achieved when recrystallization (and presumably activation) occurs during ramp-up of an UHT anneal (e.g., approximately 700 °C), as opposed to a low temperature (i.e., 585 °C) furnace anneal. To test this idea, an experiment was designed in an attempt to reduce the regrowth velocity of the α /c interface such that recrystallization of the implantation-induced amorphous layer would occur at even higher temperatures (e.g., 1000 °C). It is well known that F^+ implantation to a concentration of approximately $10^{18}/cm^3$ reduces the regrowth velocity of the α /c interface during SPER of an implantation-induced amorphous layer. Implanting F^+ to concentrations much greater than $10^{18}/cm^3$ may be sufficient to allow recrystallization to occur during the UHT anneal, thereby resulting in higher activation levels. Two 200 mm (100) n-type CZ grown Si wafers were pre-amorphized with 48 keV Ge^+ implantation to $5\times 10^{14}/cm^2$. One of the wafers was subject to a 12 keV F^+ implant to $1.5\times 10^{15}/cm^2$ and both wafers were then implanted with 3 keV BF_2^+ molecular ions to $6\times 10^{14}/cm^2$. The wafers were sectioned and annealed under various conditions to investigate the effects of the UHT annealing technique on the resulting junction characteristics. The SIMS results showed that the as-implanted junction abruptness and x_j for the wafer without the 12 keV F^+

implant to $1.5 \times 10^{15}/\text{cm}^2$ was approximately 3.3 nm/dec and 16.3 nm, respectively.

Additional SIMS results showed that the junction abruptness degraded to 11.9 nm/dec and the x_j increased to approximately 25.6 nm for the wafer with the additional F⁺ implant. It was shown through the literature that impurities such as H and F can passivate the trapping sites in α -Si by forming highly-favored bonding arrangements. When these trapping sites are occupied, interstitially diffusing species such as Pd and Cu are rejected from the passivated regions presumably due to there being no structural defects capable of preventing their motion. It is reasonable to put forward that the 12 keV F⁺ implant to $1.5 \times 10^{15}/\text{cm}^2$ is sufficient to passivate the α -Si trapping sites therefore allowing B, which is presumed to diffuse interstitially in α -Si, to diffuse into the substrate to a depth consistent with the distribution of available trapping sites. Additional experiments showed that the as-implanted F⁺ has no effect on the concentration of paramagnetic defects in α -Si as measured by electron paramagnetic resonance (EPR); therefore, the effect of the additional F implant on the observed low temperature diffusion behavior was attributed to F interactions with a fraction of the non-paramagnetic defects in the amorphous material which form highly-favored bonding arrangements and de-trap the B atoms from these defect sites. It is well known that the saturation defect density in α -Si at room temperature is approximately 0.5 at. % and that a majority of these defects are not paramagnetic,²²³ making EPR incapable of detecting these defects; therefore, it is reasonable to assume that the F is capable of interacting with a fraction of the non-paramagnetic defects which are responsible for trapping the B atoms. The preferential interaction between F and the non-paramagnetic traps or defect states in the amorphous layer would imply that the F is more strongly bonded to these

traps when compared to paramagnetic defects. It should be noted that the F concentration at the depth where B begins to form the exponentially decreasing profile is approximately $3 \times 10^{20}/\text{cm}^3$ (i.e., 0.6 at. %), which is remarkably close to the value reported by Stolk *et al.* for the saturation defect density in α -Si at room temperature (i.e., 0.5 at. %). Additional SIMS results showed that the amount of B diffusion that occurs during SPER of the implantation-induced amorphous layer increases for the wafer with the additional F^+ implant, presumably due to the F reducing the regrowth velocity of the α/c interface, allowing more time for B to diffuse in α -Si before complete recrystallization of the implantation-induced amorphous layer. Also, the SIMS results show that F^+ co-implantation is capable of preventing any additional diffusion during a 1350 °C UHT anneal when the intermediate temperature is sufficiently low (e.g., 800 °C). The TEM results show that the final EOR defect structure is dependent on both the intermediate and peak temperatures of the thermal process but relatively independent of the 12 keV F^+ implant to $1.5 \times 10^{15}/\text{cm}^2$. Additional TEM results show that the additional F^+ implant is sufficient to slow the regrowth velocity of the α/c interface such that approximately 22 nm of α -Si remains near the substrate surface after the 800 °C iRTP anneal. The SIMS results corresponding to the 760 and 800 °C intermediate temperatures show an increase in plateau concentration with increasing peak temperature during UHT annealing of the wafer with the 12 keV F^+ implant to $1.5 \times 10^{15}/\text{cm}^2$, presumably due to the higher solubility of dopants in α -Si when compared to c-Si and the thought that higher activation levels can be achieved at higher recrystallization temperatures. The values corresponding to the plateau concentrations of the SIMS data observed in this work when recrystallization of the implantation-induced amorphous layer occurs at relatively low

temperatures (e.g., 585 or 700 °C) are more than an order of magnitude greater than the solid solubility, C_s , in c-Si. The difference between the plateau concentrations observed through the SIMS data and C_s is less noticeable when recrystallization of an implantation-induced amorphous layer occurs at higher temperatures. When compared to the data from the literature, it can be seen that increase in plateau concentration has relatively low temperature dependence. Comparison between the C_s and the plateau concentrations observed through the SIMS data supports the idea that B solubility is higher in the amorphous phase. Four-point probe measurements show a decrease in R_s with the introduction of the UHT anneal when compared to the intermediate anneal, and that the R_s is generally lower for the wafer that received the additional F^+ implant before UHT annealing. The four-point probe measurements only show a slight improvement in R_s for the wafer with the 12 keV F^+ implant to $1.5 \times 10^{15}/\text{cm}^2$ presumably because of the formation of F precipitates or regrowth related defects associated with the high dose F^+ implant. It is believed that these defects cause a reduction in the carrier mobility, and that this reduction is enough to cancel any improvement in R_s due to the increase in active dose as a result of recrystallization during the fRTP anneal. The reduction in TED and increase in activation for the co-implanted wafer is presumably due to the F binding with excess Si interstitials so as to reduce point-defect mediated diffusion and the amount of inactive dopant associated with immobile B cluster formation. The improved activation is also due to F reducing the regrowth velocity of the α/c interface such that recrystallization occurs during the UHT anneal [when the intermediate temperature is sufficiently low (e.g., 800 °C)].

Although this dissertation gives an initial understanding on the activation and diffusion mechanisms that take place during UHT annealing, additional work is required to better understand some of the observations made from the empirical data. The following experiments would provide more complete knowledge of the physical mechanisms controlling the unexplained areas of this work:

Determine the effect of the fRTP anneal on the corresponding decrease in R_s :

It was shown throughout this work that, although moderate activation levels were obtained during an iRTP anneal, a significant improvement in the R_s could be achieved by using a relatively high temperature fRTP anneal. This was observed even when recrystallization of the implantation-induced amorphous layer was complete during ramp-up to the intermediate temperature, inconsistent with the possibility that improved activation occurred due to recrystallization at higher annealing temperatures. This improvement in activation could not be easily explained by an increase in the active (originally un-clustered) dose since the corresponding SIMS results showed no difference in the resulting plateau concentration. One possible explanation for the improvement in R_s is that a fraction of the originally clustered B atoms dissociate during the high temperature fRTP anneal, which improves activation without a significant amount of diffusion because of the relatively short cycle-time of the anneal. One experiment that could be performed to test this idea is to implant B to various doses into a pre-amorphized substrate. The implant conditions should cover the concentration range below B cluster formation and well above B solid solubility. Post-implant UHT annealing can be used to investigate the activation characteristics during both iRTP and fRTP annealing. The R_s values for the lower B concentrations should not vary

significantly between the two annealing techniques considering most of the B should be activated during recrystallization of the implantation-induced amorphous layer. These results can then be compared to those for the higher B concentration, which will presumably have a fraction of the B profile clustered during moderate temperature annealing. Studying the effect of f RTP annealing on the resulting activation characteristics can provide better understanding about the role of the B clusters on the observed decrease in R_s .

Understand the effect of post-UHT thermal processing on dopant activation and diffusion: Although it was shown that this UHT annealing technique is capable of producing junctions with above solid solubility activation levels and can significantly evolve the implant damage during a f RTP anneal, the effect of additional thermal processing on dopant activation and diffusion needs to be investigated. It is well known that above solid solubility activation levels deactivate to equilibrium levels during subsequent thermal processing and that defects in the space-charge region contribute to leakage current in bipolar transistors; therefore, understanding the effect of moderate thermal processing, such as during silicide formation, would be of considerable interest. One could use the implant conditions presented in this work and expand the annealing conditions to include post-UHT annealing. These results will provide insight into the activation levels and junction profiles that can be expected after complete front-end-of-line (FEOL) processing. The results of this work will have an impact on integration of this UHT annealing technique into a conventional process flow; in particular, if the deep S/D anneal is sufficient to reduce the activation levels obtained

during UHT annealing to equilibrium values, then one may have to develop a disposable spacer process so that the deep S/D anneal can be performed before the SDE anneal.

Optimize the UHT annealing conditions to minimize the resulting junction

leakage characteristics: Even though it was shown that this UHT annealing technique is capable of significantly evolving the implant damage during an fRTA anneal, damage remains. It is well known that defects in the space-charge region contribute to leakage current in bipolar transistors. It is of interest to quantify the amount of junction leakage expected to result from this UHT annealing technique and compare those values to ones obtained by more conventional methods, such as spike annealing. Once again, similar implant conditions to those used throughout this work can be used. Different diode patterns should be used to determine the individual contributions from areal and peripheral junction leakage.

Resolve the role of defects in α -Si on dopant activation and diffusion:

Although an attempt was made to better understand the effect of F⁺ co-implantation on the increase in low temperature B diffusion behavior, the results were unable to identify the exact source of such behavior. It was shown that F⁺ co-implantation had no effect on the concentration of paramagnetic defects as measured by EPR, consistent with the literature; therefore, the effect of the additional F implant on the observed low temperature diffusion behavior was attributed to F interactions with a fraction of the non-paramagnetic defects in the amorphous material which form highly-favored bonding arrangements and de-trap the B atoms from these defect sites. The preferential interaction between F and the non-paramagnetic traps or defect states in the amorphous layer would imply that the F is more strongly bonded to these traps when compared to

paramagnetic defects. Although this may be the reason for the observed increase in low temperature diffusion behavior, additional experiments need to be performed to better understand the role of these defects on both dopant activation and diffusion. It is well known that the structural defects in the amorphous phase affect both dopant activation and diffusion; in particular, it was shown that these defects increase impurity solubility and decrease impurity diffusion during post implant thermal processing. One experiment that can be performed to better understand the effect of structural defects on dopant activation and diffusion is to bring a pre-amorphized substrate to different degrees of structural relaxation by performing various low temperature (e.g., 200-500 °C) thermal anneals in a conventional tube furnace. This will reduce the amount of defects available to affect dopant activation and diffusion during SPER of the implantation-induced amorphous layer. If only one B implant condition is to be used then it should be done after the structural relaxation anneals to cancel any effect from the structural relaxation anneal on the dopant activation and diffusion (provided the B⁺ implant does not bring the amorphous layer back to a structurally de-relaxed state similar to the as-implanted case). The activation and diffusion observed after subsequent annealing can be used to determine the effect of the structural defects on dopant activation and diffusion.

APPENDIX A

CODE TO MODEL BORON DIFFUSION IN AMORPHOUS SILICON

```

math dim=1 umf
line x loc=-0.005 tag=top1 spac=0.0005
line x loc=0.0 tag=bot1 spac=0.0005
line x loc=0.4 tag=bot2 spac=0.010
line x loc=1 tag=bot3 spac=0.1
line x loc=100 tag=bot4 spac=10
region oxide xlo=top1 xhi=bot1
region silicon xlo=bot1 xhi=bot4
init
profile name=asimp inf=Data/NewAI.prn
profile name=Boron inf=Data/NewAI.prn
profile name=annealend inf=Data/550_13.prn
#pdbSetSwitch Silicon Boron DiffModel Constant
# This will set the "clustering" threshold
# was 7.68e22, .7086
#pdbSetDouble Silicon Boron Solubility {[Arrhenius 7.68e22 0.7086]}
pdbSetDouble Silicon Boron Solubility {[Arrhenius 5e24 0.7086]}
pdbSetDouble Silicon Boron D0 {[Arrhenius 7.5e-6 -1.36] * ([pdbGetDouble Si B I D0]
+ [pdbGetDouble Si B V D0])}
pdbSetDouble Silicon Boron Dp {[Arrhenius 7.5e-6 -1.36] * ([pdbGetDouble Si B I Dp]
+ [pdbGetDouble Si B V Dp])}
#temp_ramp name=test rate=400 time=1.9/60 temp=25 last
#temp_ramp name=test rate=0.0 time=.001 temp=$FinalTempC last
#sel z=1e6 name=Int store
#sel z=1e6 name=Vac store
sel z=log10(asimp)
plot.1d !cle label=As-imp max=0.1
sel z=log10(annealend)
plot.1d !cle label=Furnace-Anneal max=0.1
sel z=log10(Boron)
plot.1d !cle label=Boron-imp max=0.1
diffuse temp=550 time=13 init=1.0e-12 !adapt movie=
sel z=log10(asimp)
plot.1d cle label=As-imp max=0.1
sel z=log10(annealend)
plot.1d !cle label=Furnace-Anneal max=0.1
sel z=log10(Boron)
plot.1d !cle label=Simulation max=0.1
}

```

APPENDIX B
PARAMAGNETIC RESONANCE MEASUREMENT SETTINGS

60 keV Ge⁺ pre-amorphization implant to 1×10¹⁵/cm²

#DESC 1.2 * DESCRIPTOR INFORMATION *****

*

* Dataset Type and Format:

*

DSRC EXP

BSEQ BIG

IKKF REAL

XTYP IDX

YTYP NODATA

ZTYP NODATA

*

* Item Formats:

*

IRFMT D

*

* Data Ranges and Resolutions:

*

XPTS 2048

XMIN 3226.000000

XWID 200.000000

*

* Documentational Text:

*

TITL 'OxDC'

IRNAM 'Intensity'

XNAM 'Field'

IRUNI "

XUNI 'G'

*

*

#SPL 1.2 * STANDARD PARAMETER LAYER

*

OPER alex

DATE 02/05/04

TIME 13:17:06

CMNT

SAMP

SFOR
 STAG C
 EXPT CW
 OXS1 IADC
 AXS1 B0VL
 AXS2 NONE
 AXS3
 A1CT 0.3326
 A1SW 0.02
 MWFQ 9.34294e+09
 MWPW 0.000316514
 AVGS 4
 SPTP 0.02048
 RCAG 53
 RCHM 1
 B0MA 5e-05
 B0MF 100000
 RCPH 0.0
 RCOF 0.0
 A1RS 2048
 RCTC 0.00512
 *

 *
 #DSL 1.0 * DEVICE SPECIFIC LAYER
 *

.DVC acqStart, 1.0

.DVC fieldCtrl, 1.0

CenterField 3326.00 G
 Delay 0.0 s
 FieldFlyback On
 FieldWait Wait LED off
 SweepDirection Up
 SweepWidth 200.0 G

.DVC fieldSweep, 1.0

.DVC freqCounter, 1.0

FrequencyMon 9.342937 GHz

.DVC mwBridge, 1.0

AcqFineTuning	Never
Power	0.3165 mW
PowerAtten	28.0 dB

.DVC recorder, 1.0

BaselineCorr	Off
NbScansAcc	4
NbScansDone	4
NbScansToDo	4
ReplaceMode	Off

.DVC scanEnd, 1.0

.DVC signalChannel, 1.0

AFCTrap	True
Calibrated	True
ConvTime	20.48 ms
DModAFCTrap	True
DModAmp	1.00 G
DModCalibrated	True
DModDetectSCT	First
DModEliDelay	1.0
DModExtLockIn	False
DModExtTrigger	False
DModFieldMod	First
DModGain	60 dB
DModHighPass	True
DModModOutput	Internal
DModSignalInput	Internal
DModTimeConst	1.28 ms
DoubleModFreq	5.00 kHz
DoubleModPhase	0.0
DoubleMode	False
EliDelay	1.0
ExtLockIn	False
ExtTrigger	False
Gain	53 dB
Harmonic	1
HighPass	True
ModAmp	0.50 G
ModFreq	100.00 kHz

ModInput	Internal
ModOutput	Internal
ModPhase	0.0
Offset	0.0 %
QuadMode	False
QuadPhase	90.0
Resolution	2048
Resonator	1
SignalInput	Internal
SweepTime	41.94 s
TimeConst	5.12 ms
TuneCaps	23

*

**60 keV Ge⁺ pre-amorphization implant to $1 \times 10^{15}/\text{cm}^2$ with a 12 keV F⁺ implant to
 $1.5 \times 10^{15}/\text{cm}^2$**

#DESC 1.2 * DESCRIPTOR INFORMATION *****

*

* Dataset Type and Format:

*

DSRC EXP

BSEQ BIG

IKKF REAL

Xtyp IDX

Ytyp NODATA

Ztyp NODATA

*

* Item Formats:

*

IRFMT D

*

* Data Ranges and Resolutions:

*

XPTS 2048

XMIN 3226.000000

XWID 200.000000

*

* Documentational Text:

*

TITL 'OxDC'

IRNAM 'Intensity'

XNAM 'Field'

IRUNI "

XUNI 'G'

*

```
*****
*
#SPL 1.2 * STANDARD PARAMETER LAYER
*
OPER alex
DATE 02/05/04
TIME 13:41:17
CMNT
SAMP
SFOR
STAG C
EXPT CW
OXS1 IADC
AXS1 B0VL
AXS2 NONE
AXS3
A1CT 0.3326
A1SW 0.02
MWFQ 9.34312e+09
MWPW 0.000316514
AVGS 4
SPTP 0.02048
RCAG 53
RCHM 1
B0MA 5e-05
B0MF 100000
RCPH 0.0
RCOF 0.0
A1RS 2048
RCTC 0.00512
*
*****
*
#DSL 1.0 * DEVICE SPECIFIC LAYER
*
.DVC acqStart, 1.0

.DVC fieldCtrl, 1.0

CenterField    3326.00 G
Delay         0.0 s
FieldFlyback   On
FieldWait      Wait LED off
SweepDirection Up
```

SweepWidth 200.0 G

.DVC fieldSweep, 1.0

.DVC freqCounter, 1.0

FrequencyMon 9.343122 GHz

.DVC mwBridge, 1.0

AcqFineTuning Never
 Power 0.3165 mW
 PowerAtten 28.0 dB

.DVC recorder, 1.0

BaselineCorr Off
 NbScansAcc 4
 NbScansDone 4
 NbScansToDo 4
 ReplaceMode Off

.DVC scanEnd, 1.0

.DVC signalChannel, 1.0

AFCTrap True
 Calibrated True
 ConvTime 20.48 ms
 DModAFCTrap True
 DModAmp 1.00 G
 DModCalibrated True
 DModDetectSCT First
 DModEliDelay 1.0
 DModExtLockIn False
 DModExtTrigger False
 DModFieldMod First
 DModGain 60 dB
 DModHighPass True
 DModModOutput Internal
 DModSignalInput Internal
 DModTimeConst 1.28 ms
 DoubleModFreq 5.00 kHz
 DoubleModPhase 0.0

DoubleMode	False
EliDelay	1.0
ExtLockIn	False
ExtTrigger	False
Gain	53 dB
Harmonic	1
HighPass	True
ModAmp	0.50 G
ModFreq	100.00 kHz
ModInput	Internal
ModOutput	Internal
ModPhase	0.0
Offset	0.0 %
QuadMode	False
QuadPhase	90.0
Resolution	2048
Resonator	1
SignalInput	Internal
SweepTime	41.94 s
TimeConst	5.12 ms
TuneCaps	23

*

**60 keV Ge⁺ pre-amorphization implant to $1 \times 10^{15}/\text{cm}^2$ with a 12 keV F⁺ implant to
 $3.0 \times 10^{15}/\text{cm}^2$**

#DESC 1.2 * DESCRIPTOR INFORMATION *****

*

* Dataset Type and Format:

*

DSRC EXP

BSEQ BIG

IKKF REAL

XTYP IDX

YTYP NODATA

ZTYP NODATA

*

* Item Formats:

*

IRFMT D

*

* Data Ranges and Resolutions:

*

XPTS 2048

XMIN 3226.000000

XWID 200.000000

```
*  
*      Documentational Text:  
*  
TITL 'OxDC'  
IRNAM      'Intensity'  
XNAM       'Field'  
IRUNI "  
XUNI 'G'  
*  
*****  
*  
#SPL 1.2 * STANDARD PARAMETER LAYER  
*  
OPER alex  
DATE 02/05/04  
TIME 13:28:44  
CMNT  
SAMP  
SFOR  
STAG C  
EXPT CW  
OXS1 IADC  
AXS1 B0VL  
AXS2 NONE  
AXS3  
A1CT 0.3326  
A1SW 0.02  
MWFQ 9.34322e+09  
MWPW 0.000316514  
AVGS 4  
SPTP 0.02048  
RCAG 53  
RCHM 1  
B0MA 5e-05  
B0MF 100000  
RCPH 0.0  
RCOF 0.0  
A1RS 2048  
RCTC 0.00512  
*  
*****  
*  
#DSL 1.0 * DEVICE SPECIFIC LAYER  
*  
.DVC acqStart, 1.0
```

.DVC fieldCtrl, 1.0

CenterField 3326.00 G
Delay 0.0 s
FieldFlyback On
FieldWait Wait LED off
SweepDirection Up
SweepWidth 200.0 G

.DVC fieldSweep, 1.0

.DVC freqCounter, 1.0

FrequencyMon 9.343220 GHz

.DVC mwBridge, 1.0

AcqFineTuning Never
Power 0.3165 mW
PowerAtten 28.0 dB

.DVC recorder, 1.0

BaselineCorr Off
NbScansAcc 4
NbScansDone 4
NbScansToDo 4
ReplaceMode Off

.DVC scanEnd, 1.0

.DVC signalChannel, 1.0

AFCTrap True
Calibrated True
ConvTime 20.48 ms
DModAFCTrap True
DModAmp 1.00 G
DModCalibrated True
DModDetectSCT First
DModEliDelay 1.0
DModExtLockIn False

DModExtTrigger False
 DModFieldMod First
 DModGain 60 dB
 DModHighPass True
 DModModOutput Internal
 DModSignalInput Internal
 DModTimeConst 1.28 ms
 DoubleModFreq 5.00 kHz
 DoubleModPhase 0.0
 DoubleMode False
 EliDelay 1.0
 ExtLockIn False
 ExtTrigger False
 Gain 53 dB
 Harmonic 1
 HighPass True
 ModAmp 0.50 G
 ModFreq 100.00 kHz
 ModInput Internal
 ModOutput Internal
 ModPhase 0.0
 Offset 0.0 %
 QuadMode False
 QuadPhase 90.0
 Resolution 2048
 Resonator 1
 SignalInput Internal
 SweepTime 41.94 s
 TimeConst 5.12 ms
 TuneCaps 23

*

**60 keV Ge⁺ pre-amorphization implant to 1×10¹⁵/cm² with a subsequent 500 °C
furnace anneal for 60 min**

#DESC 1.2 * DESCRIPTOR INFORMATION *****

*

* Dataset Type and Format:

*

DSRC EXP
 BSEQ BIG
 IKKF REAL
 XTYP IDX
 YTYP NODATA
 ZTYP NODATA
 *

* Item Formats:
*
IRFMT D
*
* Data Ranges and Resolutions:
*
XPTS 2048
XMIN 3226.000000
XWID 200.000000
*
* Documentational Text:
*
TITL 'OxDC'
IRNAM 'Intensity'
XNAM 'Field'
IRUNI "
XUNI 'G'
*

*
#SPL 1.2 * STANDARD PARAMETER LAYER
*
OPER alex
DATE 02/05/04
TIME 14:07:23
CMNT
SAMP
SFOR
STAG C
EXPT CW
OXS1 IADC
AXS1 B0VL
AXS2 NONE
AXS3
A1CT 0.3326
A1SW 0.02
MWFQ 9.34517e+09
MWPW 0.000316514
AVGS 4
SPTP 0.02048
RCAG 53
RCHM 1
B0MA 5e-05
B0MF 100000
RCPH 0.0
RCOF 0.0

A1RS 2048
RCTC 0.00512
*

*
#DSL 1.0 * DEVICE SPECIFIC LAYER
*

.DVC acqStart, 1.0

.DVC fieldCtrl, 1.0

CenterField 3326.00 G
Delay 0.0 s
FieldFlyback On
FieldWait Wait LED off
SweepDirection Up
SweepWidth 200.0 G

.DVC fieldSweep, 1.0

.DVC freqCounter, 1.0

FrequencyMon 9.345169 GHz

.DVC mwBridge, 1.0

AcqFineTuning Never
Power 0.3165 mW
PowerAtten 28.0 dB

.DVC recorder, 1.0

BaselineCorr Off
NbScansAcc 4
NbScansDone 4
NbScansToDo 4
ReplaceMode Off

.DVC scanEnd, 1.0

.DVC signalChannel, 1.0

AFCTrap	True
Calibrated	True
ConvTime	20.48 ms
DModAFCTrap	True
DModAmp	1.00 G
DModCalibrated	True
DModDetectSCT	First
DModEliDelay	1.0
DModExtLockIn	False
DModExtTrigger	False
DModFieldMod	First
DModGain	60 dB
DModHighPass	True
DModModOutput	Internal
DModSignalInput	Internal
DModTimeConst	1.28 ms
DoubleModFreq	5.00 kHz
DoubleModPhase	0.0
DoubleMode	False
EliDelay	1.0
ExtLockIn	False
ExtTrigger	False
Gain	53 dB
Harmonic	1
HighPass	True
ModAmp	0.50 G
ModFreq	100.00 kHz
ModInput	Internal
ModOutput	Internal
ModPhase	0.0
Offset	0.0 %
QuadMode	False
QuadPhase	90.0
Resolution	2048
Resonator	1
SignalInput	Internal
SweepTime	41.94 s
TimeConst	5.12 ms
TuneCaps	23

*

**60 keV Ge⁺ pre-amorphization implant to $1 \times 10^{15}/\text{cm}^2$ with a 12 keV F⁺ implant to
 $1.5 \times 10^{15}/\text{cm}^2$ and a subsequent 500 °C furnace anneal for 60 min**

#DESC 1.2 * DESCRIPTOR INFORMATION *****

*

* Dataset Type and Format:
*
DSRC EXP
BSEQ BIG
IKKF REAL
XTYP IDX
YTYP NODATA
ZTYP NODATA
*
* Item Formats:
*
IRFMT D
*
* Data Ranges and Resolutions:
*
XPTS 2048
XMIN 3223.000000
XWID 200.000000
*
* Documentational Text:
*
TITL '4555'
IRNAM 'Intensity'
XNAM 'Field'
IRUNI "
XUNI 'G'
*

*
#SPL 1.2 * STANDARD PARAMETER LAYER
*
OPER alex
DATE 02/05/04
TIME 14:58:47
CMNT
SAMP
SFOR
STAG C
EXPT CW
OXS1 IADC
AXS1 B0VL
AXS2 NONE
AXS3
A1CT 0.3323
A1SW 0.02
MWFQ 9.34128e+09

MWPW 3.16514e-05
 AVGS 4
 SPTP 0.02048
 RCAG 53
 RCHM 1
 B0MA 5e-05
 B0MF 100000
 RCPH 0.0
 RCOF 0.0
 A1RS 2048
 RCTC 0.00512
 *

 *
 #DSL 1.0 * DEVICE SPECIFIC LAYER
 *

.DVC acqStart, 1.0

.DVC fieldCtrl, 1.0
 CenterField 3323.00 G
 Delay 0.0 s
 FieldFlyback On
 FieldWait Wait LED off
 SweepDirection Up
 SweepWidth 200.0 G

.DVC fieldSweep, 1.0

.DVC freqCounter, 1.0

FrequencyMon 9.341284 GHz

.DVC mwBridge, 1.0

AcqFineTuning Never
 Power 0.03165 mW
 PowerAtten 38.0 dB

.DVC recorder, 1.0

BaselineCorr Off
 NbScansAcc 4

NbScansDone	4
NbScansToDo	4
ReplaceMode	Off

.DVC scanEnd, 1.0

.DVC signalChannel, 1.0

AFCTrap	True
Calibrated	True
ConvTime	20.48 ms
DModAFCTrap	True
DModAmp	1.00 G
DModCalibrated	True
DModDetectSCT	First
DModEliDelay	1.0
DModExtLockIn	False
DModExtTrigger	False
DModFieldMod	First
DModGain	60 dB
DModHighPass	True
DModModOutput	Internal
DModSignalInput	Internal
DModTimeConst	1.28 ms
DoubleModFreq	5.00 kHz
DoubleModPhase	0.0
DoubleMode	False
EliDelay	1.0
ExtLockIn	False
ExtTrigger	False
Gain	53 dB
Harmonic	1
HighPass	True
ModAmp	0.50 G
ModFreq	100.00 kHz
ModInput	Internal
ModOutput	Internal
ModPhase	0.0
Offset	0.0 %
QuadMode	False
QuadPhase	90.0
Resolution	2048
Resonator	1
SignalInput	Internal
SweepTime	41.94 s

TimeConst 5.12 ms
 TuneCaps 23

*

60 keV Ge⁺ pre-amorphization implant to $1 \times 10^{15}/\text{cm}^2$ with a 12 keV F⁺ implant to $3.0 \times 10^{15}/\text{cm}^2$ and a subsequent 500 °C furnace anneal for 60 min

#DESC 1.2 * DESCRIPTOR INFORMATION *****

*

* Dataset Type and Format:

*

DSRC EXP

BSEQ BIG

IKKF REAL

XTyp IDX

YTyp NODATA

ZTyp NODATA

*

* Item Formats:

*

IRFMT D

*

* Data Ranges and Resolutions:

*

XPTS 2048

XMIN 3223.000000

XWID 200.000000

*

* Documentational Text:

*

TITL '4555'

IRNAM 'Intensity'

XNAM 'Field'

IRUNI "

XUNI 'G'

*

*

#SPL 1.2 * STANDARD PARAMETER LAYER

*

OPER alex

DATE 02/05/04

TIME 14:45:54

CMNT

SAMP

SFOR

```

STAG C
EXPT CW
OXS1 IADC
AXS1 B0VL
AXS2 NONE
AXS3
A1CT 0.3323
A1SW 0.02
MWFQ 9.34178e+09
MWPW 3.16514e-05
AVGS 4
SPTP 0.02048
RCAG 53
RCHM 1
B0MA 5e-05
B0MF 100000
RCPH 0.0
RCOF 0.0
A1RS 2048
RCTC 0.00512
*
*****
*
#DSL 1.0 * DEVICE SPECIFIC LAYER
*

.DVC acqStart, 1.0

.DVC fieldCtrl, 1.0

CenterField    3323.00 G
Delay         0.0 s
FieldFlyback   On
FieldWait      Wait LED off
SweepDirection Up
SweepWidth    200.0 G

.DVC fieldSweep, 1.0

.DVC freqCounter, 1.0

FrequencyMon   9.341777 GHz

.DVC mwBridge, 1.0

```

AcqFineTuning Never
 Power 0.03165 mW
 PowerAtten 38.0 dB

.DVC recorder, 1.0

BaselineCorr Off
 NbScansAcc 4
 NbScansDone 4
 NbScansToDo 4
 ReplaceMode Off

.DVC scanEnd, 1.0

.DVC signalChannel, 1.0

AFCTrap True
 Calibrated True
 ConvTime 20.48 ms
 DModAFCTrap True
 DModAmp 1.00 G
 DModCalibrated True
 DModDetectSCT First
 DModEliDelay 1.0
 DModExtLockIn False
 DModExtTrigger False
 DModFieldMod First
 DModGain 60 dB
 DModHighPass True
 DModModOutput Internal
 DModSignalInput Internal
 DModTimeConst 1.28 ms
 DoubleModFreq 5.00 kHz
 DoubleModPhase 0.0
 DoubleMode False
 EliDelay 1.0
 ExtLockIn False
 ExtTrigger False
 Gain 53 dB
 Harmonic 1
 HighPass True
 ModAmp 0.50 G
 ModFreq 100.00 kHz
 ModInput Internal

ModOutput	Internal
ModPhase	0.0
Offset	0.0 %
QuadMode	False
QuadPhase	90.0
Resolution	2048
Resonator	1
SignalInput	Internal
SweepTime	41.94 s
TimeConst	5.12 ms
TuneCaps	23

*

LIST OF REFERENCES

1. G. E. Moore, Electronics **38**, 114 (1965).
2. J. D. Plummer, M. D. Deal, and P. Griffin, *Silicon VLSI Technology – Fundamentals, Practice and Modeling* (Prentice Hall, Upper Saddle River, New Jersey, 2000).
3. Edited by J. F. Ziegler, *Ion Implantation Science and Technology* (Ion Implantation Technology Co., Edgewater, MD, 2000).
4. K. Cho, M. Numan, T. G. Finstad, W. K. Chu, J. Liu, and J. J. Wortman, Appl. Phys. Lett. **47**, 1321 (1985).
5. A. E. Michel, W. Rausch, P. A. Ronsheim, and R. H. Kastl, Appl. Phys. Lett. **50**, 416 (1987).
6. P. M. Fahey, P. B. Griffin, and J. D. Plummer, Rev. Mod. Phys. **61**, 289 (1989).
7. P. A. Stolk, H.-J. Gossmann, D. J. Eaglesham, and J. M. Poate, Nucl. Instr. and Meth. Phys. Res. B **96**, 187 (1995).
8. J. Narayan, O. W. Holland, R. E. Eby, J. J. Wortman, V. Ozguz, and G. A. Rozgonyi, Appl. Phys. Lett. **43**, 957 (1983).
9. S. C. Jain, W. Schoenmaker, R. Lindsay, P. A. Stolk, S. Decoutere, M. Willander, and H. E. Maes, J. Appl. Phys. **91**, 8919 (2002).
10. L. S. Robertson, P. N. Warnes, K. S. Jones, S. K. Earles, M. E. Law, D. F. Downey, S. Falk, and J. Liu, Mat. Res. Soc. Symp. Proc. Vol. 610, B4.2 (2001).
11. P. Ashburn, C. Bull, K. H. Nicholas, and G. R. Booker, Sol.-State Electr. **20**, 731 (1977).
12. C. Bull, P. Ashburn, G. R. Booker, and K. H. Nicholas, Sol.-State Electr. **22**, 95 (1979).
13. Semiconductor Industry Association, *International Technology Roadmap for Semiconductors* (International SEMATECH, Austin, TX, 2001).
14. F. Trumbore, Bell Sys. Tec. J. **39**, 206 (1960).

15. B. El-Kareh, *Fundamentals of Semiconductor Processing Technologies* (Kluwer Academic Publishers, 1995).
16. T. M. Buck, K. A. Pickar, J. M. Poate, and C. M. Hsieh, *Appl. Phys. Lett.* **21**, 485 (1972).
17. D. J. Eaglesham, P. A. Stolk, H.-J. Gossman, and J. M. Poate, *Appl. Phys. Lett.* **65**, 2305 (1994).
18. P. A. Stolk, H.-J. Gossman, D. J. Eaglesham, D. C. Jacobson, C. S. Rafferty, G. H. Gilmer, M. Jaraiz, J. M. Poate, H. S. Luftman, and T. E. Hayes, *J. Appl. Phys.* **81**, 6031 (1997).
19. N. Cowern and C. Rafferty, *MRS Bull.* **25**, 39 (2000).
20. M. D. Giles, *Appl. Phys. Lett.* **62**, 2395 (1996).
21. M. D. Giles, *J. Electrochem. Soc.* **138**, 1160 (1991).
22. H.-J. Gossman, T. E. Haynes, P. A. Stolk, D. C. Jacobson, G. H. Gilmer, J. M. Poate, H. S. Luftman, T. K. Mogi, and M. O. Thompson, *Appl. Phys. Lett.* **71**, 3862 (1997).
23. C. L. Claeys, G. J. Declerck, and R. J. Van-Overstraeten, *Rev. Phys. Appl.* **13**, 797 (1978); *Tenth Topical Conference on Characterization Techniques for Semiconductor Materials and Devices* (The Electrochemical Society, Pennington, NJ, 1978), p. 366.
24. U. Gosele, and W. Frank, *Defects in Semiconductors*, Proceedings of the Materials Research Society Annual Meeting (North-Holland, Amsterdam, Netherlands, 1981), p 55.
25. U. Gosele and H. Strunk, *Appl. Phys.* **20**, 265 (1979).
26. Y. M. Haddara, B. T. Folmer, M. E. Law, and T. Buyuklimanli, *Appl. Phys. Lett.* **77**, 1976 (2000).
27. H.-J. Gossman, *Semiconductor Silicon*, edited by H. R. Huff, U. Goselle, and H. Tsuya, *Elect. Chem. Soc. Proc.* Vol. **98**, 884 (1998).
28. A. Agarwal, H.-J. Gossman, and A. T. Fiory, *J. Elec. Mat.* **28**, 1333 (1999).
29. A. Agarwal, A. T. Fiory, H.-J. Gossman, C. S. Rafferty, P. Frisella, and J. Hebb, *Mat. Sci. in Semi. Proc.* **1**, 237 (1999).
30. A. Agarwal, H.-J. Gossman, and A. T. Fiory, *Mat. Res. Soc. Symp. Proc.* **568**, 19 (1999).
31. A. T. Fiory and K. K. Bourdelle, *Appl. Phys. Lett.* **74**, 2658 (1999).

32. G. Mannino, P. A. Stolk, N. E. B. Cowern, W. B. de Boer, A. G. Dirks, F. Roozeboom, J. G. M. van Berkum, P. H. Woerlee, and N. N. Toan, *Appl. Phys. Lett.* **78**, 889 (2001).
33. D. M. Camm and B. Lojek, Proc. 2nd Int. Conf. Advanced Thermal Processing of Semiconductors (RTP 94), Round Rock, TX, 259, (1994).
34. A. T. Fiory, D. M. Camm, M. E. Lefrancois, S. McCoy, and A. Agarwal, Proc. 7th Int. Conf. Advanced Thermal Processing of Semiconductors (RTP 99), Colorado Springs, CO, 273 (1999).
35. R. S. Tichy, K. Elliott, S. McCoy, and D. C. Sing, Proc. 9th Int. Conf. Advanced Thermal Processing of Semiconductors (RTP 01), New Orleans, LA, 87 (2001).
36. R. T. Hodgson, V. R. Deline, S. Mader, and J. C. Gelpey, *Appl. Phys. Lett.* **44**, 589 (1984).
37. S. Coffa, J. M. Poate, D. C. Jacobson, W. Frank, and W. Gustin, *Phys. Rev. B* **45**, 8355 (1992).
38. J. W. Mayer and S. S. Lau, *Electronic Materials Science: For Integrated Circuits in Si and GaAs* (Macmillan, New York, 1990).
39. W. D. Callister, Jr., *Materials Science and Engineering an Introduction* (John Wiley & Sons, Toronto, Canada, 1997).
40. F. F. Morehead and B. L. Crowder, *Radiat. Eff.* **6**, 27 (1970).
41. E. A. Kuryliw, Ph.D. Dissertation, University of Florida, Gainesville, FL (2003).
42. T. Y. Tan and U. Gösele, *Appl. Phys. A* **37**, 1 (1985).
43. N. A. Stolwijk, J. Hözl, W. Frank, E. R. Weber, and H. Mehrer, *Appl. Phys. A* **39**, 37 (1986).
44. H. Bracht, N. A. Stolwijk, and H. Mehrer, *Phys. Rev. B* **52**, 542 (1995).
45. P. H. Keys, Ph.D. Dissertation, University of Florida, Gainesville, FL (2001).
46. L. A. Christel, J. F. Gibbons, and T. W. Sigmon, *J. Appl. Phys.* **52**, 7143 (1981).
47. M. Thompson, G. Galvin, J. Mayer, P. Peercy, J. Poate, D. Jacobson, A. Cullis, and N. Chew, *Phys. Rev. Lett.* **52**, 2360 (1984).
48. J. Poate, *Journal of Crystal Growth* **79**, 549 (1986).
49. J. S. Custer, M. O. Thompson, D. C. Jacobson, J. M. Poate, S. Roorda, W. C. Sinke, and F. Spaepen, *Appl. Phys. Lett.* **64**, 437 (1994).

50. D. E. Polk and D. S. Boudreaux, Phys. Rev. Lett. **31**, 92 (1973).
51. F. Wooten, K. Winer, and D. Weaire, Phys. Rev. Lett. **54**, 1392 (1985).
52. F. Wooten and D. Weaire, in *Solid State Physics: Advances in Research Applications*, edited by D. Turnbull and H. Ehrenreich (Academic, New York, 1987), **40**, 2.
53. R. Car and M. Parrinello, Phys. Rev. Lett. **60**, 204 (1988).
54. T. Uda, Solid State Commun. **64**, 837 (1987).
55. R. Biswas, G. S. Crest, and C. M. Soukoulis, Phys. Rev. B **36**, 7473 (1987).
56. S. Roorda, S. Doorn, W. C. Sinke, P. M. L. O. Scholte, and E. van Loenen, Phys. Rev. Lett. **62**, 1880 (1989).
57. E. P. Donovan, F. Spaepen, J. M. Poate, and D. C. Jacobson, Appl. Phys. Lett. **55**, 1516 (1989).
58. W. Sinke, T. Warabisako, M. Miyao, T. Tokuyama, S. Roorda, and F. W. Saris, J. Non-Cryst. Solids **99**, 308 (1988).
59. S. Roorda, W. C. Sinke, J. M. Poate, D. C. Jacobson, P. Fuoss, S. Dierker, B. S. Dennis, and F. Spaepen, Mat. Res. Soc. Symp. Proc. **157**, 683 (1990).
60. R. Tsu, J. Gonzalez-Hernandez, and F. H. Pollak, Solid State Commun. **54**, 447 (1985).
61. J. E. Fredrickson, C. N. Waddell, W. G. Spitzer, and G. K. Hubler, Appl. Phys. Lett. **40**, 172 (1982).
62. S. Roorda, W. C. Sinke, J. M. Poate, D. C. Jacobson, S. Dierker, B. S. Dennis, D. J. Eaglesham, and F. Spaepen, Mat. Res. Soc. Symp. Proc. **157**, 709 (1990).
63. L. S. Robertson, Ph.D. Dissertation, University of Florida, Gainesville, FL (2001).
64. A. Claverie, B. Colombeau, G. B. Assayag, C. Bonafos, F. Cristiano, M. Omri, and B. de Mauduit, Mat. Res. Soc. Semi. Proc. **3**, 269 (2000).
65. J. W. Corbett, J. P. Karins, and T. Y. Tan, Nucl. Instr. and Meth. B **182-183**, 457 (1981).
66. N. E. B. Cowern, G. Mannino, P. A. Stolk, F. Roozeboom, H. G. A. Huizing, J. G. M. van Berkum, F. Cristiano, A. Claverie, and M. Jaraiz, Phys. Rev. Lett. **82**, 4460 (1999).
67. T. Y. Tan, Phil. Mag. A **44**, 101 (1981).

68. S. Takeda, M. Kohyama, and K. Ibe, Phil. Mag. A **70**, 287 (1994).
69. J. Kim, J. W. Wilkins, F. S. Khan, and A. Canning, Phys. Rev. B **55**, 16186 (1997).
70. A. Bourret, Inst. of Physics Conf. Series **87**, 39 (1987).
71. S. Takeda, Jpn. J. Appl. Phys. **30**, L639 (1991).
72. S. Takeda and M. J. Kohyama, Inst. Phys. Conf. Ser. **N134**, 33 (1993).
73. C. S. Rafferty, G. H. Gilmer, M. Jaraiz, D. Eaglesham, and H.-J. Gossman, Appl. Phys. Lett. **68**, 2395 (1996).
74. M. Seibt, J. Imschweiler, and H. A. Hefner, Mat. Res. Soc. Symp. Proc. **316**, 167 (1994).
75. M. Seibt, Mat. Res. Soc. Symp. Proc. **429**, 109 (1996).
76. S. Bharatan, J. Desrouches, and K. S. Jones, *Materials and Process Characterization of Ion Implantation* (Ion Beam Press, Austin, TX, 1997).
77. D. J. Eaglesham, P. A. Stolk, H.-J. Gossman, T. E. Haynes, and J. M. Poate, Nucl. Instr. and Meth. in Phys. Res. B **106**, 191 (1995).
78. J. Liu, V. Krishnamoorthy, H.-J. Gossman, L. Rubin, M. E. Law, and K. S. Jones, J. Appl. Phys. **81**, 1656 (1997).
79. R. J. Schreutelkamp, J. S. Custer, J. R. Liefing, W. X. Lu, and F. W. Saris, Mat. Sci. Reports **6**, 275 (1991).
80. L. Laânab, C. Bergaud, C. Bonafos, A. Martinez, and A. Claverie, Nucl. Inst. Meth. B **96**, 236 (1995).
81. N.-H. Cho, K.-W. Jang, J.-Y. Lee, and J.-S. Ro, Mat. Res. Soc. Symp. Proc. **396**, 781 (1996).
82. J.-H. Li and K. S. Jones, Appl. Phys. Lett. **73**, 3748 (1998).
83. C. Bonafos, D. Mathiot, and A. Claverie, J. Appl. Phys. **83**, 3008 (1998).
84. K. S. Jones, L. H. Zhang, V. Krishnamoorthy, M. Law, D. S. Simons, P. Chi, L. Rubin, and R. G. Elliman, Appl. Phys. Lett. **68**, 2672 (1996).
85. M. Seibt, J. Imschweiler, and H. A. Hefner, Mat. Res. Soc. Symp. Proc. **262**, 1103 (1992).
86. M. Seibt, Solid State Phenom **32-33**, 463 (1993).
87. G. Z. Pan, K. N. Tu, and A. Prussin, J. Appl. Phys. **81**, 78 (1997).

88. A. E. Michel, Nucl. Inst. and Meth. in Phys. Res. B **37/38**, 379 (1989).
89. E. Landi and S. Solmi, Sol. State Electr. **29**, 1181 (1986).
90. M. Omri, L. F. Giles, and A. Claverie, Mat. Res. Soc. Symp. Proc. **568**, 219 (1999).
91. L. F. Giles, M. Omri, B. de Mauduit, A. Claverie, D. Skarlatos, D. Tsoukalas, and A. Nejim, Nucl. Instr. and Meth. B **148**, 273 (1999).
92. D. A. Porter, and K. E. Easterling, *Phase Transformations in Metals and Alloys* (Chapman & Hall, New York, NY, 1992).
93. C. S. Nichols, C. G. van de Walle, and S. T. Pantelides, Phys. Rev. B **40**, 5484 (1989).
94. S. M. Hu, Mat. Sci. and Engr. **R13**, 105 (1997).
95. H.-J. Gossmann, T. E. Haynes, P. A. Stolk, D. C. Jacobson, G. H. Gilmer, J. M. Poate, H. S. Luftman, T. K. Mogi, and M. O. Thompson, Appl. Phys. Lett. **71**, 3862 (1997).
96. G. Hobler, L. Pelaz, and C. S. Rafferty, J. Electrochem. Soc. **147**, 3494 (2000).
97. L. H. Zhang, K. S. Jones, P. H. Chi, and D. S. Simons, Appl. Phys. Lett. **67**, 2025 (1995).
98. P. A. Stolk, H.-J. Gossmann, D. J. Eaglesham, D. C. Jacobson, and J. M. Poate, Appl. Phys. Lett. **66**, 568 (1995).
99. P. Packan, Ph.D. Dissertation, Stanford University, Stanford, CA (1989).
100. R. W. Olesinski and G. J. Abbaschian, Bulletin of Alloy Phase Diagrams **5**, 478 (1984).
101. T. L. Aselage, J. Mat. Res. **13**, 1786 (1998).
102. A. I. Zaitsev, and A. A. Kodentsov, J. Phase Equilibria **22**, 126 (2001).
103. F. N. Rhines, *Phase Diagrams in Metallurgy: Their Development and Application* (McGraw-Hill, New York, 1956).
104. A. Agarwal, D. J. Eaglesham, H.-J. Gossmann, L. Pelaz, S. B. Herner, D. C. Jacobson, T. E. Haynes, Y. Erokhin, and R. Simonton, Tech. Dig. Int. Electr. Dev. Meet., 467 (1997).
105. E. J. H. Collart, A. J. Murrell, M. A. Foad, J. A. van den Berg, S. Zhang, D. Armour, R. D. Goldberg, T.-S. Wang, A. G. Cullis, T. Clarysse, and W. Vandervorst, J. Vac. Soc. and Tech. B **18**, 435 (2000).

106. A. D. Lilak, V. Krishnamoorthy, D. Vieira, M. Law, and K. Jones, Mat. Res. Soc. Symp. Proc. **610**, B5.4.1 (2000).
107. W. Luo, P. B. Rasband, P. Clancy, and B. W. Roberts, J. Appl. Phys. **84**, 2476 (1998).
108. A. D. Lilak, M. E. Law, K. S. Jones, M. D. Giles, E. Andideh, M.-J. Caturla, T. Diaz de la Rubia, J. Zhu, and S. Theiss, Tech. Dig. Int. Electr. Dev. Meet., 493 (1997).
109. L. Pelaz, G. H. Gilmer, H.-J. Gossman, C. S. Rafferty, M. Jaraiz, and J. Barbolla, Appl. Phys. Lett. **74**, 3657 (1999).
110. M. J. Caturla, M. D. Johnson, and T. D. de la Rubia, Appl. Phys. Lett. **72**, 2736 (1998).
111. M. E. Law and K. S. Jones, in Proceedings of Process Physics and Modeling in Semiconductor Technology Conference, Los Angeles, CA 1996 (Electrochemical Society), **4**, 374 (1996).
112. T. E. Haynes, D. J. Eaglesham, P. A. Stolk, H.-J. Gossman, D. C. Jacobson, and J. M. Poate, Appl. Phys. Lett. **69**, 1376 (1996).
113. H. G. A. Huizing, C. C. G. Visser, N. E. B. Cowern, P. A. Stolk, and R. C. M. de Kruif, Appl. Phys. Lett. **69**, 1211 (1996).
114. N. E. B. Cowern, G. F. A. van de Walle, P. C. Zalm, and D. W. E. Vandenhoudt, Appl. Phys. Lett. **65**, 2981 (1994).
115. A. J. Mayur, A. Jaggi, and A. Jain, Proc. 8th Int. Conf. Advanced Thermal Processing of Semiconductors, 196 (2000).
116. A. Jain, L. S. Robertson, and K. A. Gable, Proc. 10th Int. Conf. Advanced Thermal Processing of Semiconductors, 31 (2002).
117. A. Mokhberi, P. B. Griffin, J. D. Plummer, E. Paton, S. McCoy, and K. Elliott, IEEE Tran. on Elec. Dev. **49**, No. 7, 1183 (2002).
118. C. D. Lindfors, Ph.D. Dissertation, University of Florida, Gainesville, FL (2003).
119. J. Narayan, J. Appl. Phys. **53**, 8607 (1982).
120. J. Narayan, O. W. Holland, and B. R. Appleton, J. Vac. Sci. Tech. B **1**, 871 (1983).
121. J. M. Poate and J. S. Williams, *Ion Implantation and Beam Processing* (Academic Press, New York 1984).
122. J. S. Williams, Nucl. Inst. and Meth. **209/210**, 219 (1983).

123. J. S. Williams, *Surface Modification and Alloying* (Plenum Press, New York, 1983).
124. P. J. Timans, R. A. McMahon, and H. Ahmed, Mat. Res. Soc. Symp. Proc. **45**, 337 (1985).
125. P. J. Timans, R. A. McMahon, and H. Ahmed, Mat. Res. Soc. Symp. Proc. **52**, 123 (1986).
126. R. G. Elliman, J. S. Williams, S. T. Johnson, and E. Nygren, May. Res. Soc. Symp. Proc. **74**, 471 (1987).
127. R. G. Elliman, J. S. Williams, W. L. Brown, A. Leiberich, D. M. Maher, and R. V. Knoell, Nucl. Inst. and Meth. in Phys. Res. B **B19/20**, 435 (1987).
128. H. Kerkow, G. Kreysch, G. Wolf, and K. Holldack, Phys. Stat. Sol. **94**, 793 (1986).
129. J. S. Williams, W. L. Brown, R. G. Elliman, R. V. Knoell, O. M. Maher, and T. E. Seidel, Mat. Res. Soc. Symp. Proc. **45**, 79 (1985).
130. S. A. Kokorowski, G. L. Olson, and L. D. Hess, J. Appl. Phys. **53**, 192 (1982).
131. G. L. Olson, J. A. Roth, L. D. Hess, and J. Narayan, Mat. Res. Soc. Symp. Proc. **23**, 375 (1984).
132. G. L. Olson, Mat. Res. Soc. Symp. Proc. **35**, 25 (1985).
133. G. L. Olson, J. A. Roth, Y. Rytz-Froidevaux, and J. Narayan, Mat. Res. Soc. Symp. Proc. **35**, 211 (1985).
134. L. Csepregi, J. W. Mayer, and T. W. Sigmon, Phys. Lett. **54A**, 157 (1975).
135. L. Csepregi, E. F. Kennedy, J. W. Mayer, and T. W. Sigmon, J. Appl. Phys. **49**, 3906 (1978).
136. R. Drosd and J. Washburn, J. Appl. Phys. **53**, 397 (1982).
137. L. Csepregi, E. F. Kennedy, T. J. Gallagher, and J. W. Mayer, J. Appl. Phys. **48**, 4234 (1977).
138. K. T. Ho, I. Suni, and M.-A. Nicolet, J. Appl. Phys. **56**, 1207 (1984).
139. H. Kerkow, G. Kreysch, and B. Lukasch, Phys. Stat. Sol. **82**, 125 (1984).
140. I. Suni, G. Goltz, M. G. Grimaldi, M.-A. Nicolet, and S. S. Lau, Appl. Phys. Lett. **40**, 269 (1982).
141. I. Suni, G. Goltz, M.-A. Nicolet, and S. S. Lau, Thin Solid Films **93**, 171 (1982).

142. G. L. Olson and J. A. Roth, Mat. Sci. Rep. **3**, 1 (1988).
143. D. H. Auston, J. A. Golovchenko, P. R. Smith, C. M. Surko, T. N. C. Venkatesan, Appl. Phys. Lett. **33**, 539 (1978).
144. J. S. Williams, W. L. Brown, H. J. Leamy, J. M. Poate, J. W. Rodgers, D. Rousseau, G. A. Rozgonyi, J. A. Shelnutt, and T. T. Sheng, Appl. Phys. Lett. **33**, 542 (1978).
145. Edited by J. M. Poate and J. W. Mayer, *Laser Annealing of Semiconductors* (Academic Press, New York, 1982).
146. A. Lietoila, J. F. Gibbons, and T. W. Sigmon, Appl. Phys. Lett. **36**, 765 (1980).
147. A. Gat, J. F. Gibbons, T. J. Magee, J. Peng, P. Williams, V. Deline, and C. A. Evans Jr., Appl. Phys. Lett. **33**, 389 (1978).
148. R. W. Bicknell and R. M. Allen, Radiat. Eff. **6**, 45 (1970).
149. G. A. Rozgonyi, H. J. Leamy, T. T. Sheng, and G. K. Celler, *Laser-Solid Interactions and Laser Processing* (American Institute of Physics, New York, 1979).
150. K. Ishida, H. Okabayashi, and M. Yoshida, Appl. Phys. Lett. **37**, 175 (1980).
151. M. Mizuta, N. H. Sheng, J. L. Merz, A. Lietoila, R. B. Gold, and J. F. Gibbons, Appl. Phys. Lett. **37**, 154 (1980).
152. R. H. Uebbing, P. Wagner, H. Baumgart, and H. J. Queisser, Appl. Phys. Lett. **37**, 1078 (1980).
153. N. M. Johnson, D. J. Bartelink, M. D. Moyer, J. F. Gibbons, A. Lietoila, K. N. Ratnakumar, and J. L. Regolini, *Laser and Electron Beam Processing of Materials* (Academic Press, New York, 1980).
154. S. Talwar, S. Felch, D. Downey, and Y. Wang, Proc. of the Conf. on Ion Implantation Technology, 175 (2000).
155. P. S. Peercy, M. O. Thompson, and J. Y. Tsao, Mat. Res. Soc. Symp. Proc. **74**, (1987).
156. H. Kodera, Jpn. J. Appl. Phys. **2**, 212 (1965).
157. P. Baeri, G. Foti, J. M. Poate, and A. G. Cullis, Phys. Rev. Lett. **45**, 2036 (1980).
158. R. Murto, K. Jones, M. Rendon, and S. Talwar, Proc. of the Conf. on Ion Implantation Technology, 182 (2000).

159. K. A. Gable, K. S. Jones, M. E. Law, L. S. Robertson, and S. Talwar, Mat. Res. Soc. Symp. Proc. **717**, C1.10 (2002).
160. H. Banisaukas, M.S. Thesis, University of Florida, Gainesville, FL (2000).
161. K. A. Gable, L. S. Robertson, K. S. Jones, and M. E. Law, Proc. 7th Int. Conf. on the Measurement, Characterization, and Modeling of Ultra-Shallow Doping Profiles in Semiconductors (USJ '03), Santa Cruz, CA, 373 (2003).
162. K. A. Gable, SRC TECHCON 2003, Dallas, TX (2003).
163. A. T. Fiory, D. M. Camm, M. E. Lefrancois, S. P. McCoy, and A. Agarwal, 195th Electrochem. Soc. Symp. Proc., 133 (1999).
164. T. Sato, Jpn. J. Appl. Phys. **6**, 339 (1967).
165. J. C. Gelpey, K. Elliott, D. M. Camm, S. P. McCoy, J. Ross, D. F. Downey, E. A. Arevalo, Proc. 9th Int. Conf. Advanced Thermal Processing of Semiconductors (RTP 99), Colorado Springs, CO, 23 (2001).
166. S. P. McCoy, J. Gelpey, K. Elliott, K. A. Gable, A. Jain, and L. S. Robertson, Proc. 7th Int. Conf. on the Measurement, Characterization, and Modeling of Ultra-Shallow Doping Profiles in Semiconductors (USJ '03), Santa Cruz, CA, 104 (2003).
167. J. P. Hebb, Ph.D. Dissertation, Massachusetts Institute of Technology, Cambridge, MA (1997).
168. H. Rogné and H. Ahmed, Mat. Res. Soc. Symp. Proc. **525**, 27 (1998).
169. M. E. Lefrancois, D. M. Camm, and B. J. Hickson, Proc. 7th Int. Conf. Advanced Thermal Processing of Semiconductors, 93 (1999).
170. R. B. Fair, and J. C. C. Tsai, J. Electrochem. Soc. **124**, 1107 (1997).
171. H. A. Storms, K. F. Brown, and J. D. Stein, Anal. Chem. **49**, 2023 (1977).
172. R. Brundle, C. A. Evans, Jr., and S. Wilson, *Encyclopedia of Materials Characterization: Surfaces, Interfaces, Thin Films* (Manning/Butterworth-Heinemann, 1992) and references therein.
173. D. B. Williams, and C. B. Carter, *Transmission Electron Microscopy* (Plenum Press, New York, 1996).
174. F. M. Smits, Bell System Technical Journal **37**, 371 (1958). (Same as BT Monograph, 3894, Part 2).
175. L. B. Valdes, Feb. Proc. of the IRE, 420 (1954).

176. J. A. Weil, J. R. Bolton, and J. E. Wertz, *Electron Paramagnetic Resonance: Elementary Theory and Practical Applications* (Wiley-Interscience, 1994).
177. D. F. Downey, C. M. Osburn, and S. D. Marcus, Solid State Technol. **40**, December (1997).
178. J. Narayan, and O. W. Holland, Phys. Stat. Sol. (a) **78**, 225 (1982).
179. S. U. Campisano, G. Foti, P. Baeri, M. G. Grimaldi, and E. Rimini, Appl. Phys. Lett. **37**, 719 (1980).
180. R. Angelucci, P. Negrini, and S. Solmi, Appl. Phys. Lett. **49**, 1468 (1986).
181. M. Servidori, Z. Sourek, and S. Solmi, J. Appl. Phys. **62**, 1723 (1987).
182. A. C. King, A. F. Gutierrez, A. F. Saavedra, K. S. Jones, and D. F. Downey, J. Appl. Phys. **93**, 2449 (2003).
183. P.-S. Chen, T. E. Hsieh, Y.-C. Hwang, and C.-H. Chu, J. Appl. Phys. **86**, 5399 (1999).
184. F. Cristiano, B. Colombeau, B. de Mauduit, C. Bonafos, G. Benassayag, and A. Claverie, Mat. Res. Soc. Symp. Proc. **717**, C5.7.1 (2002).
185. M. B. Huang, and I. V. Mitchell, Appl. Phys. Lett. **69**, 2734 (1996).
186. H.-J. Gossmann, A. M. Vredenberg, C. S. Rafferty, H. S. Luftman, F. C. Unterwald, D. C. Jacobson, T. Boone, and J. M. Poate, J. Appl. Phys. **74**, 3150 (1993).
187. R. Lindsay, B. J. Pawlak, P. A. Stolk, and K. Maex, Mat. Res. Soc. Symp. Proc. **717**, C2.1.1 (2002).
188. J.-Y. Jin, J. Liu, U. Jeong, S. Metha, and K. S. Jones, J. Vac. Sci. Tech. B **20**, 422 (2002).
189. A. Gutierrez, M.S. Thesis, University of Florida, Gainesville, FL (2001).
190. R. G. Elliman, S. M. Hogg, and P. Kringshøj, 1998 Intl. Conf. on Ion Imp. Tech. Proc., 1055 (1998).
191. W. F. J. Slijkerman, P. M. Zagwijn, J. F. van der Veen, G. F. A. van de Walle, and D. J. Gravesteijn, J. Appl. Phys. **70**, 2111 (1991).
192. B. Park, F. Spaepen, J. M. Poate, F. Priolo, and D. C. Jacobson, Mat. Res. Soc. Symp. Proc. **128**, 243 (1989).
193. J. Borland, Mat. Res. Soc. Symp. Proc., Vol. 717, C1.1.1 (2002).

194. A. Polman, D. C. Jacobson, S. Coffa, J. M. Poate, S. Roorda, and W. C. Sinke, *Appl. Phys. Lett.* **57**, 1230 (1990).
195. S. Coffa, and J. M. Poate, *Appl. Phys. Lett.* **59**, 2296 (1991).
196. J. M. Jacques, L. S. Robertson, K. S. Jones, M. E. Law, M. Rendon, and J. Bennett, *App. Phys. Lett.* **82**, 3469 (2003).
197. W. Frank, *Def. Diff. Forum* **75**, 121 (1991).
198. S. Roorda, W. C. Sinke, J. M. Poate, D. C. Jacobson, S. Dierker, B. S. Dennis, D. J. Eaglesham, F. Spaepen, and P. Fuoss, *Phys. Rev. B* **44**, 3702 (1991).
199. S. Coffa, J. M. Poate, D. C. Jacobson, and A. Polman, *Appl. Phys. Lett.* **58**, 2916 (1991).
200. E. Nygren, B. Park, L. M. Goldman, and F. Spaepen, *Appl. Phys. Lett.* **56**, 2094 (1990).
201. S. Dannefaer, D. Kerr, and B. G. Hogg, *J. Appl. Phys.* **54**, 155 (1983).
202. S. Roorda, J. M. Poate, D. C. Jacobson, B. S. Dennis, S. Dierker, and W. C. Sinke, *Appl. Phys. Lett.* **56**, 2097 (1990).
203. G. N. van den Hoven, Z. N. Liang, L. Niesen, and J. S. Custer, *Phys. Rev. Lett.* **68**, 3714 (1992).
204. S. Roorda, R. A. Hakvoort, A. van Veen, P. A. Stolk, and F. W. Saris, *J. Appl. Phys.* **72**, 5145 (1992).
205. L. S. Robertson, A. Lilak, M. E. Law, K. S. Jones, P. S. Kringshøj, L. M. Rubin, J. Jackson, D. S. Simons, and P. Chi, *Appl. Phys. Lett.* **71**, 3105 (1997).
206. K. S. Jones, K. Moller, J. Chen, M. Puga-Lambers, B. Freer, J. Berstein, and L. Rubin, *J. Appl. Phys.* **81**, 6051 (1997).
207. K. S. Jones, R. G. Elliman, M. M. Petracic, and P. Kringshøj, *Appl. Phys. Lett.* **68**, 3111 (1996).
208. W. Johnson, *Sol.-State Electr.* **13**, 951 (1969).
209. A. Agarwal, H.-J. Gossman, A. T. Fiory, V. C. Venezia, and D. C. Jacobson, *Proc. Electrochem. Soc., PV 2000*, May 14-18 (2000), Toronto, Canada.
210. N. E. B. Cowern, J. T. F. Janssen, and H. F. F. Jos, *J. Appl. Phys.* **68**, 6191 (1990).
211. N. E. B. Cowern, G. F. A. van de Walle, D. J. Gravesteijn, and C. J. Vriezema, *Phys. Rev. Lett.* **67**, 212 (1991).

- 212. C. S. Nichols, C. G. Van de Walle, and S. T. Pantelides, Phys. Rev. Lett. **62**, 1049 (1989).
- 213. N. E. B. Cowern, G. F. A. van de Walle, P. C. Zalm, and D. J. Oostra, Phys. Rev. Lett. **69**, 116 (1992).
- 214. F. Cembali, M. Servidori, E. Landi, and S. Solmi, Phys. Status Solidi A **94**, 315 (1986).
- 215. R. Angellucci, F. Cembali, P. Negrini, M. Servidori, and S. Solmi, J. Electrochem. Soc. **134**, 3130 (1987).
- 216. E. Napolitani, A. Carnera, E. Schroer, V. Privitera, F. Priolo, and S. Moffatt, Appl. Phys. Lett. **75**, 1869 (1999).
- 217. E. Schroer, V. Privitera, F. Priolo, E. Napolitani, and A. Carnera, Appl. Phys. Lett. **76**, 3058 (2000).
- 218. D. Fan, J. Huang, R. J. Jaccodine, P. Kahora, and F. Stevie, Appl. Phys. Lett. **50**, 1745 (1987).
- 219. J. P. Biersack and L. G. Haggmark, Nucl. Instr. and Meth. **174**, 257 (1980).
- 220. I. Suni, U. Shrreter, M.-A. Nicolet, and J. E. Baker, J. Appl. Phys. **56**, 273 (1984).
- 221. D. Beeman, R. Tsu, and M. F. Thorpe, Phys. Rev. B **32**, 874 (1985).
- 222. A. Battaglia, S. Coffa, F. Priolo, G. Compagnini, and G. A. Baratta, Appl. Phys. Lett. **63**, 2204 (1993).
- 223. P. A. Stolk, F. W. Saris, A. J. M. Berntsen, W. F. van der Weg, L. T. Sealy, R. C. Barklie, G. Krötz, and G. Müller, J. Appl. Phys. **75**, 7266 (1994).
- 224. S. Coffa and J. M. Poate, Appl. Phys. Lett. **63**, 1080 (1993).
- 225. P. A. Stolk, L. Calcagnile, S. Roorda, W. C. Sinke, A. J. M. Berntsen, and W. F. van der Weg, Appl. Phys. Lett. **60**, 1688 (1992).
- 226. K. A. Gable, L. S. Robertson, A. Jain, and K. S. Jones, J. Appl. Phys. (in review).
- 227. R. G. Elliman, J. M. Gibson, D. C. Jacobson, J. M. Poate, and J. S. Williams, Appl. Phys. Lett. **46**, 478 (1985).
- 228. S. U. Campisano, J. M. Gibson, and J. M. Poate, Appl. Phys. Lett. **46**, 580 (1985).
- 229. G. Muller and B. Kalbitzer, Philos. Mag. B **38**, 241 (1978).
- 230. N. F. Mott and E. A. Davis, *Electronic Processes in Non-Crystalline Materials* (Oxford University Press, Oxford, 1979).

231. S. Coffa, F. Priolo, and A. Battaglia, Phys. Rev. Lett. **70**, 3756 (1993).
232. Edited by J. H. Crawford and L. M. Slifkin, *Point Defects in Solids* (Plenum, New York, 1975).
233. W. C. Sinke, S. Roorda, and F. W. Saris, J. Mater. Res. **3**, 1201 (1988).
234. J. S. Lannin, Phys. Today **41**, 28 (1988); J. Non-Cryst. Solids **97/98**, 39 (1987).
235. F. L. Vook, Phys. Rev. **125**, 855 (1962).
236. C. A. Volkert and A. Polman, Mat. Res. Soc. Symp. Proc. **235**, 3 (1992).
237. C. A. Volkert, J. Appl. Phys. **74**, 7107 (1993).
238. R. A. Street, *Hydrogenated Amorphous Silicon* (Cambridge University Press, Cambridge, 1991).
239. T. J. McMahon and Y. Xiao, Appl. Phys. Lett. **63**, 1657 (1993).
240. P. J. Caplan, E. H. Poindexter, B. E. Deal, and R. R. Razouk, J. Appl. Phys. **50**, 5847 (1979).
241. K. L. Brower, Appl. Phys. Lett. **43**, 1111 (1983).
242. L. E. Mosley and M. A. Paesler, Appl. Phys. Lett. **45**, 86 (1984).
243. J. H. Stathis and S. T. Pantelides, Phys. Rev. B **37**, 6579 (1988).
244. N. H. Nickel and E. A. Schiff, Phys. Rev. B **58**, 1114 (1998).
245. S. T. Pantelides, Phys. Rev. Lett. **57**, 2979 (1986).
246. S. T. Pantelides, Phys. Rev. Lett. **58**, 1344 (1987).
247. S. T. Pantelides, Phys. Rev. Lett. **58**, 2825 (1987).
248. S. T. Pantelides, Phys. Rev. B **36**, 3479 (1987).
249. W. B. Jackson, C. C. Tsai, and R. Thompson, Phys. Rev. Lett. **64**, 56 (1990).
250. P. A. Thomas, M. H. Brodsky, D. Kaplan, and D. Lepine, Phys. Rev. **18**, 3059 (1978).
251. C. N. Waddel, W. G. Spitzer, J. E. Fredrickson, G. H. Hubler, and T. A. Kennedy, J. Appl. Phys. **55**, 4361 (1984).
252. P. Hautojärvi, P. Huttunen, J. Mäkinen, E. Punka, and A. Vehanen, Mat. Res. Soc. Symp. Proc. **104**, 105 (1988).

253. P. Kuo, J. L. Hoyt, J. F. Gibbons, J. E. Turner, R. D. Jacobowitz, and T. I. Kamins, *Appl. Phys. Lett.* **62**, 612 (1993).
254. N. Moriya, L. C. Feldman, H. S. Luftman, C. A. King, J. Bevk, and B. Freer, *Phys. Rev. Lett.* **71**, 883 (1993).
255. G. H. Loechelt, G. Tam, J. W. Steele, L. K. Knoch, K. M. Klein, J. K. Watanabe, and J. W. Christiansen, *J. Appl. Phys.* **74**, 5520 (1993).
256. P. Kuo, J. L. Hoyt, J. F. Gibbons, J. E. Turner, and D. Lefforge, *Appl. Phys. Lett.* **66**, 580 (1995).
257. P. Kuo, J. L. Hoyt, J. F. Gibbons, J. E. Turner, and D. Lefforge, *Appl. Phys. Lett.* **67**, 706 (1995).
258. T. T. Fang, W. T. C. Fang, P. B. Griffin, and J. D. Plummer, *Appl. Phys. Lett.* **68**, 791 (1996).
259. R. F. Lever, J. M. Bonar, A. F. W. Willoughby, *J. Appl. Phys.* **83**, 1988 (1998).
260. K. Rajendran and W. Schoenmaker, *J. Appl. Phys.* **89**, 980 (2001).
261. J. C. Bean, A. T. Fiory, R. Hull, and R. T. Lynch, *Proceedings of the First International Symposium on Si Molecular Beam Epitaxy* (Electrochemical Society, Pennington, New Jersey, 1985).
262. W. G. Spitzer, G. K. Hubler, and T. A. Kennedy, *Nucl. Instr. Meth.* **209/210**, 309 (1983).
263. S. P. Wong, M. C. Poon, H. L. Kwok, and Y. W. Lam, *J. Electrochem. Soc.* **113**, 2172 (1986).
264. J. M. Jacques, N. Burbure, K. S. Jones, M. E. Law, L. S. Robertson, D. F. Downey, L. M. Rubin, J. Bennett, M. Beebe, and M. Klimov, *Mat. Res. Soc. Symp. Proc.* **810**, C10.3 (2004).
265. O. Hellman, *Mat. Sci. & Engr.* **R16**, 1 (1996).
266. S. Roorda, J. M. Poate, D. C. Jacobson, B. S. Dennis, S. Dierker, and W. C. Sinke, *Solid State Commun.* **57**, 197 (1990).
267. P. N. Keating, *Phys. Rev.* **145**, 637 (1966).
268. C. H. Bennett, P. Chaudhari, V. Moruzzi, and P. Steinhardt, *Philos. Mag. A* **40**, 485 (1979).
269. D. F. Downey, J. W. Chow, E. Ishida, and K. S. Jones, *Appl. Phys. Lett.* **73**, 1263 (1998).

270. K. S. Jones, D. K. Sadana, S. Prussin, J. Washburn, E. R. Weber, and W. J. Hamilton, *J. Appl. Phys.* **63**, 1414 (1988).
271. P. Blood, W. L. Brown, and G. L. Miller, *J. Appl. Phys.* **50**, 173 (1979).
272. J. Narayan and O. W. Holland, *Phys. Stat. Sol.* **78**, 225 (1982).
273. S. U. Campisano, E. Rimini, P. Baeri, and G. Foti, *Appl. Phys. Lett.* **37**, 170 (1980).
274. D. Turnbull, in the Proceedings of the Workshop on Laser-Induced Nucleation in Solids, Mon, Belgium, 1979.
275. J. Narayan and O. W. Holland, *Appl. Phys. Lett.* **41**, 239 (1982).
276. H. F. Wolf, *Silicon Semiconductor Data* (Pergamon, New York, 1969).
277. J. S. Williams and R. G. Elliman, *Appl. Phys. Lett.* **40**, 266 (1982).
278. L. Pauling, *The Nature of the Chemical Bond* (Cornell U. P., Ithaca, 1948).
279. L. Calcagno, S. U. Campisano, and S. Coffa, *J. Appl. Phys.* **66**, 1874 (1989).
280. S. Roorda, J. S. Custer, W. C. Sinke, J. M. Poate, D. C. Jacobson, A. Polman, and F. Spaepen, *Nucl. Instr. and Meth. in Phys. Res. B* **59/60**, 344 (1991).
281. W. K. Chu, M. Z. Numan, J. Z. Zhang, G. S. Sandhu, and A. E. Michel, *Nucl. Instrum. Meth. Phys. Res. B* **37/38**, 365 (1989).
282. Y. Kim, H. Z. Massoud, and R. B. Fair, *J. Electron. Mater.* **18**, 143 (1989).
283. R. B. Fair, *J. Electrochem. Soc.* **137**, 667 (1990).
284. P. J. Murkin and P. Moynagh, *J. Appl. Phys.* **66**, 6191 (1990).
285. F. J. Morin and J. P. Maita, *Phys. Rev.* **94**, 1525 (1954); F. J. Morin and J. P. Maita, *Phys. Rev.* **96**, 28 (1954).
286. J. L. Regolini, T. W. Sigmon, and J. F. Gibbons, *Appl. Phys. Lett.* **35**, 114 (1979).
287. J. L. Regolini, J. F. Gibbons, T. W. Sigmon, and R. F. W. Pease, *Appl. Phys. Lett.* **34**, 410 (1979).
288. A. Gat, J. F. Gibbons, T. J. Magee, J. Peng, V. R. Deline, P. Williams, and C. W. Evans, Jr., *Appl. Phys. Lett.* **32**, 276 (1978).

BIOGRAPHICAL SKETCH

Kevin Andrew Gable was born in Falls Church, Virginia on the 14th day of September in 1978. He was raised in nearby Fairfax, Virginia where he lived with parents Pamela Jo Gable and Rhett Eric Gable, and older brother Brian Matthew Gable. After graduating from Fairfax High School in June 1997, Kevin enrolled as a freshman at the University of Florida in Gainesville, Florida. Throughout his college career, Kevin held internships with MICROFABRITECH® laboratory at the University of Florida (Gainesville, Florida); the Intelligent Materials Processing (IMP) laboratory at the University of Virginia (Charlottesville, Virginia); Verdant Technologies, Inc. (San Jose, California); and (two internships with) Texas Instruments, Inc. (Dallas, Texas). He received his B.S., M.S., and Ph.D. degrees in materials science and engineering from the University of Florida in May 2001, August 2003, and August 2004, respectively. Kevin will join Intel Corporation after completing his doctoral studies in 2004. His research interests include advanced materials development for nanotechnology applications.